PHASE STABILITY AND MICROSTRUCTURAL EVOLUTION IN V-Ti-Cr SYSTEM USING PHASE CONTRAST, HAADF IMAGING AND ELECTRON SPECTROSCOPY

By
CHANCHAL GHOSH
PHYS 02 2010 04 021

Indira Gandhi Centre for Atomic Research, Kalpakkam

A thesis submitted to the

Board of Studies in Physical Sciences

In partial fulfillment of requirements
for the Degree of
DOCTOR OF PHILOSOPHY
of
HOMI BHABHA NATIONAL INSTITUTE

August, 2016

Homi Bhabha National Institute

Recommendations of the Viva Voce Committee

As members of the Viva Voce Committee, we certify that we have read the dissertation prepared by Chanchal Ghosh entitled "**Phase Stability and Microstructural Evolution in V-Ti-Cr System Using Phase Contrast, HAADF Imaging and Electron Spectroscopy**" and recommend that it may be accepted as fulfilling the thesis requirement for the award of Degree of Doctor of Philosophy.

for N.V. Chandrasekhar (Dean, Academic)

Chairman – Dr. M. Vijayalakshmi — **Date:** 3/3/17

Guide / Convener – Dr. Divakar Ramachandran — **Date:** 03/03/2017

Examiner – Prof. N. Prabhu — **Date:** 03/03/17

Member 1- Dr. Raghvendra Tewari — **Date:** 03/03/2017

G. Amarendra

Member 2- Dr. G. Amarendra — **Date:** 03/03/2017

for N.V. Chandrasekhar (Dean, Academic)

Member 3- Mr. E. Mohandas — **Date:** 3/3/17

Final approval and acceptance of this thesis is contingent upon the candidate's submission of the final copies of the thesis to HBNI.

I/~~We~~ hereby certify that I/~~we~~ have read this thesis prepared under my/~~our~~ direction and recommend that it may be accepted as fulfilling the thesis requirement.

Date: 03/03/2017

Place: KALPAKKAM

Dr. Divakar Ramachandran

STATEMENT BY AUTHOR

This dissertation has been submitted in partial fulfillment of requirements for an advanced degree at Homi Bhabha National Institute (HBNI) and is deposited in the Library to be made available to borrowers under rules of the HBNI.

Brief quotations from this dissertation are allowable without special permission, provided that accurate acknowledgement of source is made. Requests for permission for extended quotation from or reproduction of this manuscript in whole or in part may be granted by the Competent Authority of HBNI when in his or her judgment the proposed use of the material is in the interests of scholarship. In all other instances, however, permission must be obtained from the author.

Chanchal Ghosh

Chanchal Ghosh

DECLARATION

I, hereby declare that the investigation presented in the thesis has been carried out by me. The work is original and has not been submitted earlier as a whole or in part for a degree / diploma at this or any other Institution / University.

Chanchal Ghosh

Chanchal Ghosh

List of Publications arising from the thesis

Journal

a. Published:

1. “Synthesis and structural characterization of V-4Ti-4Cr alloy”, C Ghosh, J. Basu, S. Khan, R. Divakar, E. Mohandas, M. Vijayalakshmi, *Trans. Ind. Inst. Met.,* **2013,** 66(4), 381-385.

2. “Structure imaging and Vanadium substitution in cubic $TiCr_2$ Laves phase” C. Ghosh, V. Sharma, J. Basu, R. Divakar, E. Mohandas, , *Philos. Mag.,* **2015** 95:22, 2403-2426.

3. “Alloy design and microstructural evolution in V-Ti-Cr alloys”, C. Ghosh, J. Basu, R. Divakar, E. Mohandas, *Mater. Characterization,* **2015**, 106, 292-301.

4. “Phase and microstructure evolution in V-Ti-(Cr/W) alloys”, C. Ghosh, J. Basu, R. Divakar, E. Mohandas, *Mater. Today: Proc.* **2016**, 3(9), 2920-2925.

5. “Phase separation and ω transformation in binary V-Ti and ternary V-Ti-Cr alloys”, C. Ghosh, J. Basu, R. Divakar, E. Mohandas, *Acta Mater.*, **2016**, 121, 310-324.

6. “Microstructural and microchemical studies of phase stability in V-O solid solution”, C. Ghosh, A. Singh, J. Basu, R. Divakar, E. Mohandas, *Mater. Characterization,* **2017**, 124, 129-135.

b. Under Review:

1. “Structure imaging of ω domains in phase separated V-Ti-Cr alloys”, C. Ghosh, J. Basu, R. Divakar, E. Mohandas, **(2016 - under review)** Submitted manuscript number: TPHM-16-JUL-0340.

c. Under Preparation:

1. “Spectroscopy through high-resolution electron microscopy”, C. Ghosh, J. Basu, R. Divakar, E. Mohandas, **(under preparation)**.

Conference Proceedings

1. “Experimental and computational HRTEM characterization of V-4Ti-4Cr alloys”, C. Ghosh, J. Basu, S. Khan, R. Divakar, E. Mohandas, M. Vijayalakshmi, *Proc. of 24th AGM of MRSI*, **2013**, 11-13th Feb. 2013, Kalpakkam (India), 45, 45100323.

2. “High-resolution Structural Imaging and STEM Spectroscopy Studies of Phase Transformation in V-Ti-Cr alloys”, C. Ghosh, J. Basu, R. Divakar, E. Mohandas, P. Hozák (Eds.) *Proc. of 18th International Microscopy congress,* **2014**, 07-12th Sept. 2014, Prague (Czech Republic), ISBN 978-80-260-6720-7.

3. "Complementary nature of microscopy techniques for understanding materials phenomena", C. Ghosh, J. Basu, R. Divakar, E. Mohandas, P. Hozák (Eds.) *Proc. of 18th International Microscopy congress,* **2014**, 07-12th Sept. 2014, Prague (Czech Republic), ISBN 978-80-260-6720-7.

Conference Presentations

1. "Direct structure imaging of omega domains in phse separated V-Ti-Cr alloys", C. Ghosh, J. Basu, R. Divakar, E. Mohandas, *ICMR-2016:International conference Metals and Materials Research,* **2016**, June 20-22, IISc, Bangalore (India).

2. "Spinodal decomposition and omega transformation in binary V-Ti and ternary V-Ti-Cr alloys", C. Ghosh, J. Basu, R. Divakar, E. Mohandas, *EMSI-2016:International conference on electron microscopy & 37th annual meeting of EMSI,* **2016**, June 2-4, Varanasi (India).

3. "Alloy Design and Phase Evolution in V-Ti-Cr alloys", C. Ghosh, J. Basu, R. Divakar, E. Mohandas, *ARRMA 2016: Conference on advances in refractory and reactive metals and alloys,* **2016**, Jan. 27-29, Anushaktinagar, Mumbai (India).

4. "Phase and Microstructure Evolution in V-Ti-Cr alloys", C. Ghosh, J. Basu, R. Divakar, E. Mohandas, *ICSSP6-2015: 6th Intl. conference on solidification science and processing,* **2015**, Nov. 24-27, Hyderabad (India).

5. "Quantitative HRTEM and STEM-EELS Studies of Phase Separation and ω Transformation in V-Ti-Cr alloys" C. Ghosh, J. Basu, R. Divakar, E. Mohandas, *EMSI-2015:International conference on electron microscopy & 36th annual meeting of EMSI*, **2015**, July 8-10, Mumbai (India).

6. "Chemistry at the Atomic Scale through High Resolution Imaging", C. Ghosh, J. Basu, R. Divakar, E. Mohandas, *EMSI-2015:International conference on electron microscopy & 36th annual meeting of EMSI*, **2015**, July 8-10, Mumbai (India).

7. "Quantitative HRTEM and STEM-EELS studies of phase transformation in V-Ti-Cr alloys", C. Ghosh, J. Basu, R. Divakar, E. Mohandas, *EMSI-2014: International conference on electron microscopy & 35th annual meeting of EMSI*, **2014**, July 7-11, Delhi University, New Delhi (India).

8. "Direct Structural Imaging and V Substitution in Doped $TiCr_2$ Cubic Laves Phase", C. Ghosh, J. Basu, R. Divakar, E. Mohandas, *IUMRS-ICA-2013: International Union of Materials Research Society-International Conference in Asia* - **2013**, Dec 16-20, IISc, Bangalore (India).

9. "Phase Stability Studies in 38Ti-55Cr-7V Laves Phase", C. Ghosh, J. Basu, S. Khan, R. Divakar, E. Mohandas, *EMSI-2013:International Conference on Electron Microscopy and 34th annual meeting of the EMSI*, **2013**, July 3-5, Kolkata, (India).

10. "Experimental and Computational HRTEM Characterization of V-4Ti-4Cr Alloys", C. Ghosh, J. Basu, S. Khan, R. Divakar, E. Mohandas, M. Vijayalakshmi, *MRSI-2013; 24th AGM of Materials Research Society of India*, **2013**, Februray 11-13, IGCAR, Kalpakkam (India).

11. "Synthesis and Structural Characterization of V-4Ti -4Cr Alloy", C. Ghosh, J. Basu, S. Khan, R. Divakar, E. Mohandas, M. Vijayalakshmi, *ISRS-2012: 5th International Symposium for Research Scholars on Metallurgy, Materials Science and Engineering,* **2012**, December 13-15, IIT Madras, Chennai (India).

Chanchal Ghosh

Chanchal Ghosh

Dedicated to,

All my teachers and mentors

ACKNOWLEDGEMENTS

At the onset, I gratefully acknowledge the advice and guidance given by my guide **Dr. Divakar Ramachandran** through all these years of my Ph.D. His generous foresights, vital suggestions as well as the logical way of thinking on critical scientific problems are of great learning experience for me. In the same note, I would like to thank **Dr. Joysurya Basu** for his continuous support and untiring guidance towards my work. His vast pool of ideas are always a constant source of inspiration for me. With thought provoking discussions and unconditional helping hand he has always stepped forward to solve my problems, confusions and queries both on academic and personal front.

I would like to extend my sincere gratitude towards my doctoral committee members, **Dr. M. Vijayalakshmi, Dr. Raghvendra Tewari, Dr. G. Amarendra and Mr. E. Mohandas** for their untiring support and useful suggestions given time to time to improve the work.

I thankfully acknowledge **Dr. A.K. Bhaduri**, Director, IGCAR and **Dr. G. Amarendra,** Director, Metallurgy & Materials Group for providing me an opportunity to pursue this research work.

I acknowledge my collaborators, **Dr. Vinit Sharma** and **Dr. Akash Singh** for lending their supporting hands during different occasions of the present work.

I thankfully acknowledge **Prof. S. Ranganathan, Prof. S. Banerjee** and **Prof. C. Barry Carter** for many useful discussions and suggestions on several occasions.

I would specially thank **Dr. Arup Dasgupta** for his invaluable suggestions and comments over times that have helped me to overcome different aspects of my research. I gratefully acknowledge **all my friends** and the **senior members** of Physical Metallurgy Division for their support and encouragement in carrying out this research works over the years.

On a personal note, I want to acknowledge **Ramakrishna Mission** for shaping up my younger days. I wish to express my sincere gratitude and indebtedness to my **parents**, **parents-in-law**, **brother** for their blessings and other **family members** for their love and support to me. Finally, I am extremely thankful to my wife **Sutapa** and my little daughter **Apabrita** for all of their love and understanding and always be by my side in ups and downs.

Graphical abstract of the thesis

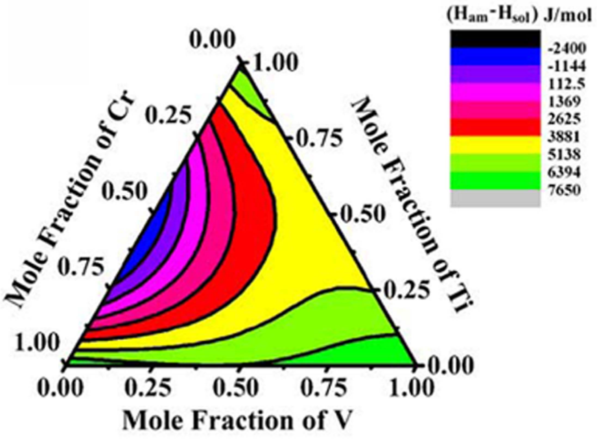

Enthalpy contour plot as calculated from Miedema model over the entire composition range of V-Ti-Cr

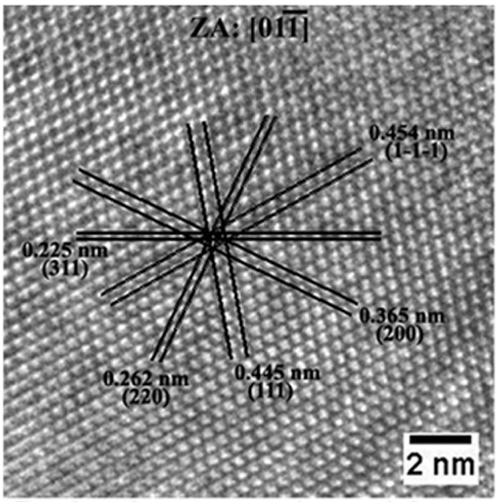

Zero-loss phase contrast micrograph from V-substituted TiCr$_2$ Laves phase alloy along [0 1 $\bar{1}$] zone axis

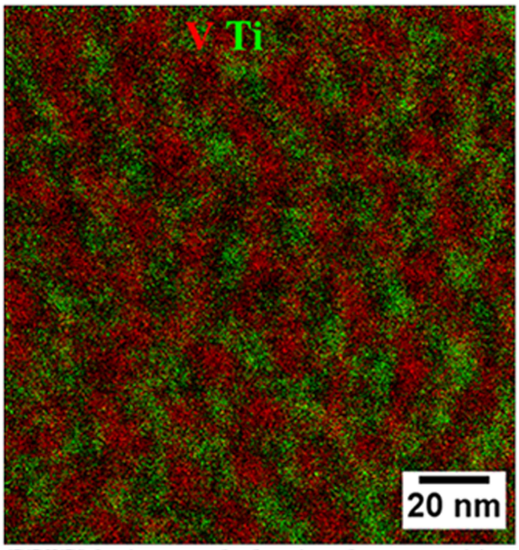

EFTEM micrograph showing the composition modulation from a Spinodally decomposed region in binary V-50Ti alloy

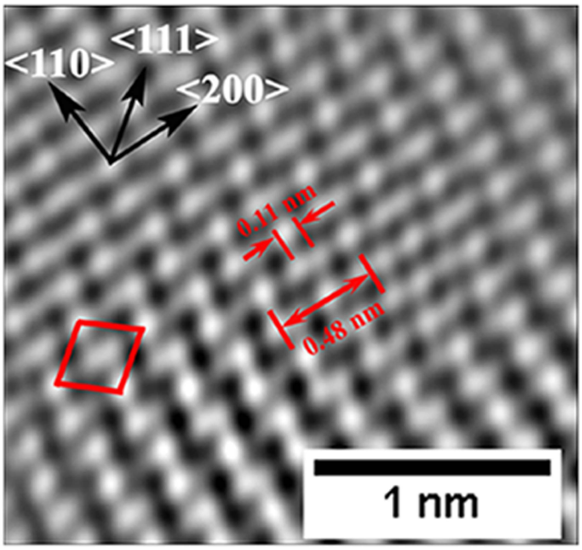

Phase contrast micrograph showing the atomic arrangement in a partially collapsed ω structure

Present figure provides a pictorial representation of the thesis entitled "Phase Stability and Microstructural Evolution in V-Ti-Cr System Using Phase Contrast, HAADF Imaging and Electron Spectroscopy". Thermodynamic calculations based on Miedema approach were instrumental to study the phase stability of V-Ti-Cr alloy system. Phase contrast microscopy aided with multislice simulation was carried out to understand the V-atom occupancy in V-substituted TiCr$_2$ Laves phase. Composition modulation through Spinodal decomposition and the subsequent ω phase formation in equiatomic V-Ti and V-Ti-20Cr alloys as well as their structural imaging are the other aspects of the thesis.

CONTENTS

I. INTRODUCTION

II. MATERIALS & METHODS

III. THERMODYNAMIC CALCULATIONS AND MICROSTRUCTURAL EVOLUTION IN V-Ti-Cr ALLOYS

IV. STRUCTURE IMAGING AND VANADIUM SUBSTITUTION IN CUBIC $TiCr_2$ LAVES PHASE

V. PHASE SEPARATION AND ω TRANSFORMATION IN BINARY V-Ti AND TERNARY V-Ti-Cr ALLOYS

VI. STRUCTURE IMAGING OF ω DOMAINS IN PHASE SEPARATED V-Ti-Cr ALLOYS

VII. SUMMARY AND FUTURE SCOPE

SYNOPSIS

Last couple of decades has seen a rapid surge in research and development activities in vanadium alloys, for possible development as advanced structural material for high-end engineering applications as well as in alternative energy technologies. Vanadium, in combination with Ti and Cr or W, has been identified as a potential candidate material for future fusion power systems, due to their superior mechanical properties coupled with reduced activation, fast decay characteristics, compatibility with liquid lithium and good figures of merit for low thermal stress generation. Additionally, over the last decade, Ti-V binary alloys have been explored extensively as potential candidates for storing hydrogen and its isotopes. The binary alloys and the phases so formed, show moderate to low hydrogen storage capacity and moderate hysteresis over charging and discharging cycles. Subsequently, V-Ti-Cr alloys and V-Ti-Mn alloys have been developed for hydrogen storage applications. As a functionally improved alternative for large scale storage of hydrogen and its isotopes, the Laves phase compounds with AB_2 and AB_5 structures are another set of materials which have also been considered widely. These types of materials have the advantages of higher hydrogen storage capacities, faster kinetics and relatively lower cost than pure V. Moreover, the thermodynamics and kinetics of the Laves phase can easily be manipulated by ternary metal substitution with Cr, Ni, Co, Fe etc.

The optimization of chemistry and processing for such advanced applications require understanding of the systems at the atomic level, supplemented by computational studies towards stability of phases. Both these fields, computational metallurgy and atomic resolution microscopy have developed rapidly, in recent years. In recent past, as a synergic effect of development in electron optics and

instrumentation, electron microscopy techniques have advanced to a considerable extent in terms of spatial resolution and elemental detection limits. Several microscopy techniques have also been developed to interface with the requirements from the materials science community. As of today the most commonly used techniques to obtain the structural and chemical information on the nanometer scale are phase contrast and Z contrast microscopy combined with electron energy loss spectroscopy (EELS) and X-ray energy dispersive spectroscopy (XEDS). Incoherent imaging of materials are directly interpretable as they rely on the fact that heavier atoms act as strong scattering centres while the lighter atoms scatter relatively weakly. In contrast, high resolution phase contrast images are not directly interpretable as the phase and amplitude of the electron wave are modified by the imaging system, in addition to the specimen potential. In order to understand the contrast quantitatively and relate it to the atom column positions unambiguously, simulation of the high-resolution image becomes highly essential.

Scope of the thesis

Successful implementation of binary Ti-V and ternary V-Ti-Cr alloys in alternative energy applications would require a thorough understanding of the phase stability and microstructural evolution. Though it is well established that a *bcc* solid-solution phase stabilizes at the V-rich corner of the phase diagram, other regions of the phase diagram are sparsely explored and require in-depth studies. Further, even though the binary Ti-Cr phase diagram is relatively complete, information regarding the formation of ordered intermetallics and the effect of ternary alloying addition such as V, at its Laves phase forming composition is scarce. Similarly, for binary V-Ti alloys, though enough thrust has been given in the last few decades, fundamentally different views still exist concerning the form of even the binary phase diagram as the phase formed upon solidification is still debated. Situation becomes even more complicated with the addition of ternary element. The phases formed on solidification are not always the equilibrium phases and the system hops along local minima in the energy landscape upon heat treatment.

In the present scenario, there is a need to understand the different phase fields of V-Ti-Cr system as well as its phase transformation behaviour for the entire composition range. Systematic studies are also required to understand the stability of different constituent phases and their structure and chemistry down to atomic level. In the present thesis, focus is on the investigation of the phase formation and microstructural evolution in V-Ti-Cr alloy systems. Keeping in mind the complexities involved in the studies of the phase transformation of an almost unexplored system, thermodynamic calculations are employed to map the phase formation behavior of binary and ternary alloys upon solidification. Thermodynamic predictions thus obtained using the Miedema approach have been employed to judiciously select alloy compositions across the entire V-Ti-Cr system to explore the phase fields. Phase stability studies on the selected binary alloys and the effect of ternary addition have been experimentally studied in the present thesis using phase contrast and *Z*-contrast microscopy techniques coupled with XEDS and EELS. Emphasis has been given in the possibilities of formation of any new phases as a phase transformation product in the alloy.

Present thesis entitled **"Phase Stability and Microstructural Evolution in V-Ti-Cr System Using Phase Contrast, HAADF Imaging and Electron Spectroscopy"** reports the results of the above empirical calculations and experimental studies and is organized into seven chapters as outlined below.

Chapter I: Introduction

This chapter gives a brief review of the applications of V-Ti-Cr alloys in alternative energy generation. A comprehensive literature survey has been provided on (i) nuclear applications and (ii) hydrogen storage applications. The history and the evolution of vanadium and V-based alloys also briefly reviewed. This is followed by a discussion on the physical metallurgical aspects of this alloy system, primarily from the perspective of phase transformations. A dedicated section discusses the advancements in various Transmission Electron Microscopy (TEM) based techniques for the microstructural and microchemical characterization of metallic and ceramic systems down to sub-nanometer scale, for resolving materials related issues in V-Ti-Cr alloys.

Chapter II: Materials and Methods

This chapter deals with the experimental techniques and procedures employed for the synthesis, characterization and evaluation of the structural and chemical stability of phases of the alloy. It also provides brief descriptions of the empirical models and the image simulation techniques used in the study. Alloy synthesis, processing and specimen preparation techniques especially for TEM would be described in the present chapter. It also consists brief descriptions of the TEM based imaging and spectroscopic techniques used in the present study. TEM characterization was carried out using a Tecnai G^2 F30 U-TWIN TEM operated at 300 kV and capable of a point resolution of 0.17 nm in phase contrast mode. It is equipped with EDAX rTEM XEDS system and the Gatan Quantum 965ER imaging filter. STEM-HAADF imaging was performed using Fischione HAADF detector.

Chapter III: Thermodynamic Calculations and Microstructural Evolution in V-Ti-Cr Alloys

In this chapter, phase formation and microstructural evolution in the constituent binaries and in ternary V-Ti-Cr alloys has been studied by Miedema approach. The compositions of the binary and ternary alloy systems have been chosen based on the predictions of the calculation and studied experimentally. Thermodynamic calculations based on Miedema model indicate that (i) V-Ti-Cr ternary alloys in the V-rich side of the phase diagram should form a solid-solution phase, (ii) ternary alloy compositions in the vicinity of binary $TiCr_2$ Laves phase should form an amorphous or intermetallics phase, and (iii) the expected solid-solution phase in binary equiatomic V-Ti and V-Ti-20Cr alloy system has phase separation tendency. Four alloy compositions, based on above observations, V-4Ti-4Cr, V-39Ti-54Cr, V-50Ti and V-40Ti-20Cr (all compositions are expressed in at%) were prepared and studied experimentally. V-4Ti-4Cr alloy forms *bcc* solid-solution phase upon solidification. In V-39Ti-54Cr alloy, V-substituted cubic $TiCr_2$ Laves phase is seen upon solidification. The *bcc* solid-solution phase in binary V-50Ti and ternary V-40Ti-20Cr alloys undergoes a phase separation reaction giving rise to V-rich and V-poor domains. In the ternary V-40Ti-20Cr alloy, the phase separation is found to be essentially binary, since Cr is distributed uniformly in the phase separated domains. Interesting possibilities deduced from the Miedema model for V-Ti-Cr alloys with reference to phase transformations and microstructural evolution have been experimentally explored. However, these results raise certain fundamental questions that require further investigations: (i) while thermodynamic calculations with the aid of electron microscopy studies confirm that V-39Ti-54Cr alloy stabilizes in a Laves phase structure; identification of the nature of this phase – ternary or

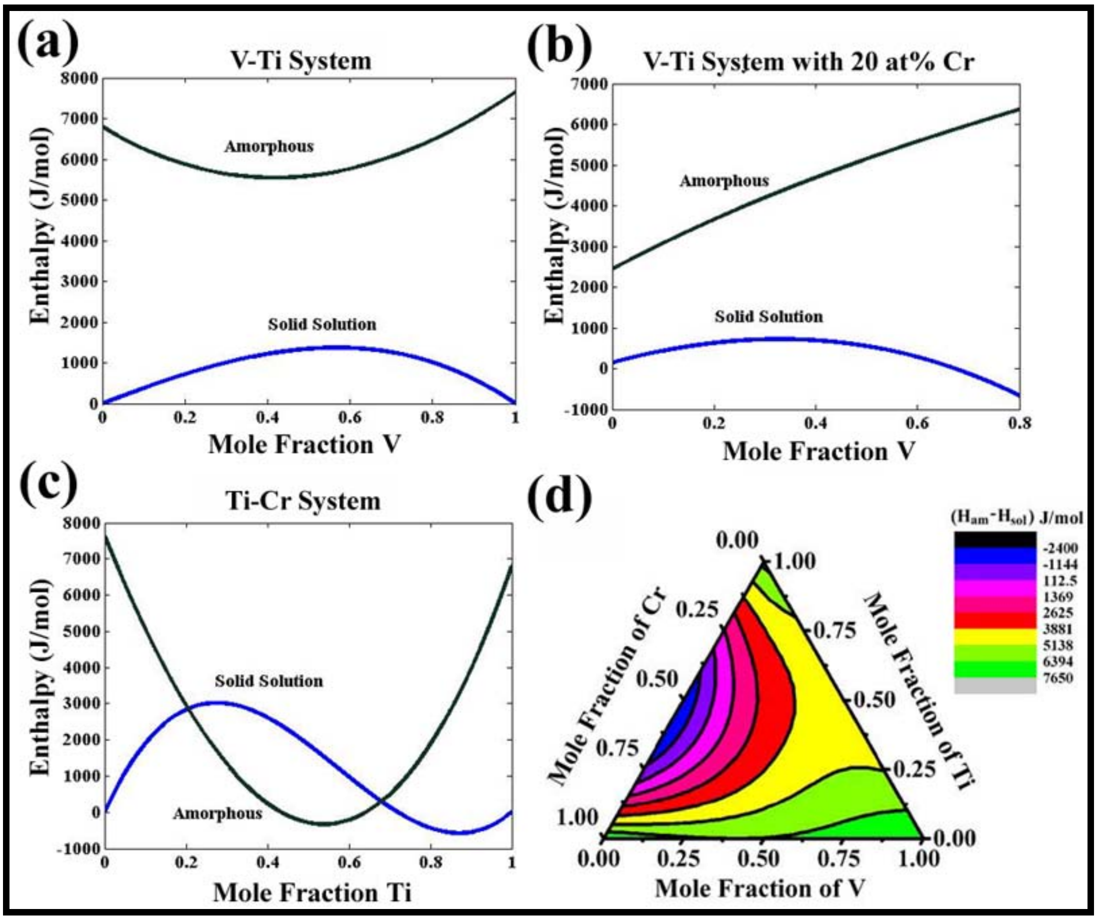

Fig. 1: (a) Enthalpy – composition plot for binary V-Ti alloy system. (b) Isopleths showing the effect of Cr addition (20 at%) in the enthalpy-composition plot for binary V-Ti alloy. (c) Enthalpy – composition plot for binary Ti-Cr alloy system. (d) Enthalpy contour plot showing the differences between the formation enthalpies of amorphous phase and solid-solution phase over the entire composition range of V, Ti and Cr. (Inset) shows the absolute values of the difference associated with the different colour codes.

pseudo-binary Laves phase requires information of V atom location in the lattice, (ii) classification of the phase separation event in binary V-Ti alloy and in ternary V-Ti-20Cr alloy; as Spinodal decomposition or as a nucleation and growth process requires systematic investigations. (iii) feasibility of the formation of any new phases in the phase separated domain as a result of local chemical modulation. These questions are addressed in the following chapters.

Chapter IV: Structure Imaging and Vanadium Substitution in Cubic $TiCr_2$ Laves Phase

Present chapter deals with direct structure imaging of the Laves phase structure as well as indirect determination of single column chemistry and V atom location in V-39Ti-54Cr alloy composition. Properties of Laves phase compounds can be tailored by alloying and microstructural engineering. V-substituted cubic $TiCr_2$ Laves phase has been studied to understand the incorporation of V atoms into the Laves phase lattice by structural imaging and first principles computations. It is found that V preferentially substitutes the Ti lattice producing anti-site defects. The defect formation energy for V substitution in Ti lattice and in Cr lattice has been calculated to be 0.29 eV and 0.40 eV respectively. Atomic numbers of V, Ti and Cr being very close, this phase is not quite suitable for incoherent imaging to understand the structure and the chemistry. However, V replacement in the Ti lattice generates measurable atomic scale strain. The modification in the intensity distribution of any particular atom by the presence of foreign atom has been used to detect the position of V atoms in the Laves phase matrix. Further, the difference in channeling behavior of electron waves along the Ti columns and along the Cr columns is exploited to preferentially image the individual atom columns. Nature of the phase and amplitude part of the exit phase wave has been used to understand the contrast qualitatively. This method could be extended to study other Laves phases and complex intermetallics structures to understand their structure, defects and interfaces.

Chapter V: Phase Separation and ω Transformation in Binary V-Ti and Ternary V-Ti-Cr Alloys

This chapter reports interesting findings on the phase transformation behaviour in binary V-Ti system and the effect of Cr addition. Thermodynamic

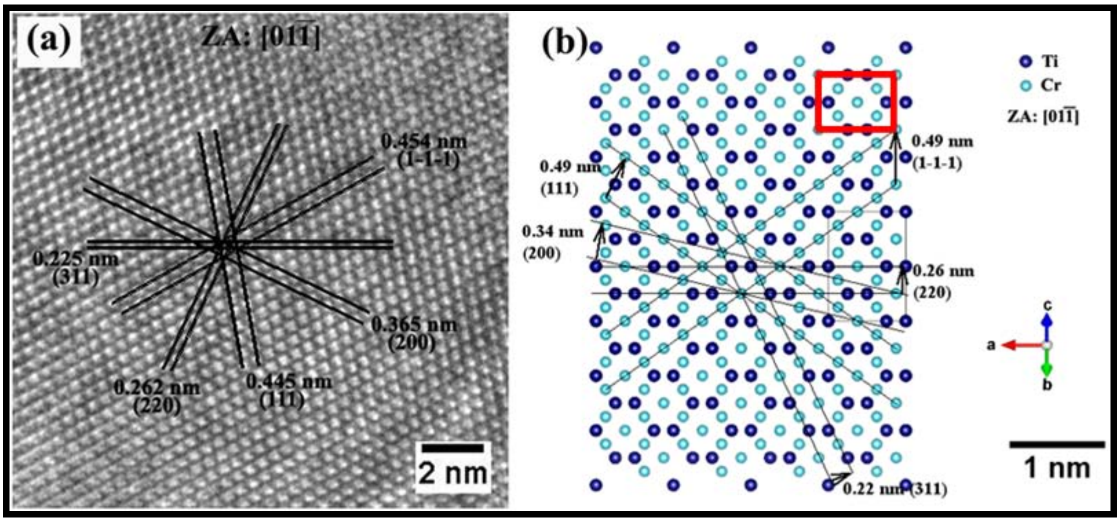

Fig. 2: (a) Zero-loss energy filtered phase contrast micrograph of V-substituted TiCr$_2$ Laves phase along [0 1 $\bar{1}$] zone axis. (b) Projected structure of cubic TiCr$_2$ Laves phase along same direction. Entire structure of the Laves phase can be described by the unit shown in red.

calculations reported in chapter III indicated a composition range in the V-Ti system, where a prominent miscibility gap exists and this reflects a propensity for phase separation that decreases with the addition of Cr to the binary system. Alloys with nominal composition of V-50Ti and V-40Ti-20Cr were prepared through vacuum arc melting and detailed microstructural and microchemical analyses have been carried out. Diffraction contrast and phase contrast images confirm the occurrence of phase separation in both the alloys, with following signatures: (a) lamellar and interconnected nanostructured domains with coherent interfaces as seen in the phase contrast mode (b) wavelength distribution and composition modulation in as-melted and heat treated alloys - as confirmed by Energy-filtered TEM (EFTEM), High-angle annular dark-field (HAADF) imaging associated with XEDS and EELS and (c) propagation of the fluctuation wave along elastically soft directions for cubic systems. These features–confirmed that the phase separation propagates through a Spinodal decomposition mechanism in this alloy and is not limited by nucleation and growth kinetics. Another interesting result reported in this chapter is the formation of nanostructured ω phase in the phase separated domains. Metastable ω phase formation ubiquitous in group IV-B transition metals (Ti, Zr, Hf) when subjected to very high pressures or over specific composition ranges when alloyed with *bcc* stabilizing elements. It is the latter effect that is seen in one of the phase separated domains, i.e, the phase separation shifts a part of the alloy to a composition regime where lattice instability leads to ω-phase formation. Selected area electron diffraction images in select orientations and the subsequent dark field imaging confirms the presence of distorted hexagonal zones of ω phase in the phase separated domains of the alloys. Shape, size and morphology of the ω structured phases have also been studied in the present chapter.

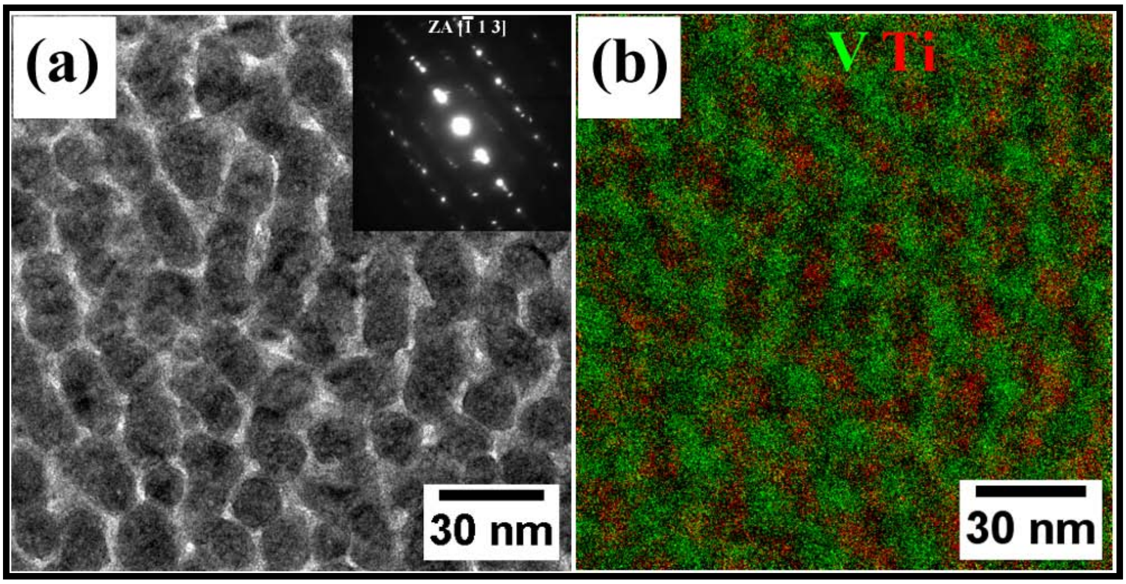

Fig. 3: (a) Bright field micrograph from aged and quenched V-50Ti alloy specimen showing the spinodal decomposed microstructure with the modulation length of ~ 18-20 nm. Satellites shown in the electron diffraction pattern (inset) confirm phase separation in the alloy. (b) Energy filtered TEM micrograph shows the chemical partitioning between vanadium (green) and titanium (red) rich regions in phase separated domain.

Chapter VI: Structure imaging of ω Domains in Phase Separated V-Ti-Cr Alloys

Binary V-Ti and ternary V-Ti-Cr alloys undergo a phase separation on solidification which results in nanoscale Ti-rich and Ti-lean domains, one of which further undergoes a displacive transformation to form ω phases, as shown in the previous chapter. This chapter deals with direct structure imaging of the ω structured domains along various crystallographic directions and the extent of lattice plane collapse during atomic level reshuffling. The structural details of the ω phase are revealed through high-resolution electron microscopy and phase contrast image simulation. It further invokes quantum mechanical effects to explain the contrast seen for atoms at the vertices of the ω unit cell and for the atoms in the collapsed planes in the ω structured domains. The observed differences in contrast of the collapsed atoms and the corner atoms are understood through systematic analysis of the experimental images and the intensities as seen along simulated exit waves and their phase and amplitude parts along different zone axis.

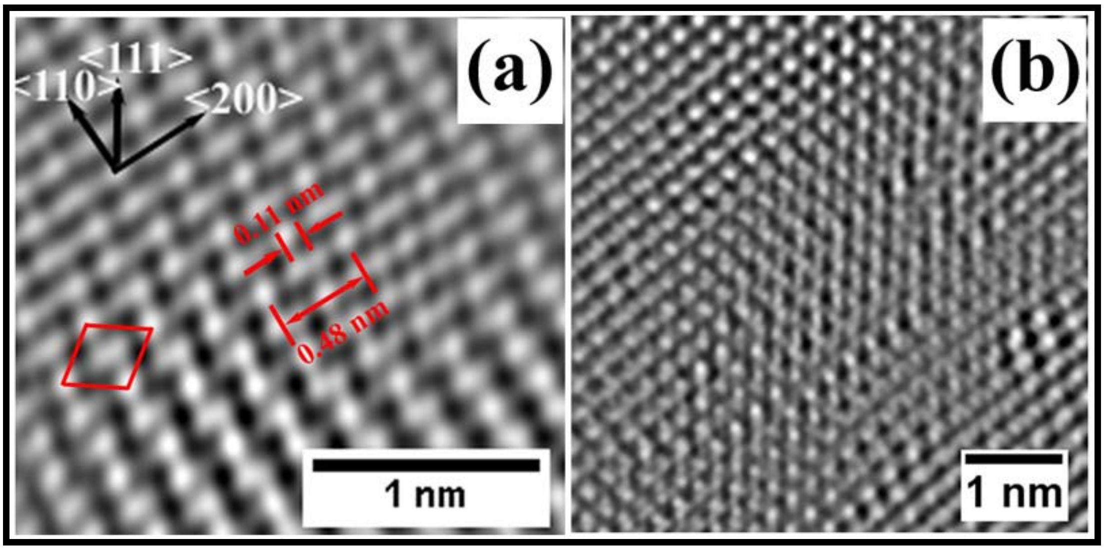

Fig. 4: (a) Phase contrast image showing the partially collapsed ω structure with trigonal symmetry along [1 1 0] orientation of *bcc* structured phase in an aged V-50Ti alloy specimen. A unit of the ω structure is marked in the image itself. (b) Phase contrast image showing the ω structure along $[\bar{1}\ 1\ 3]$ zone axis of *bcc* phase.

Chapter VII: Summary and Future Scope

Present chapter summaries the salient features of the thesis and discusses the outcome of the described work. It also presents the scope for the future work from both experimental and theoretical point of view. During the course of the work, detailed thermodynamic calculations were carried out to investigate the entire phase field of V-Ti-Cr systems, which was scarce in literature. Theoretical predictions are further been supported through different electron microscopy based techniques both from experimental and quantitative simulations. Several fundamental problems were encountered with systematic investigations. Present work can be extended by theoretically modelling the phase structural information for other transition metal based alloy systems and the predictions can be verified through similar experimental procedures. On the other hand, many more different experimental modifications can also be designed to re-verify the theoretical data obtained for the V-Ti-Cr system. Efforts are to be continued to find the newer and improved materials for energy applications and also to understand their structure-property correlation in the atomic scale.

LIST OF FIGURES

LIST OF TABLES

Chapter I

Introduction

Chapter I

Introduction

1.1: Introduction

Diminishing fossil-fuel resources, ever increasing energy demands with increase in global populations, current geo-political scenario and environmental concerns have accelerated the search for alternate energy technologies capable of integration with both existing and emerging infrastructure. As a consequence, research and developments on alternate energy strategies are gaining momentum at a rapid pace in the search for a secure, sustainable, clean, climate-friendly and environmentally acceptable energy sources (Nature materials editorials, 2009, 2010). World-wide research interests have been focussed to develop cleaner energy sources to meet the ever-increasing energy demands without any further environmental damage (Dresselhaus and Thomas, 2001). In a synergetic effect, nuclear energy has emerged as an alternative source to achieve these goals.

The need for abundant energy sources that do not rely on the fossil fuels is the great technological challenge of the twenty-first century - fundamental to further economic development without serious environmental issues (Matsui *et al*., 2008; Kanoh, 2006). Fossil fuel depletion and carbon dioxide emission is driving this quest for alternate energy resources and in turn the search for cleaner, cheaper, sustainable, efficient and abundant energy technology demands the development of new materials. Over the last few decades significant thrust have been given worldwide in research and development on the requirement of a renewable and CO_2 – free energy (Tarascon and Grätzel, 2011) particularly in the field of solar energy (Atwater, 2010; Grätzel, 2001), nuclear energy (Vujić *et al.*, 2012; Duffey, 2005), hydrogen and fuel cells (Steele and Heinzel, 2001), hydroelectric and biomass. However, as a substitute of the fossil fuel, fission, fusion or the hydrogen are the only practical options for reliable large scale based energy sources (Raj and Rajan, 2007). In the alternate energy sector, generation of fusion power with sustainable Deuterium-Tritium (D-T) reaction is considered as the major technological breakthrough of modern science. In a synergetic effect with the energy generation, significant thrust has been applied in the energy and hydrogen storage also where hydrogen is being considered as the ideal energy carrier for a multitude of industrial and other large scale applications (Marban and Solis, 2007; Züttel, 2003). In a true sense hydrogen has emerged as a potential energy currency of the future. However, materials and their service life performance has been a major road block for development and commercial deployment of such alternative energy technologies. Along with the research in alternative energy technology, a rapid surge is also noted in the development of the advanced materials relevant for the nuclear, solar and fuel cell power industries.

Materials development is a key factor for efficient energy generation, storage and use. The associated issues that need to be considered are their performance in operation and environmental effects especially in high-temperature and radiation fields. In this regard, several materials have attracted attention. In recent past vanadium in combination with Ti, Cr, W or Ta emerged as a promising candidate for advanced high temperature structural applications (Ehrlich, 1999). In fusion based reactors, it is not only considered as a first wall heat extraction material for magnetic confinement but also acts as potential hydrogen permeable material useful for tritium breeding (Muroga *et al.* 2014, 2002).

Moreover, V-Ti alloy has also emerged as a hydrogen storage material for high end technological applications (Kumar, 2012).

Vanadium belongs to the Group VB of the periodic table and like other metals of the same period it exhibits a body centred cubic (*bcc*) structure and does not undergo any allotropic changes. The reported lattice parameter for vanadium is 0.30240 nm. However, due to its higher affinity towards the elements hydrogen, nitrogen and oxygen, a considerable amount of them goes in the solid-solution with vanadium which in turn increases its lattice parameter. The density of vanadium is 6110 kg/m^3 and in comparison with the other structural materials, it is 22% lighter than iron and 28% denser than titanium. Vanadium is considered as a refractory metal in broader definition with reported melting point of 1910^o C and boiling point at 3409^o C. Thermal conductivity of vanadium is significantly lower than that of copper but higher than other prominent structural materials e.g. steel and titanium. Electrical resistivity of vanadium increases with an increase in the dissolved hydrogen, nitrogen or oxygen (Gupta and Krishnamurthy, 1992).

1.2: V-Ti-Cr alloys for nuclear applications

Vanadium alloyed with Ti and Cr or W are considered as the possible candidate for low activation structural materials for fusion based (Muroga *et al.*, 2014, 2002; Kurtz *et al.*, 2004) and future generation IV fast neutron fission based (Le Flem *et al.*, 2013) nuclear reactors. Worldwide the vanadium alloy development programmes are focussed on the V-Ti-Cr system with an emphasis on compositions in the range V- (4-5)wt%Cr-(4-10)wt%Ti. An alloy with a composition of V-4Cr-4Ti is considered the reference composition in many international alloy development programs (Zinkle *et al.*, 1998;

Chen *et al*., 2011). Suitability of the vanadium based alloys in the nuclear applications is driven by its superior mechanical properties at elevated temperature with reduced activation, fast decay characteristics, resistance to radiation damage and void swelling at moderately high temperature, good thermal conductivity, low coefficient of thermal expansion etc.

Moreover, V- (4-5)Cr- (4-10)Ti alloy stands only amongst a few with respect to the strength at maximum service temperature. Based on available literature reports, relative positions of V-4Ti-4Cr alloys have been inserted in Ashby's materials property map of strength vs density and also in strength vs. maximum service temperature as shown in figure 1.1. In the mechanical design chart as proposed by M.F. Ashby (Ashby, 2011), the entire sets of materials are divided into six important families: metals, ceramics, glasses, polymers, elastomers and hybrids (combination of the properties of two or more of the others). These materials also showed certain common features amongst them. Ceramics and glasses as a family are hard, brittle and corrosion resistant. Metals are ductile, tough and good thermal and electrical conductors. Polymers are light, easily formable and electrical insulators. Finally, the elastomers are the materials which have the ability to deform elastically to large strains. The idea of these property maps is that, instead of the material name as an identifier for a certain property profile, the design requirements guides the choice of the materials. Figure 1.1 shows that V-4Ti-4Cr alloys positioned at the higher end in both the maps and a combination of both of these properties make V-Ti-Cr alloys as a preferable choice for high temperature applications.

The high compatibility and low corrosion of vanadium alloys with liquid Li is another governing factor in the design concepts of liquid Li blanket with vanadium alloys

(Tsisar, 2013). Moreover, the high tritium breeding ratio (TBR) in a Li/V blanket without using the neutron multiplier as beryllium and ceramic breeder ensure the reduced replacement frequency of the blanket which leads to superior plant efficiency.

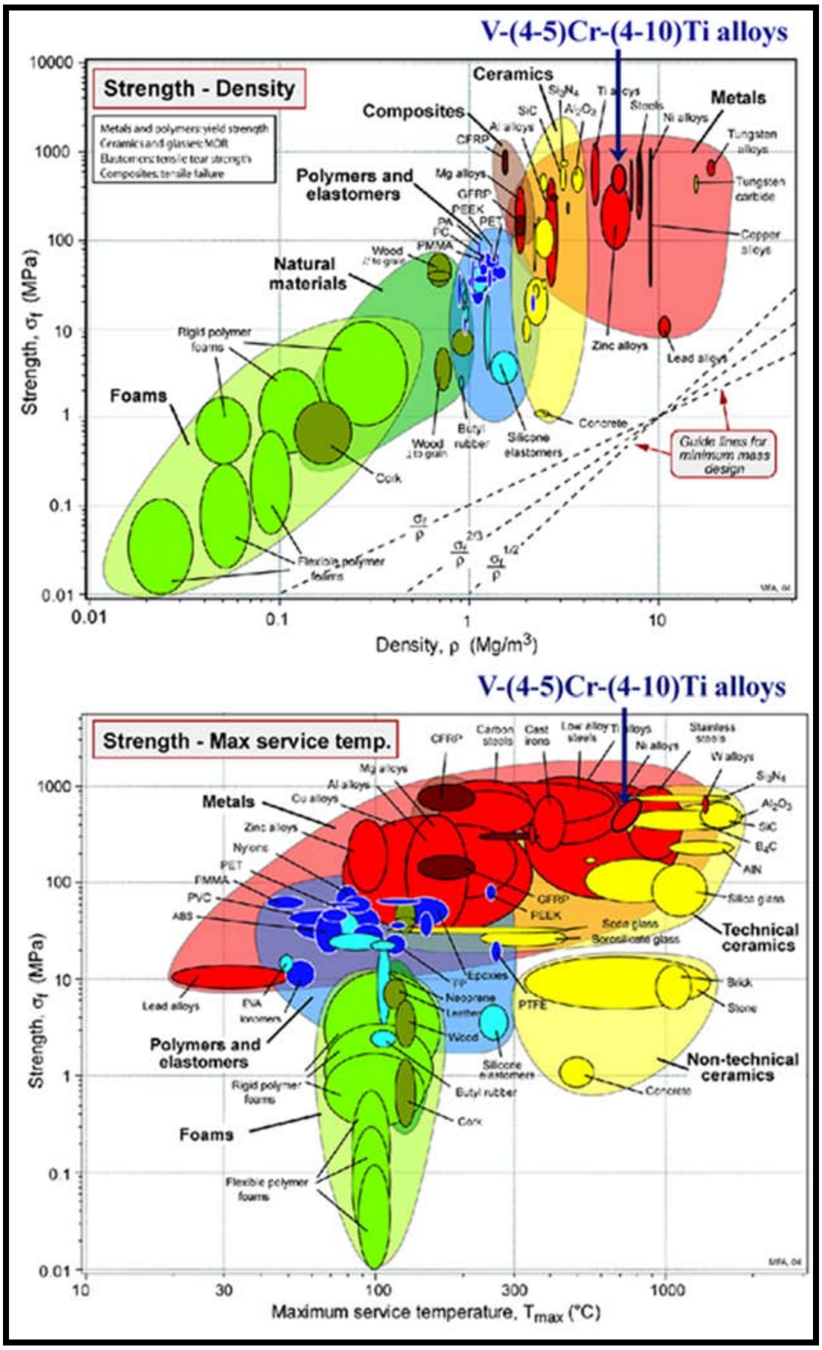

Fig. 1.1: Ashby maps (Ahsby, 2011) for strength vs density and strength vs maximum service temperature. Relative position of V-(4-5)Cr-(4-10)Ti has been inserted in the map from the available literature data.

However, the corrosion behaviour of the vanadium and vanadium based alloys in liquid Li greatly depends on the alloy composition and the Li chemistry, especially on the impurity inclusions (Li *et al*., 2013; Hatakeyama *et al*., 2011; Hoelzer *et al*., 2000).

It has been established through a series of studies from different researchers that V-Ti-Cr alloy shows excellent mechanical properties and good irradiation resistance at moderately high temperature (Zheng *et al*., 2011; Chen *et al*., 2008). Though, variations in the alloying compositions have a significant effect in its yield strength and ultimate tensile strength at high temperatures. It is reported that an increase in Ti and Cr content increases the YS and UTS significantly throughout the temperature range (Zhu *et al*., 2016, 2015). However, after irradiation, this alloy loses certain amount of ductility due to irradiation hardening and can be attributed to the generation of the radiation defects as well as on the irradiation effects on the impurity inclusions. The mechanical properties, especially the fracture toughness under dynamic loading conditions do not deteriorate significantly and there is no significant rise in ductile-brittle transition temperature (DBTT) upon irradiation. Mainly due to these properties V-Ti-Cr alloys are considered as one of the three possible structural materials in fusion based reactors. The other two materials are reduced activation ferritic/ martensitic steels (including ODS ferritic alloys), which is the primary option and SiC/ SiC composites which are the advanced option along with V based alloys. However, V alloys enjoys the superiority over the other two due to its non-ferromagnetic nature and ductility (Muroga *et al*., 2014). Another advantage of using vanadium alloys as the structural material is that it can withstand higher blanket operation temperature than RAFM steels, where the probable coolants are liquid metals, molten salts or He gas. An excellent overview of the research and development of the V-Ti-Cr alloys has been presented by Muroga *et al.* (2014, 2002) in a series of classic reviews.

1.3: V-Ti-Cr alloys for hydrogen storage application

In the last few decades vanadium and V-based alloys drew the world wide attention for its potential application as a storage material of hydrogen and its isotopes. Vanadium, in its metallic form, is known to consist of the highest volumetric hydrogen storage capacity in γ- VH_2 phase after complete hydrogenation – which is 0.16 gm/cm^3, almost 2 times the density of the liquid hydrogen (~ 0.07 gm/cm^3). In comparison with the other hydrogen absorbing transition elements such as, Ti, Ni, Zr, Mn; V has relatively lower desorption temperature though the earlier metals can absorb relatively higher amount of hydrogen (Nomura and Akiba, 1995). The prominent mechanism of the hydrogen storage application in vanadium metal is the absorption-desorption in which a vanadium-hydrogen solid-solution forms in the initial stage of the reaction (Lin *et al.*, 2007; Arashima *et al.*, 2003). This on further hydrogenation evolves as metal hydride phases and transforms further with the increased amount of hydrogen absorption (Reilly and Wiswall, 1970). However, the phase stability of the hydrides as well as the absorption-desorption kinetics of vanadium-hydrogen interaction can be modified with the addition of alloying elements, e.g. the alloying elements with the atomic radii less than that of V can significantly improve the activation process of the V- based alloys (Basak *et al.*, 2008). In their pioneering work, Matumara and his co-workers discussed the selection of the suitable alloying elements based on the existence of a critical e/a ratio, which in other way governed the hydrogen absorption capacity and the activation process (Matumara *et al.*, 1999).

The hydrogen absorption-desorption properties of V significantly improves through alloying with other elements. Both Ti and Cr increase the hydrogen absorption property of metallic V with H/M = 2. V, when alloyed with Ti, stabilizes with a body centred cubic (*bcc*) structure for the entire composition region, though the structures of their hydrides strongly depend on the extent of the hydrogenation of the alloy: V(Ti)H composition with H/M = 1, stabilizes as *bcc* structure whereas $V(Ti)H_2$ composition with H/M = 2, stabilizes as *fcc* structure. Alloying of Cr or Fe also stabilizes the V-Cr(Fe) system in a *bcc* structure and it remains so even at higher temperatures. However, alloys with Ti have higher lattice parameter and hence larger space for accommodating hydrogen. Moreover, at room temperature, Ti-H bond is stronger than Cr-H bond in the hydrogenated state and also V-Ti alloy shows better pressure-composition-isotherm (P-C-T) characteristics for metal hydride reactions as compared to V-Cr.

V-Ti forms the solid-solution in all proportions and reacts with hydrogen at ambient temperature without any disproportionation (Iba and Akiba, 1995; Kuriiwa *et al.*, 1999). However, in practice they are having certain drawbacks, such as rigorous activation prior to hydrogen storage, slow kinetics and relatively sloping plateau in the PCT diagram (Nomura and Akiba, 1995; Basak *et al.*, 2007; Lototsky *et al.*, 2005). Hydrogen absorption capacity of elemental V or the V-Ti binary alloy drastically improves with the substitution of small amount of transition metal elements e.g. Fe, Co, Ni, Mn and Cr. Among the Ti-V alloys, Ti-Cr-V based alloys have been studied extensively in the recent past due to their promising hydrogen storage characteristics (Cho *et al.*, 1999; Tamura *et al.*, 2003; Song *et al.*, 2008; Kumar *et al.*, 2015). The ternary V-Ti-Cr alloys consist of maximum and effective hydrogen storage capacities of 3.5 and

2 wt.% respectively because of its superior cyclic life and high hydrogen absorption capacity at room temperature (Lototsky *et al.*, 2005; Kumar *et al.*, 2015). Apart from Cr, the alloying of Mn, Fe, Co or Ni also significantly improves the hydrogen absorption-desorption kinetics of binary V-Ti alloy (Matsunaga *et al.*, 2009; Liu *et al.*, 2009; Giovanni, 2008; Asano *et al.*, 2010). However, the practical challenge with Ti-V-Cr alloy is its low plateau pressure, due to which the residual hydrogen releases only at very low pressure or at high temperature.

Intensive investigations have been carried out to improve the hydrogen desorption properties of Ti-V-Cr alloys and one such way to modify the hydrogen storage properties of Ti-V-Cr based solid-solution is to make composite with AB_2 or AB_5 type of materials (Young and Nei, 2013; Banerjee *et al.*, 2016). AB_2 types of intermetallics belong to a family of materials known as Laves phases with three different polymorphs: cubic (C15 Laves phase), hexagonal (C14 Laves phase) and double-hexagonal (C36 Laves phase) (Stein, 2004; Gschneidner and Pecharsky, 2006). Microstructural evolution as well as the contribution of these phases in hydrogen storage is still a subject of extensive research. These types of materials have the advantages of higher hydrogen storage capacities, faster absorption-desorption kinetics and relatively low cost than pure V (Kumar, 2012; Banerjee, 2013). Yu *et al.* (2005) has reported about the higher hydrogen discharge capacity in Ti-30V-15Mn-15Cr + 10 wt.% AB_5 composite generated due to enhanced electrochemical-catalytic activity from the alloy surface. Literature reports suggest Laves phase acts as the catalyst for the absorption and desorption of hydrogen in case of Ti-V-Cr alloys (Akiba and Iba, 1998, Pei *et al.*, 2009). Moreover, the thermodynamics and kinetics of absorption and desorption in the Laves phases can easily be tailored by ternary

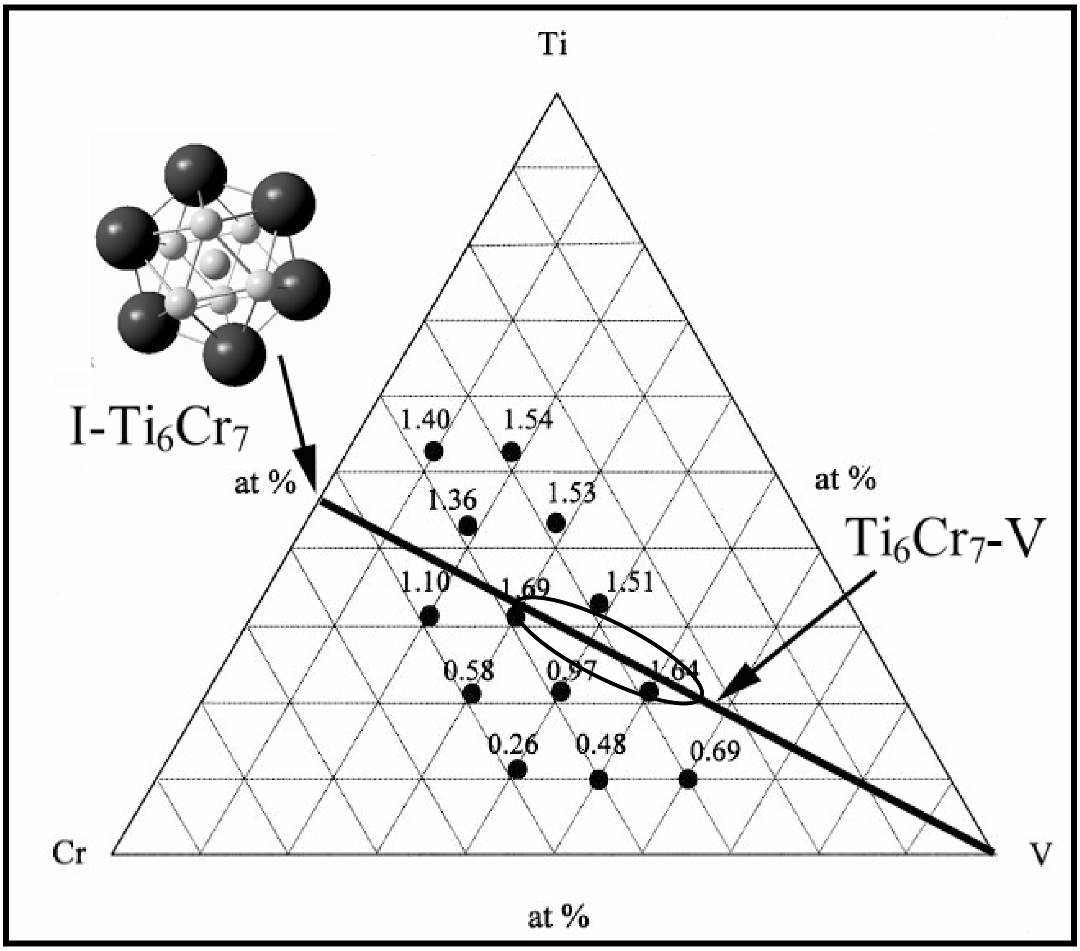

Fig. 1.2: Variation of hydrogen absorption capacity of V-Ti-Cr alloys as shown by Wang *et al.*, (2008). It can be noted that the icosahedral cluster line V-Ti_6Cr_7 traverses exactly the same composition range with large hydrogen storage capacity.

metal substitution with Cr, Ni, Co, Fe etc (Loomis *et al.*, 1994; Akiba and Iba, 1998; Basak *et al*, 2007). For V-Ti-Cr system, the binaries of V-Ti and V-Cr are stabilized in solid-solutions whereas Ti-Cr forms the Laves phase. Wang *et al.* in his classic work has introduced the concept of cluster-plus-glue-atom model for these classes of materials. According to this model, for a A-B-C ternary system, where A-B alloy forms a Laves phase of AB_2 stoichiometry while A-C and B-C tend to form solid-solutions, a cluster line can be constructed by linking A_6B_7 to C. The icosahedral cluster A_6B_7 describes the local structure of AB_2 Laves phase and is surrounded by the C atoms. Wang and his co-workers has thoroughly applied and studied this model to describe the hydrogen storage capacity of the V-Ti-Cr alloys (Wang *et al*., 2008; Wang *et al*., 2016; Miracle *et al*., 2003). It has already been discussed that Ti-Cr alloy stabilizes as cF24-$MgCu_2$ type of Laves phase at relatively low temperature and as hp12-$MgNi_2$ type of Laves phase at high temperature. According to the described cluster model, the $TiCr_2$ structure can be described as a Cr-centered icosahedral Ti_6Cr_7 cluster. The cluster line as it is constructed in V-Ti-Cr ternary alloy by connecting V with the Ti_6Cr_7 cluster is shown in figure 1.2. Ternary V-Ti-Cr alloy compositions as well as their corresponding hydrogen absorption capacity measured in (H/M) are shown in the figure itself. Interestingly it can be observed that the Ti_6Cr_7 – V cluster line traverses along the V-Ti-Cr alloy compositions for which maximum (H/M) is observed; which verifies the validity of this model for V-Ti-Cr alloy also. Moreover, Ti-40Cr-30V alloy composition, which shows the highest hydrogen absorption capacity (H/M = 1.69) can successfully be modelled with the cluster-plus-glue-atom model.

1.4: Phase transformations in V-Ti-Cr system

Enhanced applicability as well as the better assessment of operational behaviour of any advanced material does require a thorough understanding of the structure-property correlation which in turn greatly depends on the phase stability of the system. In the last few decades, considerable efforts have gone so far the phase structural information of the binary Ti-Cr, V-Cr and V-Ti as well as the ternary V-Ti-Cr alloys are concerned.

However, the ambiguities related to the phase equilibria still exists and need serious attention.

1.4.1: Binary V-Ti, Ti-Cr and V-Cr alloy systems

The accepted phase diagrams of the binary Ti-Cr and V-Cr systems are shown in figure 1.3 (a-b) respectively (Lee *et al.*, 1999). In the case of Ti-Cr system, the alloys consists three equilibrium phases over solidification; α-Ti and β-(Ti,Cr) as solid-solution and $TiCr_2$ as an intermetallic compound, belonging to the class of Laves phases, at approximately 63-66 at.% of Cr addition. The intermetallic phase has three structural modifications designated as α-, β- and γ-$TiCr_2$. For V-Cr system, the accepted phase diagram shows a complete *bcc* solid-solution for the entire range of composition. It further shows a congruent minimum freezing point at ~ 70 at.% of Cr addition. However, the V-Cr solid-solution is completely miscible and no intermediate phases exist (Lee *et al.*, 1999; Enomoto, 1992).

For binary V-Ti alloys, though significant efforts have been made by researchers worldwide, fundamentally different views still exist concerning the general form of even the binary phase diagram as shown in figure 1.4 (a, b). Although theoretical support exists for each form of the diagram; there is a lack of agreement even about the phase formed on solidification in the binary V-Ti alloy (Fuming and Flower, 1989; Murray, 1988; Ramsteiner, 2006). This arises since the phases formed on solidification are not always the equilibrium phases as well as the appearance of different metastable phases over heat treatment. One group of researchers predict a continuous decrease in the α+β / β boundary with increasing vanadium content in high purity alloys without the existence of any miscibility gap in the β phase field (Chernov, 1982). Moreover, the presence of the β

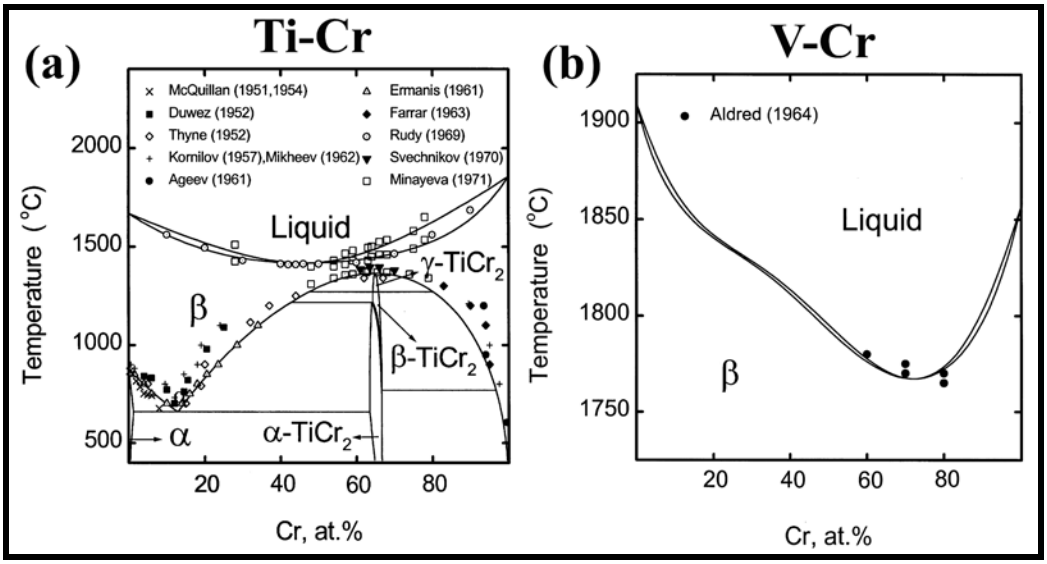

Fig. 1.3: Accepted phase diagrams for binary Ti-Cr and V-Cr alloy systems, in comparison with measured data (Lee *et al.*, 1999).

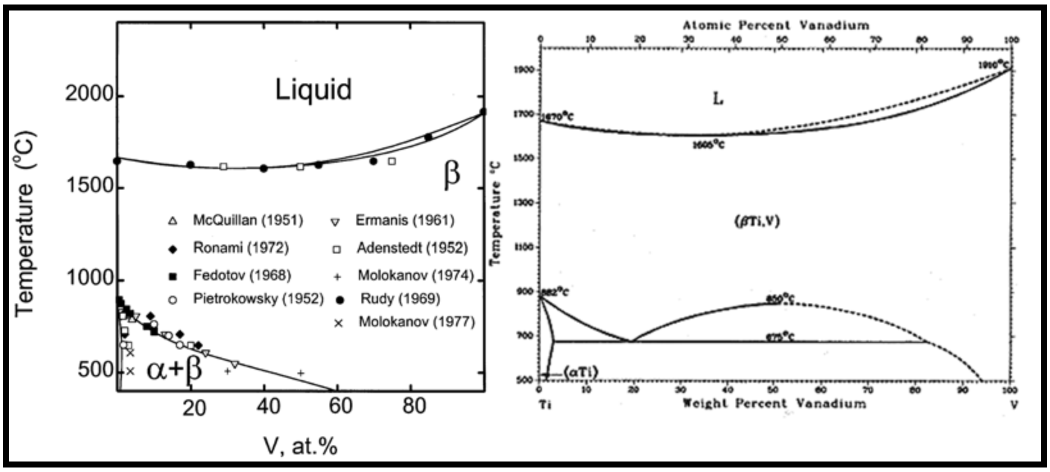

Fig. 1.4: Proposed forms of the two different binary V-Ti phase diagrams. Two fundamentally different views exists regarding the existence of the phase separation tendency in this alloy system.

monotectoid was attributed to the interaction with the interstitial impurities (eg. O, C, N) which are thought to increase the β interaction parameter in the alloy. Another group of researchers also predicts the decrease in α+β / β transus, but emphasises the role of interstitial O in decreasing the α free energy curve with respect to that of β rather than the evolution of any stable β monotectoid. In support of this assumption, Khaled and his co-workers (1981) showed in the case of Ti-V-Mo alloy, the α+β phase field of the binary V-Ti system at 600°C widened above 50 wt.% of V composition as the impurity level of O increased from 0.07 to 0.12 wt%.

Another school of thought is in support of the existence of a metastable miscibility gap within the stable α+β of Ti-V system. Several authors have reported the existence of a metastable miscibility gap within the stable α+β phase field. This manifests itself through the development of two minima in the β free energy curve below 700°C, making way for the low temperature phase separation of β before the precipitation of α. However, Koul and Breedis (1970a, b) proposed a different explanation for the decomposition in V-Ti system – that phase separation occurs in β phase at high temperature, while β decomposes into α+ β phase field at relatively lower temperature; this supports the monotectoid form of the diagram. However, this interpretation was disagreed by Narayanan and Archbold in their work (1970). They obtained evidence for phase separation above 18 wt.% of V content with a stable monotectoid around 675°C with a maxima in β_1 + β_2 phase field at 50 wt.% of V composition. However, all of these postulates are essentially based on theoretical calculations and lack suitable microstructural and microchemical confirmation. These inconsistencies form the basis for the reinterpretation of the equilibrium V-Ti binary phase diagram.

1.4.2: Ternary V-Ti-Cr system

Compared to the binary V-Ti system, the situation is even more complicated for ternary V-Ti-Cr alloys since very few reports exist in the literature regarding the phase transformation behaviour of this system. Enomoto (1992) in his classic work described the solid phases relevant to the V-Ti-Cr system. Major equilibrium phases appearing in the ternary system were reported as the solid-solution phases along with intermetallics compounds, primarily C15 (α-$TiCr_2$), C14 (β-$TiCr_2$) and C36 (γ-$TiCr_2$) Laves phases. β-$TiCr_2$ intermetallic phase is the higher temperature form of the $TiCr_2$ Laves phase with a slightly higher Cr concentration than the cubic Laves phase. The C36 Laves phase structure is stable at even higher temperatures (≥ 1270°C). The pseudo-binary section of V-$TiCr_2$ through the V-Ti-Cr phase diagram is shown in figure 1.5 as reported in the literature (Lee *et al.*, 1999; Samsonova and Budberg, 1967). It is seen from this pseudo-binary section that with addition of V, the β structure of the Laves phase and the β solid-solution form the α-$TiCr_2$ at ~ 1275°C through a peritectoid transformation and at this temperature the present phase field extend till 4 to 14 at.% of V concentration range. Moreover, the α-$TiCr_2$ phase can contain upto 7 at.% V and does not vary significantly even at low temperatures. However, the α-$TiCr_2$+β phase field can extend upto 33 at.% of V at 600° C.

The solidus surface projections of the V-Ti-Cr alloy system as well as the isothermal sections of the ternary system are studied by several researchers over the last four decades. The solidus surface or the surface of incipient melting between β/(β+Liquid) as calculated by Lee *et al.* (1999) is shown in figure 1.6(a) and has been compared with experimentally measured solidus contours by Samsonova and Budberg (1967) as shown in figure 1.6(b). It can be observed that the curves near the three binary sides are well in agreement with the already existing phase field information of binary V-Ti, Ti-Cr and V-Cr systems. The isothermal sections of the calculated ternary diagram along with the experimental validations as shown by Lee and his co-workers (1999) at four different temperatures e.g. 700°C, 900°C, 1000°C and 1200°C are shown in figure 1.7(a-d). A detailed comparison shows that overall there is a good agreement between the calculations and measurements. The details of the stable phases formed in this system as reported by the ASM alloy phase diagram centre are shown in Table 1.1(Villars, 2007).

Even though the solidus behaviour of the V-Ti-Cr system is well documented, information available regarding the site occupancy of V in V-$TiCr_2$ alloys or the effect of Cr addition in binary V-Ti system is relatively sparse. Information regarding formation of any metastable phases is also not been well documented in available literatures. In the present thesis sincere efforts have been made to focus in these gaps and to develop a bridge with the already available knowledge bases.

1.5: Review of the major phases observed in V-Ti-Cr alloy system

1.5.1: Physical metallurgy of Laves phase

Laves phases, a group of topologically close-pack hard intermetallic compounds with AB_2 stoichiometry, are stated to form at a particular radius ratio of A and B (r_A/r_B=1.22) atoms (Berry and Raynor, 1953; Stein *et al.*, 2004). However, a considerable deviation from ideal radius ratio (r_A/r_B=1.05-1.67) (Liu *et al.*, 2000) is observed in practice and the phase can often accommodate non-stoichiometry (Stein *et al.*, 2005). Laves phase can exists in three allotropic polymorphs - cubic (cF24), hexagonal (hP12) and double-hexagonal (hP24). Structural projections along ‘c’ directions for all these three polymorphs are shown in figure 1.8.

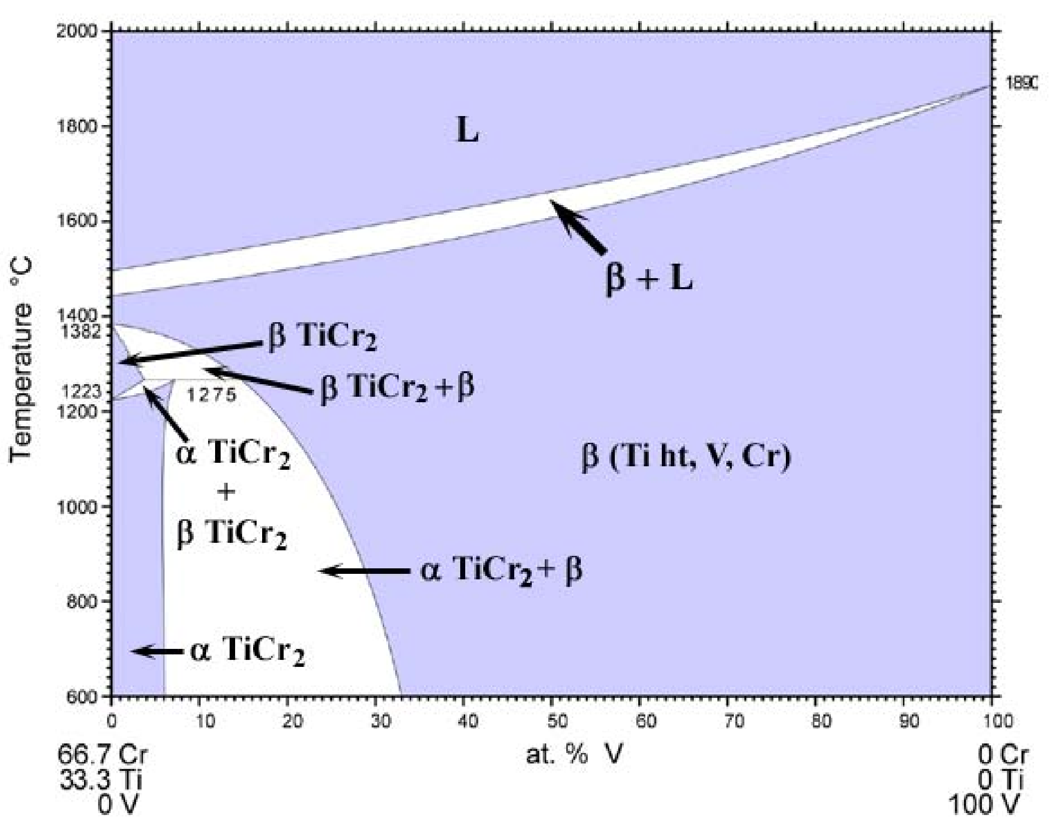

Fig. 1.5: Pseudobinary TiCr$_2$-V section through the V-Ti-Cr phase diagram as reported by Samsonova and Budberg (1967).

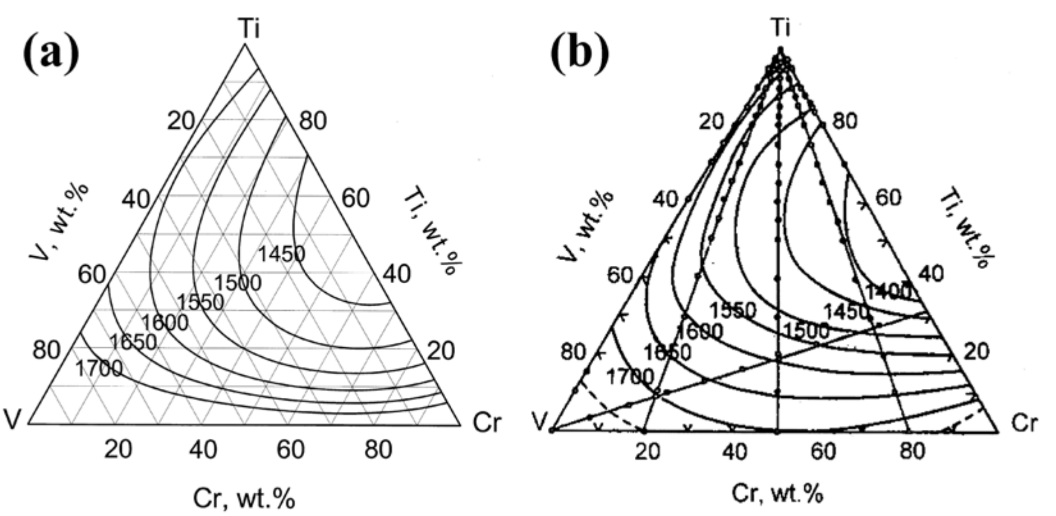

Fig. 1.6: (a) Calculated solidus, β/(β+Liquid) contour (in °C) in the ternary V-Ti-Cr system as given by Lee *et al.*, (1999) and (b) experimental solidus contour measured by Samsonova and Budberg (1967).

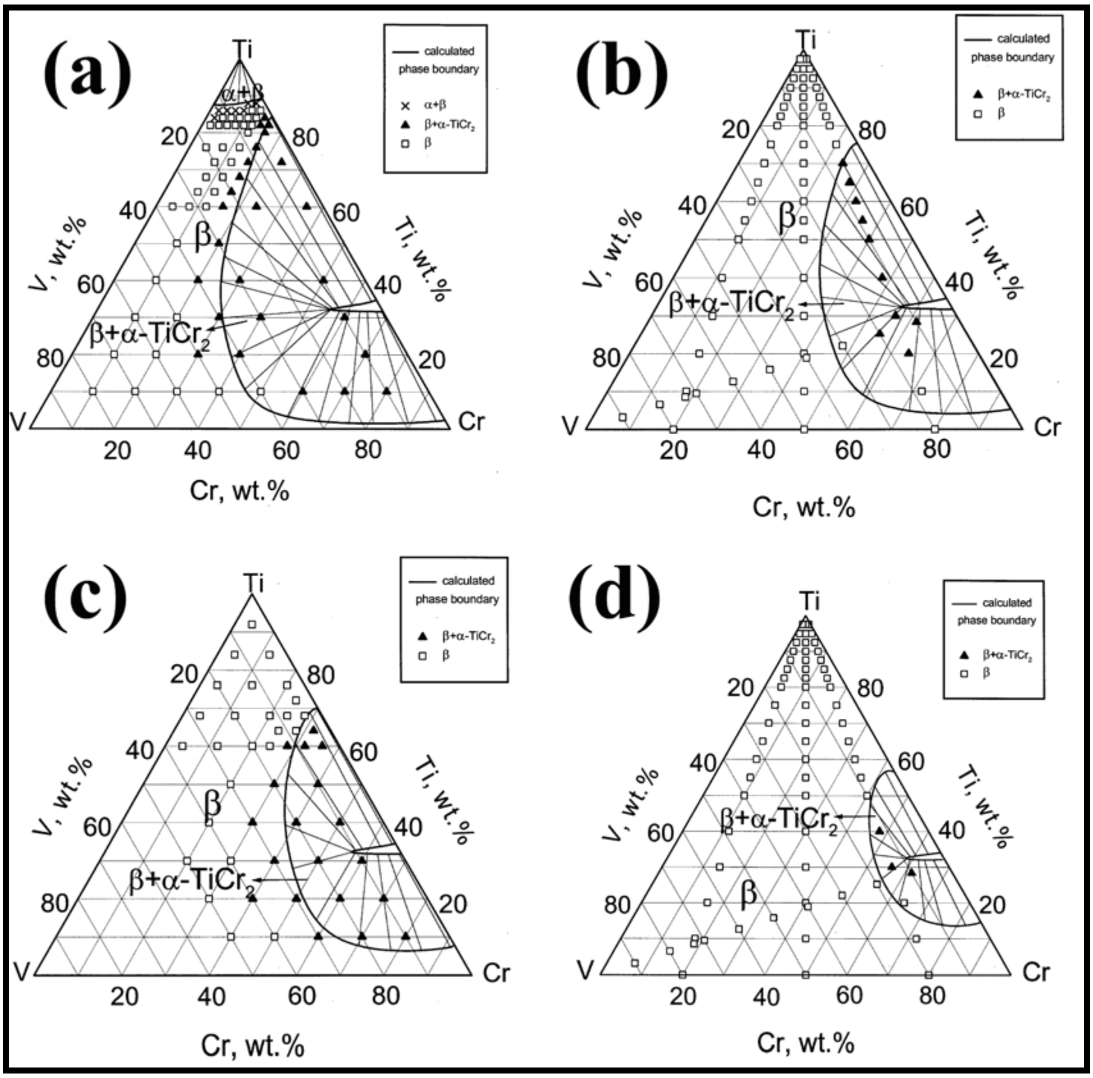

Fig. 1.7: Isothermal sections of the ternary V-Ti-Cr phase diagram calculated by Lee *et al.*, (1999) at (a) 700 (b) 900 (c)1000 and (d)1200° C. Already existing experimental data sets shown in (a & c) are measured by Farrar and Margolin (1967) while those in (b & d) are from Samsonova and Budberg (1967).

Table 1.1: List of stable phase fields in V-Ti-Cr system as adapted from Villars (2007)

Published Phase label	Formula	Prototype	Pearson Symbol	Density Mg/ m^3	Cell parameters	
			Space Group	Volume nm^3	nm	degree (°)
α, Ti	Ti	Mg	hP2	4.52	a=0.29486	α=90
			P63/mmc	0.0352	b=0.29486	β=90
					c=0.467	γ=120
					T=298 K	
α-$TiCr_2$	$TiCr_2$	$MgCu_2$	cF24	6.04	a=0.6939	α=90
			Fd$\bar{3}$m	0.33411	b=0.6939	β=90
					c=0.6939	γ=90
β(Cr,Ti,V)	$Ti_{0.357}V_{0.143}Cr_{0.5}$	W	cI2	6.07	a=0.30207	α=90
			Im$\bar{3}$m	0.0276	b=0.30207	β=90
					c=0.30207	γ=90
(Ti,Cr)	$Ti_{0.14}Cr_{0.86}$	W	cI2	6.78	a=0.2932	α=90
			Im$\bar{3}$m	0.02521	b=0.2932	β=90
					c=0.2932	γ=90
β-$TiCr_2$	$TiCr_2$	$MgZn_2$	hP12	5.98	a=0.4932	α=90
			P63/mmc	0.16863	b=0.4932	β=90
					c=0.8005	γ=120
					T=1598 K	
γ-$TiCr_2$	$TiCr_2$	$MgNi_2$	hP24	5.98	a=0.4932	α=90
			P63/mmc	0.33726	b=0.4932	β=90
					c=1.601	γ=120
					T=1513 K	
(V,Cr)	$V_{0.5}Cr_{0.5}$	W	cI2	6.7	a=0.29435	α=90
			Im$\bar{3}$m	0.0255	b=0.29435	β=90
					c=0.29435	γ=90
					T=1000 K	
(Ti,V)	$Ti_{0.5}V_{0.5}$	W	cI2	5.21	a=0.3158	α=90
			Im$\bar{3}$m	0.03149	b=0.3158	β=90
					c=0.3158	γ=90
					T=295 K	

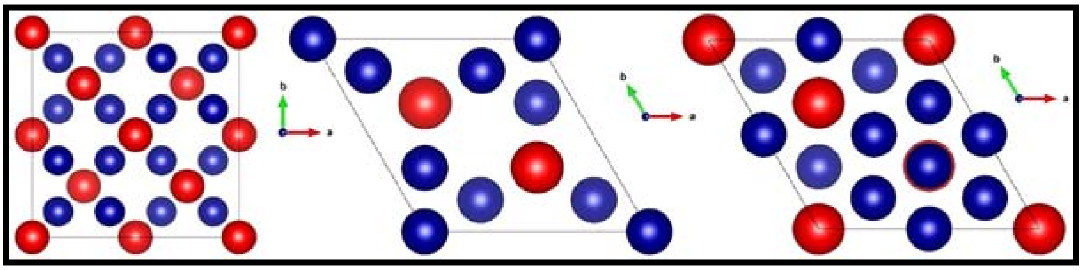

Fig. 1.8: Structural projections showing the relative arrangements of Ti (in red) and Cr (in blue) atoms along 'c' direction in C15 (cubic; cF24), C14 (hexagonal; hP12) and C36 (double-hexagonal; hP24) polymorphs of the Laves phase respectively. The structures are generated using VESTA software (Momma and Izumi, 2011).

A comprehensive review on the phase stability, point defects and fracture toughness of single phase and dual phase binary Laves phase has been provided by Liu *et al*., (2000). Since discovery of this phase, more than a thousand binary and ternary Laves phase forming compounds with a range of interesting properties and varying crystal chemistry have been reported in literature and an elaborate review of this development has been provided by Paufler (2011). These attributes could be exploited to design single phase or multiphase alloys (Senkov *et al*., 2013) and thin films based on Laves phase (Ranchal *et al*., 2012). Additionally, these compounds are often observed as precipitate phases also (Jeong *et al*., 2013). High hardness, high melting point, relatively low specific density, moderately good oxidation resistance and creep resistance has made this material a candidate for many engineering applications (Kazantzis *et al*., 2007).

As a functionally improved alternative to metal hydrides for large scale storage of hydrogen and its isotopes and as hydrogen compressor in fuel cells, AB_2 and AB_5 alloys have been discovered with different alloying additions (Levin *et al*., 2012) in which Ti-V alloys and its derivatives are worth mentioning (Shashikala *et al*., 2011, 2009; Basak *et* *al.*, 2007; Akiba and Iba, 1998). Microstructural constituents of these alloys consist of a composite of the solid-solution phase and the Laves phase. This class of alloys with proper microstructural design exhibit better volumetric storage capacity, kinetics and improved hysteresis due to the interface effects arising from significant density of interface boundaries (Banerjee *et al.*, 2016). They further increase the flatness of the plateau and hydrogen desorption temperature of the *bcc* phase (Singh *et al.*, 2014). In addition, they can also be activated very easily and has high plateau pressure (Bobet *et al.*, 2000; Liu *et al.*, 1996). Even though, dramatic improvement in terms of functionality has been achieved, very little is known about the atomistic mechanisms attributing to this improved functional character. An understanding of atomistic mechanisms directly attributing to the functional properties will definitely co-operate the scientific community to design advanced materials for energy production and storage.

Laves phases are hard and generally exhibit very limited dislocation plasticity at ambient temperature (Kazantzis *et al.*, 2007). Hardness and limited plasticity have been exploited in dispersion strengthened alloys. However, uncontrolled precipitation may lead to deterioration of mechanical properties in high strength structural materials. Although, the physics of dispersion strengthening is relatively better understood, degradation of mechanical properties due to uncontrolled precipitation of Laves phases in structural materials and steels is not well understood (Sathyanarayanan *et al.*, 2013). It has been shown that the precipitation of Laves phases in steel matrix reduces solid-solution strengthening effects. Additionally, contributing factors like inherent limited plasticity of the phase and the weak precipitate-matrix interface lead to the material embrittlement (Ghosh *et al.*, 2012). It definitely warrants further studies to understand the structure and chemistry of such phases and interfaces in order to mitigate such problems. There has been a constant effort to improve ductility of such phases. Alloying route has been explored most extensively to impart ambient temperature ductility in such phases (Takasugi *et al*., 1996). In order to explain the deformation behavior of the intermetallic, a model based pseudo-shear mechanism has been proposed; which is not completely understood (Hazzledine *et al*., 1992). The model is based on vacancy generation upon alloying and a planar fault mediated deformation process. It is not quite understood as to how the alloying elements generate defects in the parent lattice of Laves phases. According to published literature alloying elements may generate anti-site defects or vacancies depending on the site-specificity of the alloying elements.

Since the discovery of bulk metallic glasses, nuances of alloy design that will lead to the formation of bulk metallic glasses under slow cooling and its crystallization behaviour have been very interesting subject of study. As bulk metallic glasses are considered to be a frozen form of liquid alloy, it provides a unique opportunity to study the structure of metallic liquids (Inoue, 2000). It has been observed experimentally and computed theoretically that Laves phase forming compositions are better glass formers (Ghosh *et al*., 2012). Moreover, bulk metallic glasses give rise to a plethora of microstructures which could be tailored to design properties (Basu *et al*., 2003). Precipitation of Laves phases in the glassy matrix has often been observed during solidification and during initial stages of crystallization with concomitant enhancement in properties. It is thought that atomic configuration of bulk metallic glass forming liquids is not totally random and there might be a structural correlation between clusters in bulk metallic glass forming liquids and structural sub-units of Laves phases as the latter are often seen as precipitates (Basu and Ranganathan, 2008, 2009). Laves phases also exhibit other interesting physical properties. For example, rare earth based pure and doped cubic Laves phases have been found to exhibit giant magnetostriction. Optimization of magnetostrictive properties depends on crystal chemistry, minimization of magneto-crystalline anisotropy and development of preferred orientation in a polycrystalline material (Palit *et al.*, 2010). Understanding functional properties and extrapolation of Laves phase structure to other advanced materials require an understanding the crystallography and crystal chemistry at atomic scale.

1.5.2: Phase separation phenomenon of β ($\beta \rightarrow \beta_1 + \beta_2$)

In the previous section it has already been discussed that, for the binary V-Ti as well as for the ternary V-Ti-Cr system, several researchers speculated the existence of a miscibility gap from theoretical calculations. This may lead to the phase separation in the β rich region of the alloy resulting the formation of a two phase immiscible system (Duerig and Williams, 1984; Nag, 2008; Nag *et al.*, 2009). In transition metal systems, phase separation phenomenon may proceed either through nucleation and growth or by spinodal decomposition reaction. While the former one is more frequently observed and studied, there is a need to investigate the equally intriguing spinodal decomposition mechanism which is otherwise has been less studied in the materials community. In the present section a brief description of the governing concepts of the spinodal decomposition mechanisms as well as its determining microstructural features are overviewed.

In the literature, nucleation and growth is defined as "A process in phase transition in which a nuclei of a new phase are first formed, followed by the propagation of the new phase at a faster rate." Whereas spinodal decomposition is defined as, "A clustering reaction in a homogeneous supersaturated solution (solid or liquid) which is unstable against infinitesimal fluctuations in density or compositions. The solution therefore separates spontaneously into two phases, starting with small fluctuations and proceed with a decrease in the Gibbs energy without a nucleation barrier" (Findik, 2012; Favvas and Mitropoulos, 2008). Physical meaning of spinodal is that it is a boundary between the unstable and the metastable part of a two phase region and has been demonstrated in the literature through the change in sign of the curvature of the free energy curve subject to infinitesimal composition fluctuation. The resultant phases generated in this process differ in the composition from that of the parent phase, with consequent changes in their lattice parameters. However, the crystal structure essentially remains the same for the product phases. In literature, one of the earliest evidence of spinodal decomposition was reported by Paul Merica in Cu-Al alloy – the observed features were termed as Merica's knots (Merica, 1932). Later it was known as G.P. zones and has been observed by several researchers as the side band formation in other alloys (Daniel and Lipson, 1943). Theoretical justifications of these phenomena were described on the basis of uphill diffusion. Hillert (1961) first made an attempt to provide the flux equations of this phenomenon based on the classical nucleation theory proposed by Gibbs (1948). Later in a series of classic papers, Cahn and Hilliard (1958, 1959) re-investigated the concept of the spinodal decomposition by introducing the additional effects of coherency strains and anisotropy for the elastic energy contributions in the flux equations (Cahn, 1964, 1965, 1968).

A brief discussion relating the concepts governing the progress of the spinodal decomposition reaction and its dependence on each of the constraints is as follows.

1. The spinodal mechanism is an impulsive unmixing or diffusional clustering phenomena different from the classical nucleation and growth and hence does not have any thermodynamic barrier for transformation to occur. It does not need any nucleation stage in contrary to nucleation and growth; hence nucleation theory of Gibbs (1948) does not apply to spinodal mechanism.

2. At the initiation stage several fluctuation waves originate in the system, however the one with wavelength √2 times the critical wavelength would finally persist and and increase in intensity. The interfacial energy of the system determines the critical wavelength, and fluctuation waves greater than this critical wave can only lead to chemical partitioning in the system. It does not allow the matrix to decompose into too small a scale (Cahn, 1961).

3. The most important aspect of the Cahn-Hilliard model is the elastic anisotropy term. It controls the morphology of the phase separated domains by promoting fluctuation waves along the elastically soft crystallographic directions. Once the spinodal reaction starts the preferred wavelength dominates over the others. The composition modulation will follow the elastically soft directions which for a cubic system are <100> or <111> as determined by the lattice mismatch and elastic anisotropy. Moreover, the pairing of different {111} waves would also form compositional fluctuations along any of the six <110> directions. The choices of the preferred direction depend on the stiffness constants which in turn affects the gradient energy coefficient term. However, in case of hexagonal system, the elastic energy is not solely dependent over the orientation of the elastic constants but also

depends on the relative change in ‘c’ and ‘a’ resulting from the composition fluctuation (Wang *et al*., 1993).

4. It has further been shown by Cahn and his co-workers that at the later stage of the spinodal reaction only one dominant wave will exist and grow further. This can be predicted from the spinodal equations. In the solution of the spinodal equations, the odd harmonics limit the growth rate while the even harmonics produce distortions that increase the composition difference and decrease the spatial extent of the phase separated domains.

5. The kinetics of the spinodal decomposition mechanism is governed by the equation of $x^2 = 2 \times D \times t$ (where x = length of the spinodal decomposition domains; D = diffusion coefficients and t = time). The nature of this rate equation as well as the small diffusion distance over which such a reaction occurs makes the rate of reaction extremely fast. In fact, in liquids and metallic glasses, no amount of quenching can prevent the spinodal decomposition. Hence the governing equations have to be modified for the continuous cooling studies keeping in view that the modulation length of the fastest growing component increases with decreasing undercooling.

Distinction between nucleation and growth and spinodal decomposition always poses a major challenge for metallurgists and materials scientists. The problem becomes much more obvious in the situations when nucleation is easy and copious. A comprehensive description distinguishing the microstructural features between nucleation process and spinodal decomposition had been provided by Favvas and Mitropoulos (2008) and is shown in figure 1.9(a-b) respectively.

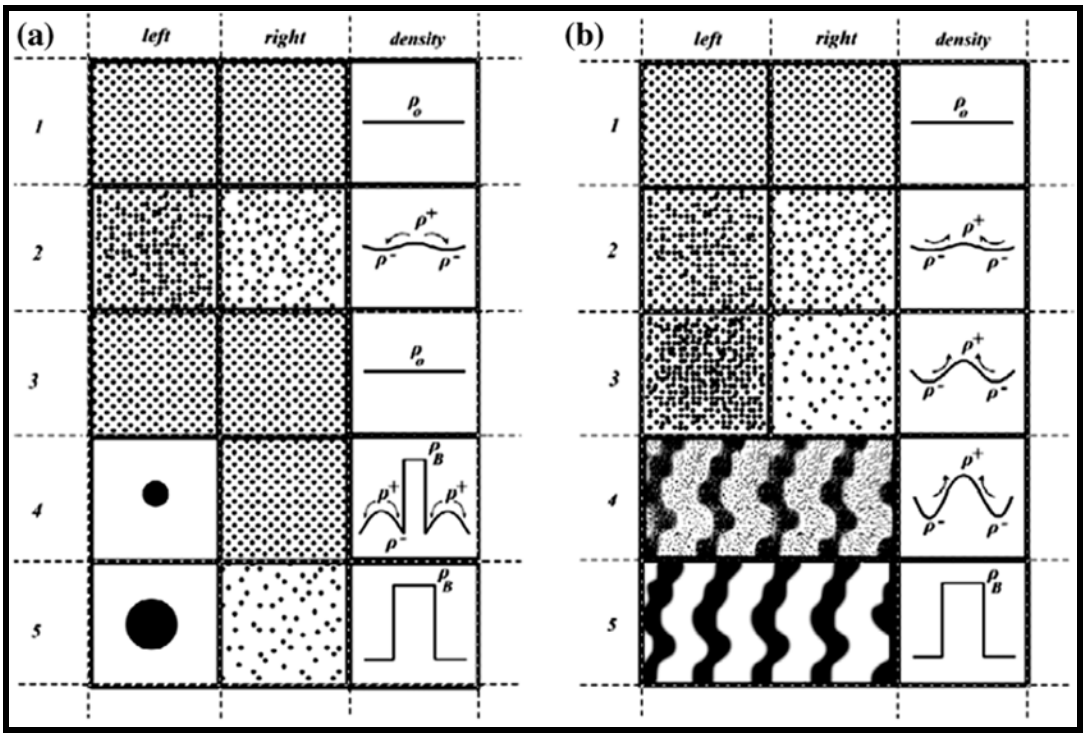

Fig. 1.9: Schematic descriptions of microstructural evolution during nucleation and growth and spinodal decomposition as adapted from Favvas and Mitropoulos (2008). Detail descriptions of this figure are given in table 1.2.

Details of figure 1.9 as adapted from Favvas and Mitropoulos (2008) is given in table 1.2. Nucleation can occur anywhere and everywhere of the grain, whereas the spinodal reactions normally do not occur near the defects and grain boundaries as the rate of reaction is affected by the presence of the defect cores. However, the most distinct feature between these two mechanisms is the orientation of the secondary phases. Because of the anisotropy in the elastic energy, spinodal decomposition occurs only along certain elastically soft directions and the signature of similar effects can also be seen in the electron diffraction pattern through the presence of prominent characteristic sidebands. Another distinguishing feature is that the interconnected phase separated domains can be seen over a large region under the microscope in case of spinodal decomposition in comparison with the nucleation and growth (Cahn, 1965).

Table 1.2: Description of microstructural evolution during nucleation and growth process and spinodal decomposition mechanism as adapted from Favvas and Mitropoulos (2008) and shown in figure 1.9

(a) Nucleation and growth	In figure 1.9 the columns represent two adjacent local regions in the solution denoted as ‘left’ and ‘right’and the rows five stages of the transformation denoted from 1 to 5. • The first three stages represents the situation when a small fluctuation takes place and the embryos does not cross the critical radius while the last two stages represents when a large fluctuation takes place. Black dots represents one of the two components eg. B. • In the 1st row the solution has been brought in to the metastable region and at the moment there is not difference in the local concentration; $C_B^{left} = C_B^{right}$. • In the 2nd row an infinitesimal fluctuation causes a concentration difference, such as $C_B^{left} > C_B^{right}$, hence diffusion is expected between the left and the right regions. • In the 3rd row, diffusion results $C_B^{left} = C_B^{right}$. Here the diffusion occurs from a higher to lower concentration (down-hill) and the system comes back to the situation described in 1st row. • In the 4th row, a large fluctuation causes the the formation of a nucleus of a critical size. In the present case the figure was drawn such as all component B on the left region is spent to form the nucleus; hence $C_B^{left} =0< C_B^{right}$. Now down-hill diffusion takes place from right to left. • Once some B reaches to the left is arrested by the nucleus and hence it grows as described in 5th row. Phase separation in this way is known as the nucleation and growth and the fingerprint of this mechanism is the formation of a nucleus.

(b) Spinodal decomposition	The columns denoted as ‘left’ and ‘right’ represents two adjacent local regions in the solution and the rows denoted by 1 to 5 represents five stages of the transformation process.The black dots represents one of the two components eg. B. The column denoted as ‘density’ represents the density profile of the system at a given stage. • In the 1st row the solution has been brought, very carefully, into the unstable region. This unstability is introduced in such a way that there is not any differences in the local concentrations; $C_B^{left} = C_B^{right}$. Since there is not concentration gradient, no diffusion between left and right takes place and the solution remains a one-phase system. The density of the system at this stage has a flat profile equal to an average value, ρ_O . • In the 2nd row an infinitesimal fluctuation causes a concentration difference, such as $C_B^{left} > C_B^{right}$, and therefore diffusion is expected between left and right regions. The density of system has now a wavy profile with maxima and minima around the average density. • In the 3rd row, the expected diffusion process results to $C_B^{left} >> C_B^{right}$, however, the diffusion does not take place from left to right, ie from higher to lower concentration (down-hill) rather the diffusion takes place from right to left ie from lower to higher concentration (uphill) direction. If the diffusion takes place normally, ie if it was downhill diffusion then it would result $C_B^{left} = C_B^{righ}$ and the system would have gone back to the equilibrium concentration depicted in 1st row. This can not be happened as it contradicts the initial condition that the system is already in a unstable region. • Here the density is large in extent but small in degree; the arrows show the diffusion direction. As diffusion proceeds the density increases and finally reaches a point where it becomes equal to that of pure B. The entire transformation proceses are shown in rows 3-5. Phase separation occurs in this way is known as spinodal decomposition and the fingerprint of this mechanism is uphill diffusion.

1.5.3: Features of ω phase transformation

The metastable ω phase is a structural derivative of the body centred cubic (*bcc*) phase that usually forms with group IV B transition metals Ti, Zr and Hf, when alloyed with *bcc* stabilizing elements (e. g. V, Mo, Nb, Fe, Cr etc.) (Banerjee and Mukhopadhyay, 2004). This phase forms while quenching the alloy from the *bcc* phase field or during aging of the quenched alloy (Chen *et al.*, 2015; McCabe and Sass, 1971; de Fontaine, 1970, 1988; de Fontaine *et al.*, 1971; de Fontaine and Kikuchi, 1974; Cook, 1974, 1975a, 1975b; Sanchez and de Fontaine, 1978). The ω phase does also form as a metastable intermediate in the phase transformation sequence of Zr-Al and Ti-Al-Nb alloys, where it forms as an ordered intermetallic phase in the phase transformation sequence of $B2 \rightarrow \omega \rightarrow B8_2$. Here ω is reported as a metastable intermediate phase, which is of lower symmetry than either the initial B2 or final $B8_2$ state of the system (Bendersky *et al.*, 1990a, 1990b; Banerjee and Cahn, 1983; Tewari *et al.*, 1999).

In the initial days of its discovery, it was generally believed that ω phase can form in elemental Ti, Zr and Hf only through high pressure treatments (Frost *et al.*, 1954; Jamieson, 1963; Bridgman, 1952; Bundy, 1965; Jayaraman *et al.*, 1963; Hickman, 1969). An enormous volume of work has been done till date on the high pressure ω phase synthesis. In this context, the pioneering work by Jamieson on the structure of ω in elemental Ti and Zr under static high pressure is worth mentioning. In addition to that, electrical resistivity measurement to detect the ω phase transition in elemental Zr subjected to 60 Kbar of pressure by Bridgman and co-workers and detection of ω phase transformation in Ti (80-90 kbar) and Zr (50-60 kbar) by high pressure resistivity measurement by Jayaraman and coworkers are notable milestones in ω phase research.

Apart from research on synthesis and properties, crystallography, nucleation and growth, thermodynamics and kinetics of ω transformation gained interest quite early. A detailed review on ω phase transition research in 1960's and 70's has been published by Sikka *et al*. (1982). The ω phase transformation through different other routes is of relatively recent vintage and among them the most successful is the ω phase transition in Ti, Zr and Hf with suitable alloying elements (Schryvers and Tanner, 1990; Banerjee *et al*, 2003; Ramsteiner *et al*., 2008). The similar effects of high pressure treatment were observed with the addition of d-rich transition metal elements e.g. V, Mo, Cr etc. in group IV B elements. These elements are said to increase the occupancy of the d-band and stabilize the *bcc* phase at low temperature (Dyakonova *et al*., 2008; Dutta *et al*., 2012; Kim *et al*., 2015). In these alloys ω phase transition occurs either by quenching the alloy from the *bcc* phase field or by ageing the alloy at a temperature just below the *bcc* → ω transformation temperature. In the former case, it is called athermal ω and in the latter, the resulting product phase is termed as isothermal ω. Athermal and isothermal ω phases are microstructurally different and can be distinguished under an electron microscope based on their structure and morphology. The work by Ming *et al*. (1981), Banerjee and Mukhopadhyay (2004) and Dey *et al*. (2004) on the ω phase transition in Ti and Zr based alloys are worth mentioning in this context.

The structure of ω can be understood as the reshuffling of *bcc* atomic planes along <1 1 1> direction as shown in figure 1.10. The alternate collapse of (111) pairs of planes generated through a displacive wave of amplitude less than a/6 produces a partially collapsed ω with a trigonal symmetry. The complete collapse generates a two layered structure of ω, which is of hexagonal symmetry (AlB2 type structure) (Banerjee and

Mukhopadhyay, 2004; Sikka *et al*, 1982). However, the formation of ω in these alloys can be bypassed with the addition of higher amount of *bcc* stabilizing elements. With the higher amount of *bcc* stabilizing elements, a diffused ω structure forms in the *bcc* matrix resulting in a deviation in the position of the diffraction spots of crystalline ω. The deviation would increase in commensuration with the addition of higher amount of the *bcc* stabilizer. McCabe and Sass in their earlier work on the ω phase formation in Ti-V alloys had shown that in the low V content relatively large clusters of the ω domains are present in the matrix which decreases with the increase in the V content. They further showed that with the increase of the V content the ω reflections moved away from the positions expected from that of the ideal structure (McCabe and Sass, 1971).

In the last four decades the ω phase and the associated phase transformation phenomena have attracted considerable attention resulting in a wide range of discussions in the literature. Pynn (1978) in his classic work has discussed the physical origin of the diffuse ω scattering in Zr and Ti alloys. Durig *et al.* (1980) had discussed the growth mechanism of ω in Ti alloys on the basis of chemical stabilization of the *bcc* matrix, coherency strains and dilatation strain fields overlap. They further proposed a model for the isothermal precipitation of ω in Ti alloys. De Fontaine and his associates (1973) in their classic work, proposed a model for the β to ω transformation based on the two dimensional ordering of one dimensional defects. With the aid of Monte Carlo simulation it has further been postulated that in the displaced segment of the closed packed atomic planes, the linear defect consists of a compressive and dilatational defect pairs. Banerjee and his co-workers had reported on the crystallographic description and atomic reshuffling mechanism of ω phase formation in Zr-Nb alloy. Cook *et al.* (1974, 1975a,

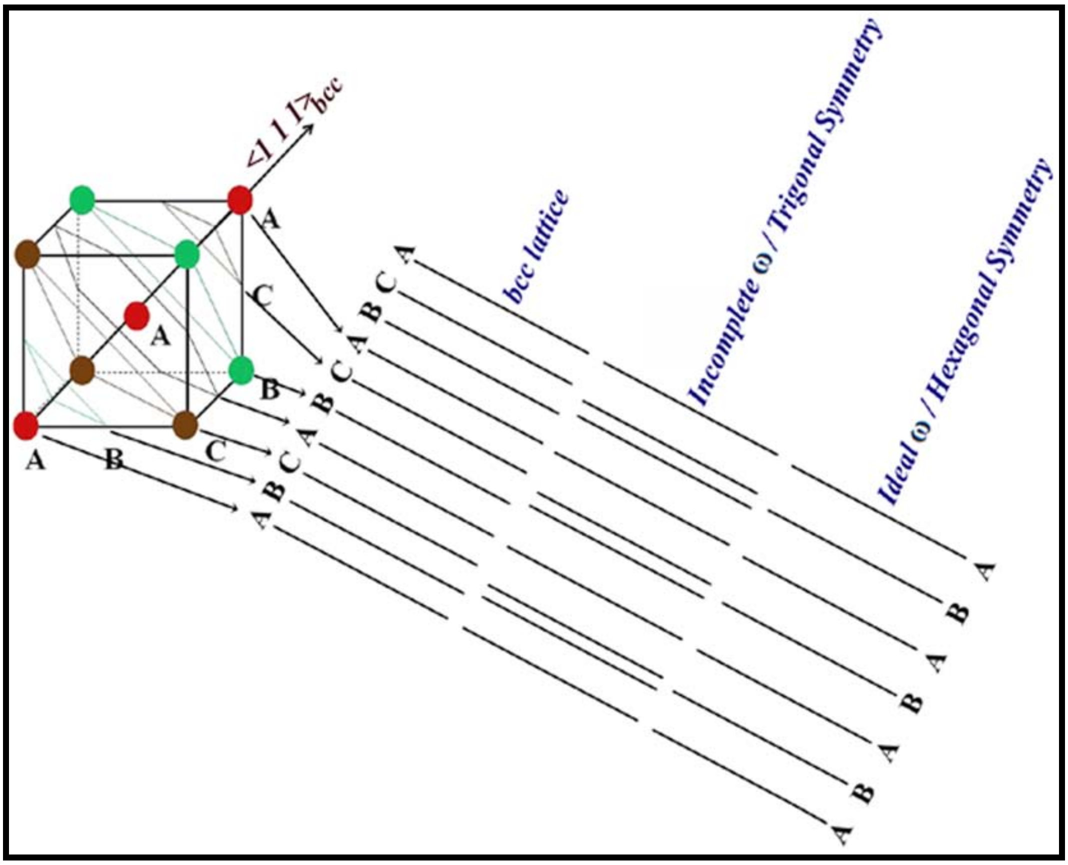

Fig. 1.10: bcc → ω structural transformation explained in terms of displacement wave mechanism. The atomic collapse could be incomplete (of trigonal symmetry) or complete (of hexagonal symmetry).

1975b) had described the free energy change associated with the ω transformation using a Born-von-Karman anharmonic planar lattice model where it is proposed that a two phase structure of ω and *bcc* can be formed immediately after the *bcc* → ω transformation temperature.

However, in most of the cases the identification of the ω phases is based on indirect detection methods, which are essentially diffraction based experiments or changes in mechanical properties of the alloy. This is mainly because of unavailability of the sophisticated electron microscopes with enhanced spatial and compositional resolution as it is available today. Hence direct structure imaging of ω phases, nature and extend of collapse and structure of interfaces between *bcc* - ω phases have received relatively little attention.

With the development of the electron microscope instrumentation, more and more attempts are being made to study the structural details of the ω phase. In this context, the works carried out by Banerjee *et al.* (2003), Ng and his colleagues (2011), Devaraj and co-workers (2011, 2012), Bennett *et al.* (2015), Nag and his co-workers (2009, 2011) on the structure, composition and 3-D morphology of ω precipitates in the Ti based alloys with aberration corrected (S)TEM and atom probe techniques are worth mentionable. The results are further supported by density functional theory calculations. Phase contrast microscopy analysis on the ω structured domains in Zr- based alloys by Okunishi *et al.*, on Ti-Mo alloys by Sukedai and his coworkers and the work carried out by Sankaran and his colleagues in gum metal related alloys also provide deep insights in the structural aspects of ω phase (Okunishi *et al.*, 2013; Sankaran *et al.*, 2014; Sukedai *et al.*, 1993, 1994, 1997). Dehai *et al.* provides a nice and comprehensive review over the recent efforts on the structure imaging of ω domains (Dehai, 2014).

1.6: Development of electron microscopy in interfacing materials related issues

Materials Science and Engineering research is fascinating and it is multidisciplinary in the true sense of the term as it starts with the fundamental understanding of condensed matter physics and basic chemistry and ends with the materials properties meeting the needs and standards of high-end technological applications. Since the genesis of metallurgy / materials science as an independent subject of study, research was confined to the extraction, processing, treating and shaping of materials for use in engineering components. With the advent of nanotechnology, the scale of interest has not only gone down by several orders of magnitude in scale, but materials chemistry has also become enormously complex and atomistic origin of properties have thrown open many fundamental questions (Van Tendeloo *et al*., 2012; Yang *et al*., 2012). At this juncture, it is important not only to synthesize novel materials but also to characterize them at the atomic scale in order to understand their properties. It would not be wrong to say that the developments in instrumentation have enabled to the development of materials. The resolution of microscopes has kept on improving and there is a continuous effort to push the resolution limit well below one angstrom through overcoming aberrations in the electron-optical system (Urban, 2008). Along with that, development in analytical techniques has made it possible to characterize chemistry of the materials also at the atomic scale (Williams and Carter, 2009).

"Seeing is believing" is a traditional philosophy in materials science. As a result of which there has always been a drive to see things in order to understand it better. This led to the observation of pearlite by Henry Clifton Sorby in 1863 by visible light microscope. Unfortunately, the resolving power of microscopes at that time was poor and improvements of microscopes did not happen very rapidly either. As a result of which, in materials science many things were postulated before they were experimenatlly observed. A classic example of that is dislocation. Presence of dislocation was predicted much before in order to explain the origin of the observed serrated bands in the rolled sheets. This helped the growth of science of microscopy to keep pace with the development in materials science. Although Ernst Ruska and Max Knoll developed the first microscope based on the accelerated electron around 1931 but it is primarily after the World War II that the technology development of the electron microscope took a sharp rise. Several research groups were involved throughout the world with keeping the focus to improve the resolution of the instrument. Menter, in the middle of 1950s first came up with a high resolution micrograph showing lattice resolution, imaging lattice imperfections with a resolution ~ 1 nm (Menter, 1956). However, it took another two decades for the first atomic resolution images of the heavy atoms such as, thorium or gold (Crewe *et al.*, 1970). This opened up a new window in the materials science research and marks a paradigm shift in the area of research on defect studies at atomic or near atomic scale. In this context the works on high resolution studies on different materials by Iijima and his associates are worth mentioning (Iijima, 1973; Iijima and Allpress, 1973). During 1980s and 1990s the resolution of the TEM were steadily improving and by the turn of the century the point resolution for most 'high-resolution' commercial instruments were in the range of 0.1 - 0.2 nm. The main limitation for the improvement of the resolution was the aberrations coming from the lenses.

Development of the electron microscopy techniques took another big leap in achieving of sub-angstrom resolution in the late 1990s and early 2000s because of the invention of spherical aberration corrected lenses (Haider *et al.*, 1998). A detailed account of the development of aberration correctors have been given by Rose (2008) and later by Urban (2008), Van Tendeloo and his group (2012) in a series of comprehensive reviews. The commercialization of the aberration corrected microscope came as a big boon to the materials scientists and enabled them to extract the structural information at the atomic scale from different beam-sensitive materials even at lower kV. In this context the research on the nanotubes, graphenes and other 2D materials are worth mentioning. A pictorial representation showing chronology of the development of the electron microscope resolution has been nicely accounted by Rose (2008) and later by Muller (2009) and is reproduced in figure 1.11.

In a synergetic effect with the improvement of the spatial resolution at the atomic scale in transmission electron microscopy (TEM) or scanning transmission electron microscopy (STEM), a rapid surge was also there to develop the electron energy loss spectroscopy (EELS) and X-ray energy dispersive spectroscopy (XEDS) for yielding the single column chemistry and eventually the electronic information at that same level (Muller, 2008). STEM-HAADF imaging, which is essentially an incoherent imaging process, coupled with electron spectroscopy techniques provides the most complete picture of structure and chemistry of the materials in the atomic scale. Such images are directly interpretable as the contrast develops based on the atomic number of the constituent elements only. In contrast, high resolution phase contrast images are not directly interpretable and the major challenge is to correctly interpret the underlying data. In order to quantitatively understand the contrast and relate it to the atom column position unambiguously, simulation of the high-resolution image is extremely essential (Williams and Carter, 2009; Kirkland, 2016, 2009).

The impact of the development of electron microscopy techniques is quite prominent in the present era of materials research. Quest to know the structure and property of the materials in its ultimate building blocks i.e. in atoms increased in manifolds. Focus has shifted towards the quantitative understanding of defects, interfaces and induced strains of the materials. More and more researchers came up to study the fundamental aspects of the metallic phase transformations and different equilibrium and

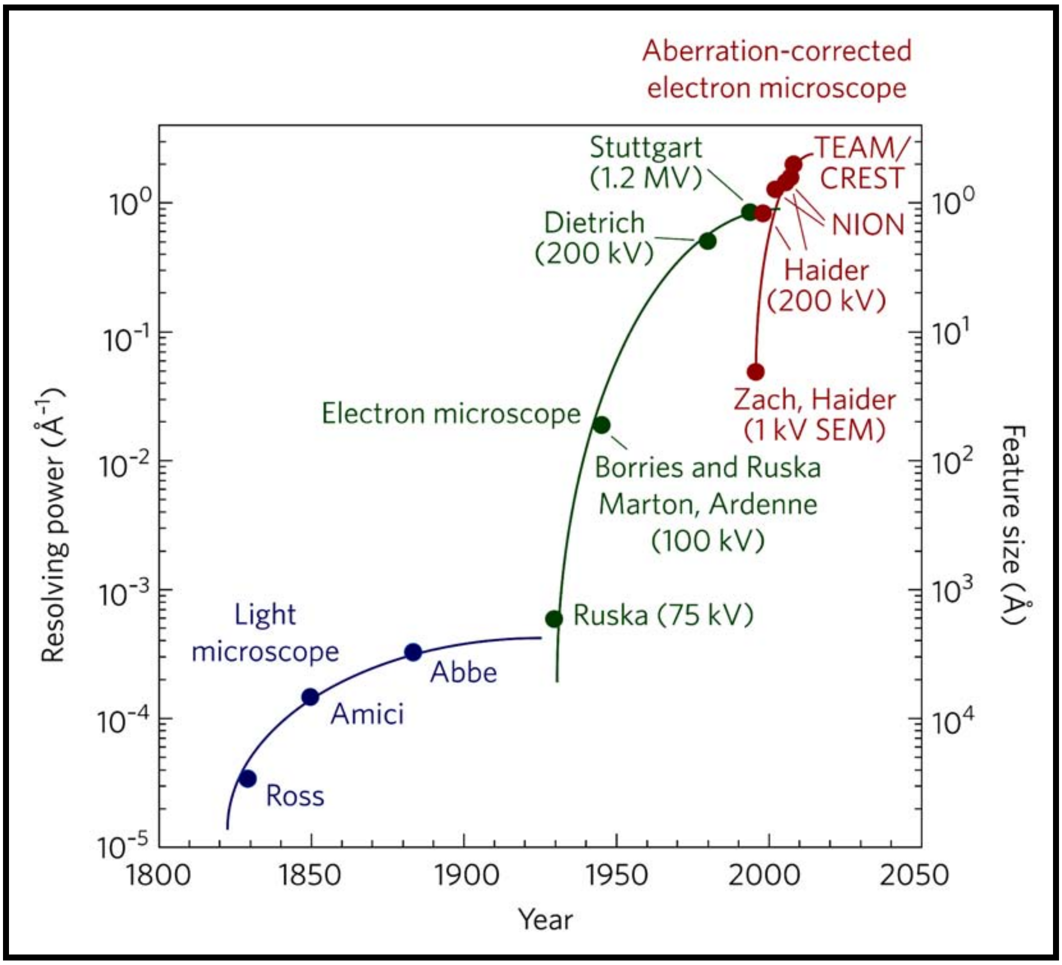

Fig. 1.11: Increase of resolution in diffraction-limited microscopy as a function of time. Visible light microscopy reached its far-field diffraction limit roughly a century ago. Electron microscopy, exploiting the reduction in wavelength with increase in accelerating voltage, steadily increases the rosolving power for over 50 years, until limited by radiation damage. In recent times, development of electro-optical aberration corrected lenses have led to the improvements in resolving power drastically improves the resolving power even at relatively lower electron beam energy (Rose, 2008 ; Muller, 2009).

metastable phases. Research and development on the low dimensional materials as well as on the functional materials boosted significantly; more and more nanoparticles are synthesized with tailor made properties (Scott *et al*., 2012). All of these developments are of enormous importance towards the atomic level understanding of materials property as well as to the advancement of materials science research in general.

1.7: Scope of the thesis

Successful implementation of binary Ti-V and ternary V-Ti-Cr alloys in alternative energy applications requires a thorough understanding of the phase stability and microstructural evolution. Though it is well established that the V rich side of the ternary phase diagram stabilizes in a *bcc* structure, it is also required to explore the other phase fields of the ternary alloy system. It is already been discussed in the previous sections, that the information available regarding the physical metallurgical aspects of the ordered intermetallics formed in the vicinity of the Ti-Cr rich side or the phase formation and compositional fluctuations in the binary V-Ti and ternary V-Ti-Cr alloys are relatively sparse. Situations become even more complicated with the formation of metastable phases as the system hops along the local minima over the energy landscape as a function of processing parameter.

In the present scenario, it is extremely essential to understand the different phase fields as well as their phase transformational behavior of the ternary V-Ti-Cr alloy system. Systematic studies are also required to understand the stability of different constituent phases and their structure and chemistry down to atomic level. In the present thesis, focus is on the investigation of the phase formation and microstructural evolution in V-Ti-Cr alloy systems using phase contrast, HAADF imaging and electron spectroscopy. A pictorial representation of the scope of the thesis in the form of materials tetrahedron is shown in figure 1.12. It shows that the methodology adapted in the present thesis covers all vertices of the tetrahedron represent modeling, synthesis and processing,

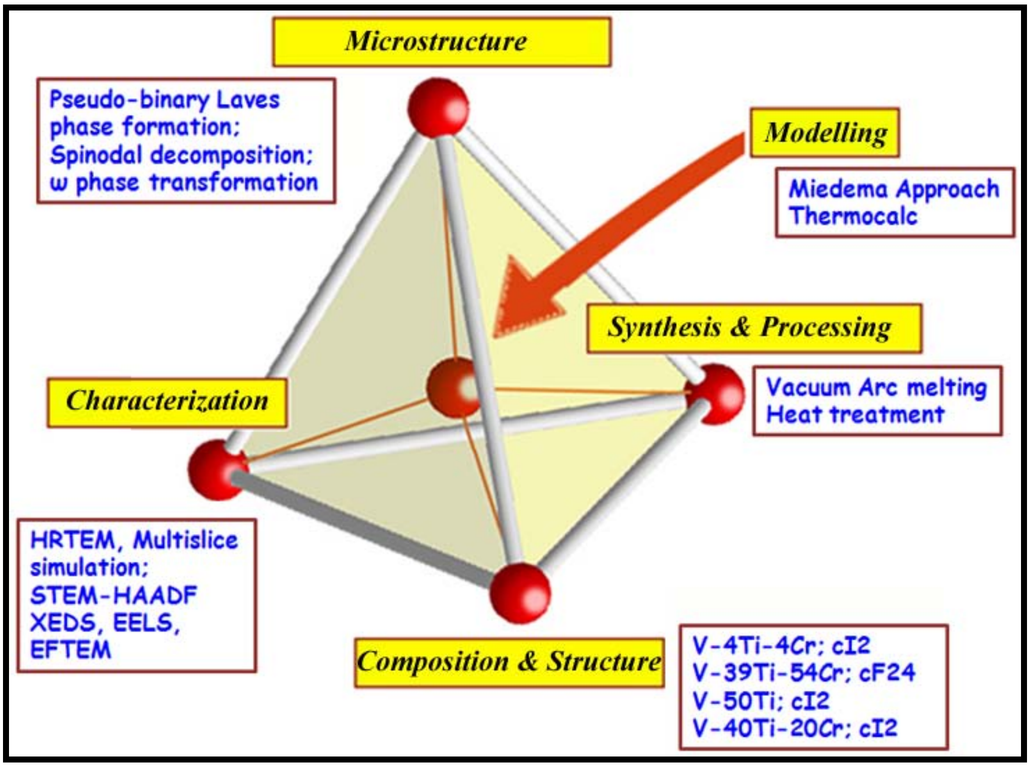

Fig. 1.12: Scope of the thesis explained in terms of materials tetrahedron. Tetrahedron of materials design showing the correlation among modeling, synthesis and processing, composition and structure, characterization and microstructure.

composition and structure, characterization and microstructure. Keeping in mind the complexities involved in studies of the phase transformation of an almost unexplored system, thermodynamic calculations based on Miedema approach are employed to map the phase formation behavior of binary and ternary alloys upon solidification. Selected binary and ternary alloys from different regions of the enthalpy-composition diagram were prepared by vacuum arc melting and heat treated as per requirement. Phase stability studies on the selected binary alloys and the effect of ternary addition over them as well as the possibilities of the formation of new phases have been studied in the present thesis using phase contrast and *Z*-contrast microscopy coupled with XEDS and EELS.

1.8: Organization of the thesis

Present thesis entitled **"Phase Stability and Microstructural Evolution in V-Ti-Cr System Using Phase Contrast, HAADF Imaging and Electron Spectroscopy"** is organized into seven chapters as outlined below. **Chapter I** provides a brief review on the application of V-Ti-Cr alloys as a structural material for fusion based nuclear reactors as well as in hydrogen storage. It also provides a literature survey on phase transformational aspects of V-Ti-Cr alloy and the advancement of electron microscopy techniques to address materials related issues. **Chapter II** describes the different experimental techniques and procedures deployed for synthesis, characterization and evaluation of different phases in V-Ti-Cr system. **Chapter III** deals with the phase stability studies in the constituent binaries and ternary V-Ti-Cr system with Miedema model which have been re-assessed by ThermoCalc and Pettifor structure map approaches. **Chapter IV** describes the direct structure imaging of V substituted $TiCr_2$ Laves phase alloy. It also describes the method for indirect determination of single column chemistry and determination of preferential site substitution of V in $TiCr_2$ Laves phase. **Chapter V** deals with the phase separation behaviour and the feasibility of ω transformation in binary V-Ti and ternary V-Ti-Cr alloys. It further discussed about the phase separation mechanism in these set of alloys i.e. whether it is dominated by spinodal decomposition mechanism or nucleation and growth process. **Chapter VI** describes the structure imaging and the atomic level reshuffling in ω structured domains in V-Ti and V-Ti-Cr alloys. Finally **Chapter VII** provides a comprehensive summary of the thesis and also the scope for future work. A pictorial representation of the thesis organization as well as the brief contents of each of the chapter is shown in figure 1.13.

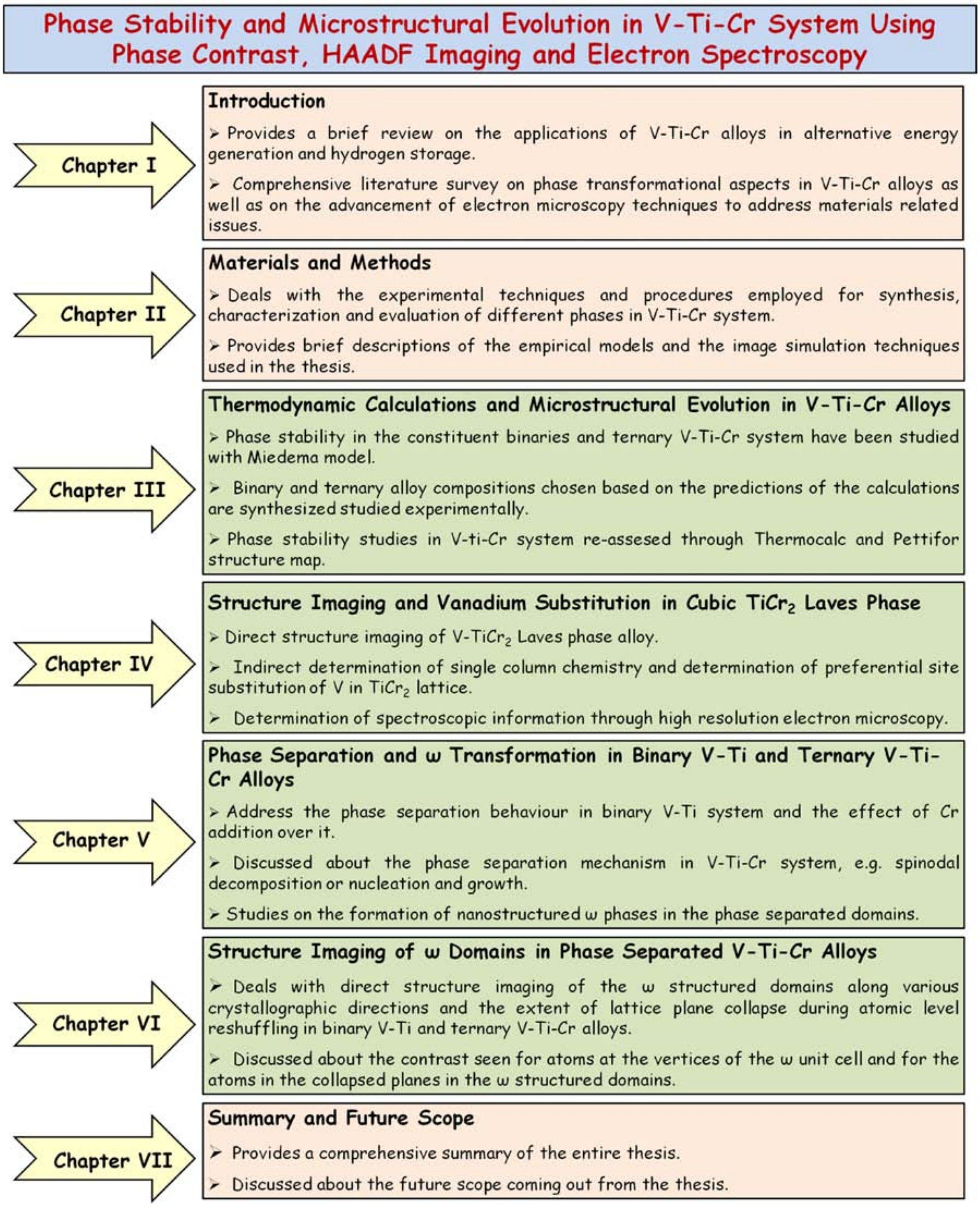

Phase Stability and Microstructural Evolution in V-Ti-Cr System Using Phase Contrast, HAADF Imaging and Electron Spectroscopy

Chapter I

Introduction

- Provides a brief review on the applications of V-Ti-Cr alloys in alternative energy generation and hydrogen storage.
- Comprehensive literature survey on phase transformational aspects in V-Ti-Cr alloys as well as on the advancement of electron microscopy techniques to address materials related issues.

Chapter II

Materials and Methods

- Deals with the experimental techniques and procedures employed for synthesis, characterization and evaluation of different phases in V-Ti-Cr system.
- Provides brief descriptions of the empirical models and the image simulation techniques used in the thesis.

Chapter III

Thermodynamic Calculations and Microstructural Evolution in V-Ti-Cr Alloys

- Phase stability in the constituent binaries and ternary V-Ti-Cr system have been studied with Miedema model.
- Binary and ternary alloy compositions chosen based on the predictions of the calculations are synthesized studied experimentally.
- Phase stability studies in V-ti-Cr system re-assesed through Thermocalc and Pettifor structure map.

Chapter IV

Structure Imaging and Vanadium Substitution in Cubic $TiCr_2$ Laves Phase

- Direct structure imaging of V-$TiCr_2$ Laves phase alloy.
- Indirect determination of single column chemistry and determination of preferential site substitution of V in $TiCr_2$ lattice.
- Determination of spectroscopic information through high resolution electron microscopy.

Chapter V

Phase Separation and ω Transformation in Binary V-Ti and Ternary V-Ti-Cr Alloys

- Address the phase separation behaviour in binary V-Ti system and the effect of Cr addition over it.
- Discussed about the phase separation mechanism in V-Ti-Cr system, e.g. spinodal decomposition or nucleation and growth.
- Studies on the formation of nanostructured ω phases in the phase separated domains.

Chapter VI

Structure Imaging of ω Domains in Phase Separated V-Ti-Cr Alloys

- Deals with direct structure imaging of the ω structured domains along various crystallographic directions and the extent of lattice plane collapse during atomic level reshuffling in binary V-Ti and ternary V-Ti-Cr alloys.
- Discussed about the contrast seen for atoms at the vertices of the ω unit cell and for the atoms in the collapsed planes in the ω structured domains.

Chapter VII

Summary and Future Scope

- Provides a comprehensive summary of the entire thesis.
- Discussed about the future scope coming out from the thesis.

Fig. 1.13: Schematic description of the thesis organization.

Chapter II

Materials and Methods

Chapter II

Materials and Methods

This chapter describes various experimental and computational techniques employed in course of the present work. Different sections individually deal with the details of the alloys and their processing through melting, heat treatment and subsequent characterisation. A brief description of the high-resolution image simulation through multislice method has also been provided in this chapter. The last section deals with the computational techniques used to study the phase stability in binary V-Ti, Ti-Cr, V-Cr and ternary V-Ti-Cr alloys essentially through thermodynamic modelling.

2.1: Alloy compositions and their processing

In the present thesis one binary and three ternary alloys chosen from different regions of the entire V-Ti-Cr system are studied. The alloy selections are based on the thermodynamic calculations performed to study the phase stability for the V-Ti-Cr system. The details of the alloy design and phase stability studies as well as the alloy selection criteria are described in chapter 3. Based on the thermodynamic modelling the following alloy compositions are chosen for experimental studies:

Table 2.1: Alloy compositions studied in the thesis

Alloy System	Composition (at%)
V-Ti-Cr	V-4Ti-4Cr
V-Ti-Cr	V-39Ti-54Cr
V-Ti	V-50Ti
V-Ti-Cr	V-40Ti-20Cr

These alloys were synthesized by arc melting method. They were arc melted in high-purity Ar atmosphere on a water cooled copper hearth, starting from elemental V, Ti and Cr (> 99.9% purity) procured from M/s Testbourne Ltd., UK. Details of impurities in the raw metals as reported by the supplier are shown in Table 2.2.

Table 2.2: Details of the impurities in raw metals of V, Ti and Cr

Vanadium (V)		**Titanium (Ti)**		**Chromium (Cr)**	
Contaminants	Amount (in ppm)	Contaminants	Amount (in ppm)	Contaminants	Amount (in ppm)
Al	10	Fe	28	Fe	8
Cr	45	Al	6	Si	8
Fe	110	Mg	6	Al	2
Si	8	Mo	5	P	5
C	42	C	18	C	8
N	40	N	10	N	5
O	130	O	30	O	5

2.1.1: Arc melting of the alloys

In case of an arc melting furnace electrical energy is transferred to thermal energy in the form of an electric arc to melt the raw materials held by the furnace. The arc is established in between the electrode and the melting hearth and is characterised by low voltage and high current. The arc melting set up available in the author's laboratory can melt upto a few tens of grams samples and the temperature can reach ~ 3000° C. During melting the non-consumable tungsten electrode acts as cathode and the water cooled Cu hearth acts as anode. Cu hearth is primarily used for its good thermal and electrical conductivity. Prior to melting, the melting chamber was evacuated and back-filled with high-purity Ar gas several times in order to reduce the partial pressure of oxygen and also to remove other adsorbed gases. Ti sponge is kept inside the melting chamber acts as an oxygen getter and greatly reduces the oxygen impurity. This further reduces probability of oxide formation and inclusion in the alloy melt. Maintenance of this clean environment inside the melting chamber is extremely essential as V and Ti have very high affinity towards environmental O, C or N. The arc zone volume was also optimized based on the Ar pressure in the chamber and the applied current. The zone volume increases as Ar pressure decreases and increases with the increase in current. The zone volume also depends on the nature of the inert gas and increases with an increase in the ionization potential of the gas.

During melting the melted alloy was re-melted several times in order to ensure complete melting and compositional homogeneity. After melting the melted alloy buttons were kept in the water cooled Cu hearth under inert Ar atmosphere for about 1 hour, before taking out. The targeted charge weight was 20 grams and the combined raw elements were taken in accordance with that inside the melting chamber. The weight of the alloy buttons were acquired every time after melting in a high precession balance and compared with that of the raw metals acquired before melting. In none of the alloys, the weight loss measured was above 0.1 gram after melting.

2.1.2: Heat treatment of the as melted alloys

The melted and homogenized alloy buttons are subjected to heat treatments as per requirements. All the heat treatments were carried out in a furnace attached with electrical temperature controller encapsulated in fused quartz tube. At first, the melted and homogenized buttons are sectioned using a low speed diamond saw. One section from each of the alloys was inert gas sealed in a fused quartz tube. During sealing, titanium sponge was used as a getter. V-50Ti and V-40Ti-20Cr alloys were solutionized at 1100° C for 5 hours, aged at 750° C for 48 hours and ice-water quenched. V-4Ti-4Cr alloy was heat treated at 1100° C for 5 hours and then furnace cooled in order to determine the stability of the phases. Microstructural and microchemical characterizations were carried out for both the as-melt and heat treated alloys.

2.2: Transmission electron microscopy studies of the alloys

The as melted as well as aged alloy slices were thinned down to ~ 100 μm thicknesses by mechanical grinding and polishing in a Struers make grinding and polishing unit successively using 600, 800, 1000, 1200, 2400 and 4000 grit papers of SiC followed by diamond polishing in a special polishing cloth. Discs with 3 mm diameter were cut from the thin slices by a Fischione make ultrasonic disc cutter with extreme care and then further dimpled to ~10 μm thickness in a Fischione make dimple grinder. Finally the dimpled discs were thinned to electron transparency by ion beam thinning under liquid nitrogen temperature using a Fischione 1010 and Technoorg Linda IV4 Ar ion mill units. The ion beam thinning was done at 5 keV with a very low ion current in order to minimise ion beam damage. The ion beam artefacts in the already milled samples were removed by further milling them in a Technoorg Linda IV6 Gentle Mill unit at 4° angles using 1.2 keV Ar ions. The electron transparent samples were plasmacleaned prior to introduction into the microscope for observation using a Fischione make plasma cleaner unit.

All specimens were characterized using a FEI Tecnai G^2 F30 U-TWIN Transmission Electron Microscope (TEM) operated at 300 kV and capable of a point resolution of 0.17 nm in phase contrast mode. The microscope consist an ultra-twin objective lens with 0.65 mm spherical (C_s) and 1.4 mm chromatic aberration (C_c) coefficients. It is equipped with a low background EDAX RTEM system for X-ray Energy Dispersive Spectroscopy (XEDS) and the Gatan Quantum 965ER imaging filter for Electron Energy Loss Spectroscopy (EELS) and Energy Filtered TEM (EFTEM) for elemental mapping. The zero-loss peak at the EELS mode has a FWHM of ~ 0.65 eV at 300 kV. High Angle Annular Dark Field (HAADF) imaging was performed in Scanning TEM (STEM) mode using a high sensitivity Fischione HAADF detector. The microscope is also equipped with a high speed digital search and view camera (2k x 2k) of Gatan Inc make for image and spectrum acquisition and analysis.

2.3: Multislice simulation

Multislice simulations consists a significant portion of the present thesis to understand the high-resolution structure images and diffraction patterns. High resolution images are not directly interpretable and cannot be used for chemical identification of atoms as these images are formed upon interference of the direct electron beam with the diffracted beams, the phase part of which is lost upon reaching the image plane. The situation becomes even more complicated as the exit wave function is further been modified by the instrument aberrations. Hence it is extremely essential to simulate the propagation of the fast electrons inside a specimen which provides insight into the imaging process and helps to interpret the experimental results properly. Careful comparisons between the simulated and the experimental images often reveal the key structural and compositional information about a specimen which cannot be inferred by simple inspection of the experimental results alone. Such examples are found throughout the thesis in chapters 4, 5 and 6, where multislice simulation are performed to explain the experimental observations as well as to retrieve useful information from the experimental data.

In the present thesis the image simulations were performed using Java based EMS software developed by Prof. P. Stadelmann (1987). In the following chapters multislice simulation has been carried out to simulate cF24 cubic $TiCr_2$ structure, cI2 phase of V-50Ti solid solution and ω phase for $Ti_{0.8}V_{0.2}$ alloy composition. In all the cases, high resolution images have been simulated under varying thickness and defocus condition along different zone axis through JEMS software. For some of these systems projected potential, exit wave, phase and amplitude part of the exit waves have also been simulated with varying thickness. The single atom potentials for elemental V, Ti and Cr are determined through Hartree-Fock method by solving the parametric equations as described by Kirkland (2009).

C15 cubic $TiCr_2$ Laves phase has a lattice parameter a=0.6932 nm. Its space group is $Fd\overline{3}m$. C15 phase has eight 'a' type positions and sixteen'd' type positions. The atomic positions are (000) and (0.625, 0.625, 0.625) respectively. In order to simulate the results, pure $TiCr_2$ lattice has been generated through symmetry operation of the point groups using the crystallographic information available in Pearson's handbook

(Villars, 1997). In similar fashion, structures corresponding to the *bcc* phase (space group: $Im\overline{3}m$) of V-50Ti alloy and the ω phases (space group: P6/mmm) for $Ti_{0.8}V_{0.2}$ alloys have also been generated by symmetry operation of the point groups using the available crystallographic information (Villars, 1997). For all of these structures high resolution images have been simulated under varying thickness and defocus condition by JEMS software (Stadelmann, 1987).The simulated thickness-defocus maps generated in all the cases are systematically compared with the recorded high resolution images.

2.4: Computational techniques

In this work the phase stability studies of V-Ti-Cr alloys has been determined by computational techniques. Formation enthalpies for the binary V-Ti, Ti-Cr, V-Cr and ternary V-Ti-Cr system have been calculated by Miedema's model. They are further verified by the thermodynamic calculations using Thermocalc software. Brief descriptions for both of these computational techniques are given in the present section.

During late 1970s and early 1980s, Miedema and his co-workers (1976, 1983) developed a semi-empirical approach to predict the enthalpies of formation for binary alloys. Later this model was extended for the ternary alloy systems by Gallego and his colleagues (1990). Miedema model is based on the "macroscopic atom" picture where the stability of any given phase is determined by its free energy with reference to the competing phases. Thus an amorphous phase will be stable if its formation enthalpy is lower than that of the competing crystalline phases. By calculating the enthalpy of formation of the solid solution and the amorphous phases as a function of composition, the relative stabilities of the two phases could be determined at any given composition. In fact, it is the free energy and not the enthalpy that should be considered to determine the stability of a phase. However, the entropy contribution is much lower than that from enthalpy in metallic systems, and therefore the entropy contribution to the free energy term can be neglected and only the enthalpy term is used. The theoretical justification of this approach is not rigorous. Moreover, after a number of years of tuning the parameters in the model, the formation enthalpies calculated through Miedema model are now fairly reliable. The details of the Miedema approach as it is applied for V-Ti-Cr system are elaborately described in chapter 3.

Thermo-calc is another powerful software package for the calculation of thermodynamic and phase equilibria in different materials. It comes under the data mining approach of the alloy design principles and in conjunction with suitable databases can assess (i) the phase diagrams for binary, ternary, isopleths and isothermal sections, (ii) phase transformation temperatures e.g. solidus, liquidus and solvus, (iii) amounts of phases and their compositions as a function of temperature and chemistry, (iv) thermochemical data such as enthalpies, heat capacities and activities, (v) stable and meta-stable heterogeneous phase equilibria and many more. Results derived from this software for V-Ti-Cr system are discussed in the following chapter in details.

2.5: Summary

A comprehensive description of alloy processing, heat treatments and their microstructural and microchemical characterizations have been given in the present chapter. Brief descriptions of all the computational techniques used in the present thesis such as Miedema model and Thermocalc as well as the multislice method for phase contrast image simulation also have been provided in this chapter.

Chapter III

Thermodynamic Calculations and Microstructural Evolution in V-Ti-Cr Alloys

Chapter III

Thermodynamic Calculations and Microstructural Evolution in V-Ti-Cr Alloys

3.1: Introduction

Last couple of decades has seen a rapid surge in research and development activities in vanadium alloys for possible exploitation in alternative energy technologies as well as hydrogen storage applications. Vanadium in combination with Cr and Ti has been identified as a potential blanket material for future fusion power systems due to its superior mechanical properties coupled with reduced activation, fast decay characteristics (Zinkle *et al.*, 1998; Smith *et al.*, 1995, 1985), compatibility with liquid lithium, resistance to irradiation damage and void swelling (Ohnuki *et al.*, 1988) at moderately high temperature, good figures of merit for low thermal stress generation (Loomis & Smith, 1992; Loomis *et al.*, 1994; Candra *et al.*, 1999) i.e. good thermal conductivity, low coefficient of thermal expansion etc.

Additionally, over the last decade, binary Ti-V alloys and ternary Ti-V-TM (TM=Cr, Ni, Co, Fe) have been explored extensively as a potential candidate for storing hydrogen and its isotopes (Akiba & Iba, 1998; Basak *et al.*, 2007). Of late, as a functionally improved alternative for large scale storage of hydrogen and its isotopes, AB_2 and AB_5 alloys have been discovered in which binary Ti-V alloys and its derivatives are worth mentioning (Levin *et al.*, 2012; Shashikala *et al.*, 2011).

Successful implementation of binary Ti-V alloys and its transition metal containing ternary derivatives in alternative energy applications would require a thorough understanding of the phase and microstructural evolution and their stability. Even though, the binary Ti-V phase diagram is relatively complete, its phase formation upon solidification is still debated in the scientific community as the phases so formed upon solidification are not always stable equilibrium phases and they are susceptible to further transformation upon heat treatment and during service exposure. Very little information of ternary V-Ti-Cr phase diagram is available in literature. Although, it has been reported in earlier literature that *bcc* solid-solution phase forms at the V-rich corner of the phase diagram, phase and microstructure evolution and its stability is almost not understood in the other regions of the phase diagram (Lee *et al.*, 2000).

In the present chapter, Miedema based thermodynamic approach (Miedema, 1976) has been applied to understand the phase stability in binary V-Ti, Ti-Cr, V-Cr and ternary V-Ti-Cr alloy system upon solidification. Binary and ternary alloy compositions, so obtained by the application of the Miedema's model have been synthesized and characterized through phase contrast and Z contrast transmission electron microscopy coupled with spectroscopy. Details of the calculations and experimental results have been described in the following sections.

3.2: Composition and phase stability studies through Miedema approach of alloy design

Miedema approach has been applied to calculate the enthalpy of formation and to understand the relative stability of the amorphous phase and the corresponding solid-solution phase in binary V-Ti, V-Cr, Ti-Cr and in ternary V-Ti-Cr systems. According to Miedema's model enthalpy of formation of a solid-solution phase (ΔH^{sol}) comprises of three components i.e. chemical, elastic and structural contribution which can be mathematically represented as

$\Delta H^{sol} = \Delta H^{c} + \Delta H^{e} + \Delta H^{s}$

Where ΔH^{c}, ΔH^{e} and ΔH^{s} are the chemical, elastic and structural contributions to enthalpy, respectively. The chemical contribution of enthalpy originates from the interactions amongst the constituent atoms. The elastic contribution of enthalpy originates due to atomic size mismatch of atoms and the structural contribution of the enthalpy originates from the valence and crystal structure of the solute and the solvent atoms. In a metallic system, structural contribution to enthalpy is quite small and it can be neglected for every practical purpose. Niessen *et al.*, (1983) has shown that the chemical contribution to enthalpy of mixing of a binary solid-solution can be expressed as,

$\Delta H^{c} = X_A X_B \left[X_A \Delta h^{sol}_{BinA} + X_B \Delta h^{sol}_{AinB}\right]$

Where, X_A and X_B represent mole fractions of the constituent A and B atoms respectively and h^{sol} is the enthalpy of solution of one element in another at infinite dilution. The binary elastic contribution to enthalpy can be expressed as

$\Delta H^{e} = X_A X_B \left[X_A \Delta h^{e}_{BinA} + X_B \Delta h^{e}_{AinB}\right]$

Where, $\Delta h^{e}_{iinj} = 2\mu_j (V_i - V_j)^2 / V_j (3 + 4\mu_j K_i)$

In the above equation, μ_j = shear modulus of the solvent;

V_i = molar volume of the solute;

V_j = molar volume of the solvent;

K_i = compressibility of the solute.

In case of the enthalpy of formation of the amorphous phase, the entire contribution comes from the chemical contribution and the enthalpy of fusion of individual atoms.

Here the structural and the elastic contributions have a negligible role. The enthalpy of the binary amorphous phase (ΔH^{am}) can be expressed as,

$\Delta H^{am} = \Delta H^{c} + X_A H^{a}_{A} + X_B H^{b}_{B}$

In the above equation ΔH^{c} is the chemical enthalpy of mixing of the pure metals A and B, X_A and X_B are the mole fractions of the components A and B, and H^{a}_{A} and H^{b}_{B} are the enthalpies of fusion of the pure metals A and B. It has been assumed that enthalpies of the crystalline pure metals are zero and the enthalpy of fusion of the amorphous pure metals (H^{a}_{i}) can be expressed as, $H^{a}_{i} = \alpha T_{f,i}$, where $T_{f,i}$ is the melting point of the ith component and $\alpha = 3.5$ J mol^{-1} K^{-1}. The enthalpy of formation of the binary amorphous phase can be written as

$\Delta H^{am} = X_A X_B [X_A \Delta h^{c}_{BinA} + X_B \Delta h^{c}_{AinB}] + 3.5[X_A T^{m}_{A} + X_B T^{m}_{B}]$

T_A and T_B are the melting points of metals A and B respectively.

On similar lines, enthalpy of formation for ternary solid-solution phases can be written as, $\Delta H^{sol}_{ABC} = \Delta H^{c}_{ABC} + \Delta H^{e}_{ABC} + \Delta H^{s}_{ABC}$

ΔH^{c}, ΔH^{e} and ΔH^{s} are the chemical, elastic and structural contributions of enthalpy, respectively. Gallego *et al.*, (1990) have extended the Miedema's model for binary alloys to ternary systems by breaking the ternary system into three corresponding binaries and neglecting the ternary interaction. In this formalism, the chemical and elastic contribution to enthalpy could be expressed as

$\Delta H^{c}_{ABC} = \Delta H^{c}_{AB} + \Delta H^{c}_{BC} + \Delta H^{c}_{CA}$

$\Delta H^{e}_{ABC} = \Delta H^{e}_{AB} + \Delta H^{e}_{BC} + \Delta H^{e}_{CA}$

The symbols have their usual meaning and the binary chemical and elastic enthalpy of mixing is calculated in the same way as expressed above. The enthalpy of formation of the amorphous phase can be calculated as,

$$\Delta H^{am}_{ABC} = X_AX_B[X_A\Delta h^c_{BinA} + X_B\Delta h^c_{AinB}] + X_BX_C[X_C\Delta h^c_{BinC} + X_B\Delta h^c_{CinB}] + X_AX_C[X_C\Delta h^c_{AinC} + X_A\Delta h^c_{CinA}] + 3.5[T^m_A + T^m_B + T^m_C]$$

X_A, X_B and X_C are the mole fractions of A, B and C and T_A, T_B and T_C are the melting point of pure A, B and C respectively. The required inputs for the calculations of formation enthalpies for binary and ternary alloys in the V-Ti-Cr system are collected from the Smithell's Metals Reference Book (Gale and Totemeier, 2004). The melting point, shear modulus, molar volume and compressibility for the V, Ti and Cr are shown in table 3.1 and the corresponding chemical and elastic enthalpies are given in tables 3.2 and 3.3 respectively.

Table 3.1: Melting points, shear modulus, molar volume and compressibility of the elements

Elements	Melting point (K)	Shear modulus (GPa)	Molar volumes (m^3)	Compressibility (GPa^{-1})
V	2183	47.0	8.32×10^{-6}	6.25×10^{-3}
Ti	1941	44.0	10.64×10^{-6}	9.09×10^{-3}
Cr	2180	115.0	7.23×10^{-6}	6.25×10^{-3}

Table 3.2: Chemical enthalpy of mixing: $\Delta h^{c}_{B\ in\ A}$ in 10^3 J/mol

Solute → Solvent ↓	V	Ti	Cr
V	—	-7	-8
Ti	-6	—	-27
Cr	-8	-33	—

Table 3.3: Elastic enthalpy of mixing: $\Delta h^{e}_{B\ in\ A}$ in 10^3 J/mol

Solute → Solvent ↓	V	Ti	Cr
V	—	12.91	3.21
Ti	10.85	—	23.46
Cr	6.43	51.51	—

3.2.1: Enthalpy-composition plots: binary V-Ti, Ti-Cr and V-Cr alloys

The enthalpy-composition plots for binary V-Ti, Ti-Cr and V-Cr as calculated by Miedema approach are given in figure 3.1(a-c) respectively. It is observed from the plots for V-Ti and V-Cr systems that the enthalpy of formation for the amorphous phase is positive. For the above two systems the enthalpy of formation of solid-solution phase is always below than that of the amorphous phase over the entire composition range.

However, for the Ti-Cr system there is a cross over and the enthalpy of formation of amorphous phase is lower than that of solid-solution phase over a composition range of 0.2-0.7 mole fraction of Ti. Moreover, in the V-Ti system, the nature of the enthalpy-composition curve for solid-solution phase is convex upward throughout the composition range and the convexity maximizes at about 50-50 composition of V and Ti. This indicates that an alloy of almost equi-molar composition of V and Ti may undergo phase separation at low temperature. For Ti-Cr system, the enthalpy-composition curve is predominantly convex upward in the composition range of 0.2-0.4 mole fraction of Ti. However, in this composition range enthalpy of formation of amorphous phase is less than that of the solid-solution phase. This indicates that the stability of the solid-solution phase is less and even if the amorphous phase is not formed due to kinetic constraints, other phase/phases with intermediate enthalpy of formation may result upon solidification of such an alloy.

3.2.2: Enthalpy-contour plots: ternary V-Ti-Cr alloys

The ternary composition range in V-Ti-Cr system in which the solid-solution phase is more stable than the amorphous phase of similar composition i.e. the composition range in which the enthalpy of formation for solid-solution phase is less than the amorphous phase of similar composition is given in figure 3.2(a). It is observed from the figure that the relative stability of the solid-solution phase is always more than that of the amorphous phase almost all through the ternary phase field including the V rich side, except a narrow composition range close to Ti-Cr binary system. In order to quantitatively understand the relative stability of the amorphous phase and the solid-

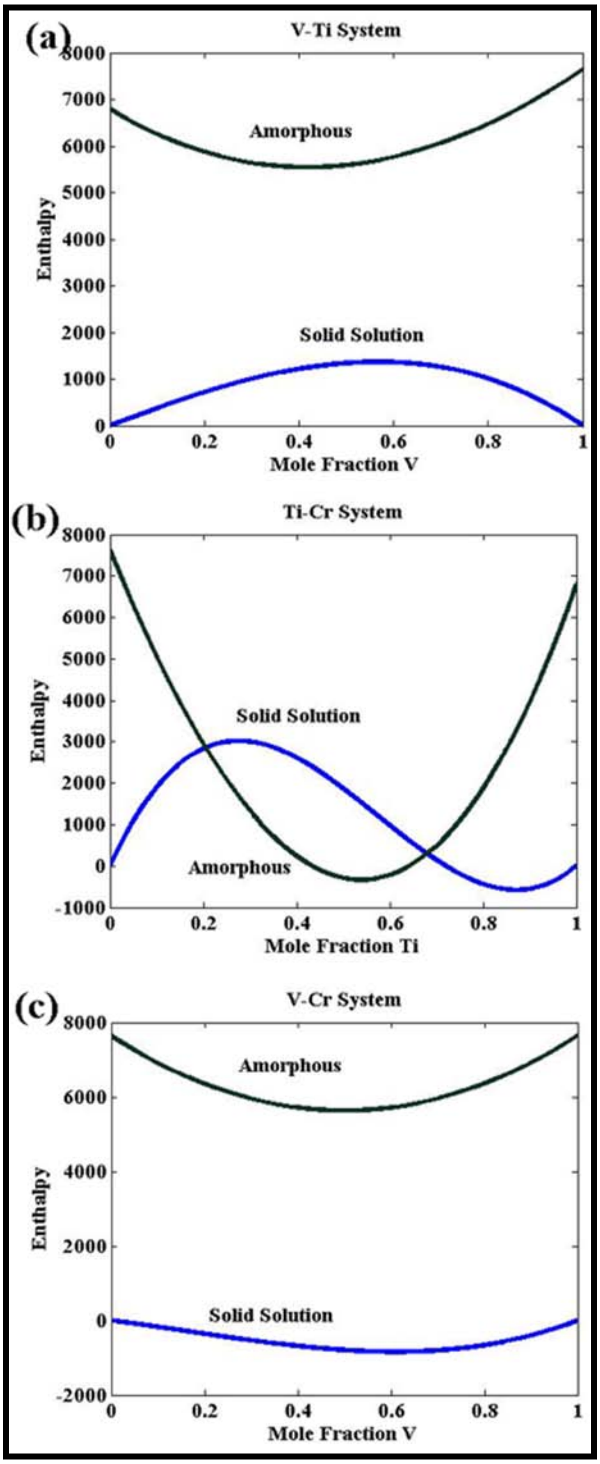

Fig. 3.1(a-c): Enthalpy – composition diagram for the binary V-Ti, Ti-Cr and V-Cr alloy system as calculated from the Miedema model. The enthalpy values are in J/mol.

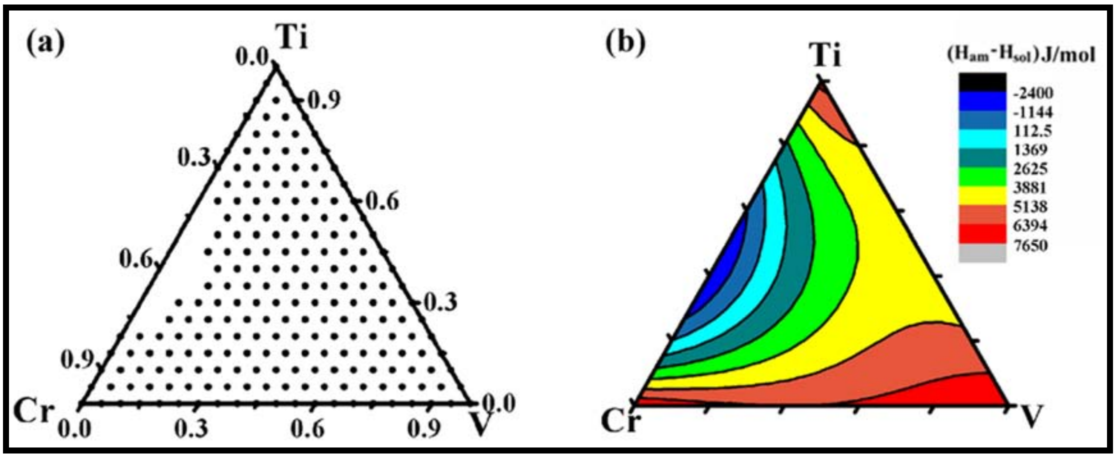

Fig. 3.2 (a) Enthalpy difference – composition plot over the entire ternary composition range of V-Ti-Cr system. The marked region shows the composition range in which solid-solution phase is thermodynamically stable over the amorphous phase. (b) Enthalpy contour plot showing the differences between the formation enthalpies of amorphous phase and solid-solution phase over the entire composition range of V, Ti and Cr. Inset shows the absolute values of the difference associated with the different colour codes.

solution phase, the difference in enthalpy of formation between the amorphous phase and the solid-solution phase is plotted in figure 3.2(b). It is observed from the enthalpy-contour plot that the enthalpy difference is almost always positive except for a narrow region close to Ti-Cr binary system up to ~0.15 mole fraction of V addition. This observation necessarily indicates that close to the Ti-Cr binary system up to ~0.15 mole fraction of V addition amorphous phase is relatively stable. In case the amorphous phase is not formed due to the kinetic constraints other phase/phases with intermediate stability are likely to form upon solidification.

3.2.3: Effect of Cr addition in V-Ti formation enthalpy: Isopleths of V-Ti-Cr ternary diagram

In V-Ti binary system, the enthalpy-composition plot for the solid-solution phase is mildly convex upward which indicates a possibility of phase separation at low temperature in this alloy system over the entire composition range of V. The convexity maximizes at the 50-50 composition range of Ti and V. In order to investigate as to how this behavior is affected on addition of Cr, enthalpy-composition plots for the amorphous and the solid-solution phase has been plotted over the V-Ti-Cr isopleths with varying Cr concentrations from 0.00 mole fraction to 0.95 mole fractions. The enthalpy-composition plots are given in figures 3.3 to 3.7. The isopleth of V-Ti-Cr system with 0.0 mole fraction of Cr is essentially the binary V-Ti alloy only and the detailed feature of this plot has already been described earlier. It is observed over the other isopleths that, till 0.30 mole fraction of Cr, enthalpy of formation of solid-solution phase is less than that of the amorphous phase for the entire composition range of V. However, over 0.35 mole fraction of Cr addition, enthalpy of formation of amorphous phase become less than that of the solid-solution phase for the lower V content and the trend continues till the addition of 0.75 mole fraction of Cr. The difference between the formation enthalpy of the solid-solution phase and the amorphous phase maximizes at ~ 0.6 mole fraction of Cr where the amorphous phase pretends to be more stable than the solid-solution phase till 0.1 mole fraction of V. This is essentially the composition range of binary Ti-Cr alloy in which the Laves phase forms. Moreover, the amorphous phase shows higher stability than the solid-solution phase in the V lean side of the V-Ti isopleths over the range of 0.35 – 0.75 mole fraction of Cr, but the difference maximizes on and around the Laves phase forming composition. This further supports the earlier obtained result that till the addition of 0.1 mole fraction of V, thermodynamically amorphous phase shows higher stability than the solid-solution phase. Beyond 0.6 mole fraction of Cr addition, amorphous phase field reduces and completely disappear over and around of 0.8 mole fraction of Cr. Over 0.8 mole fraction of Cr addition, again the solid-solution phase become thermodynamically more stable for the entire composition range of V and the difference between the enthalpy of formation of the amorphous phase and solid-solution phase increases with the increase in Cr addition. Actually with the enhancement of the Cr content the alloy predominantly behaves as V-Cr alloy, which is a highly miscible system and shows the stability of the solid-solution phase for the entire composition range of Cr. The nature of the enthalpy composition curve for the solid-solution phase in the isopleths also changes with Cr content. The convexity of the curve maximizes for the binary V-Ti alloy and the convexity decreases with the increase in the Cr content and finally becomes linear beyond 0.8 mole fraction of Cr addition. From this calculation, it is clearly understood that binary V-Ti solid-solution phase exhibit a tendency for phase separation throughout the entire composition range and the tendency maximizes close to equi-molar composition. However, the phase separation tendency decreases with the addition of Cr in the alloy.

3.2.4: Effect of V in elastic contribution of Ti-Cr formation enthalpy

The individual enthalpy component due to elastic contribution and the chemical contribution of the solid-solution phase as well as their variation with respect to the formation enthalpy of the amorphous phase for similar composition of binary V-Ti, V-Cr

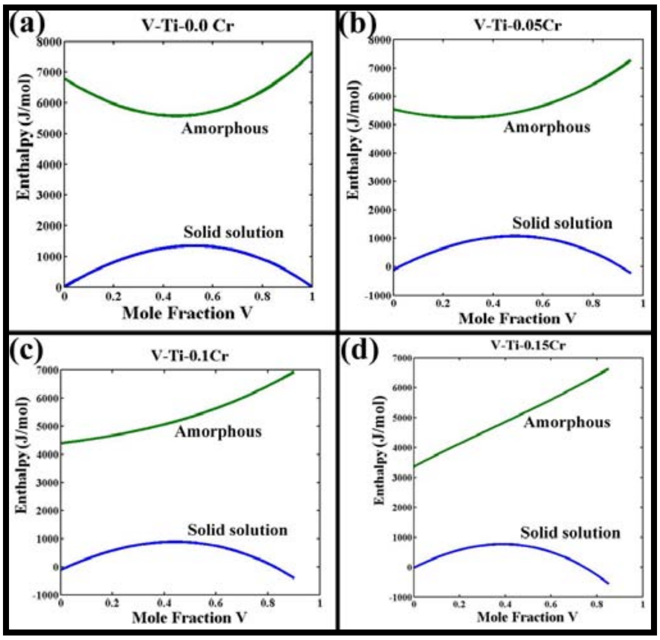

Fig. 3.3(a-d): Isopleths of the V-Ti-Cr enthalpy – composition plot showing the effect of Cr addition (from 0 to 15 at%) in the enthalpy diagram for the solid-solution phase of binary V-Ti alloy.

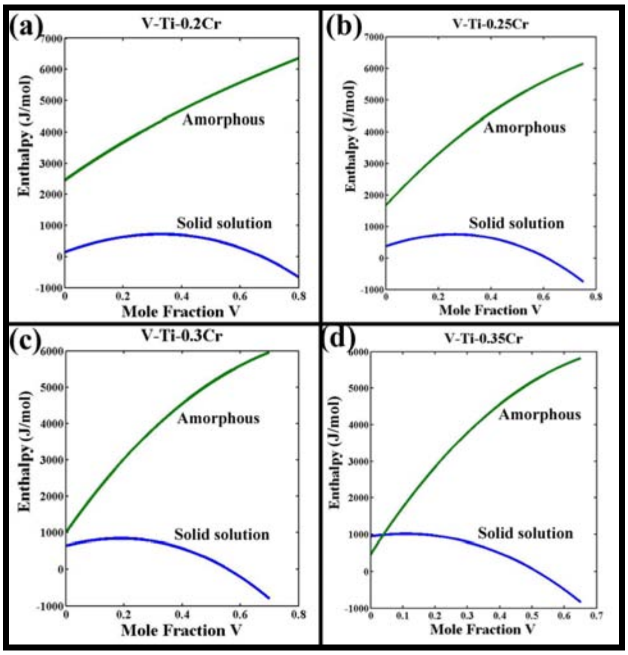

Fig. 3.4(a-d): Isopleths of the V-Ti-Cr enthalpy – composition plot showing the effect of Cr addition (from 20 to 35 at%) in the enthalpy diagram for the solid-solution phase of binary V-Ti alloy.

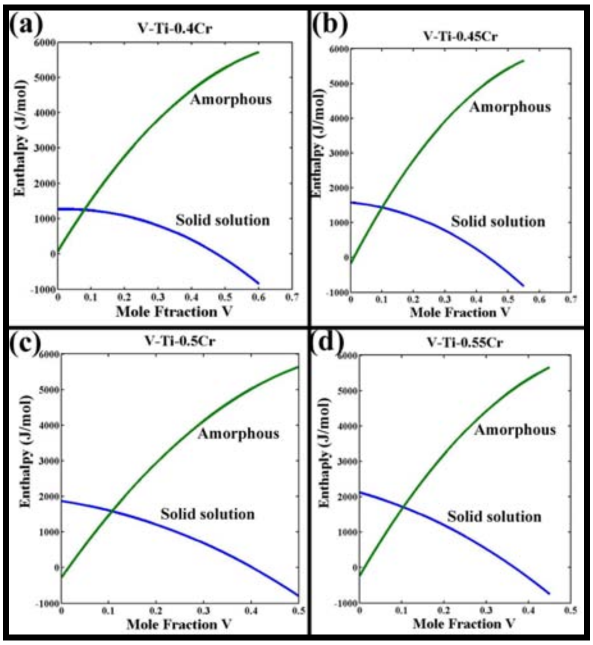

Fig. 3.5(a-d): Isopleths of the V-Ti-Cr enthalpy – composition plot showing the effect of Cr addition (from 40 to 55 at%) in the enthalpy diagram for the solid-solution phase of binary V-Ti alloy.

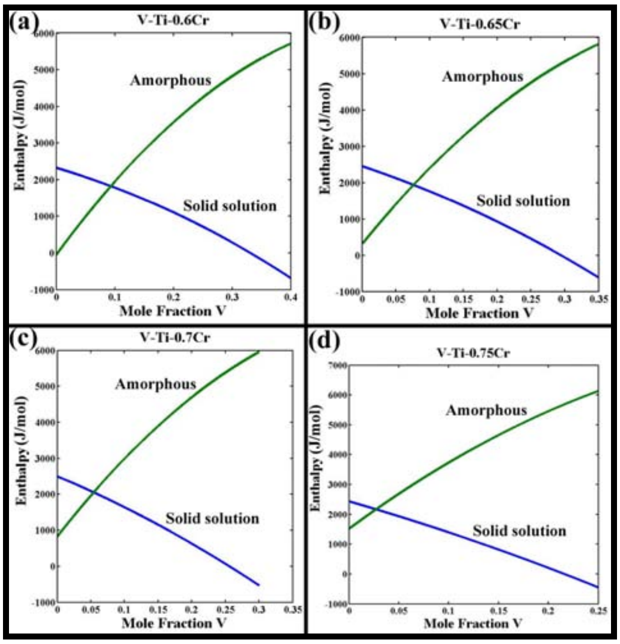

Fig. 3.6(a-d): Isopleths of the V-Ti-Cr enthalpy – composition plot showing the effect of Cr addition (from 60 to 75 at%) in the enthalpy diagram for the solid-solution phase of binary V-Ti alloy.

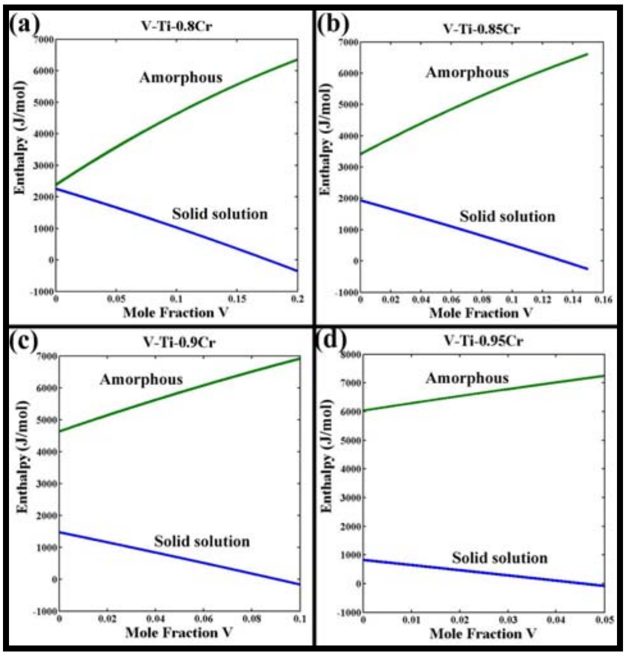

Fig. 3.7(a-d): Isopleths of the V-Ti-Cr enthalpy – composition plot showing the effect of Cr addition (from 80 to 95 at%) in the enthalpy diagram for the solid-solution phase of binary V-Ti alloy.

and Ti-Cr alloys are shown in figure 3.8 (a-c). For the binary V-Ti and V-Cr alloys, formation enthalpy of the amorphous phase is always higher than both of the elastic contribution and chemical contribution of the solid-solution phase. However, for the binary Ti-Cr alloy system, elastic contribution of the formation enthalpy for the solid-solution phase becomes higher than the enthalpy of amorphous phase over the composition range of 0.2 to 0.8 mole fraction of Ti. Moreover, the elastic component maximizes around the Laves phase composition of $TiCr_2$ phase as shown in the figure. Figure 3.8(d) shows the difference between the elastic and the chemical contribution of the formation enthalpy for the solid-solution phase of the Ti-Cr alloy. The nature of these curves remains almost same with the addition of V as shown in figure 3.9(a-c). However, the peak of the (H_{el}-H_{ch}) curve gradually shifts towards the lower Ti concentration side with the addition of V. It can be noted that, Miedema model only predicts the stability of the amorphous and solid-solution phases and cannot provide details about the other constituent intermetallics e.g. V-$TiCr_2$ Laves phase alloy or the metastable phases e.g. ω phases in Ti-V alloys; hence required extensive experimental support.

3.3: Experimental validation of Miedema's model

By analyzing the enthalpy-composition diagrams in V-Ti-Cr alloy systems, as obtained by the Miedema approach, alloy compositions from binary V-Ti alloy as well as from different regions of the ternary V-Ti-Cr system have been selected and studied experimentally to understand the phase evolution in those alloys. The details of the selected alloys and their microstructural and microchemical characterization analysis are shown in the following sections.

3.3.1: Selection of alloy compositions

Based on these thermodynamical calculations, four alloy compositions were chosen. The composition of the alloys has been given in table 3.4. In view of the present calculations, the V-4Ti-4Cr alloy should form solid-solution phase upon solidification. In V-39Ti-54Cr alloy, the solid-solution phase is not likely to form due to its less stability. However, should the amorphous phase not form upon solidification on a water cooled copper hearth where typical cooling rate achieved is ~10-100 K/s, other phase/phases with intermediate stability may be expected. In general, the amorphous phase forms at a typical cooling rate ~ 10^5-10^6 K/s (Basu, 2004) which is much higher than the water cooled copper hearth. The V-50Ti alloy should form solid-solution phase and the solid-

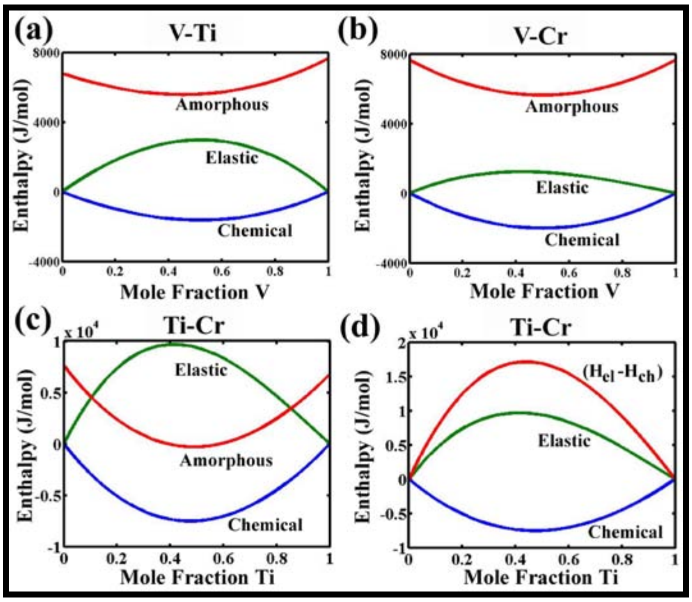

Fig. 3.8(a-c): Formation enthalpy for the amorphous phase and the change in the elastic contribution and chemical contribution of enthalpy with composition for binary V-Ti, V-Cr and Ti-Cr alloys. (d) Difference between the elastic and chemical contribution of enthalpy for binary Ti-Cr alloy.

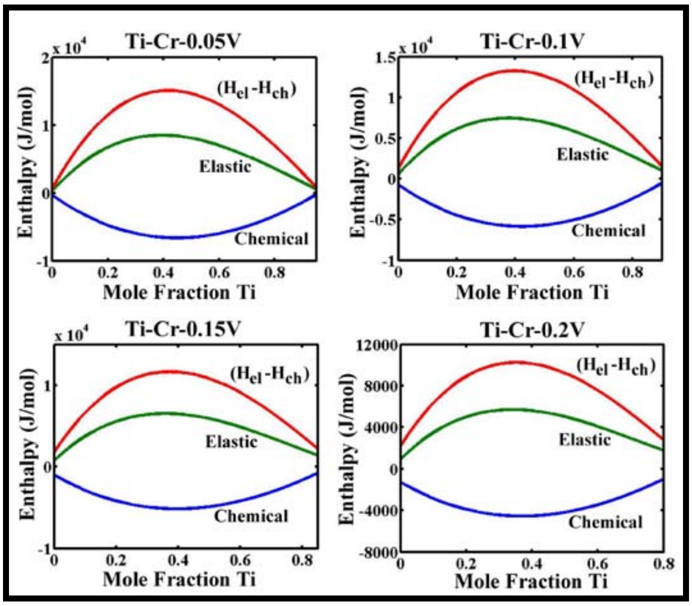

Fig. 3.9(a-d): Change in elastic and chemical contribution of enthalpy and their difference (H_{el}-H_{ch}) with composition as an effect of V addition in Ti-Cr system. The calculations are carried out for 0.05, 0.10, 0.15 and 0.20 mole fraction of V addition.

solution phase may show a tendency for phase separation. A similar behavior is expected from the V-40Ti-20Cr alloy.

Table 3.4: Alloy systems and their compositions

Alloy system	**Composition (at%)**	**Stable phases predicted from Miedema's calculation**
V-Ti-Cr	V-4Ti-4Cr	Solid-solution
V-Ti-Cr	V-39Ti-54Cr	Amorphous (as frozen liquid)
V-Ti	V-50Ti	Solid-solution with a phase separation tendency
V-Ti-Cr	V-40Ti-20Cr	Solid-solution with a reduced phase separation tendency from that of V-50Ti

3.3.2: Preparation of the alloys

Nominal composition of the alloys as stated in table 3.4 have been arc melted in high-purity argon atmosphere on a water cooled copper hearth, starting from elemental V, Ti and Cr (>99.9% purity). The melting chamber was evacuated several times and back filled with high-purity argon gas in order to reduce the partial pressure of oxygen. The melted alloy buttons were inverted and re-melted several times in order to ensure complete melting and compositional homogeneity. The alloys were heat treated after encapsulation in a fused quartz tube back filled with Ar.

3.3.3: Microstructural and microchemical studies: V-4Ti-4Cr, V-39Ti-54Cr, V-50Ti and V-40Ti-20Cr alloys

TEM bright field image, electron diffraction pattern, high resolution phase contrast image and the EELS spectrum from the V-4Ti-4Cr alloy is given in figure 3.10(a-d) respectively. The mottled contrast seen in the TEM bright field image mainly originates due to diffraction effects. The diffraction pattern from the same alloy along [001] direction (figure 3.10b) indicates the presence of single cubic phase. The 110 and 200 principal reflections are marked in the diffraction pattern. The lattice parameter as calculated from the diffraction pattern turns out to be a=0.30 nm which is very close to pure *bcc* V with a=0.30274 nm (ICDD # 022-1058) as well as to that calculated from the earlier recorded X-ray diffraction pattern of the same alloy with a=0.30356 nm (Ghosh *et al.*, 2013). In the high resolution phase contrast image along [001] direction 0.223 nm and 0.158 nm spacings corresponding to {110} and {200} planar spacing of the *bcc* solid-solution phase can be observed. In the EELS spectrum characteristic core-loss edges for V, Ti and Cr can be observed at 512 eV, 454 eV and 574 eV respectively. The relative intensities of the Ti-L and Cr-L edges indicate that they are present in this alloy as minor alloying elements. Quantification of the EELS spectra indicates the composition of the alloy to be close to V-4Ti-4Cr which the as melted nominal composition. Based on these studies it is confirmed that the present alloy has solidified as a *bcc* phase.

TEM bright field image, electron diffraction pattern, high resolution phase contrast image and the EELS spectrum from the V-39Ti-54Cr alloy are given in figure 3.11(a-d) respectively. The electron diffraction pattern in figure 3.11(b) matches closely with [111] zone axis pattern of cubic $TiCr_2$ Laves phase. The lattice parameter as

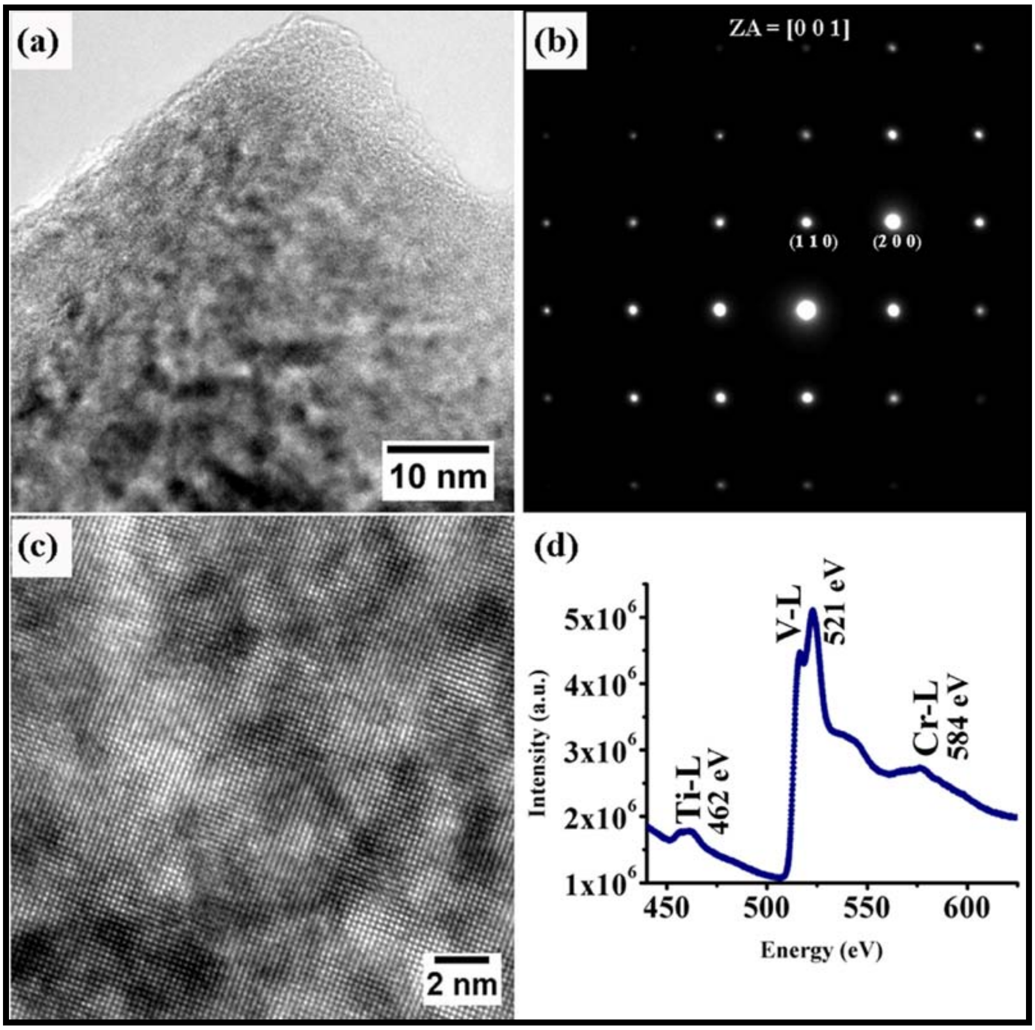

Fig. 3.10: (a) Bright field image from a region of the alloy with nominal composition V-4Ti -4Cr. (b) Selected area electron diffraction pattern from the same region of the alloy along [0 0 1] zone axis. This pattern has been indexed with a *bcc* structure (cI2) where (1 1 0) and (2 0 0) spots are marked. (c) Phase contrast structure image showing the lattice planes when the region is oriented along [001]. (d) Electron energy loss spectra showing the energy loss edges correspond to Ti-L, V-L and Cr-L. The relative intensity indicates that Ti and Cr are present in the alloy as the minor alloying elements.

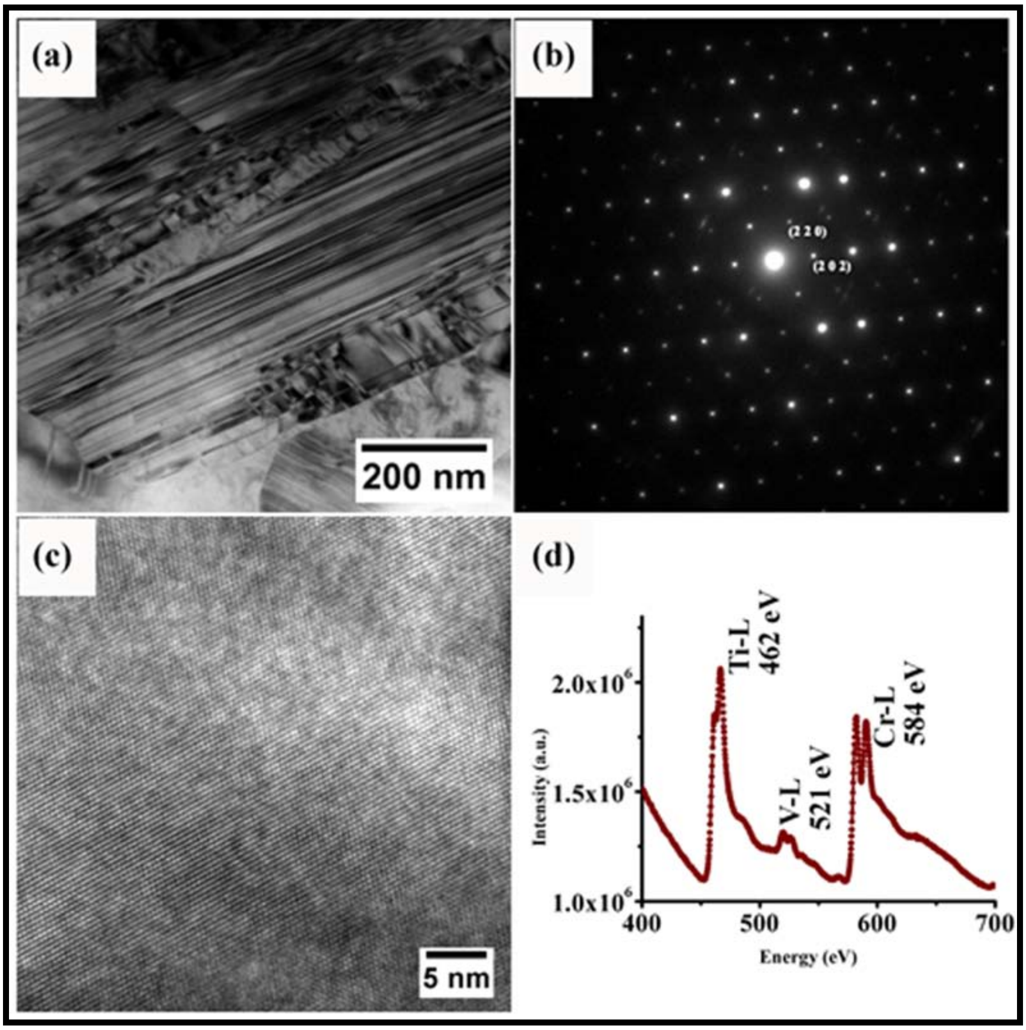

Fig. 3.11: (a) Relatively low magnification bright field micrograph showing the Laves phase structure in the V doped $TiCr_2$ Laves phase with nominal composition of V-39Ti-54Cr. The high density of the defects present in Laves phase can be identified by the linear contrast seen in the image. (b) Selected area electron diffraction pattern along [1 1 1] zone axis of the specimen from a relatively defect free region of the alloy. This pattern has been indexed with cubic $TiCr_2$ Laves phase of cF24 structure. (c) zero-loss energy filtered phase contrast structure image showing the lattice planes along $[01\overline{1}]$ zone axis of V doped cubic $TiCr_2$ Laves phase. (d) Electron energy loss spectra showing the energy loss edges correspond to Ti-L, V-L and Cr-L.

calculated from the diffraction pattern turns out to be a=0.69 nm which is close to the reported value of pure $TiCr_2$ cubic Laves phase. From the bright field image (figure 3.11a) it is observed that the Laves phase grain has a high density of planar faults which can be ascertained from the linear contrast observed in the grain body. The EELS spectrum (figure 3.11d) from the grain shows the characteristics V-L, Ti-L and Cr-L core-loss edges. The relative intensity of the V-L edge indicates that it is present only as an alloying element. The elemental composition as determined from the EELS spectra is similar to the nominal composition of the as melted alloy. In order to determine the location of the V atoms in the $TiCr_2$ Laves phase lattice high resolution imaging was carried out along various crystallographic orientations. One such image is given in figure 3.11(c). High resolution image of $TiCr_2$ Laves phase is quite complex and it can be quantitatively interpreted only with phase contrast image simulation. The details of which have been discussed in chapter 4 of this thesis.

TEM bright field image from the V-50Ti binary alloy is given in figure 3.12(a). In the image periodically spaced and interlinked bright and dark striations are observed. The spacing between two consecutive striations is ~2-4 nm and it remains almost constant. The electron diffraction pattern from such a region along [012] zone axis is given in figure 3.12(b). The principal reflections match with the [012] pattern of a *bcc* phase. The 200 and $12\overline{1}$ type spots are marked on the diffraction pattern. The lattice parameter as calculated from the diffraction pattern turns out to be a=0.32 nm which is very close to the reported lattice parameter for the *bcc* V-Ti solid-solution phase (a=0.3165 nm). Apart from the principal reflections, diffused scattering in between the reflections and faint satellite spots are also observed in the diffraction pattern. This observation indicates that the alloy is phase separated. In order to confirm the chemical nature of the phase separated domains EFTEM chemical mapping with V-L and Ti-L edges has been carried out. The EFTEM chemical map is shown in figure 3.12(c). The striations seen in the bright-field images of figure 3.12(a) are also observed in the chemical map. These observations suggest that the alloy has undergone phase separation creating a V-rich phase and a Ti-rich phase. Even though there is a composition modulation, both the phases are *bcc*. The EELS spectrum from the alloy is given in figure 3.12(d). In the EELS spectrum, characteristics V-L and Ti-L core-loss edges are observed. Composition determination from the EELS spectrum after background subtraction indicates that the nominal composition of the alloy is V-49Ti which is very close to the as-melted composition. Determination of chemical modulation by EFTEM at such a fine scale may not be confirmatory always. In order to ascertain the chemical nature of the phase separated domains STEM-EELS has been carried out on the striations.

TEM bright field image and the corresponding electron diffraction pattern from the V-40Ti-20Cr alloy have been given in figure 3.13(a-b) respectively. In the bright field image alternate bright and dark striation same as that of V-50Ti alloy is observed. The periodicity of spacing between two consecutive bright or dark striations is ~5-6 nm. In the corresponding diffraction pattern along [012] zone axis, apart from the principal reflections, diffused scattering and faint satellite reflections are observed. In the diffraction pattern 200 and $12\bar{1}$ type principal reflections are marked. The lattice parameter as calculated from the diffraction pattern turns out to be a= 0.31 nm which is very close to the *bcc* solid-solution phase of V and Ti. Morphological observation from the image and presence of diffuse scattering in the diffraction pattern essentially indicates

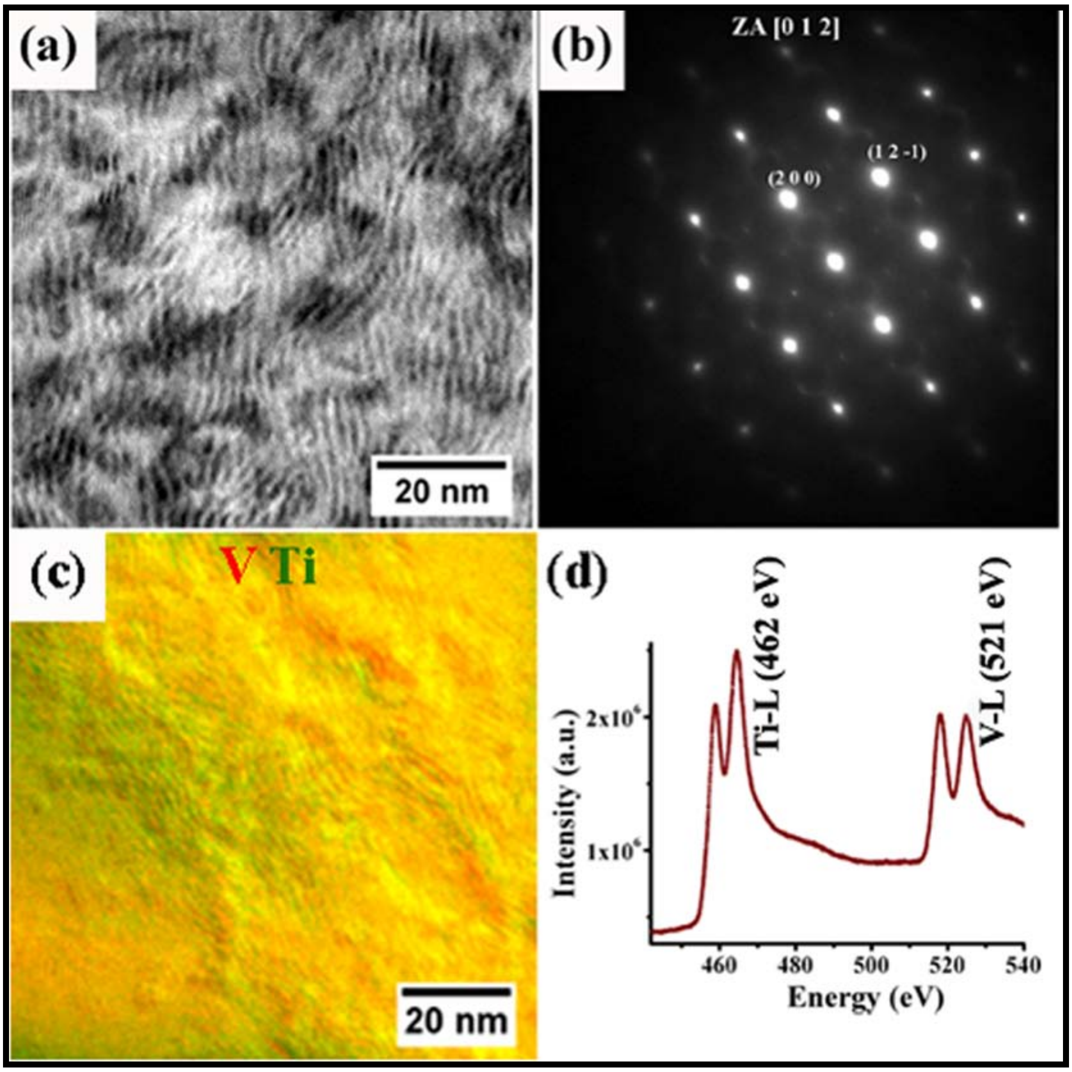

Fig. 3.12: (a) Diffraction contrast micrograph from a region of V -50Ti alloy showing the alternate bright and dark striations contrast typical to a phase separation phenomena. This has further been confirmed by the diffused intensities seen around the main diffraction spots in the selected area electron diffraction pattern shown in (b). The diffraction pattern has been indexed with [0 1 2] zone axis pattern of cI2 structure where (2 0 0) and (1 2 $\bar{1}$) spots are marked in the image. (c) Energy filtered TEM (EFTEM) micrograph acquired with Ti-L and V-L energy loss edges showing the relative distribution of Ti and V in the *bcc* matrix (d) Electron energy loss spectra showing the energy loss edges correspond to Ti-L and V-L. The elemental compositions of V and Ti calculated from the EELS profile matches quite well with the as melted elemental compositions.

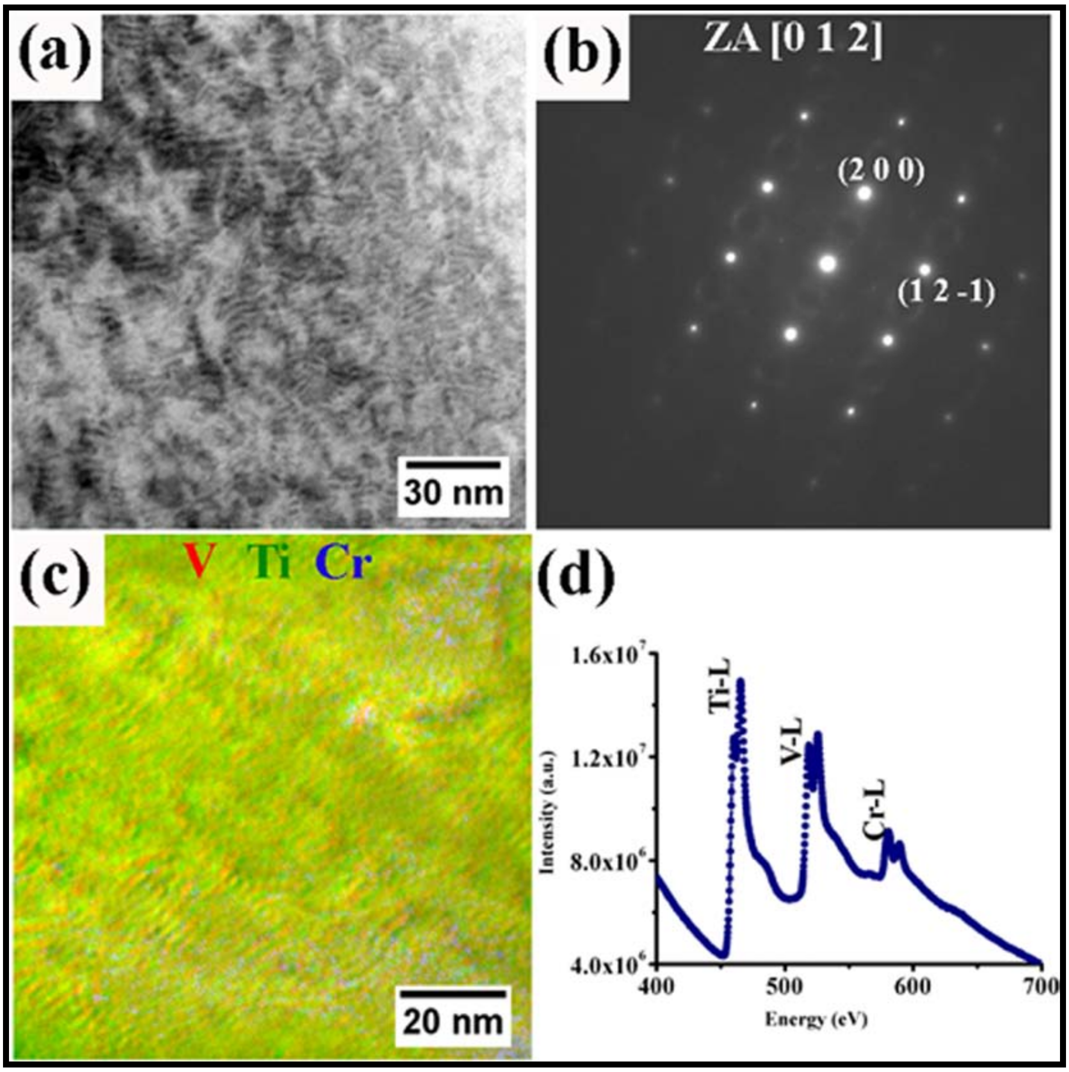

Fig. 3.13: (a) Bright field micrograph from a region of V -40Ti -20Cr alloy showing the bright and dark striations contrast. (b) Electron diffraction pattern along [0 1 2] zone axis of cI2 structure showing the diffused intensities around the main diffraction spots. (c) Energy filtered TEM (EFTEM) micrograph acquired with Ti-L, V-L and Cr-L energy loss edges showing the relative distribution of Ti, V and Cr in the *bcc* matrix (d) Electron energy loss spectra showing the energy loss edges correspond to Ti-L, V-L and Cr-L. The elemental compositions of V, Ti and Cr calculated from the EELS profile matches quite well with the as melted elemental compositions.

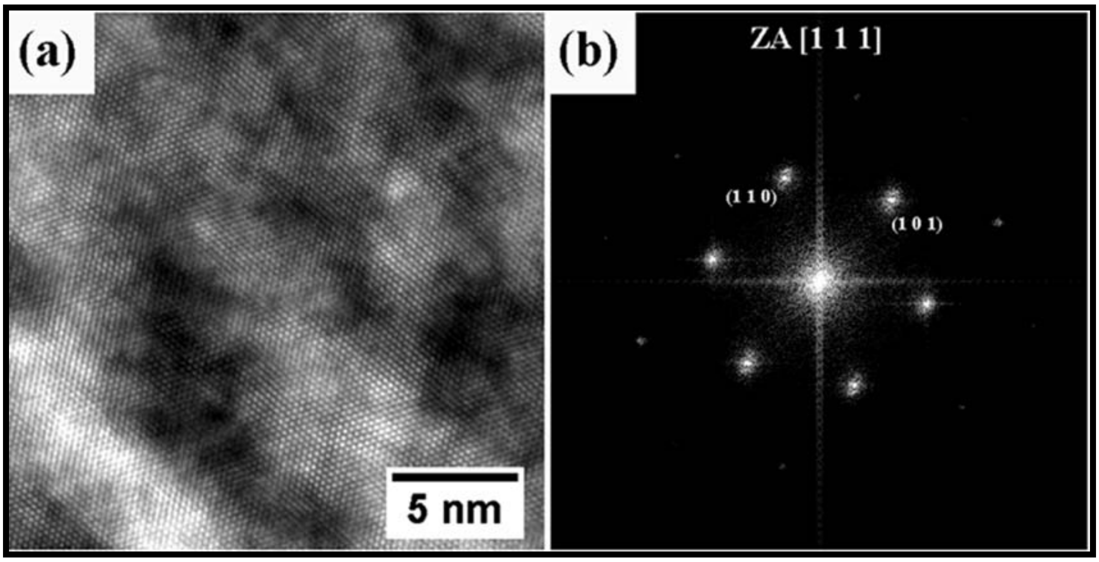

Fig. 3.14(a-b): Phase contrast image and the corresponding power spectrum from V-40Ti-20Cr alloy specimen showing the structural details from the phase separated domain in the nm level. The image has been taken along [1 1 1] zone axis where (1 1 0) and (1 0 1) spots are marked in the power spectrum.

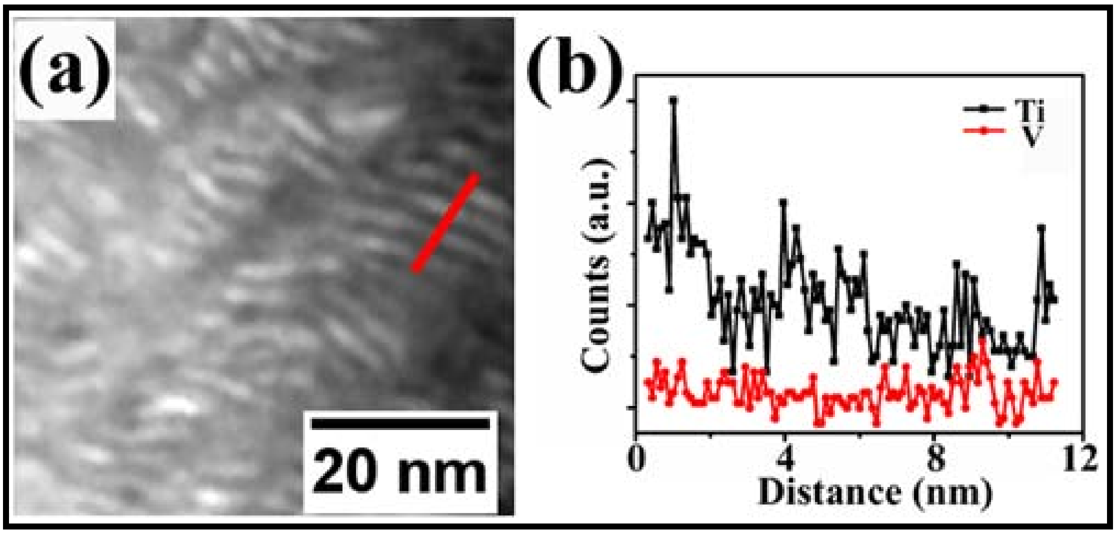

Fig. 3.15: STEM-HAADF image and the corresponding XEDS profile of V and Ti along the marked region of V-Ti alloy. Compositional modulation can be seen in the HAADF image which is further confirmed by the XEDS profile map.

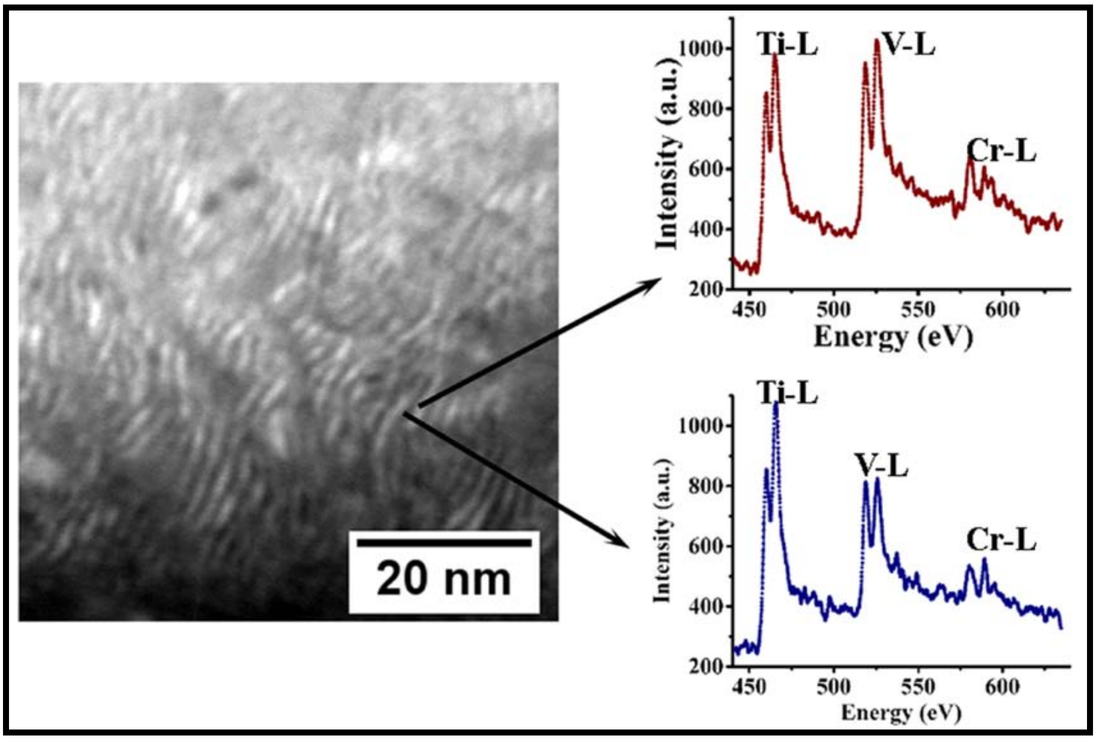

Fig. 3.16: STEM-HAADF image from the phase separated region of V -40Ti -20Cr alloy showing the compositional fluctuations along the bright and dark striations. (inset) EELS profile from the bright and the dark contrast region of the STEM–HAADF image shows the intensity variation of the Ti-L and V-L energy loss edges. The relative intensity of the Cr-L energy loss edge remains almost constant in both the profiles.

phase separation in this alloy also. In order to ascertain the chemistry of the alloy and the compositional modulation in the alloy EFTEM and EELS has been done. The EFTEM chemical map and the EELS spectrum are given in figure 3.13(c-d) respectively. In the EELS spectrum characteristics V-L, Ti-L and Cr-L edges are observed. However, the EFTEM composition map striations are still observed and it appears that the alloy undergoes a phase separation giving rise to V-rich and Ti-rich phase.

In order to understand the interface structure of the phase separated domains in V-40Ti-20Cr alloy specimen, high resolution phase contrast image and the corresponding FFT calculated are shown in figure 3.14(a-b) respectively. In the high resolution image alternating bright and dark contrast is still observed. However, the lattice fringes are continuous irrespective of the contrast. This indicates that the interface between two chemically modulated regions is coherent which further substantiate the phase separation event. The FFT indicates that the sample is oriented along [111] zone axis.

In order to ascertain the chemical nature of the phase separated domains and for quantitative understanding the compositional partitioning, STEM-XEDS and STEM-EELS have been carried out for both binary V-50Ti and ternary V-40Ti-20Cr alloys and shown in figures 3.15 and 3.16 respectively. In the HAADF micrographs from both the alloys, interconnected and regularly spaced striations are observed. This indicates periodic oscillation of average atomic number arising out of composition modulation perpendicular to the striations. For V-50Ti alloy, XEDS profile along the bright and dark striations confirm the presence of V rich and V poor domains. This observation confirms that the alloy upon solidification undergoes phase separation giving rise to V-rich and V-poor phase separated domains. For V-40Ti-20Cr alloy, HAADF image and EELS spectra in the fine probe mode from two consecutive striations are given in figure 3.16. In the HAADF image alternating and periodically spaced bright and dark contrast is observed which confirms compositional modulation arising out of variation in average atomic number perpendicular to the striations. The EELS spectra from the striations indicate that the bright lamella is V-rich and the dark lamella is V-poor. The Cr-L edge is observed from both the lamella. This indicates that V-40Ti-20Cr alloy also undergoes phase separation upon solidification giving rise to V-rich and V-poor phases and Cr atom is evenly distributed in both the phases.

3.4: Discussions

3.4.1: Metastability, energy landscape and microstructural design

It has been mentioned in the earlier sections that V-alloys have emerged as a potential candidate material for various technological applications in which V-Ti-Cr and V-Ti-W are worth mentioning. V-Ti binary and V-Ti-Cr ternary alloys are of particular interest as a candidate material for hydrogen storage. However, most of the effort has gone towards V-4Ti-4Cr alloy. Even the interaction of this alloy with minor interstitials such as O, C, N has been studied in detail. It has been reported in earlier literature that the interstitial elements interact with the alloy above ~200 °C to either form precipitate or at least mobility of these interstitials are affected (Zinkle *et al.*, 1998; Hoelzer *et al.*, 2000; Muroga *et al.*, 2002). It is important to explore other parts of the phase diagram, understand the phase and microstructural evolution with concomitant change in properties. Even though, V-Ti binary phase diagram is reasonably complete, very little information is available in V-Ti-Cr ternary alloy system (Ghosh, 2002). Moreover, phases present in the phase diagram may not result under practical processing conditions where the processing parameters are far from quasi-static equilibrium. Metastability is best defined as a kinetic hold-up of a material at a particular energy state which may not be the minimum possible one with respect to its composition, structure and microstructure. Due to the requirement of properties, several processing steps are often involved in the designing of a material which does not allow it to go the minimum possible energy state; instead, it is kinetically held up in a higher energy state. The material in this state behaves as such a stable material unless an energy fluctuation is introduced which will make this material move over an energy barrier to the stable state or another metastable state. Under practical processing conditions, many metastable phases may appear due to the processing and service life exposure and can be understood only in terms of potential landscape of the material. These metastable phases may undergo further transformation upon heat treatment or during the service exposure. Furthermore, as it has been mentioned in earlier literature (Hoelzer *et al.*, 2000; Muroga *et al.*, 2002), dissolved impurities may influence the precipitation behavior and consequent properties. Present study is mostly oriented towards understanding the evolution of major constituent phases upon solidification. Minor impurity elements are not likely to change the evolution of major phases. It is supposed to affect the precipitation behavior at the later stages of heat treatment.

3.4.2: Miedema model vis-a-vis heuristic approach and data mining of alloy design

The basic alloy design approach can broadly be divided into four segments, namely heuristic approach, model based approach, data mining and *ab initio* calculations. The Hume-Rothery rule for the solid-solution formation and Inoue's criteria for glass formation are some common examples of the heuristic approach whereas Pettifor structural map for the synthesis of intermetallic phases comes under the data mining approach of alloy design. Though the heuristic approach is quite reliable in predicting general trends of alloying behaviour but it has certain limitations as only a limited numbers of parameters are considered in these methods. In the present work, a model based thermodynamic approach has been adapted to predict the phase formation in V-Ti-Cr alloys. Miedema approach provides a quick finger print as to how the alloy should behave for practical purposes. Ghosh *et al.* (2012) have used Miedema's model based approach for iron and early transition metal alloys in order to understand the energy landscape for such alloys. Bera *et al.* (2007) have used the same approach to access the stability of hydrogen storing 1:2 compounds. The same model based approach has been used by several authors to understand and extend a scientific basis for glass forming ability of different alloy systems (Basu *et al.*, 2008; Figueroa *et al.*, 2013; Tavoosi *et al.*, 2011). In the present case two states i.e. amorphous and solid-solution phases have been considered for all possible binaries and the ternary alloys of V-Ti-Cr systems. In case the liquid state of the alloy is frozen at the room temperature by cooling it down from the melting point, an amorphous phase will appear. On the other hand, a solid-solution phase may also appear in the alloy. As at ambient temperature, entropy does not play a dominant role in determining the free energy, enthalpy can be used as an estimate of free energy for all practical purposes. Atomic radii of V, Ti and Cr are 171 pm, 176 pm and 166 pm respectively. Similarly, the binary heats of mixing as observed from table 3.2 are not highly negative except for Ti-Cr pair. According to Inoue's criteria of amorphous phase formation, V-Ti-Cr system should not have a very high glass forming ability. It may form glass under very high cooling rate i.e. of the order of 10^6 K/s or more. On solidification in water cooled copper hearth, where the typical cooling rate is 10-100 K/s, amorphous phase in this alloy is not expected even though formation of amorphous phase is a thermodynamic possibility in some composition domains. As a result, amorphous phase has not been observed experimentally in V-Ti-Cr alloys. It has been observed from the Miedema approach that for V-Cr and V-Ti systems, solid-solution phase is always more stable than the amorphous phase over the entire composition range. However, for

Ti-Cr system, over ~0.2-0.7 mole fraction of Ti, amorphous phase is more stable than the solid-solution phase. Again due to the low glass forming ability and insufficient cooling rate has not resulted in amorphous phase formation. In the same composition region $TiCr_2$ Laves phase is observed in the binary phase diagram. The binary heat of mixing of Ti and Cr being highly negative, it favors intermetallic phase formation though the atomic size difference between Ti and Cr are well within the limit (< 15%) of Hume-Rothery rule. Ghosh *et al.* (2012) have shown that amorphous phase forming tendency is higher around the Laves phase composition in iron early transition metal binary and ternary alloy systems. Similarly, in the ternary calculations for V-Ti-Cr, it has been observed that around binary Laves phase region enthalpy of formation of amorphous phase is more negative than the solid-solution phase. Moreover, little ternary addition of V does not change the enthalpy of mixing significantly. As mentioned earlier, glass forming ability of V-Ti-Cr alloy is low and typical cooling rate that is achieved in water cooled copper hearth would not lead to amorphous phase formation. This necessarily indicates that V-Ti-Cr alloy in the vicinity of $TiCr_2$ Laves phase would form V-substituted Laves phase under normal cooling rates as obtained in an arc melting furnace. Enthalpy of formation curve for binary V-Ti and for ternary V-Ti-Cr at 0.2 mole fraction of Cr is convex upward. This indicates that even though the solid-solution phase is stable in these systems, a tendency of phase separation may be observed. From binary V-Ti phase diagram similar signatures are obtained. However, experimental evidence being scarce, the issue of phase separation is still a subject of research. Experimental evidence of phase separation in V-Ti-Cr system is not available in literature. However, phase separation in V-Ti alloys has been predicted theoretically and has been observed experimentally also (Sluiter & Turchi, 1991; Suwarno *et al.*, 2014; Koul & Breedis, 1970a,b). Present study indicates that in absence of complete phase diagram information, Miedema's thermodynamic approach could extend a finger print about phase evolution in alloys. It has been shown for other alloy systems before. However, the same approach is applicable for V-Ti-Cr alloys.

3.4.3. Thermocalc studies of V-Ti-Cr alloys: re-validation of Miedema model

Thermocalc modeling has also been carried out to study the phase stability in the binary V-Ti, Ti-Cr, V-Cr and also in ternary V-Ti-Cr system. The calculated phase diagrams for the binary alloys are shown in figure 3.17. All the binary calculations were performed using the TCBIN database. Fig 3.18 shows the calculated liquidus projection of the V-Ti-Cr alloys. The contours represent the phase boundaries of the iso-liquidus surfaces. Figures 3.19 to 3.21 show the calculated phase diagrams for the ternary system. The calculations were performed using the SSOL 4 database with the temperature varying from RT to 1100° C. The calculated phase diagrams show that, apart from the Ti-Cr rich side, solid-solution phase is stable throughout the entire composition range. In the Ti-Cr rich side the primary phase field comprises of C15 Laves phase along with *bcc* and *hcp* solid-solution phases and beyond 900° C, C14 Laves phase also appears in the system. Moreover, the *bcc* phase field at the V-rich corner increases with the increase in temperature and beyond 1000° C it covers almost the entire composition range. Figures 3.22 to 3.24 shows the calculated isopleths of V-Ti-Cr system where the phase stability corresponding to V-4Ti-4Cr, V-39Ti-54Cr and V-40Ti-20Cr are shown. The phase stability shown for these compositions are in accord with results obtained from Miedema

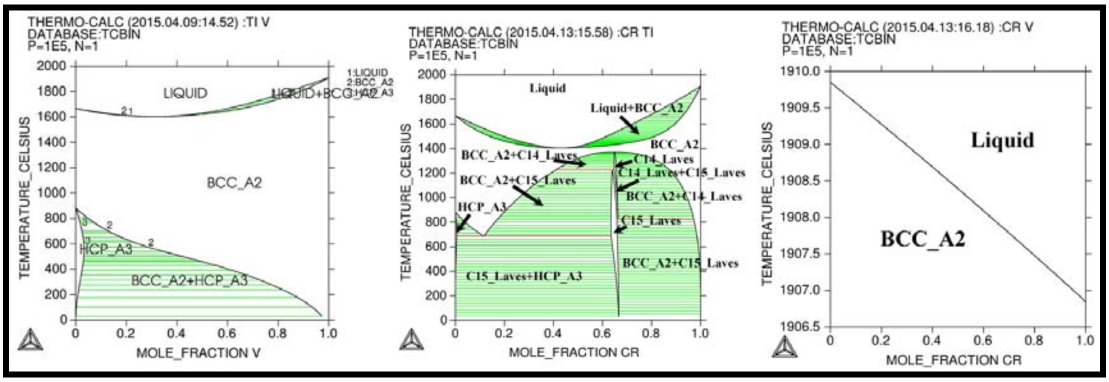

Fig. 3.17(a-c): Calculated phase diagrams for binary V-Ti, Ti-Cr and V-Cr alloy systems. These phase diagrams are calculated using Thermocalc Software.

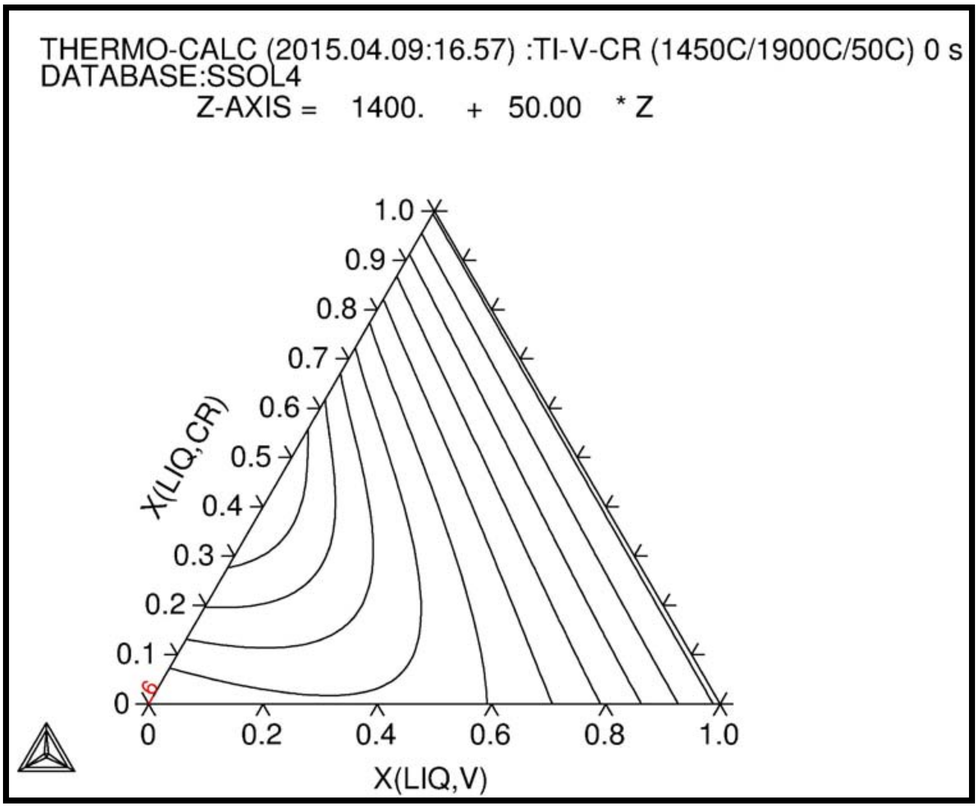

Fig. 3.18: Calculated liquidus projection of the V-Ti-Cr system. The contours represent the phase boundaries of the iso-liquidus surfaces.

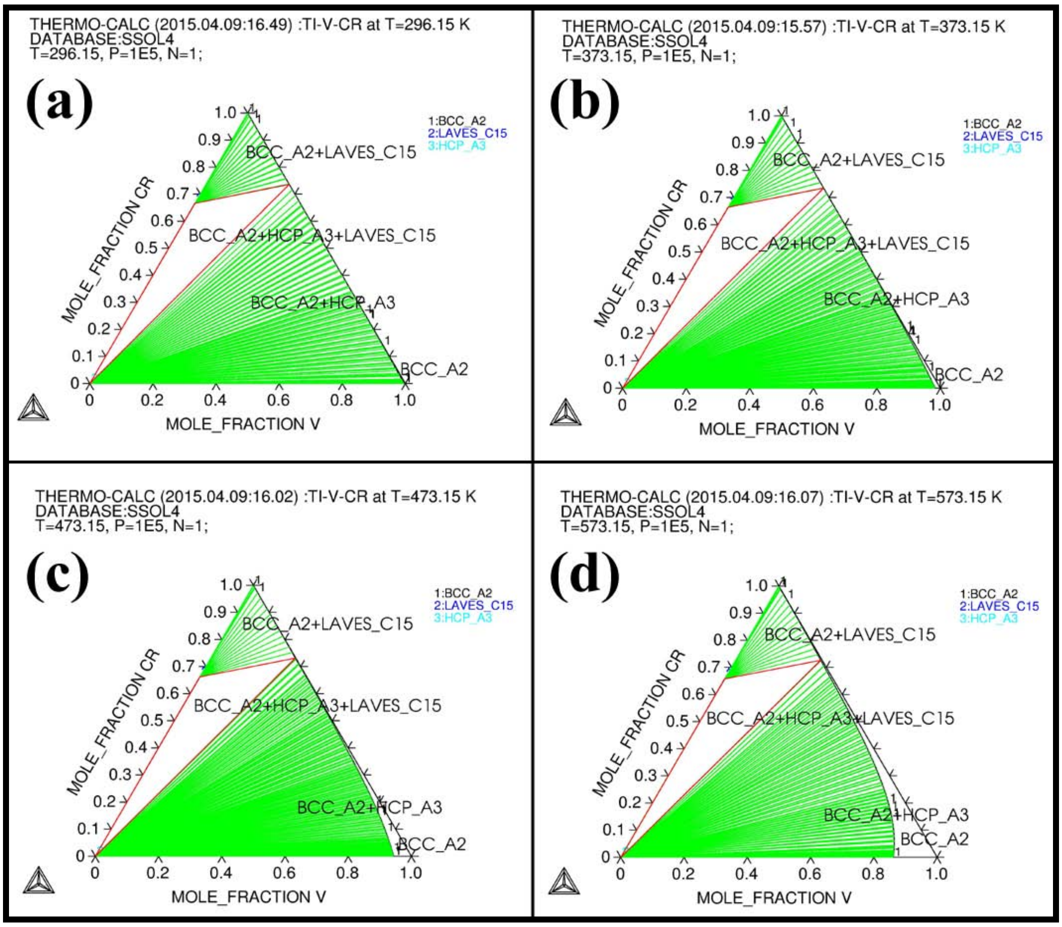

Fig. 3.19: Isothermal sections from the calculated V-Ti-Cr phase diagram at 23°C, 100°C, 200°C and 300°C. Apart from the Ti-Cr rich side, solid-solution phase is stable throughout the entire composition range. In the Ti-Cr rich side the primary phase field comprises of C15 Laves phase along with *bcc* and *hcp* solid-solution phases.

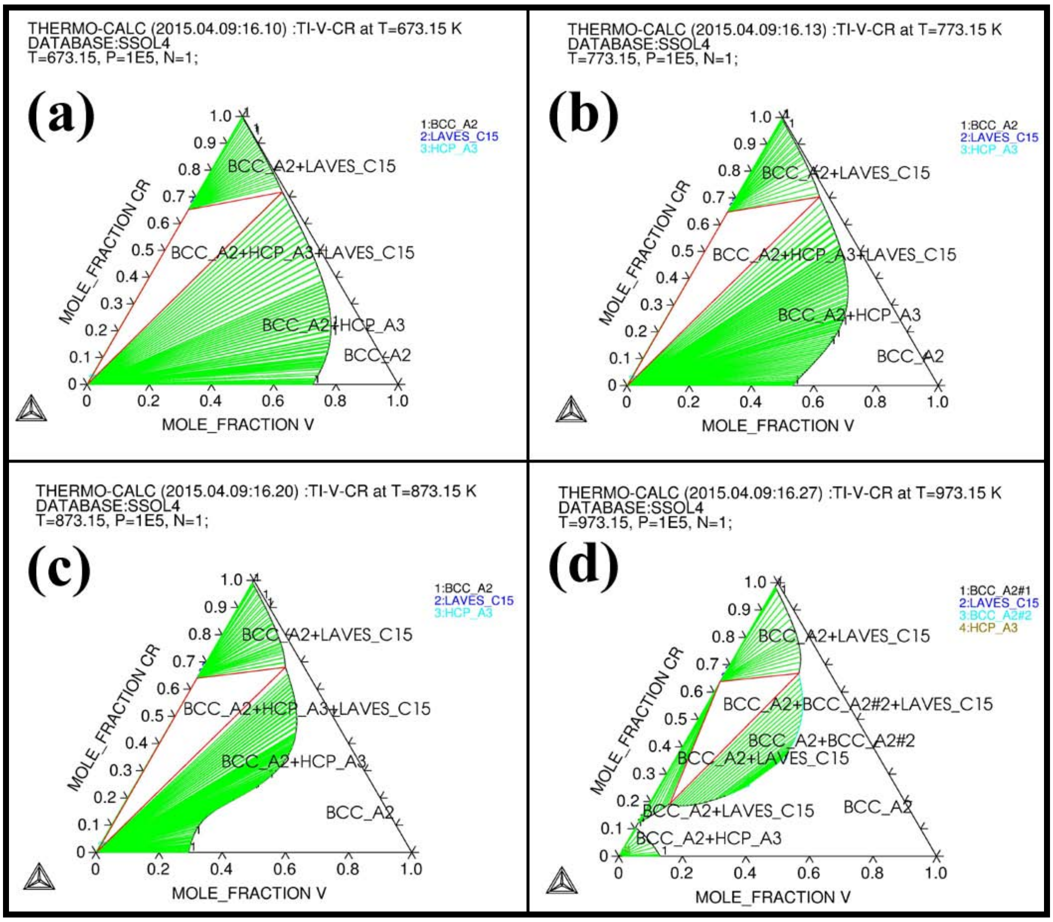

Fig. 3.20: Isothermal sections from the calculated V-Ti-Cr phase diagram at 400°C, 500°C, 600°C and 700°C. The *bcc* phase field at the V rich corner increases with the increase in temperature.

approach assuming the amorphous phase cannot form at the cooling rate of 10-100 K/s accessible in water cooled copper hearth of the arc-melting unit.

3.4.4: Pettifor structure map approach in V-Ti-Cr system:

Pettifor structure map approach comes under the data mining category of alloy design which brought new insights in predicting the structure of binary and pseudo-binary intermetallics. In a series of phenomenal works, D.G. Pettifor (1986, 1988) re-defined the Hume-Rothery approach of alloy formation and introduced a unique chemical

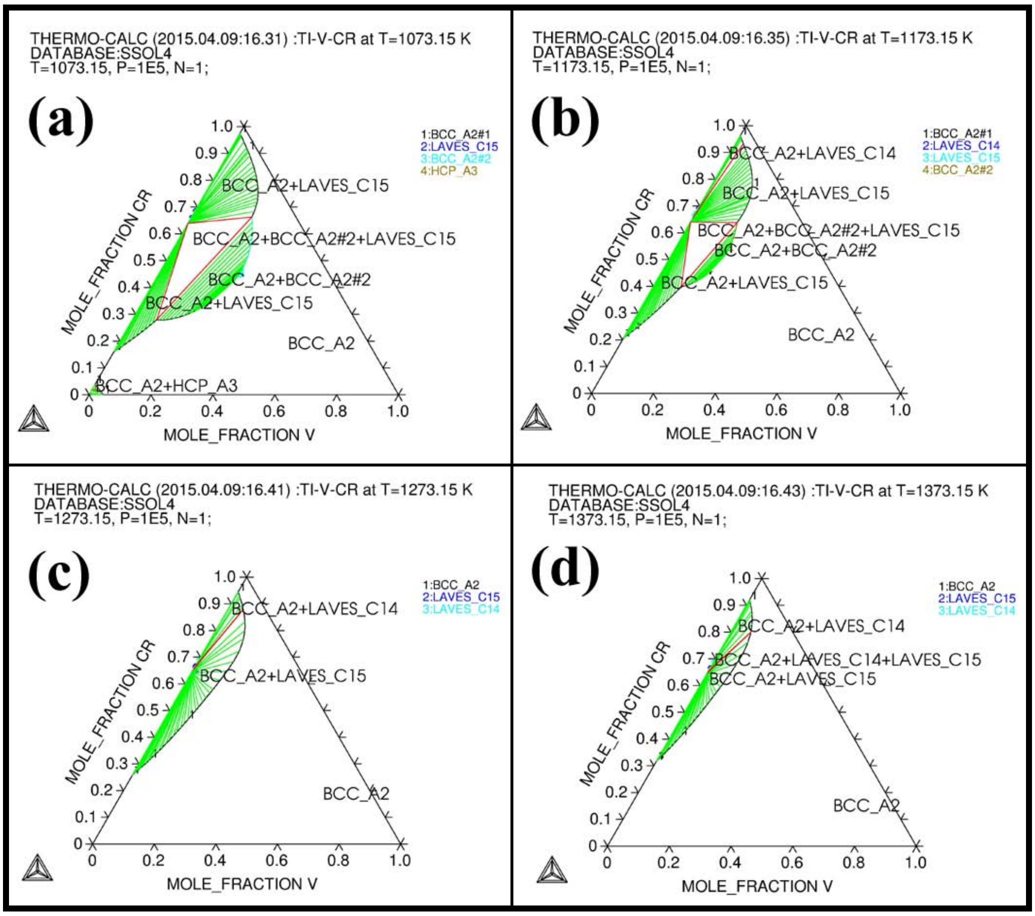

Fig. 3.21: Isothermal sections from the calculated V-Ti-Cr phase diagram at 800°C, 900°C, 1000°C and 1100°C. C14 Laves phase have also started to appear from 900°C onwards.

scale which captures a fourth factor of bond orbital instead of various independently variable factors such as size, electronegativity and valence. According to this approach, each of the elements in the periodic table have been assigned a unique phenomenological co-ordinate, called the Mendeleev number (M), determined by running a one dimensional string through the two dimensional periodic table as shown in figure 3.25. With pulling the ends of the string apart, all the elements of the periodic table order along a one-dimensional axis. The sequence of this ordering is maintained by M. Moreover, it is also

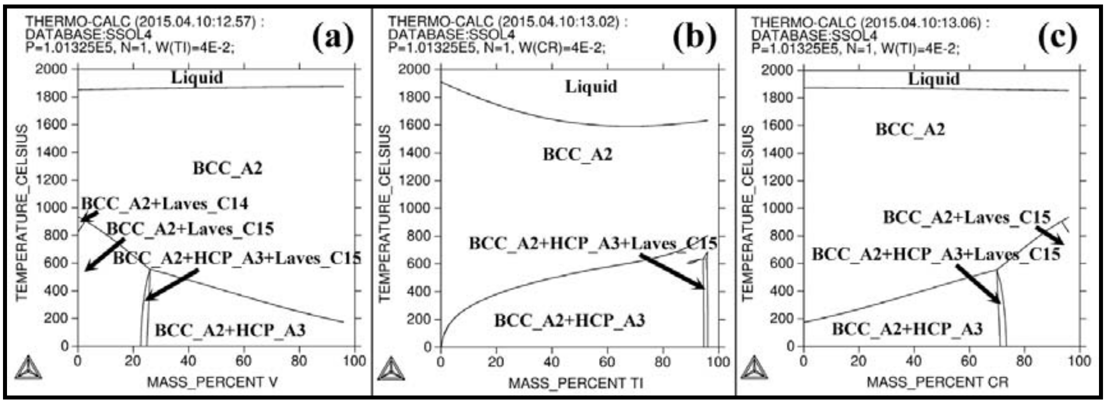

Fig. 3.22: Isopleths of the ternary V-Ti-Cr system showing the stable phases keeping the Ti concentration fixed at 4 at% in (a) & (c), and Cr concentration fixed at 4 at% in (b).

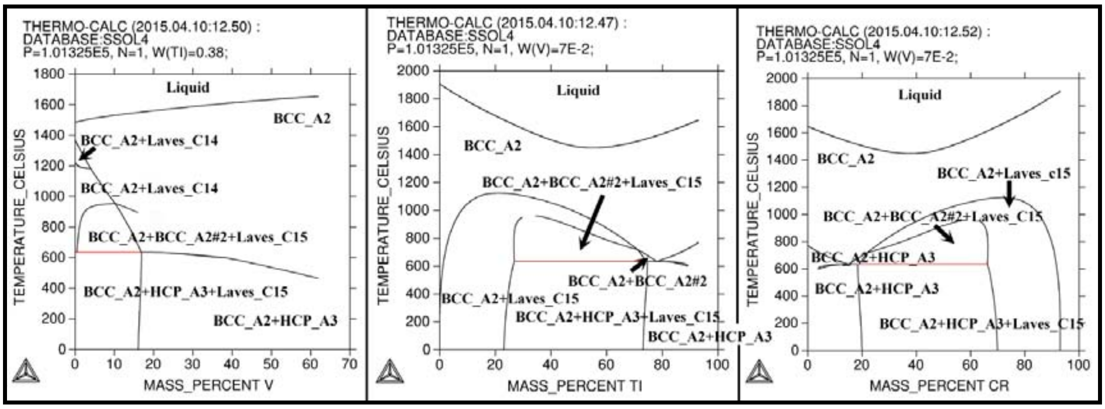

Fig. 3.23: Isopleths of the ternary V-TI-Cr system showing the stable phases keeping the (a) Ti concentration fixed at 38 at%; (b) & (c) V concentration fixed at 7 at%.

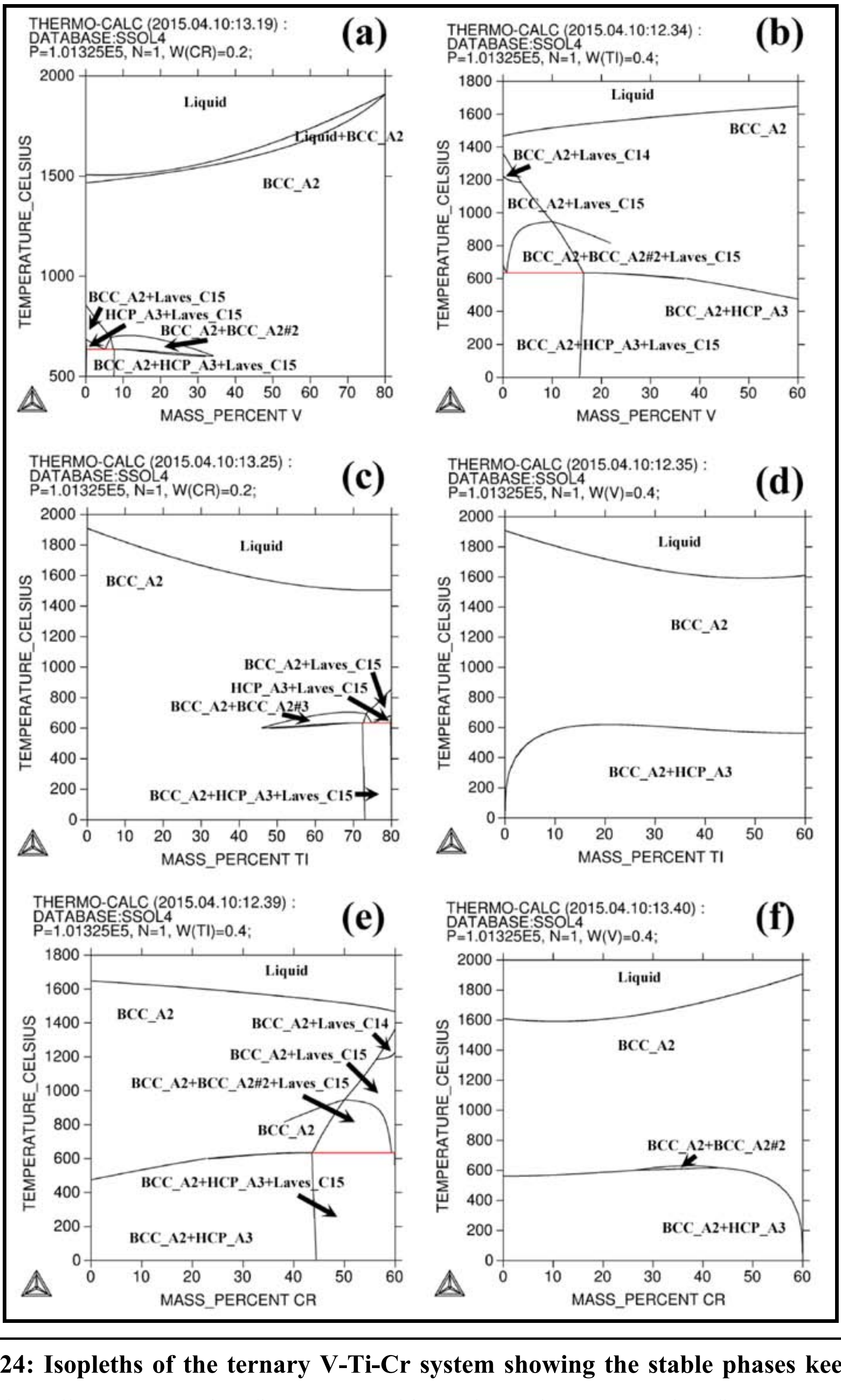

Fig. 3.24: Isopleths of the ternary V-Ti-Cr system showing the stable phases keeping the (a & c) Cr concentration fixed at 20 at%; (b & e) Ti concentration fixed at 40 at%; (d & f) V concentration fixed at 40 at%.

possible to order the structures of the binary compounds with a given stoichiometry A_mB_n within a two dimensional structure map (M_A, M_B). The sequence of the string was chosen in such a fashion that it provides the best structural separation for binary compounds with stoichiometries AB, AB_2, AB_3, AB_4, AB_5, AB_6, AB_{11}, AB_{12}, AB_{13}, A_2B_3, A_2B_5, A_2B_{17}, A_3B_4, A_3B_5, A_3B_7, A_4B_5 and A_6B_{23} respectively. Hence to ensure that the binary compounds with similar types of structures positioned in the similar region of the 2D structure map, quite a few situations arise where elements with neighbouring atomic numbers could have different Mendeleev numbers and elements with two consecutive Mendeleev numbers may be positioned far apart in periodic table. For example, the Mendeleev number string of the rare earths (M = 20-33) runs in the reverse order of their atomic numbers and Y (M = 25) is placed in the middle of the chain. Two divalent rare earths Yb (M = 17) and Eu (M = 18) was separated out from the rare earth family and placed with Ca and Sc with Mendeleev numbers 16 and 19 respectively. Be and Mg shifted from group IIA to IIB respectively (Ranganathan & Inoue, 2006). Pettifor (1988) had also showed that the binary structure map can be extended for the ternary and quaternary alloys also by considering them as pseudo-binary compounds. The quaternary alloy of $(A_xC_{1-x})_m(B_yD_{1-y})_n$ with binary structure A_mB_n can be considered a pseudo binary compound with redefined Mendeleev number as,

$$M_A^* = xM_A + (1-x)M_C \text{ and } M_B^* = yM_B + (1-y)M_D$$

With the redefined M, the pseudo-binaries are found to fall in same region of that of the pure binaries and have been verified with a number of compounds by several researchers. Present section deals with the phase and structure evolution in binary Ti-Cr, V-Ti, V-Cr and ternary V-Ti-Cr alloy systems with the aid of Pettifor structure map approach.

As it is seen in figure 3.25, the assigned Mendeleev numbers for Ti, V and Cr are 51, 54 and 57 respectively. However, for these three set of elements their assigned group remains same with that of the periodic table. Ohta and Pettifor (1992) in their classic work described the structure map for the AB_2 transition metal compounds to analyze the roles played by atomic size and electronic factors in stabilizing the transition metals Laves phase. As can be seen from the map in figure 3.26, $TiCr_2$ Laves phase stabilizes as C15 (cF24) structure with prototype of $MgCu_2$. In the similar context it would have been interesting to study the structural stability of the earlier studied V substituted $TiCr_2$ Laves phase of 7V-38Ti-55Cr alloy composition. By considering that V would substitute Ti from its regular lattice site, the ternary intermetallics compound $(Ti_{0.85}V_{0.15})Cr_2$ can be considered a pseudo binary compound with modified Mendeleev numbers as,

$M_{Ti} = (0.85 \times 51) + (0.15 \times 54) = 51.45$ and $M_{Cr} = 57$;

From the above calculations it is very much evident that V substituted $TiCr_2$ Laves phase co-exists with $TiCr_2$ phase in the same region of the structure map and structurally stabilized as C15 Laves phase. However, successful implementation of this approach for ternary and quaternary alloys demands a prior knowledge of specific site substitution behaviour of the constituent elements.

The crystal structure prediction map for the binary compounds with AB stoichiometry is shown in figure 3.27. A careful look into the map predicts the stability for cubic cI2 structure for the binaries of V-Ti and V-Cr alloys with the prototype structure of W and the region has been marked in the image itself. In this particular plot, all the intermetallic binary alloys constitute the data sets and the descriptors are the chemical scales as assigned by Pettifor for each individual element.

More recently with the advent of efficient and accurate theoretical tools and inexpensive computers a rapid surge can be seen in the area of computational materials science or high throughput (HT) computational materials design (Curtarolo *et al.*, 2013; Morgan *et al.*, 2005). It combines the computational quantum-mechanical-thermodynamic approaches along with the multitude of techniques for database construction and intelligent data mining. A successful combination of Pettifor structure map and high throughput computational materials design not only brings out more sophistication in the predictability of binary intermetallics properties but it also made it possible to perform massive analyses in binary systems. Curtarolo et al (2013) demonstrated the HT analysis of binary intermetallics where the descriptor is the ordering tendency of the binary alloy mixtures as shown in figure 3.28. All the elements in this map are ordered by Pettifor scale of Mendeleev numbers. In this map the top left triangle describes the ordering tendency of the mixtures and the bottom right triangle shows a relative comparison between calculation and experimental results. It is interesting to note that for binary V-Ti alloy, this map predicts complete immiscibility and for which both calculation and the experiment agrees. This is in support of the thermodynamic calculations for V-Ti system shown earlier. However, for Ti-Cr and V-Cr systems it predicts formation of binary mixtures.

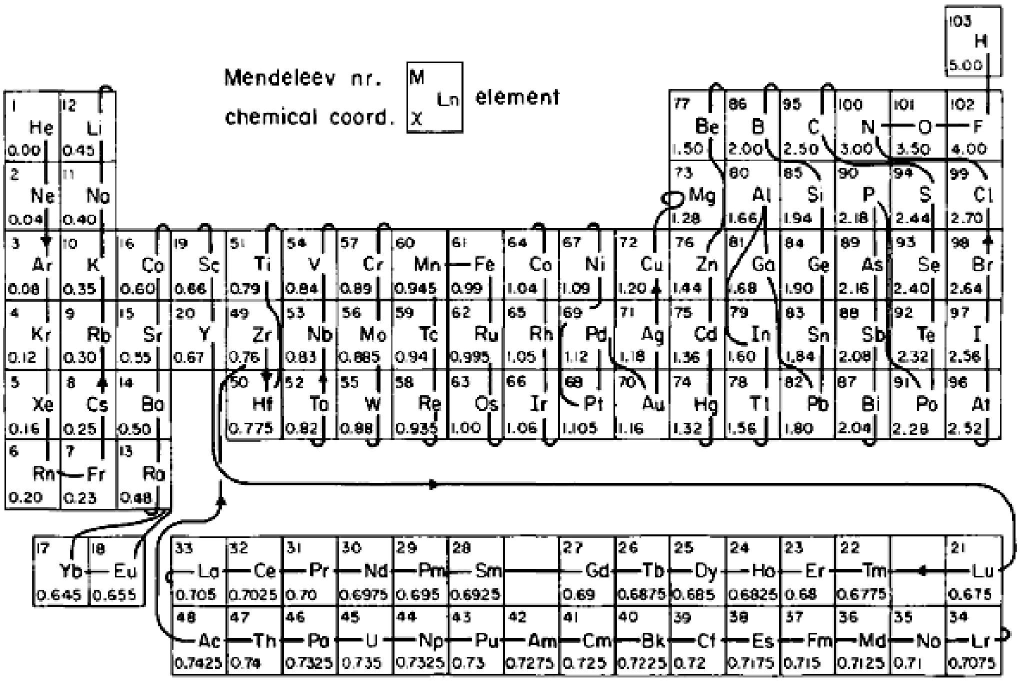

Fig. 3.25: Modified periodic table as described by Pettifor with the assignments of Mendeleev numbers to each of the elements using a one-dimensional string in a sequential manner.

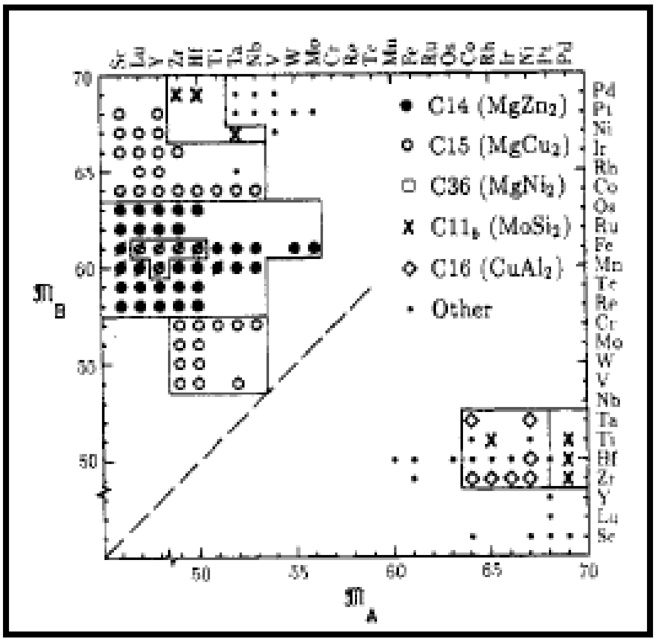

Fig. 3.26: The structure map for the AB_2 transition metal compounds.

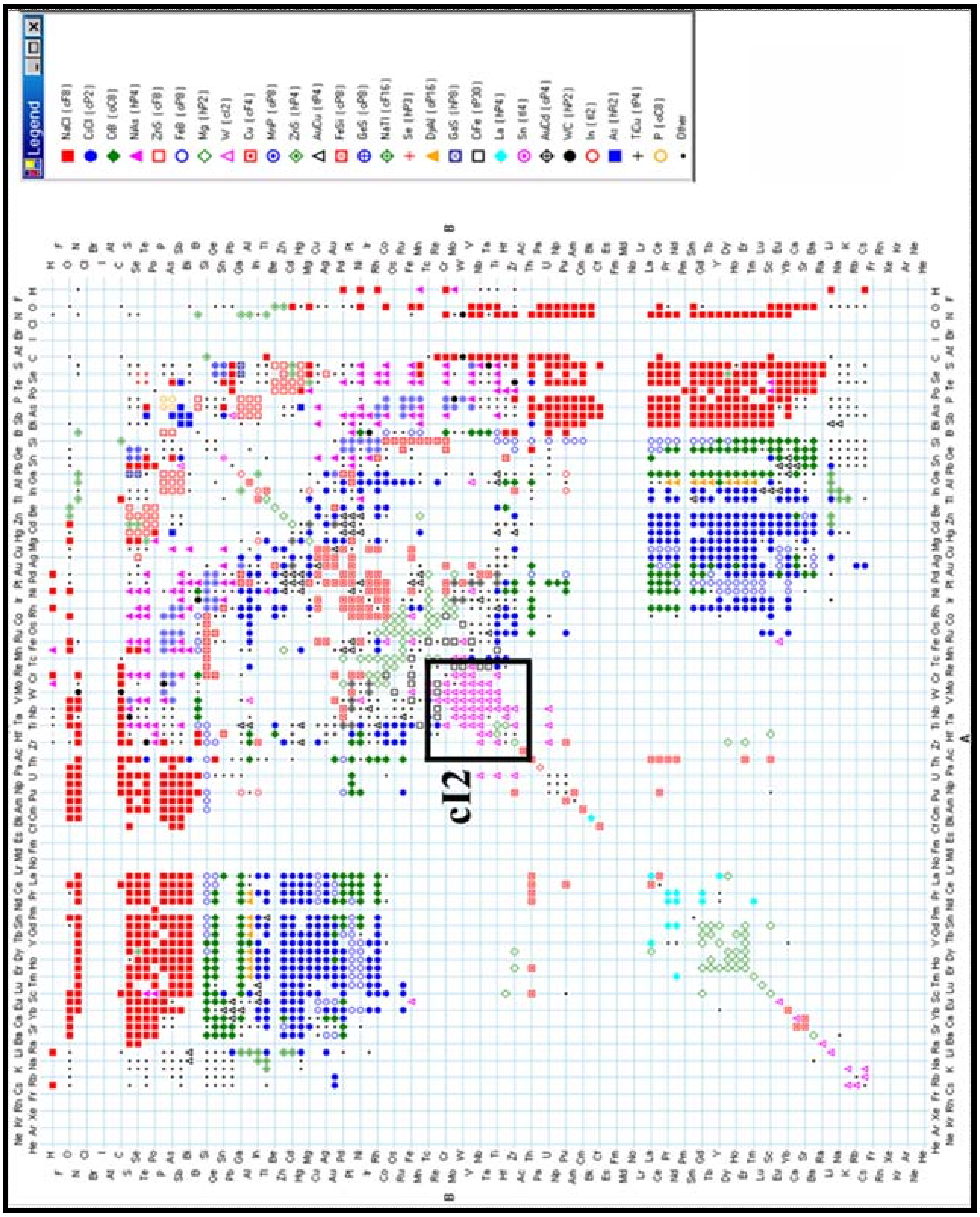

Fig. 3.27: Structure map for the binary compounds. The domain with the compounds of cI2 structure is marked in the map itself. Binary V-Ti and V-Cr alloys fall in this domain.

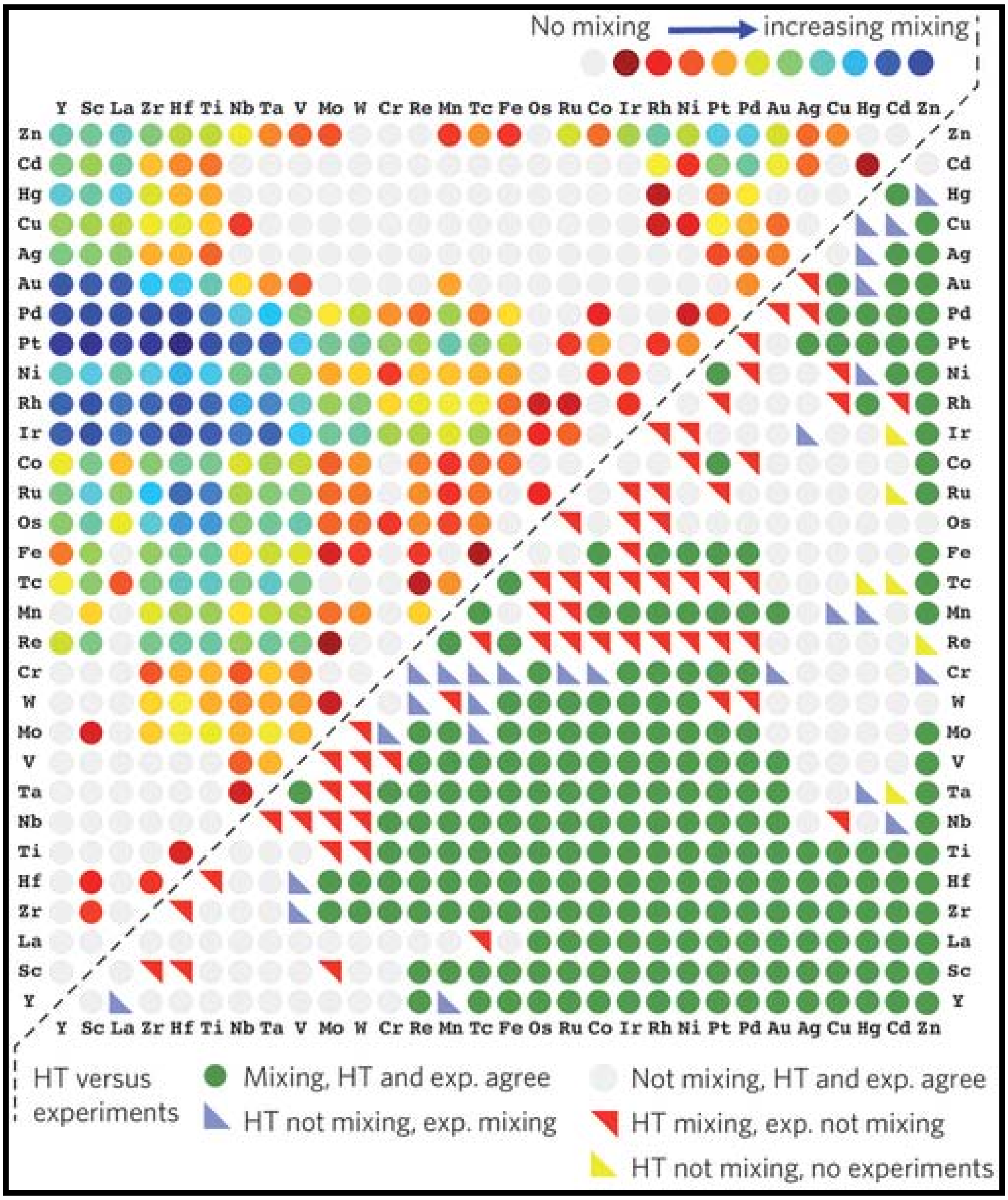

Fig. 3.28: High throughput analysis of the binary intermetallics (Curtarolo et al., 2013). Top left triangle shows the ordering tendency of the alloy mixtures and the bottom right triangle indicates the agreement between the high throughput calculation and experimental results. For V-Ti system, it predicts the non mixing of the alloying elements for which HT and experiments agrees.

3.5: Conclusions

According to Midedema's approach V-Ti-Cr alloys in the V-rich side of the phase diagram should form a solid-solution phase, compositions close to the binary $TiCr_2$ Laves phase composition should form amorphous phase or intermetallic phase. Binary V-Ti and ternary V-Ti-Cr alloys with 0.2 mole fraction Cr should form solid-solution phase, with phase separation tendncy. Arc melted alloys and their microstructural characterization establishes the validity of Miedema approach in assessing the phase evolution in V-Ti-Cr alloys. Miedema model predicts the stability of a solid-solution phase for the V-rich corner of the phase diagram. *bcc* solid-solution phase has been experimentally observed in V-4Ti-4Cr alloy. In accordance with Miedema calculation for the phase stability in V-39Ti-54Cr alloy composition, a V-substituted cubic $TiCr_2$ Laves phase has been observed to form in the alloy. According to Miedema calculation, solid-solution phase is more stable than the amorphous phase over the entire composition range in binary V-Ti and ternary V-Ti-20Cr alloy systems. Moreover, solid-solution phase with almost equimolar composition of V and Ti should show phase separation. Phase separation has been experimentally observed in both the alloys. It has been proved by STEM-EELS that a composition modulation occurs in terms of V and Ti in the phase separated domains. Cr essentially does not take part in the phase separation process in V-Ti-Cr alloy. Even though the alloy is ternary, the phase separation event is binary. The interfaces between the chemically modulated lamella are perfectly coherent. However, the present chapter also poses certain fundamental questions which require critical attention.

(i) Thermodynamic calculations as well as electron microscopy studies confirm that V-39Ti-54Cr alloy stabilizes in a Laves phase structure, where V dissolves in the Laves phase matrix and be termed as V-doped $TiCr_2$ Laves phase. However, it remains questionable whether V atoms occupy any independent positions in the matrix and stabilizes as a ternary Laves phase or it substitutes either Cr or Ti or both atoms from their regular lattice sites. In the later case it will essentially be stabilizes as a pseudo-binary Laves phase.

(ii) It is well established from the present work that binary V-50Ti alloy and ternary V-Ti-Cr alloy with 20 at% of Cr show a phase separation tendency over solidification. However, the phase separation event in the as solidified alloy is not complete due to kinetic constraints and requires systematic heat treatment to complete the transformation. The mechanism of the phase separation event i.e. whether the transformation is governed by the Spinodal decomposition or dominated by the nucleation and growth kinetics is another interesting aspect and requires detailed investigations.

(iii) Phase contrast and Z contrast microscopy coupled with spectroscopic investigations confirm the chemical partitioning in the binary V-50Ti and ternary V-40Ti-20Cr alloy which manifests as a periodic Ti lean and Ti rich domains. Moreover, significant probability exists that this composition modulation can act as a driving force and initiate further phase transformation reactions in the phase separated domains of the alloy. Systematic diffraction contrast and phase contrast microscopy studies with the aid of multislice image simulation along different zone axis of the specimen can only detect the phase transformational reactions in the nm scale.

Sincere efforts have been made in the following chapters to answer these questions.

Chapter IV

Structure Imaging and Vanadium Substitution in Cubic $TiCr_2$ Laves Phase

Chapter IV

Structure Imaging and Vanadium Substitution in Cubic $TiCr_2$ Laves Phase

4.1: Introduction

In previous chapter it has been already discussed that for ternary V-Ti-Cr system enthalpy of formation of the amorphous phase is more negative than the solid solution phase in the vicinity of $TiCr_2$. As at the lower temperature enthalpy dominates over entropy so far free energy is concerned, it can be concluded in that composition range other intermetallic phases may form, as the amorphous phase is metastable in nature. An alloy with nominal composition from that particular domain was chosen at Ti-55Cr-7V. It was confirmed experimentally that this particular alloy composition solidifies as Laves phase. However, questions on the nature of the Laves phase remained to be answered: (i) being a highly stoichiometric compound, can $TiCr_2$ Laves phase accommodate 7 at% of V, and (ii) is this a ternary Laves phase or a pseudo-binary Laves phase where V atoms substitute at either Ti-sites or Cr-sites. The present chapter addresses the phase stability of Ti-55Cr-7V Laves phase composition and preferential site substitution behavior of V.

From the perspective of the electron microscopy techniques, present chapter also discusses about the single column chemistry determination through high resolution electron microscopy. It is worth mentioning that development of microscopy techniques and instrumentation has kept pace with the needs of materials characterization in order to understand the atomistic origin of properties (Smith, 2012). It is possible to image complex structures at atomic scale and determine its chemistry by application of suitable spectroscopic techniques. Over last two decades scanning transmission electron microscopy (STEM) coupled with electron energy-loss spectroscopy (EELS) or X-ray energy dispersive spectroscopy (XEDS) has been developed and successfully implemented to image complex structures at atomic scale with simultaneous determination of chemistry (Browning and Pennycook, 1996; Browning *et al.*, 1998; Pennycook *et al.*, 1999). Alternatively, high resolution phase contrast imaging coupled with energy filtering and image simulation can also be a viable technique to characterize complex structures and its chemistry at atomic scale. Even though, understanding the image contrast and interpretation of data are difficult in case of phase contrast imaging, there are certain advantages depending on the structure under consideration. Application of phase contrast imaging to characterize complex structures at atomic scale is limited. In the present chapter, V-substituted $TiCr_2$ cubic laves phase has been characterized by energy-filtered phase contrast imaging coupled with image simulation to understand the order of the alloy (binary or ternary) as well as the site-specificity of the V atom in the lattice. Further, a novel approach has been proposed to characterize such complex structures at atomic scale where difference in atomic number among the constituent elements is very small.

4.2: Structure imaging of V- substituted $TiCr_2$ Laves phase

4.2.1: Zero-loss phase contrast microscopy studies of the alloy

V-substituted cubic $TiCr_2$ Laves phase has been synthesized by arc melting a V-Ti-Cr alloy with nominal composition Ti-55Cr-7V (composition is expressed in at %) in high-purity argon atmosphere on a water cooled copper hearth, starting from elemental V, Ti and Cr (>99.9% purity). Details of the alloy melting and TEM specimen preparation methods have been already described in chapter 2.

TEM bright-field image of the as-melted alloy along with the diffraction pattern and the EELS spectrum are shown in figure 4.1(a-c). The bright-field micrograph shows a typical Laves phase grain embedded in the matrix. There is a high density of defects in the Laves phase as can be confirmed from the linear contrast in the grain body. The Laves phase grain is irregular in shape. The diffraction pattern from a defect-free region of the same grain along B= [111] zone axis is shown in figure 4.1(b). The lattice parameter as calculated from the diffraction pattern is a=0.69 nm which is very close to the reported lattice parameter for pure $TiCr_2$ cubic Laves phase (ICDD # 050-1106). In the EELS spectrum, figure 4.1(c), characteristic core-loss edges for V, Ti and Cr can be observed. The characteristics L-edges of V, Ti, Cr appear at 512 eV, 454 eV and 574 eV respectively. The core-loss near edge spectra of the V-L edge indicates that it is present in the $TiCr_2$ lattice as a minor alloying element. Quantification of the EELS spectrum indicates the composition of the phase as Ti-54Cr-7V (Composition in at%), which is very close to the as melted composition. A defect-free area on the grain body was selected for the zero-loss high resolution imaging in energy filtered TEM mode. The same grain was oriented along B=$[01\bar{1}]$ direction for phase contrast imaging. This particular zone axis was chosen since individual Ti and Cr atom columns are observable in this direction. The zero-loss phase contrast image from a defect free area of the Laves phase grain is shown in figure 4.2. In case of zero-loss energy-filtered TEM imaging (FWHM of Zero-loss peak = 0.65 eV at 300 kV) only the elastically scattered electrons

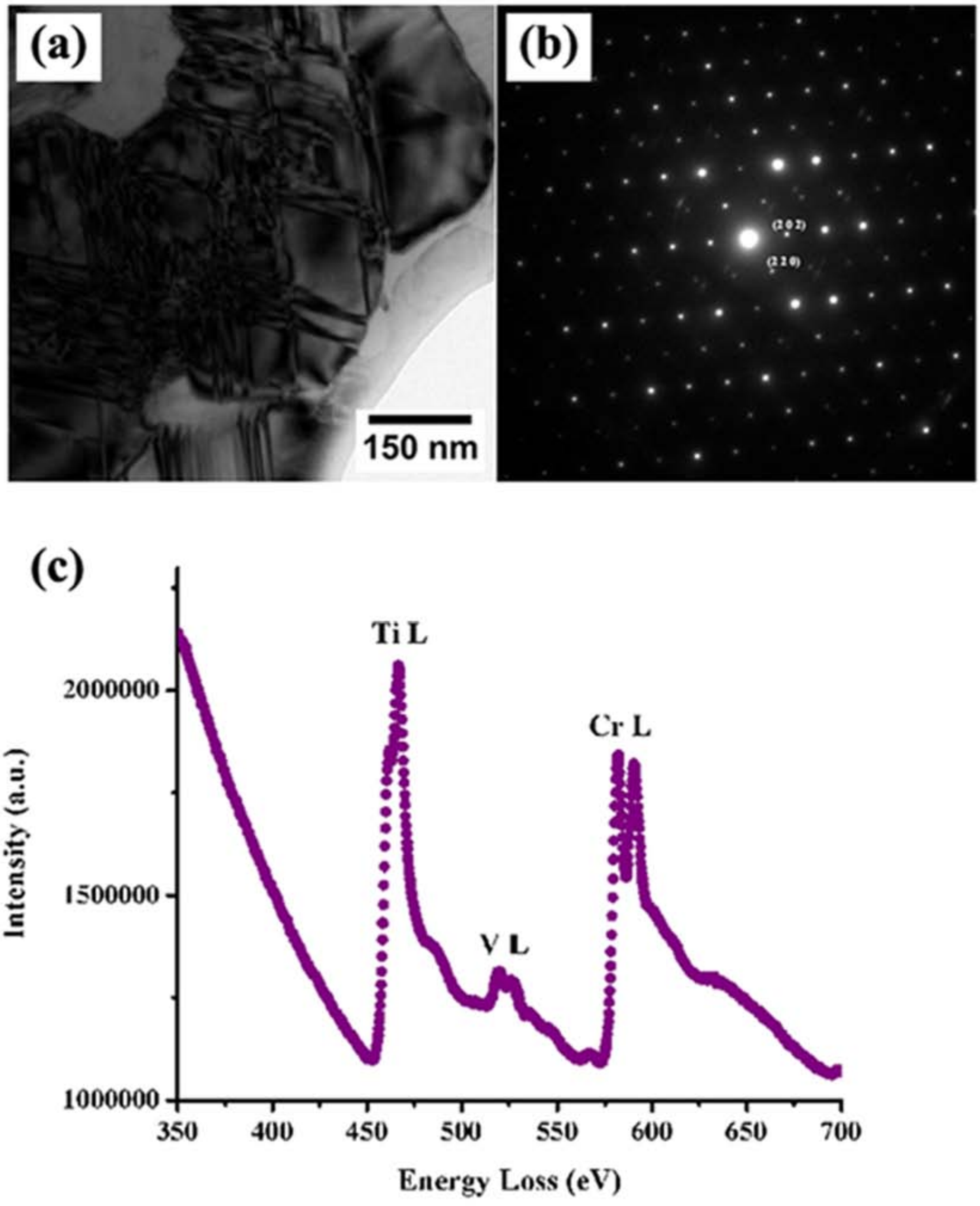

Fig. 4.1: (a) TEM bright-field image (b) diffraction pattern along B=[111] from a relatively defect free region (c) EELS spectra from the Laves phase region of the specimen.

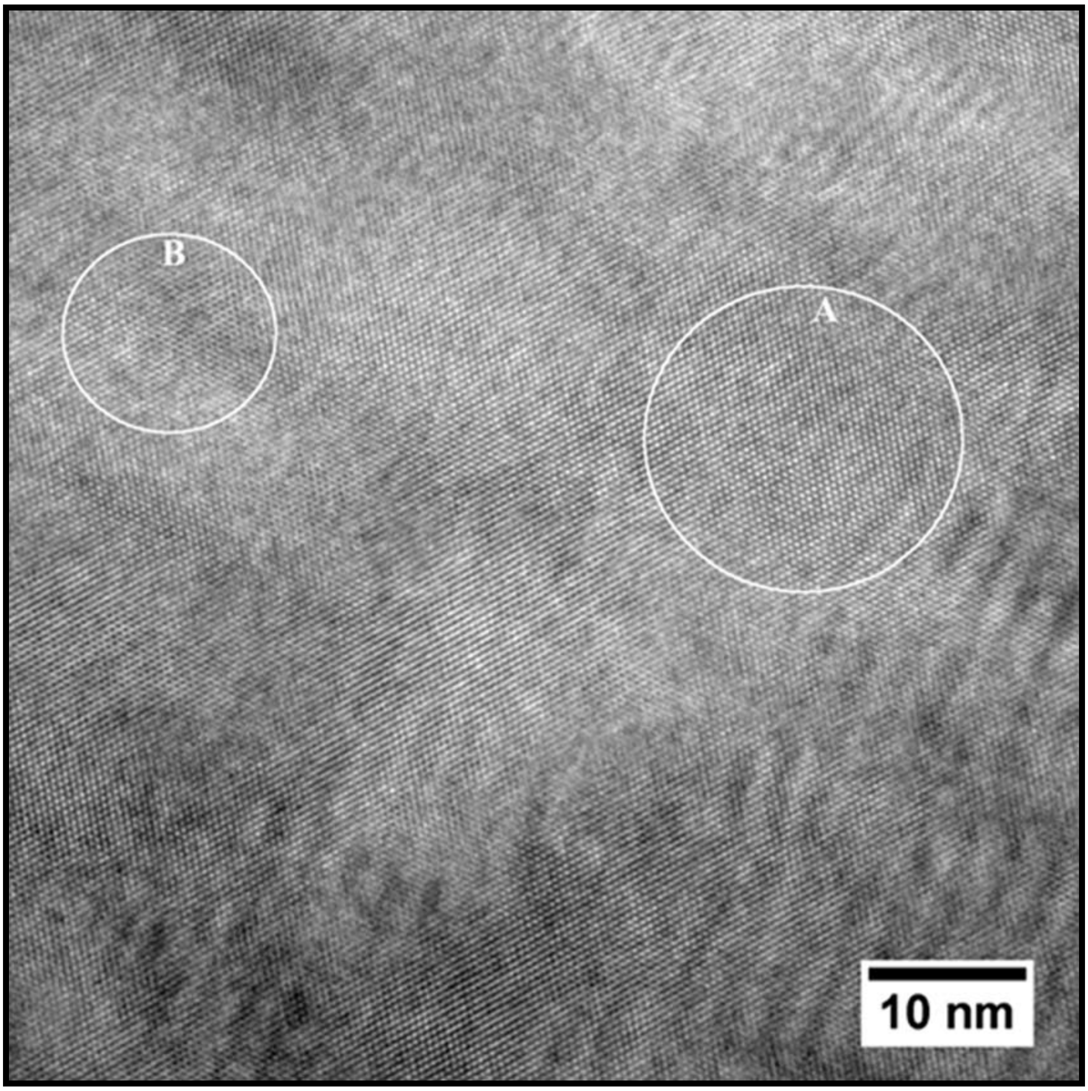

Fig. 4.2: Zero-loss (ΔE=0.65 eV) phase contrast image of cubic V-doped $TiCr_2$ Laves phase along B= $[01\bar{1}]$ direction. Regions marked as 'A' and 'B' has been analyzed further in order to understand the contrast and the location of V atoms.

contribute to the image formation. Hence the contrast of the image improves due to the absence of inelastically scattered electrons. In the recorded image the fringe pattern is quite regularly observed. However, the Moiré contrast at the bottom right corner of the image comes due to the presence of the solid solution phase underneath the Laves phase in that region. The regions marked 'A' and 'B' in the image, which are free from Moiré contrast were chosen for quantification of lattice planes and understanding the contrast.

Higher magnification image of the region 'A' as shown in figure 4.2 along with the projected structure of cubic $TiCr_2$ Laves phase along $[01\bar{1}]$ direction are given in figure 4.3(a-b) respectively. In the image regularly spaced bright atom column like contrast is observed. The {111}, {200}, {220} and {311} planar spacings as measured from the experimental image turn out to be 0.445 nm, 0.365 nm, 0.262 nm and 0.225 nm respectively. The experimentally measured planar spacings match quite closely with the reported values for pure $TiCr_2$ cubic Laves phase (ICDD # 050-1106). The reported values are marked on the projected image. The deviation of the planar spacings from the reported values could be explained in the light of V addition in the lattice. However, when the traces of planes are superimposed on the projected structure, it is observed that quite a few atom columns are systematically missing. It is seen from the projected structure image and from the traces of the planes that only a fraction of the Cr atom columns are being imaged. Quite a few Cr atom columns and all the Ti atom columns are missing from the image. As the phase contrast image is not directly interpretable and bright contrast does not necessarily mean the presence of atom columns, it can only be used for intuitive understanding.

Higher magnification image of the region 'B' as marked in figure 4.2 along with the corresponding projected $TiCr_2$ cubic Laves phase structure are given in figure 4.4(a-b) respectively. Even though all the experimental images as given in figures 4.3(a) and 4.4(a) are captured under same experimental conditions, the qualitative appearance of the

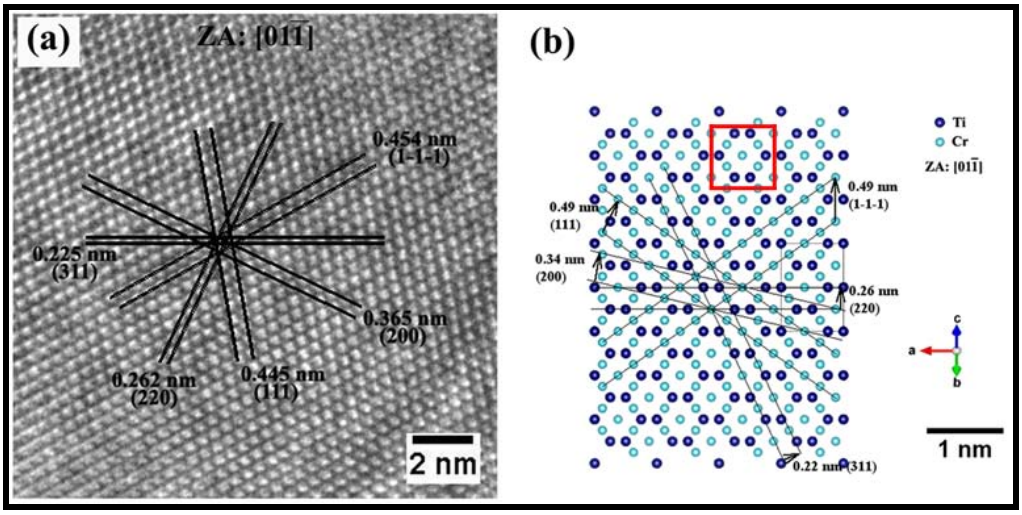

Fig. 4.3: (a) Higher magnification zero-loss phase contrast image of V-doped $TiCr_2$ Laves phase along B= $[01\bar{1}]$ direction as marked 'A' in figure 4.2. (b) Projected structure of cubic V-doped $TiCr_2$ Laves phase along $[01\bar{1}]$. The entire structure can be described by the periodic repetition of the unit shown in red. Lattice planes along with the measured d-spacings are overlaid on the experimental image. Traces of same lattice planes are shown on the projection in (b).

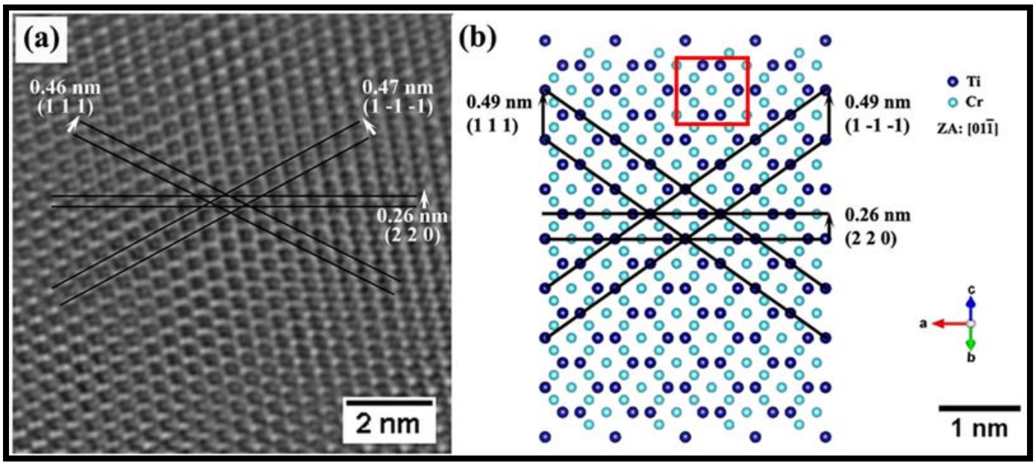

Fig. 4.4: (a) Higher magnification zero-loss phase contrast image of V-doped $TiCr_2$ Laves phase along B= $[01\bar{1}]$ direction as marked 'B' in figure 4.2. (b) Projected structure of cubic V-doped $TiCr_2$ Laves phase along $[01\bar{1}]$. Lattice planes along with the measured d-spacings are overlaid on the experimental image. Traces of same lattice planes are shown on the projection in (b).

image in figure 4.4(a) is quite different. The trace of {111} and {220} planes are shown on the image and they are measured as 0.47 nm and 0.26 nm respectively. The deviation from the reported values which are given in figure 4.4(b) can be attributed to alloying with V. However, when the same planes are traced on the projected structure, it is seen that almost all the Ti columns are being imaged and none of the Cr columns are being imaged. Such intuitive understanding cannot be used as a confirmatory proof for phase contrast images and more so for a complicated structure like cF24 cubic Laves phase.

4.2.2: Effect of channelling behavior: Site specific atomic contrast generation

In order to understand the contrast and match the phase contrast image with the structure of cubic $TiCr_2$ Laves phase, multislice simulation was carried out for the same structure under similar experimental conditions. C15 cubic $TiCr_2$ Laves phase has a lattice parameter a=0.6932 nm. Its space group is $Fd\overline{3}m$. C15 phase has eight 'a' type positions and sixteen'd' type positions. The atomic positions are (000) and (0.625, 0.625, 0.625) respectively. In order to simulate the results, pure $TiCr_2$ lattice has been generated within the JEMS software (Stadelmann, 1987) by symmetry operation of the point groups using the crystallographic information available in Pearson's handbook (Villars, 1997). The high resolution images have been simulated under varying thickness and defocus condition by multislice method. The thickness-defocus map for the cubic $TiCr_2$ Laves phase along $[01\overline{1}]$ direction is given in figure 4.5. The experimental images were captured close to Scherzer defocus which is ~-36 nm under 300 kV acceleration voltage and C_s=0.65 mm. It is observed that there is a considerable change in contrast with the change in defocus and thickness. Close to Scherzer defocus and at ~15 nm thickness, bright atom contrast from some Cr atom columns is observed and the jagged linear contrast from in between the columns comes from the Ti columns and some Cr columns. Under this imaging condition, it is not possible to identify the Ti column position uniquely. With the increase in thickness the bright contrast from the Cr columns become stronger and all the Ti columns and some Cr columns do not give rise to any contrast. At ~30-40 nm thickness both Ti and Cr columns are imaged. At ~40-50 nm thickness bright contrast from only the Cr atom columns is observed. At ~50 nm thickness and above, bright contrast is generated from the Ti column doublets and almost none of the Cr columns are imaged. There is a very small window of defocus and thickness (Δf~ -30 to -35 nm, t~ 30-40 nm) where both the columns are imaged.

Higher magnification image from the region 'A' as shown in figure 4.2 along with the FFT from the same region, the simulated image and the projected structure are given in figure 4.6(a-d) respectively. The image simulated close to Scherzer defocus at ~ 25 nm, at ~ 45 nm thickness matches with experimental image. It is obvious from the projected structure that only some of the Cr atom columns are imaged under such experimental condition and all the Ti columns are missing. The FFT from the experimental image shows that the region is oriented along B=$[01\bar{1}]$. Similarly, high magnification experimental image from region 'B' as shown in figure 4.2 along with the FFT from the same region, the simulated image and the projected structure are given in figure 4.7(a-d) respectively. It is obvious from figure 4.7 that the experimental image matches with simulated image close to Scherzer defocus and above 50 nm thickness. Under this imaging condition only the Ti doublets are being imaged as seen in the projected structure. The FFT from the experimental image confirms $B=[01\bar{1}]$ orientation in this region also. High resolution phase contrast images are quite sensitive to tilt. Misorientation could lead to change in contrast (Malm and O'Keefe, 1997). FFT from both the regions indicate that they are oriented along $B=[01\bar{1}]$ direction. The change in contrast is not due to misorientation or local bending of the sample. It is clear that $TiCr_2$ cubic Laves phase all the atom columns can be imaged over a very narrow window of thickness and defocus which might not be always possible to achieve experimentally. However, Ti and Cr atom columns can be imaged separately by varying the thickness and defocus. In order to experimentally validate the simulated contrast and rule out the possibility of local bending, zero-loss high resolution images have been recorded from different regions of Laves phase. The experimental zero-loss high resolution phase contrast image in Figure 4.8(a) has been recorded from some defect free region of the Laves phase grain oriented along $B=[01\bar{1}]$ direction close to Scherzer defocus. The FFT from the same region confirms that the region is oriented along $B= [01\bar{1}]$ direction. Under this imaging condition only Cr atom columns are imaged. The experimental image in the Figure 4.9(a) has been recorded from a different region of the grain close to Scherzer defocus. The image contrast is quite different due to the change in thickness. Comparison with the simulated image indicates that the local thickness in this region is ~ 30-40 nm. Under this condition both Ti and Cr atom columns are imaged. However, the FFT indicates that the region is oriented along $B= [01\bar{1}]$. This further confirms that the sample is not locally bent nor the change in contrast is due to

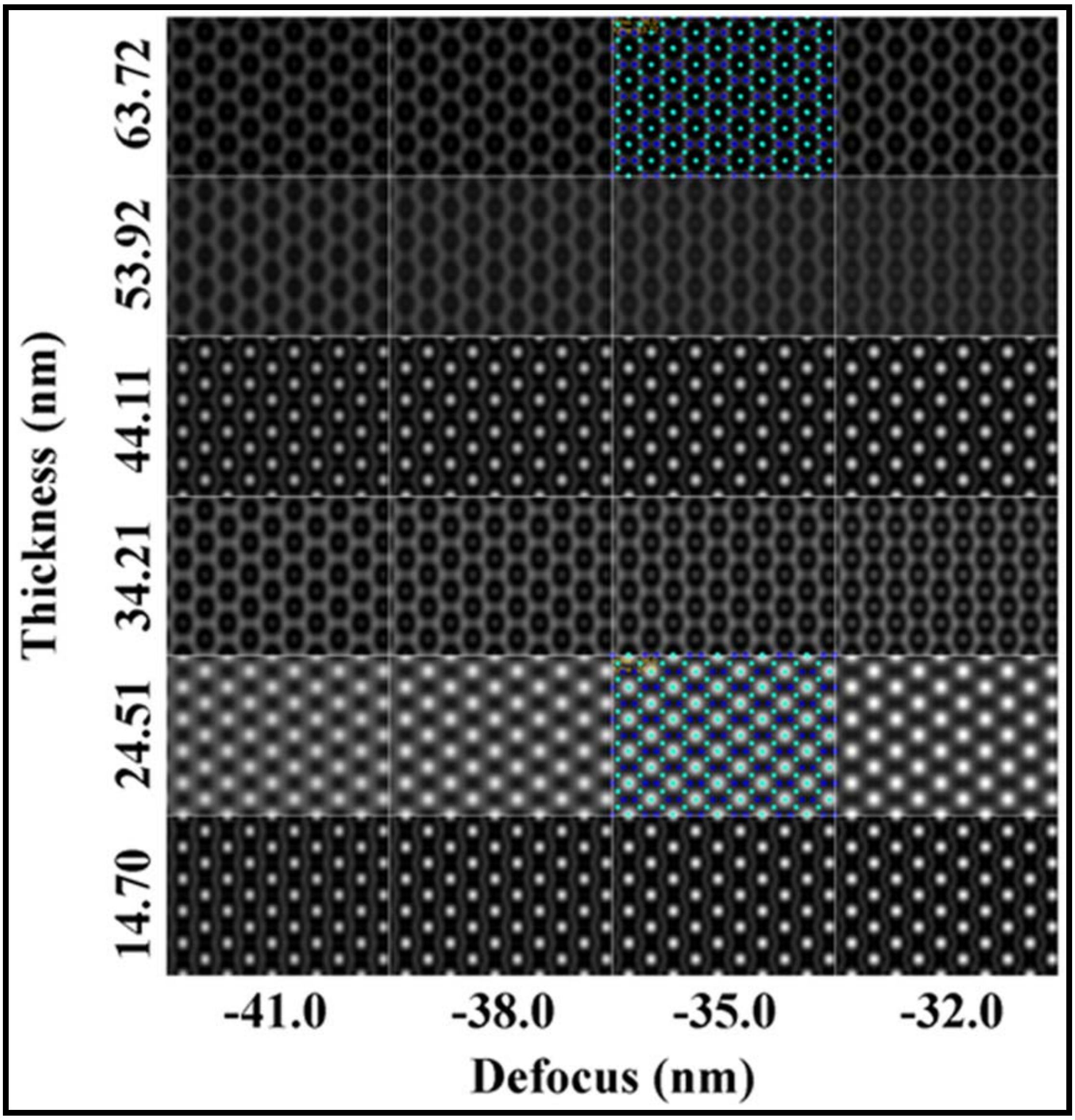

Fig. 4.5: Simulated defocus-thickness map of cubic $TiCr_2$ Laves phase along B= $[01\bar{1}]$ by multislice method. Cubic $TiCr_2$ structure is also projected on the simulated image at lower and higher thicknesses. Accelerating voltage = 300 kV, C_s = 0.65 mm and ΔE=0.65 eV.

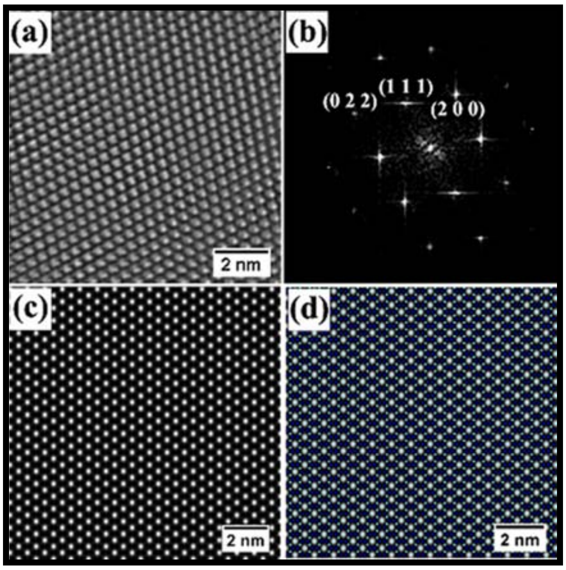

Fig. 4.6: (a) Zero-loss phase contrast image along B = $[01\bar{1}]$ from the region 'A' as marked in Fig 4.2. (b) FFT from the same region (c) Simulated image of cubic $TiCr_2$ Laves phase (d) Overlay of the projected structure on the simulated image. Under this experimental condition, only the Cr-atom columns are imaged.

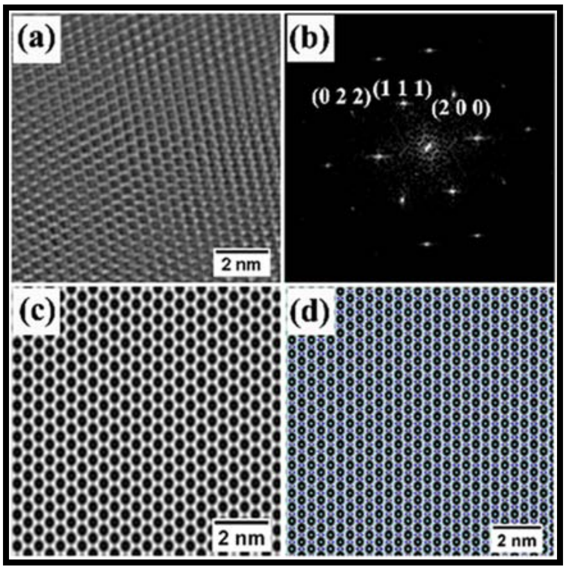

Fig. 4.7: (a) Zero-loss phase contrast image along B = $[01\bar{1}]$ from the region 'B' as marked in Fig 4.2. (b) FFT from the same region (c) Simulated image of cubic $TiCr_2$ Laves phase (d) Projected atomic structure on the simulated image for Ti-atom columns.

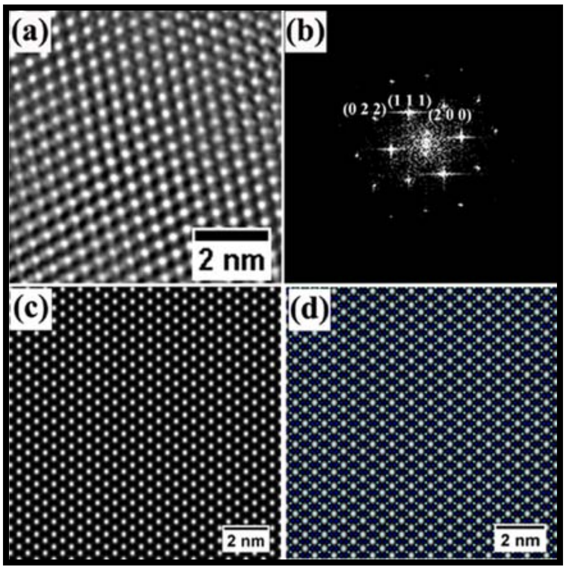

Fig. 4.8: (a) Zero-loss high resolution image from V substituted $TiCr_2$ Laves phase along B = $[01\bar{1}]$. (b) FFT from the same region (c) Simulated image along the same direction (d) Projected atomic structure on the simulated image for Cr-atom columns.

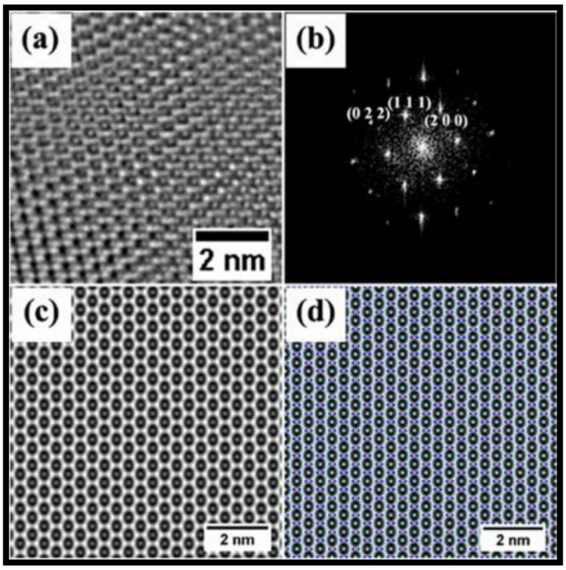

Fig. 4.9: (a) Zero-loss high resolution image from V substituted $TiCr_2$ Laves phase along B = $[01\bar{1}]$. (b) FFT from the same region (c) Simulated image along the same direction (d) Projected atomic structure on the simulated image for Ti-atom columns.

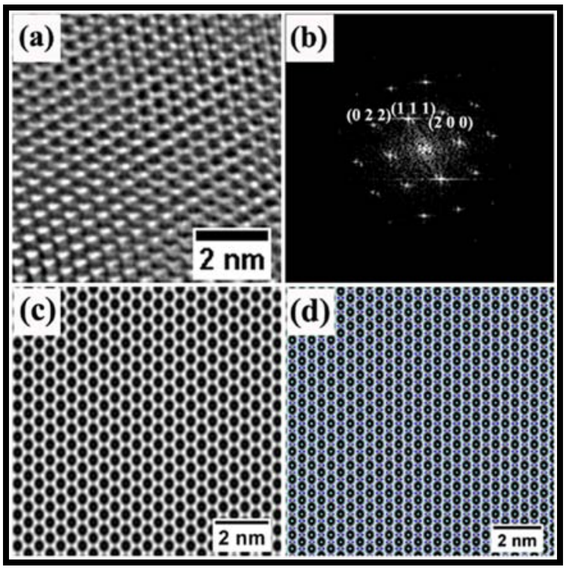

Fig. 4.10: (a) Zero-loss high resolution image from V substituted $TiCr_2$ Laves phase along B = $[01\bar{1}]$. (b) FFT from the same region (c) Simulated image along the same direction (d) Projected atomic structure on the simulated image for Ti-atom columns.

misorientation. The experimental image in Figure 4.10a has been recorded from a different region of the same grain. The image has been recorded close to Scherzer defocus. In this image only the Ti doublets are observed. The FFT indicates that the region is oriented along B=$[01\bar{1}]$. The change in contrast and the appearance of the Ti doublets is due to the local change in thickness. In this case the local thickness is ~ 50 nm or above which is in accordance with the thickness determined by intensity log ratio method in EELS.

4.3: Determination of V atom location: Electron intensity profile calculation of the atomic column contrast

It has been mentioned earlier and substantiated by electron energy loss spectroscopy that V is present in this phase as an alloying addition. Till now, by experimental zero-loss phase contrast imaging and simulation, the Ti and the Cr atom columns have been identified and matched with the pure $TiCr_2$ cubic Laves phase structure. In order to find out the location of V atoms, intensity profiles in the experimental and in the simulated images were compared in detail. The experimentally observed and simulated intensity profiles from the Cr atom columns along with the respective images are given in figure 4.11(a-d). The intensity profiles from the Cr atom columns as given in figure 4.11(d) indicates that ideally the intensities should sharply peak at the column position. These peak positions could be treated as the position of the atom columns and the separation between two subsequent peaks should reflect the separation between two Cr atom columns. The separation between two consecutive Cr-atom columns is ~ 0.49 nm. The nature of the intensity distribution should match with the experiment. Experimentally observed profile is given in figure 4.11(b). The nature of the profile indicates that the Cr atom columns are pure and atomic scale strain resulting into positional shift is not observed. However, the spacing between two consecutive Cr-atom column is ~ 0.45 nm. The difference between the experimentally observed and simulated spacing is ~ 8.16%. Similar intensity profiles from experimental and simulated images for Ti doublets are given in figure 4.12(a-d). As expected, the intensity profile from the simulated images shows a split at each peak position indicating the presence of Ti doublets. However, when it is compared with the experimental image, in some positions the split is not quite regular and commensurate with the simulated one. As observed from the simulated image and the intensity profile, the spacing between two Ti atoms in a single doublet and the spacing between two consecutive doublets are ~ 0.27 nm and ~ 0.82 nm respectively. However, similar spacings in the experimental image are ~ 0.35 nm and ~ 0.91 nm respectively. The experimentally observed spacing between two consecutive Ti atoms in a single doublet is ~ 29.6% different from the simulated pattern, whereas the experimentally observed spacing between two consecutive Ti doublets is ~ 10% different from the simulated pattern. This could be attributed to the fact that V atoms preferentially occupy the Ti positions. Due to small variation in atomic radius between Ti and V, atomic scale strain is introduced in the lattice, as a result of which the split is enhanced. It could be further concluded that the introduction of V atom in the Ti sub-lattice changes the spacing between two consecutive Ti atoms in a single doublet. However, the average spacing between two consecutive doublets remains almost same. It is worth mentioning that the observed difference between the experimental and simulated intensity profiles is partially due to atomic scale strain and partially due to the experimental uncertainty. It is worth mentioning that introduction of V atom into the sub-lattice introduces a static displacement field, as well as the dynamic displacement field also gets modified as the phonon behavior of V is different from that of Ti. As the image is time averaged with respect to phonon scattering, it is not possible to distinguish them at this moment. Similar Ti and Cr profiles have been generated from different regions of the Laves phase oriented along the same direction.

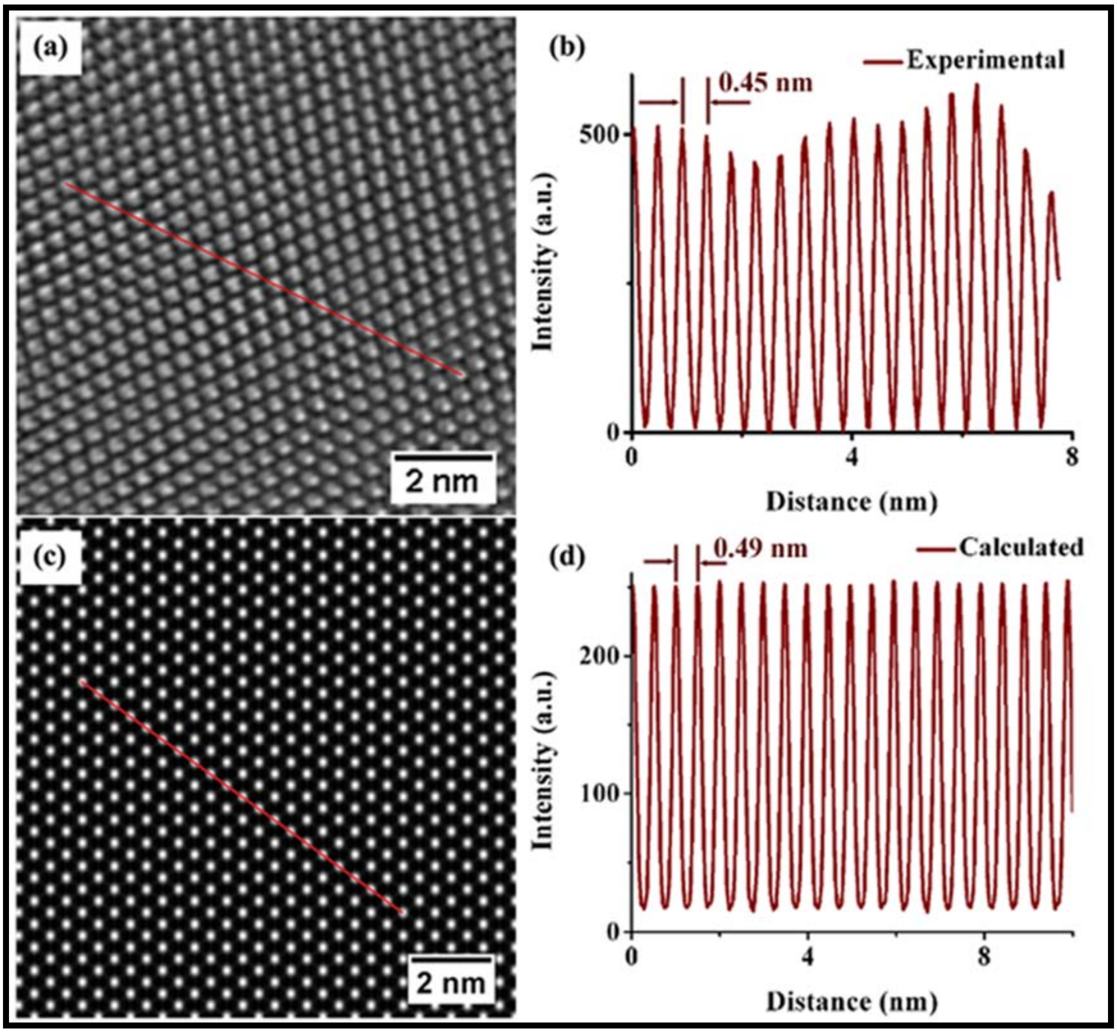

Fig. 4.11: (a) Experimental zero-loss phase contrast image from the region 'A' as marked in figure 4.2 (b) Intensity profile along the line drawn on the image (c) Simulated image of cubic $TiCr_2$ Laves phase along B=[01$\bar{1}$] and (d) the intensity in the simulated image along the line drawn on the image. Nature of intensity distribution matches quite well in the experimental and in the simulated image.

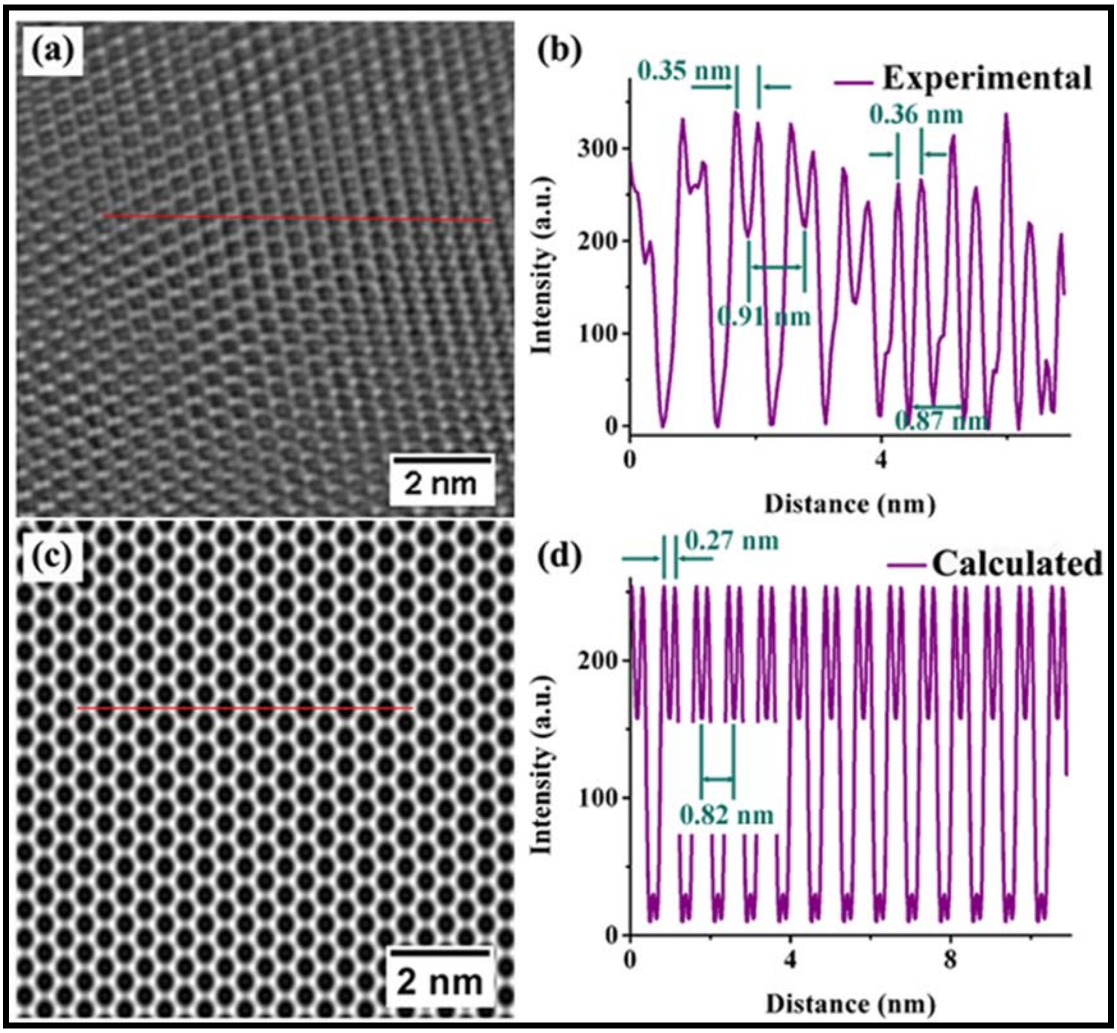

Fig. 4.12: (a) Experimental zero-loss phase contrast image from the region 'B' as marked in figure 4.2 (b) Intensity profile along the line drawn on the image (c) Simulated image of cubic TiCr$_2$ Laves phase along B=[01$\bar{1}$] and (d) the intensity in the simulated image along the line drawn on the image. Nature of intensity distribution is quite different in the experimental and in the simulated image which could be attributed to induced strain due to alloying with V.

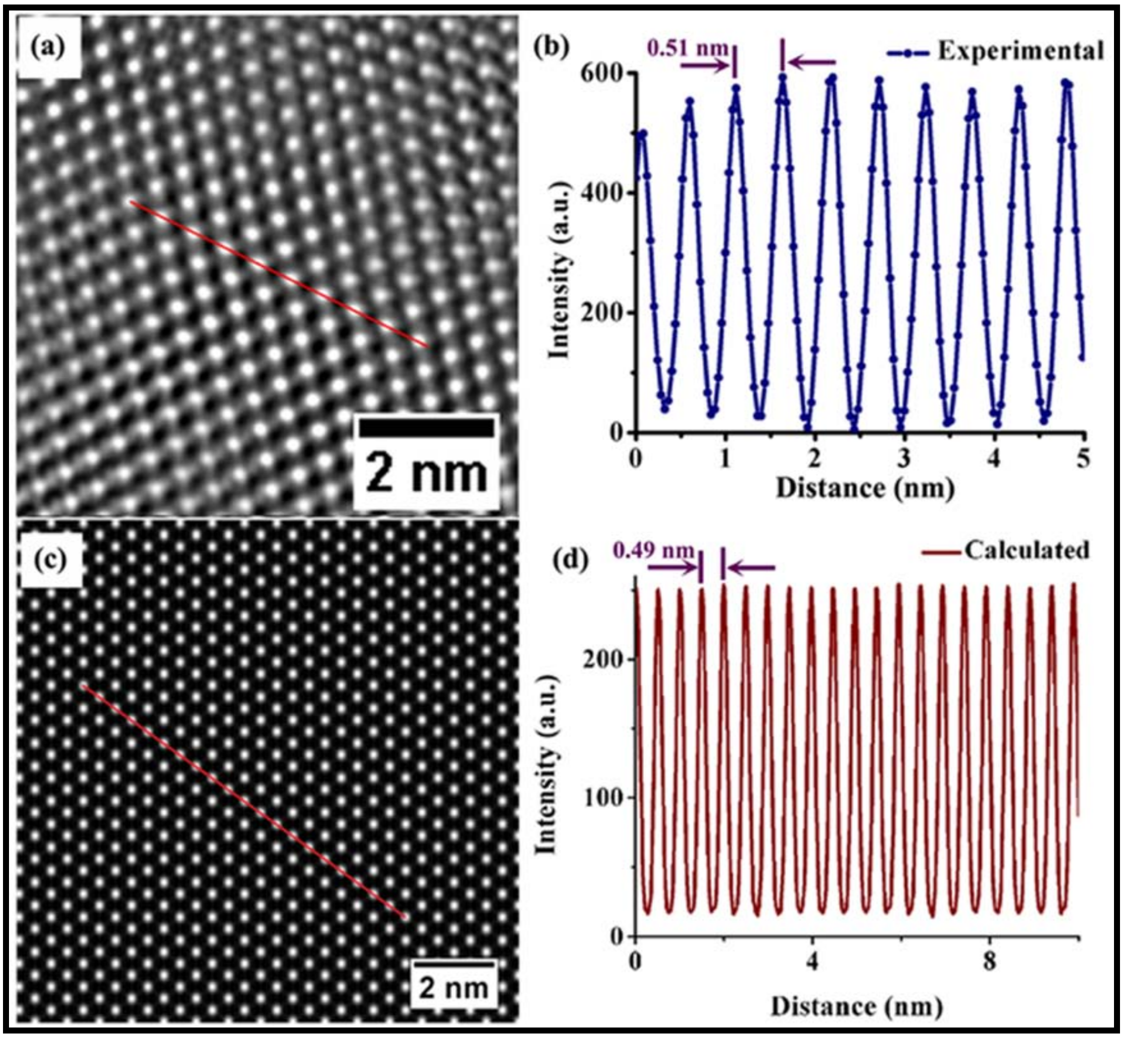

Fig. 4.13: (a) Experimental zero-loss high-resolution image of V-substituted cubic $TiCr_2$ Laves phase oriented along B= $[01\overline{1}]$ zone axis. (b) Intensity profile along Cr columns in the experimental image (c) Simulated image of V-substituted cubic $TiCr_2$ Laves phase under similar thickness-defocus condition. (d) Intensity distribution along the Cr-atom columns in the simulated image.

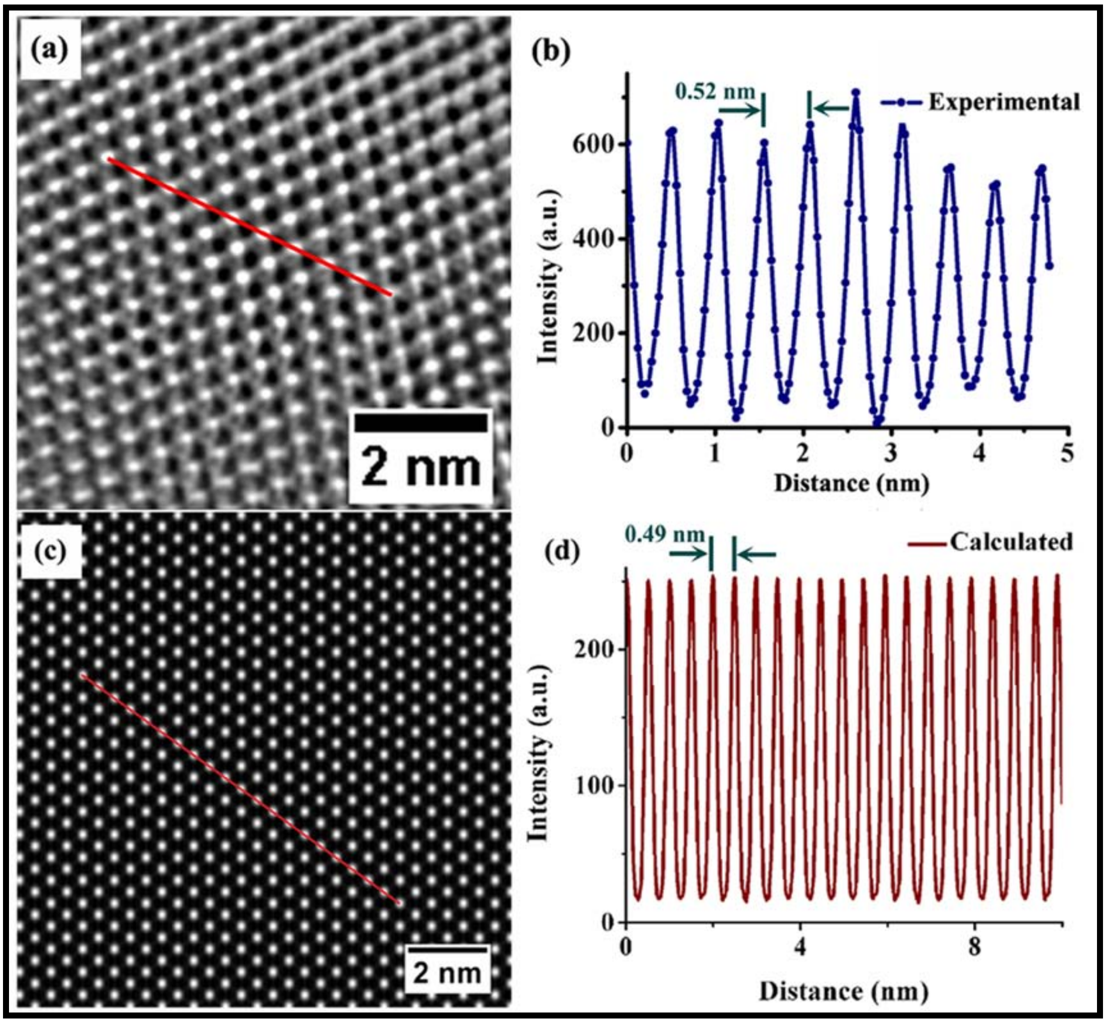

Fig. 4.14: (a) Experimental zero-loss high-resolution image of V-substituted cubic $TiCr_2$ Laves phase oriented along B= $[01\bar{1}]$ zone axis. (b) Intensity profile along Cr columns in the experimental image (c) Simulated image of V-substituted cubic $TiCr_2$ Laves phase under similar thickness-defocus condition. (d) Intensity distribution along the Cr-atom columns in the simulated image.

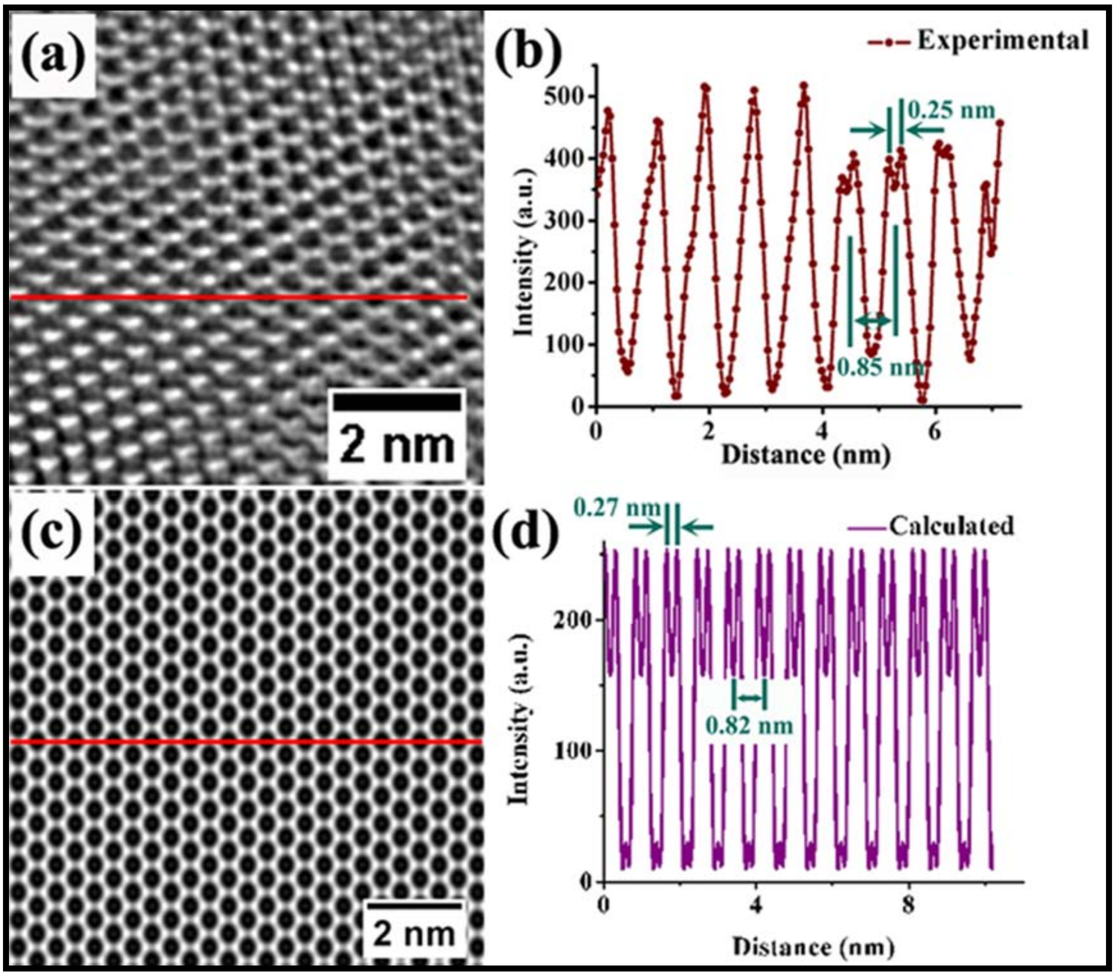

Fig. 4.15: (a) Experimental zero-loss high-resolution image of V-substituted cubic $TiCr_2$ Laves phase oriented along B= $[01\bar{1}]$ zone axis. (b) Intensity profile along Ti columns in the experimental image (c) Simulated image of V-substituted cubic $TiCr_2$ Laves phase under similar thickness-defocus condition. (d) Intensity distribution along the Ti-atom columns in the simulated image.

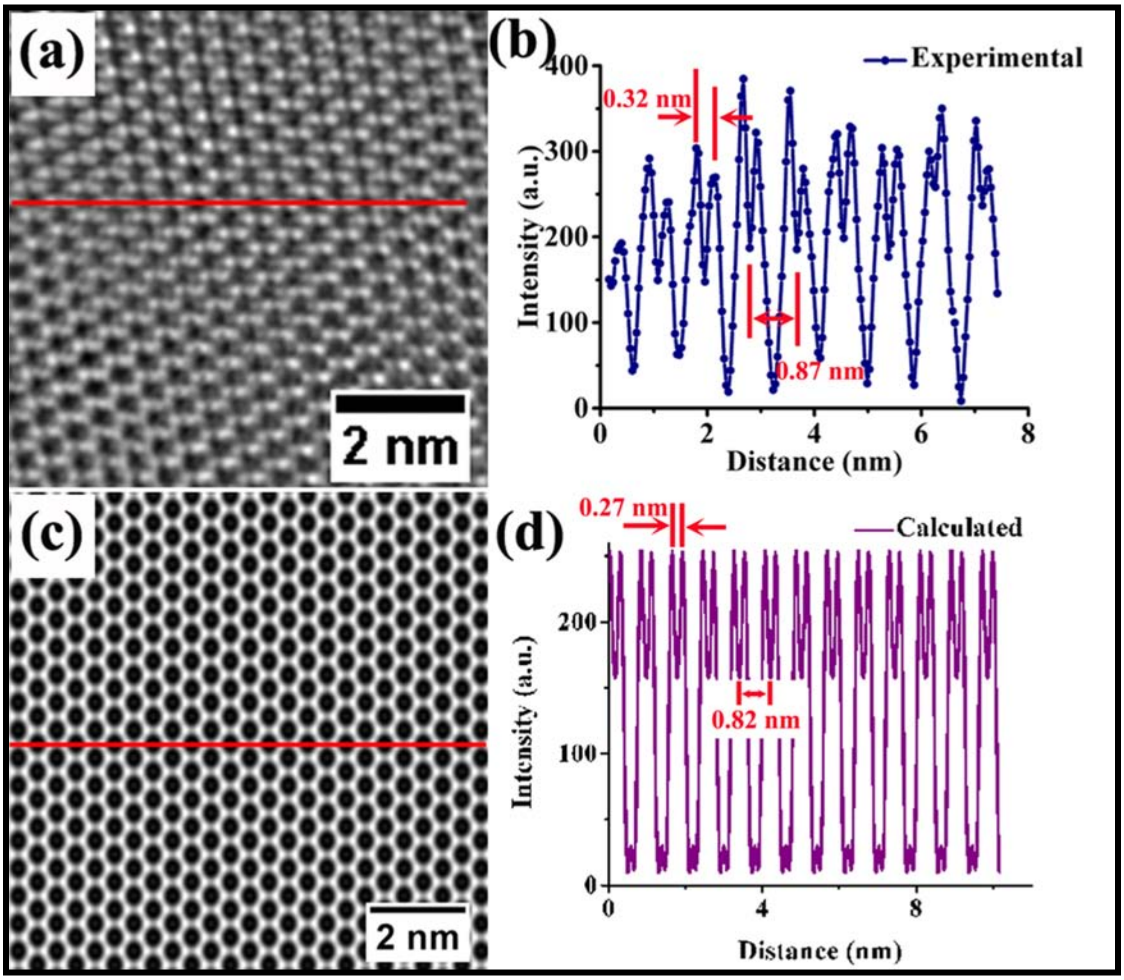

Fig. 4.16: (a) Experimental zero-loss high-resolution image of V-substituted cubic $TiCr_2$ Laves phase oriented along B= [01 $\overline{1}$] zone axis. (b) Intensity profile along Ti columns in the experimental image (c) Simulated image of V-substituted cubic $TiCr_2$ Laves phase under similar thickness-defocus condition. (d) Intensity distribution along the Ti-atom columns in the simulated image.

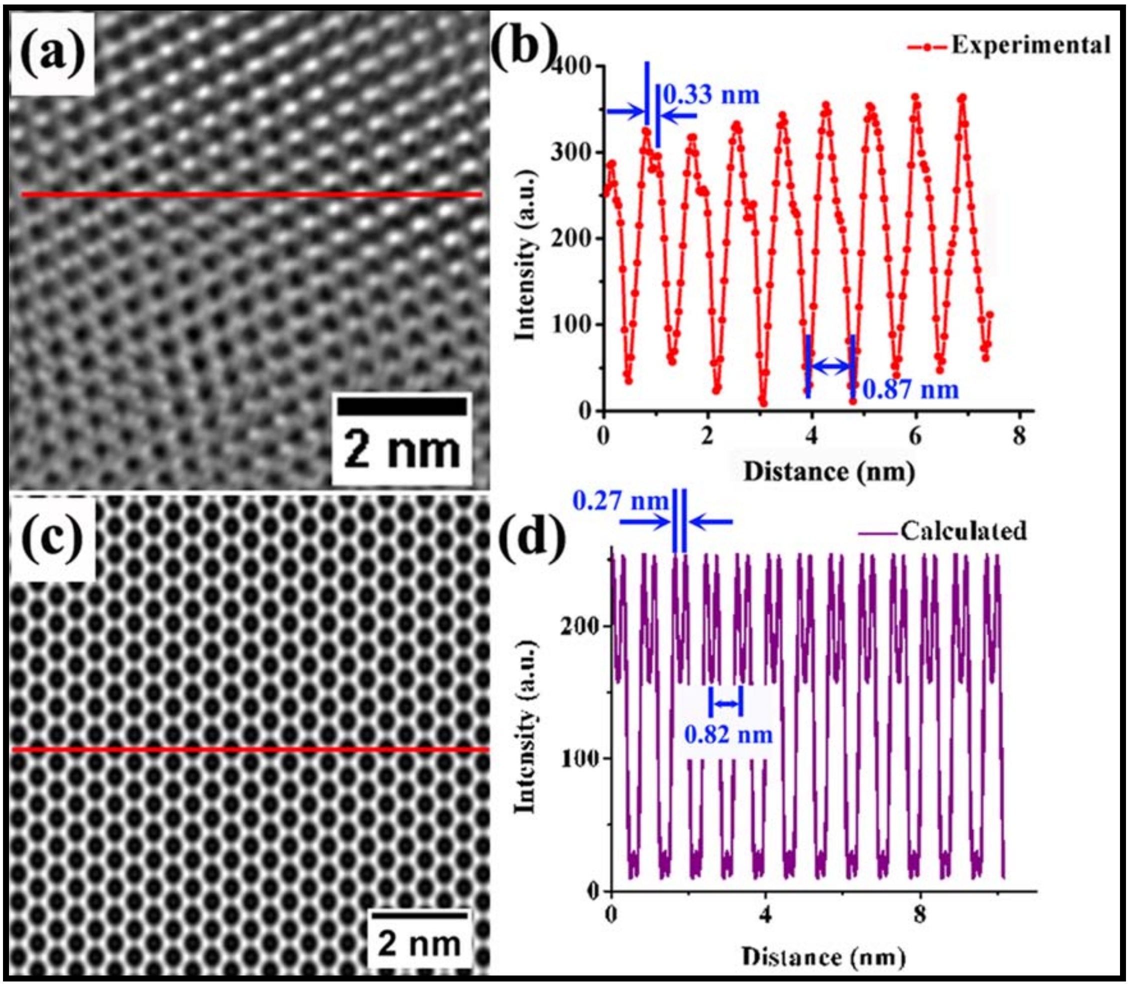

Fig. 4.17: (a) Experimental zero-loss high-resolution image of V-substituted cubic $TiCr_2$ Laves phase oriented along B= $[01\bar{1}]$ zone axis. (b) Intensity profile along Ti columns in the experimental image (c) Simulated image of V-substituted cubic $TiCr_2$ Laves phase under similar thickness-defocus condition. (d) Intensity distribution along the Ti-atom columns in the simulated image.

Experimental and simulated images from two different regions from the same Laves phase oriented along the same direction along with the intensity distribution profiles are given in figures 4.13(a-d) and 4.14(a-d) respectively. In both the images only the Cr atom columns are imaged. It is seen from the above figures that intensity distribution along the Cr atom columns in the experimental image is quite similar to the simulated image. The spacing between two consecutive Cr atom columns is also quite similar to the ideal value. Similar set of experimental and simulated images along with the intensity profile from another region is given in figure 4.15(a-d). Under this condition only Ti columns should be imaged. It has been observed that the experimentally observed intensity profile is quite different from the simulated profile. In the experimental profile the split due to the presence of the doublets is not observed quite often. This difference is attributed to the presence of atomic scale strain in the lattice due to the V substitution. Similar types of analysis are shown in Figures 4.16(a-d) and 4.17(a-d) also in order to increase statistical reliability of the results.

4.4: First principles calculation of dopant formation energy in cubic $TiCr_2$ structure

To understand as to which site (i.e., Ti or Cr) the dopant (V) would prefer to occupy, first principles calculations were carried out. The first-principles computation is performed within the framework of density functional theory (DFT), using the projector augmented wave method as implemented in the Vienna *ab initio* simulation package (Kresse and Hafner, 1994; Kresse and Furthmuller, 1996a, b). In the present spin polarized calculations, the exchange correlation interaction is treated within the generalized gradient approximation (GGA) using the Perdew-Burke-Ernzerhoff (PBE) function (Perdew *et al.*, 1996). The electronic wave functions were expanded in a plane wave basis with a cut off energy of 500 eV. The relaxation of atomic positions and optimization of lattice parameters are performed by the conjugate gradient method. The atomic positions are relaxed until the maximum component of the force on each atom is smaller than 0.02 eV/Å. The Brillouin zone sampling was done using a Monkhorst-Pack mesh of 4 x 4 x 4, to achieve the convergence within 0.1 meV per formula unit.

The calculated reduced cell lattice parameter (0.486 nm) for pure $TiCr_2$ is in good agreement with the corresponding experimental values (0.49 nm) (ICDD # 050-1106). To calculate the dopant formation energies V is substituted either in the Ti or the Cr site in a 48-atom supercell. Introduction of the dopants at the Ti or the Cr sites preserved the cubic symmetry of the overall supercell at the dopant concentration considered. Owing to the large size of the V, interstitial doping was not considered here.

The energetics of dopant formation, E_D^f, at 0 K is defined as (Sharma *et al.*, 2013),

$$E_D^f = E^{Doped} - E^{Host} - \mu_D - \mu_H$$

where E^{Doped} and E^{Host} are the respective DFT energies of the doped and host (undoped) supercells. μ_D and μ_H are the elemental chemical potentials of the dopant and the replaced host atoms, respectively.

The calculated dopant formation energies for both the Ti (0.29 eV) and the Cr (0.40 eV) site substitutions suggest that V prefer to replace Ti. It has been reported earlier that the stability and the location of a dopant is mainly governed by the mismatch in the atomic size and oxidation state of the dopant with respect to the host (Sharma *et al.*, 2013). In case of V substituted $TiCr_2$, the host and dopant atoms are similar in radii and their oxidation state is also similar. Under this condition, it is the defect formation energy that determines the substitution site.

4.5: Interfacing microscopy with materials structure and chemistry

It has been mentioned earlier that Laves phases are a class of intermetallic compounds with interesting properties and technological promise. The properties of such phases could be tailored by modification of structure and chemistry. The detrimental effects imparted in materials by uncontrolled precipitation of Laves phases are strongly correlated with the structure, defects and interfaces. The Laves phase precipitation causes the removal of solutes from the matrix, which results in loss of strength and corrosion resistance. Being a hard intermetallics phase, they further affect the movement of the dislocations too and hence the mechanical properties. Complete understanding of structure, defects, interfaces and chemistry could pave the pathway for novel materials design. V-substituted $TiCr_2$ cubic Laves phase is an important material for energy conversion and storage applications. However, insight developed from this study could be extended to other Laves phase forming compositions. In the subsequent sections insight developed from this study will be discussed with respect to $TiCr_2$ Laves phase and it would be extended to this class of materials as a whole.

Over the last couple of decades, there has been a constant effort to design novel materials with exciting combination of properties. It was realized quite early that in order to achieve this goal, understanding the physics of materials phenomena and chemistry at atomic scale is extremely important (Gronsky, 1988). Towards that direction, several microscopy techniques have been developed to interface with the requirement from the materials science community. As of today most widely used technique to understand structure and chemistry of materials at atomic scale is STEM combined with EELS or XEDS (Dickey *et al.*, 1999). Several pure and doped complex oxide materials have been studied successfully by this technique (Browning and Pennycook, 1996; Browning *et al.*, 1998; Dickey *et al.*, 1999; Pennycook *et al.*, 1999). During incoherent imaging of complex oxides, heavier cations act as strong scattering centers while the relatively lighter oxygen anions scatter weakly. So the image contrast is mostly dominated by the scattering from the cations. In this technique, even though the oxide structure is complex only the cation sub-lattice is imaged. The scattered intensity from the cation sub-lattice is directly proportional to the square of the atomic number of the cations. Such images are directly interpretable as the contrast develops based on the atomic number of the cations only. V-substituted $TiCr_2$ Laves phase is quite different in nature from the complex oxides. The atomic numbers of V, Ti and Cr are pretty close and all of them will scatter almost equally. As a result differential contrast as is generated in a complex oxide will not happen for V-substituted $TiCr_2$ phase. Direct interpretation of image contrast from such phases is extremely difficult, if not impossible. Moreover, single-atom column chemistry by EELS or XEDS is strongly dependent on the nature of the probe and on the chemistry of the atomic columns. In V-substituted $TiCr_2$ Laves phase it is not quite known as to where V substitution will take place. In this light STEM-EELS or STEM-XEDS is not the best suited technique for structure imaging and detection of V atoms in $TiCr_2$ Laves phase.

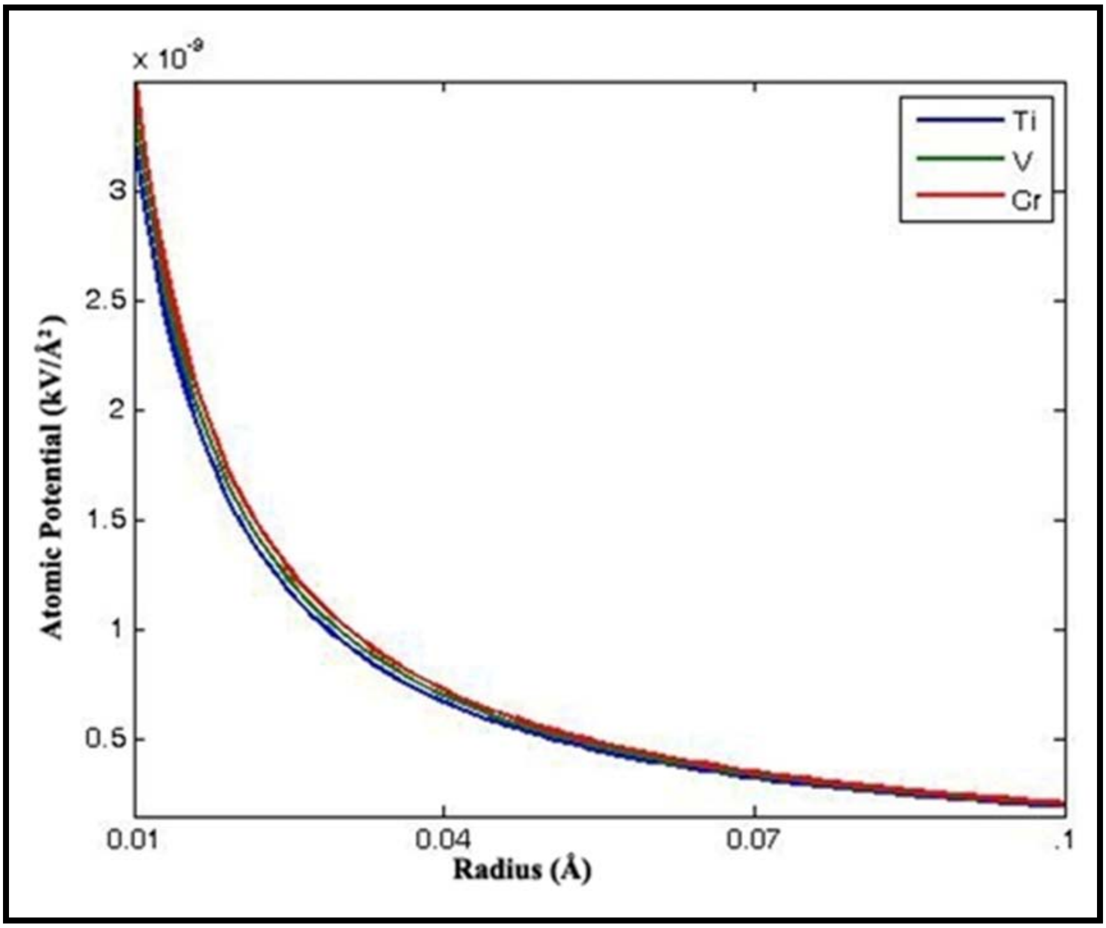

Fig. 4.18: Calculated single-atom potentials for Ti, V and Cr atoms. The potentials for three atoms are almost similar. The potentials peak sharply near the nucleus and it dies asymptotically away from the nucleus.

4.5.1: Origin of atomic contrast generation in phase contrast imaging: A quantum mechanical approach

High resolution phase contrast images are not directly interpretable (Glaisher *et al.*, 1989a). The phase and amplitude of the electron wave is modified as it interacts with the specimen potential. The single atom potential for V, Ti and Cr atom as calculated by Hartree-Fock method (Kirkland 2009) is shown in figure 4.18. A custom written code in

Matlab has been used to calculate the single atom potentials for these elements. It is observed from the figure that the potential sharply peaks at the nucleus and it dies asymptotically away from the nucleus. Otherwise the potential for the constituent elements of the alloys in this study are very similar. In the presence of bonding atoms, the nature of potential field gets significantly modified. For ionic compounds as in ceramics, electrons cloud is localized around the nucleus because of which potential field is sharply peaked at the nucleus and dies down very fast away from the nucleus. Potential fields for metals, alloys and intermetallics, as in the present case of V-substituted $TiCr_2$, are quite different because of metallic bonding. This is considered to be an added disadvantage for interpretation of contrast from metals, alloys and intermetallics. For very simple structures image contrast varies in a systematic manner over a range of defocus and thickness (Dyck *et al.*, 1982). In such cases the image could be interpretable intuitively; however, there is a good possibility of being misled. In order to quantitatively understand the contrast and relate it to the atom column position, one has to do simulation and match with the image (Kauffman *et al.*, 2011). Several variants of this technique e.g. Multislice simulation, Bloch wave analysis, iterative reconstruction of exit plane wave etc. have been developed towards this end. A combination of such techniques has been used successfully for imaging interfaces, semiconductors with tetrahedral voids partially filled, oxides, solid-liquid interfaces (Glaisher *et al.*, 1989b, c; Browning *et al.*, 1998; Dickey *et al.*, 1999; Kauffman *et al.*, 2011) etc. In the present case, as the atomic positions in cubic $TiCr_2$ Laves phase is known, simulated images could directly be matched with the experimental ones. As a result of this complex process of image formation, the contrast on the image plane is extremely sensitive to the variation of thickness, defocus, aberration etc. As a result two different structures may give rise to similar contrast. In the present study, imaging has been carried out at a predefined defocus value with fixed values of aberrations (C_s = 0.65 mm; C_c = 1.4 mm). Moreover, systematic diffraction experiments confirmed that the present Laves phase alloy is of cF24 structure and for cubic cF24 structure all the atomic positions are well defined (Villars, 1997). So the possibility of confusing some other structure with Laves phase is quite minimal. Still, the images have been recorded over a range of defocus values and compared them with the simulated images. Simulated images along with the experimentally observed images from the cubic $TiCr_2$ Laves phase have been given in Figure 4.19.

For Laves phase intermetallics, channeling enhanced microanalysis (ALCHEMI) has been used extensively to identify the atom columns and determine the position of alloying elements (Chu *et al.*, 1998; Okaniwa *et al.*, 1999). Even neutron scattering has been used to study the hydrogen and its isotopes induced local ordering in Laves phases (Levin *et al.*, 2012). However, very limited success has been achieved for complex intermetallic structures so far as structure imaging is concerned. Yang *et al.* (2012) have used this technique to study defect structures in $NbCr_2$ Laves phase. Even though, direct image matching has been pointed out as a viable technique to understand contrast in phase contrast images, it has also been pointed out in literature that simulated images often do not match with the experimental one. Apart from Stobbs factor, several other reasons have been pointed out which are responsible for such kind of mismatch (Boothroyd, 1998). Although phase contrast imaging is a coherent imaging process, a

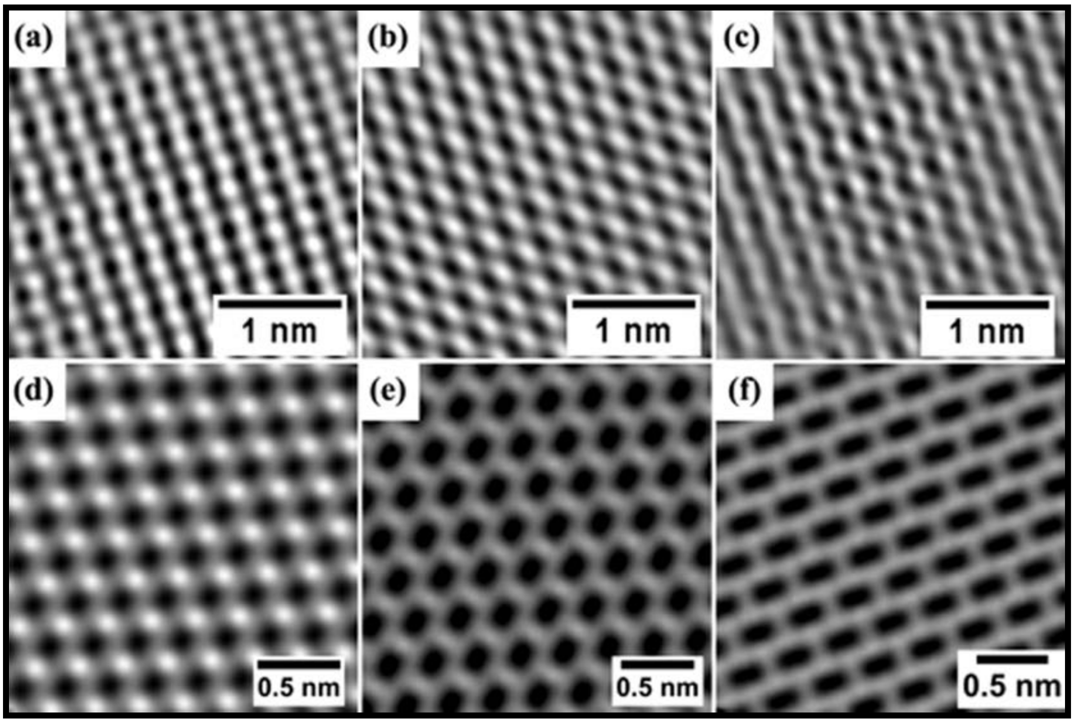

Fig. 4.19: (a-c) Experimentally observed and (d-f) simulated images of cubic $TiCr_2$ Laves phase along [1 1 0] direction obtained at different defocus and at 26.5 nm thickness. Simulated and experimental images are obtained at C_s = 0.65 mm, V = 300 kV. The defocus values for (a) and (d), (b) and (e), (c) and (f) are -36, -41 and -47 nm, respectively.

significant contribution comes from inelastically scattered electrons also, which in turn degrade the image contrast. In order to overcome this problem zero-loss phase contrast imaging has been carried out in the present study.

Mathematically, the contrast in a phase contrast image could be understood as a combination of three different contributions. Those are contribution to the background intensity which basically depends on the amplitudes of the direct beam and the diffracted beams, linear component which basically depends on the amplitudes and phases of the direct beam and the diffracted beams and non-linear component which also depends on the amplitudes and phases of the direct and the diffracted beams. For a complex structure like Laves phase with many beams contributing to the contrast, it is extremely difficult to understand the contrast over the image plane computationally. However, qualitatively the nature of the exit waves could be understood. Potential, exit-plane wave, exit-plane phase and exit-plane amplitude map for $TiCr_2$ cubic Laves phase are given in figure 4.20. It is seen from the potential map that over a range of thickness, all the atomic columns are present. However, exit-plane wave phase and amplitude from the Ti and from the Cr column are quite different (Figure 4.21). It is observed that in the exit-plane wave that comes out of the Cr column, the phase part is continuously present and it sharply undergoes a phase reversal at about 50 nm thickness and the amplitude of the same exit plane wave is almost constant all over the thickness, however it suddenly peaks at ~ 26 nm thickness. In contrast to that the phase of the exit wave from the Ti columns either vanishes or weakens over every 10 nm thickness. At lower thickness the phase is present and at ~ 50 nm thickness the phase is most strongly present. Similarly, the exit phase wave amplitude from the Ti columns exhibits variation over thickness and at certain thicknesses they are absent. It is clear that the channeling characteristics of electron waves along the Ti and Cr columns are different. While the characteristic half length of the electron wave along the Cr column is ~ 50 nm, the same along the Ti columns is ~ 10 nm. It can be qualitatively said that as from the Ti columns either the phase or the amplitude becomes weak very often over thickness, either it does not contribute anything to the contrast or it merges with the background. At about 50 nm thickness the phase is strongly present and amplitude is moderately present, so contrast from the Ti columns are observed at ~ 50 nm thickness. In the similar line, at ~ 50 nm thickness the exit wave

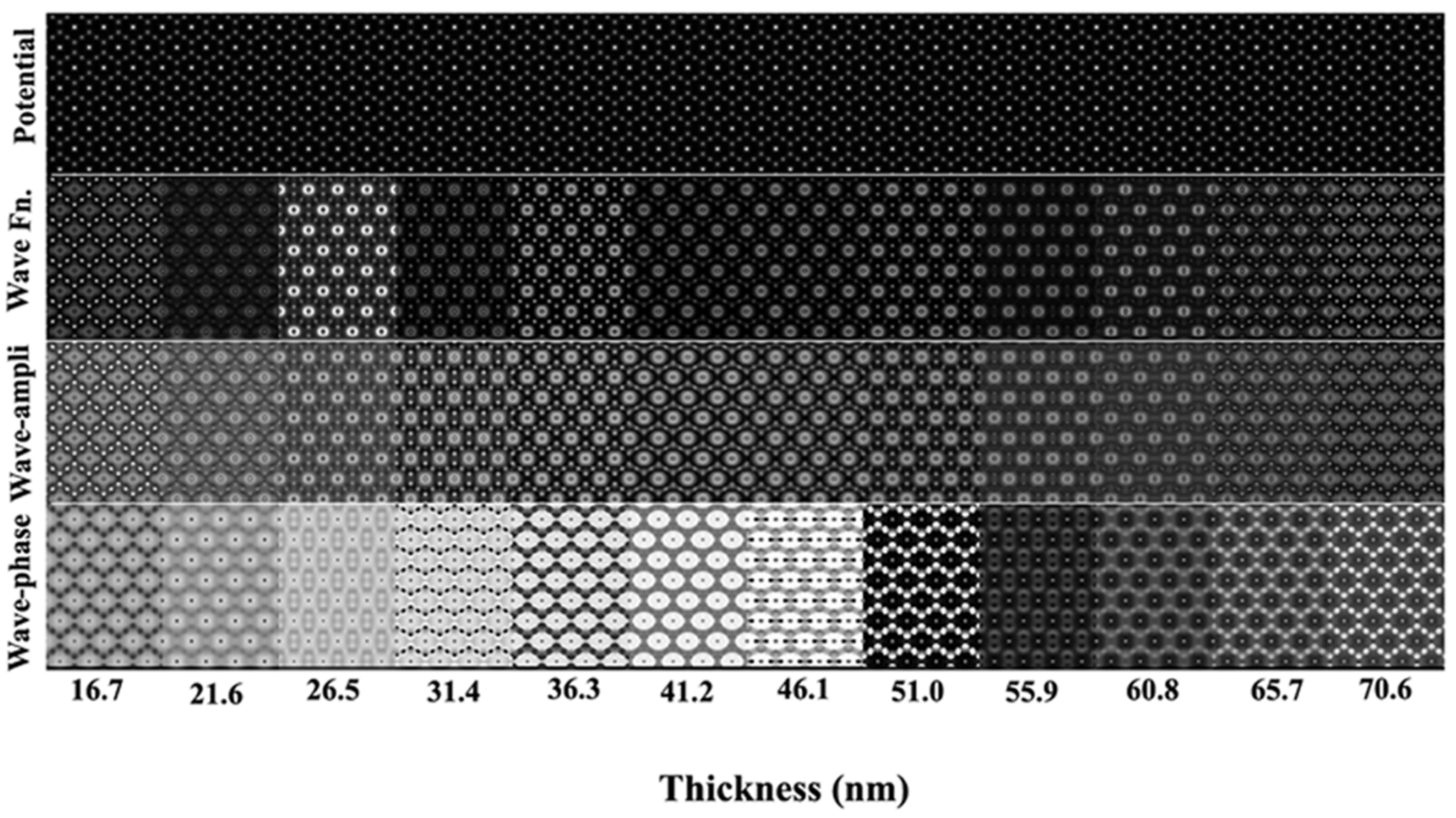

Fig. 4.20: Plot of projected potential and exit plane wave function, wave amplitude and wave-phase with thickness, for cubic $TiCr_2$ Laves phase along $[01\overline{1}]$.

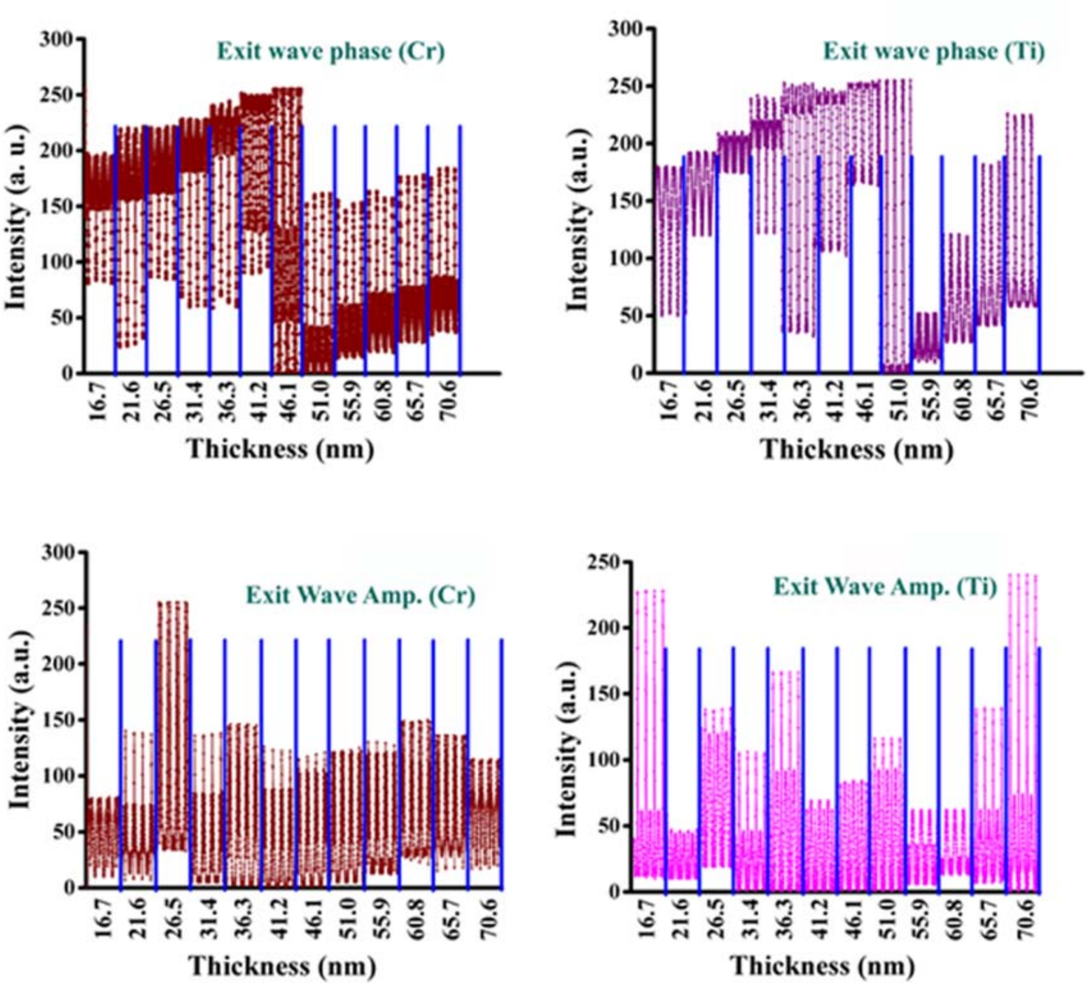

Fig. 4.21: Variation with thickness of the exit-plane wave phase and amplitude along the Ti and the Cr columns in cubic $TiCr_2$ Laves phase.

phase from the Cr column undergoes phase reversal and amplitude is weakly present. A combination of these two effects leads to either disappearance or weak presence of electron intensity from Cr columns (Ghosh *et al.*, 2015b).

4.5.2: Location of V atom in Laves phase matrix: Chemistry at the atomic scale through high-resolution imaging

It has been mentioned earlier that there are three polymorphs of Laves phase. The crystallography of the polytypes is understood in terms of crystal symmetry. In $TiCr_2$ cubic Laves phase Ti atoms form the *fcc* lattice and four Ti atoms occupy four tetrahedral voids. Remaining four tetrahedral voids are filled out by four tetrahedra of Cr atoms. Exact position of each atom can be obtained by linear combination of lattice vectors. Presence of a third alloying element atom introduces minor shift in the lattice positions. Even though a large number of atoms are present in the lattice, it is not as densely packed as *fcc* or *hcp* lattice. The structure could also be looked at as an interpenetration of a tetrahedral network of Ti and a tetrahedral network of Cr (figure 4.22). Under such atomic arrangement, it is observed that the coordination numbers for the A and B atoms are 12 and 16 respectively. Apart from this crystallographic description, several other description of the structure has evolved. Cubic Laves phase can be seen as an interpenetration of two icosahedra with a tetrahedra common in between. It is understood that such interpenetrated icosahedral clusters built up the entire structure (Basu and Ranganathan, 2008). Such phases with icosahedral clusters in the structure are categorized as Frank-Kasper phases. These phases can accommodate non-stoichiometry and alloying is a possible avenue for tailoring properties. It has been a long standing question as to which site an alloying element would occupy. It has been postulated in earlier literature that in AB_2 Laves phase the B atom could be replaced by B′ and B′′ atom where $B^{'}$ and $B^{''}$ are in the same period as of B and located on either side of B (Kuo 1953). It is intuitively understood as average atomic radius of B′ and B′′ is almost equal to B and does not introduce much of lattice distortion. First principles calculations have been carried out to understand the generation of point defects and site-specificity of alloying elements (Yao *et al.*, 2006; Jiang, 2007). It has been concluded that atomic size is not the only determining factor. Electronic structure and energy associated with defect generation should also be taken into account to understand the site-specificity of alloying elements. In this light, atomic resolution microscopy should provide direct and unambiguous evidence of point defects in alloyed Laves phases. In case of V-substituted $TiCr_2$ Laves phase, the constituent elements Ti, V and Cr appear in the same period next to each other in the periodic table. It is equally probable as to which site V would occupy or it would be preferentially occupying a specific lattice site. Atomic radius of Ti (a_{Ti}=176 pm) is more than that of V (a_V=171 pm) and that of V is more than that of Cr (a_{Cr}=166 pm), introduction of V into Ti or Cr site would result in a tensile or compressive strain. Introduction of strain in the lattice results in atomic shift. It has been observed in the present study that V occupies the Ti site as distribution of intensity pattern along the Ti column is modified from that of the ideal nature, which is further confirmed using first principles computations. There is no evidence of V replacing Cr. It has been postulated in earlier literature that V replaces Cr giving rise to $TiCr_{2-x}V_x$ stoichiometry (Santos *et al.*, 2002). In the present study it is clearly established that V can replace Ti also in the lattice. Location of alloying element in Laves phase has been identified before by ALCHEMI technique (Chu *et al.*, 1998). To the best of the knowledge of the author, identification of V atoms in $TiCr_2$ cubic Laves phase by direct structural imaging and analysis of contrast has not been done before. Keeping in mind the complexity associated

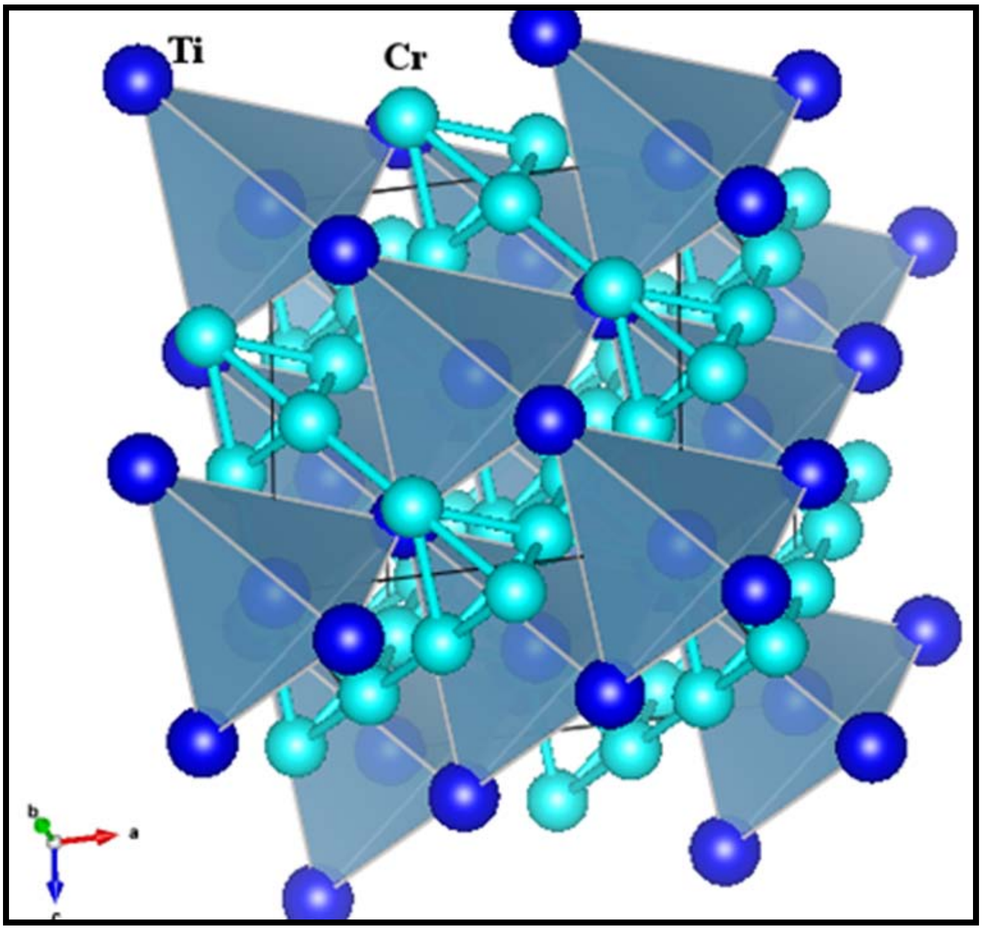

Fig. 4.22: Schematic structural diagram of cubic $TiCr_2$ Laves phase along arbitrary direction. It is two inter-sparced tetrahedral networks of Ti and Cr atoms that build up the Laves phase structure.

with atom column chemistry determination by STEM-EELS and STEM-EDS technique, present thesis propose that careful high resolution phase contrast imaging, atom column identification and nature of intensity distribution could also be explored as a viable technique for qualitative determination of atom column chemistry.

4.5.3: Order of V- substituted $TiCr_2$ Laves phase

Having said the fact that V replaces Ti in the cubic $TiCr_2$ lattice, the question naturally arises as to how this phase would be classified. According to the definition

(Kuo, 1953), a Laves phase could be termed as a truly ternary phase when there is no terminal binary Laves phase exists for the ternary alloying constituents. In Ti-V-Cr system, there is no reported Laves phase in Ti-V or in V-Cr system. However, binary Laves phase exists in Ti-Cr system. According to this definition it is not a truly ternary Laves phase. According to the second condition, binary Laves phases may exist but the structure of the ternary phase should be different from the binaries. In the present study V-substituted $TiCr_2$ Laves phase is cubic in structure. Cubic and hexagonal polymorph of $TiCr_2$ binary Laves phase has been reported in earlier literature. In the present case the secondary condition is also not satisfied. According to the third condition, one binary counterpart can exist, however it should be structurally different from the ternary one. This condition is also not met in the present study (Kuo, 1953). In this light, it can be concluded that the phase under study is a pseudo-binary Laves phase.

It has been pointed out in earlier literature that addition of a third element in a binary Laves phase significantly alters mechanical properties also (Takasugi *et al.*, 1996). The deformation characteristics of the alloyed Laves phase strongly depends upon what kind of defect it produces i. e. anti-site defect or vacancy. In the present study it has been observed that V occupies Ti sites leading to the formation of anti-site defects. It is worth mentioning that this could be viable method to study the alloying behavior and defect chemistry of Laves phases. Complete understanding of the nature of the defects may lead to better insight of the pseudo-shear mechanism of Laves phases, strong theoretical conceptualization and experimental validation of which is still missing. Mechanistic understanding of hydrogen storage behavior of this phase is possible by this technique. Hydrogen atom might not be imaged directly; however the lattice distortion due to hydrogen incorporation may provide useful insight about the mechanism of hydrogen storage. Moreover, it has been reported that Laves phase transforms to B2 structure after irradiation (Sinkler 1996). The structural correlation that exists between the Laves phase and the transformed B2 phase is due to the vacancy generation during irradiation. This method might provide new insight into the atomistic mechanism of such transformation.

4.6: Conclusions

(i) Ti-55Cr-7V alloy precipitates a pseudo-binary V-substituted cubic $TiCr_2$ Laves phase over solidification. The composition of the Laves phase is very close to the as melted composition.

(ii) V-atoms preferentially substitutes at Ti-sites in the $TiCr_2$ Laves phase. Atomic size is not the only factor in determining the site substitution behaviour. Relative oxidation state, electronic structure and energy associated with the defect formation should also be taken into account in understanding the site substitution behaviour in Laves phase. The defect formation energy for V in Ti lattice and in the Cr lattice are 0.29 eV and 0.40 eV respectively.

(iii) Difference in channeling behavior of the electron wave along Ti and along Cr columns can be exploited in preferentially imaging one type of atom column to understand its structure and chemistry.

(iv) Deriving spectroscopic information from phase contrast images aided with image simulation could be extended to other Laves phase systems to understand their defects, interfaces and chemistry which in turn would help in understanding its deformation behavior, hydrogen storage mechanisms and irradiation induced phase transformations.

Chapter V

Phase Separation and ω Transformation in Binary V-Ti and Ternary V-Ti-Cr Alloys

Chapter V

Phase Separation and ω Transformation in Binary V-Ti and Ternary V-Ti-Cr Alloys

5.1: Introduction

It has already been discussed in the earlier chapters that for the better understanding of structure-property correlation and in-service behaviour of binary V-Ti and its ternary derivative of V-Ti-Cr systems, detailed studies of phase and structural behaviour down to the atomic level is extremely essential. For binary V-Ti alloy though sufficient literature support is available, fundamentally different views still exist concerning the general form of even the binary phase diagram. This lack of agreement exists, as the phases formed on solidification are not always the equilibrium phases and the metastability hops along local minima in the energy landscape upon heat treatment (Ramsteiner *et al.*, 2006, 2008; Fuming and Flower, 1989; Suwarno *et al.*, 2014). Moreover, as far as the phase transformation in ternary V-Ti-Cr system is concerned, very scarce information is available in the scientific community. Earlier thermodynamic calculations using Miedema's model from the author's group predicted the existence of a miscibility gap in the equiatomic V-Ti and V-40Ti-20Cr alloys. This had further been supported by the experimental analysis using phase contrast, HAADF imaging and STEM coupled spectroscopic investigations and have already shown in chapter 3.

Another interesting aspect of phase transformation in this alloy system is the formation of ω phase. Over the last four decades, several researchers have significantly contributed in the phase transformational aspects of the ω phase and their evolution from the *bcc* structured matrix. ω phase usually forms with group IV B transition metals (Ti, Zr and Hf) when alloyed with *bcc* stabilizing elements (e. g. V, Mo, Nb, Fe, Cr etc.) upon quenching from the *bcc* phase field or it may form during aging of the quenched alloy (Banerjee and Mukhopadhyay, 2004).

However, almost in all the cases, group IVB transition metals acts as the major alloying element (Bendersky *et al.*, 1990a, b). Very few reports are available regarding the structural transformation of ω phase in equiatomic Ti or Zr based alloys. McCabe *et al.* have discussed the feasibility of the ω phase formation in the Ti-V alloys with variation in the V addition from 10 at% to 55 at% (McCabe and Sass, 1971). It is further concluded that with the higher amount of *bcc* stabilizing elements, a diffuse ω structure forms which results in a shift in the spot position of the crystalline ω in the electron diffraction pattern and this shift would increase with the increase in concentration of the *bcc* stabiliser. However, all these experiments were supported only with diffraction data. Detailed phase contrast and Z contrast microscopy coupled with EELS and XEDS, with current instrumental capabilities will provide a deeper insight to ω-phase formation and its characteristics in these alloy systems, where information available is sparse with reference to effect of ternary alloying addition on the ω transformation behaviour.

In the present work, comprehensive investigations have been carried out to study the phase transformation behaviour in binary V-Ti and ternary V-Ti-Cr alloys with the aid of phase contrast and Z contrast microscopy coupled with XEDS and EELS. The phase separation mechanism has been studied through phase contrast microscopy and energy filtered TEM imaging by suitably heat treating the V-Ti and V-Ti-Cr alloys. Moreover, the formation of nanostructured ω domains as well as their shape, size and distribution have been studied with the aid of diffraction contrast microscopy along different zone axis. Attempts have also been made to study the structural details of the partially collapsed ω domains and their interfaces with the *bcc* structured matrix through suitable atomic resolution microscopy experiments.

In short, the present chapter deals with;

(i) Studies of the phase separation phenomenon in V-50Ti alloy and the effect of ternary addition in the phase transformation behaviour through similar studies in V-40Ti-20Cr alloy.

(ii) Understanding the mechanism of the phase separation i.e. whether the propagation of the fluctuation wave is dominated by nucleation and growth or spinodal decomposition has also been studied by suitably heat treating both the alloys and comparing phase separated domains with that of the as melted alloys.

(iii) Evidence of the formation of ω in V-50Ti and V-40Ti-20Cr alloy through proper diffraction contrast and phase contrast experiments along different zone axis.

(iv) Interface structure studies between nanostructured ω and the *bcc* matrix down to the atomic scale.

5.2: Experimental details

Binary V-Ti and ternary V-Ti-Cr alloys were synthesized by arc melting. A binary V-Ti alloy with nominal composition of V-50Ti and a ternary alloy with nominal composition of V-40Ti-20Cr (all compositions are expressed in at%) were arc melted in high-purity Ar atmosphere on a water cooled copper hearth, starting from elemental V, Ti and Cr (> 99.9% purity). The melted alloy was re-melted several times in order to ensure complete melting and compositional homogeneity. The details of the alloy design and selection of the composition have already been described in chapter 3. These alloys are termed as the as melted alloys and this terminology will be used in the rest of the paper. Both the melted and homogenized buttons have further been sectioned using a low speed diamond saw. One section from each of the alloys was inert gas sealed in a fused quartz tube, solutionized at 1100° C for 5 hours, aged at 750° C for 48 hours and ice-water quenched. These alloy sections are termed as aged alloys. The as melted as well as aged alloy slices were undergone different metallographic treatments and finally electron transparent TEM specimen were prepared through grinding, dimpling and subsequent ion milling. Details of the TEM thin foil specimen preparation technique as well as the experimental details of the TEM characterization were already described in chapter 2 of the present thesis.

5.3: Microstructural and microchemical evidence of phase separation in binary V-50Ti and ternary V-40Ti-20Cr alloys

5.3.1: Microstructural features of the phase separated domains in as-melt alloys

Results of TEM characterisation of V-50Ti alloy in the as-melted condition are shown in figure 5.1(a-d). In the relatively low magnification TEM bright-field micrograph shown in figure 5.1(a), alternate bright and dark striations can be observed. The striations appear to be periodic in nature with an observed modulation length of ~ 3-4 nm. A selected area electron diffraction pattern from the area is shown in figure 5.1(b). The diffraction pattern has been indexed as [0 1 3] zone axis pattern of a *bcc* structured phase, with principal reflections corresponding to 200 and $23\bar{1}$ type of planes marked in the figure after careful measurement of the lattice spacings and interplanar angles. The calculated lattice parameter from the diffraction pattern is a= 0.32 nm, which is very close to the reported lattice parameter for the *bcc* V-Ti solid-solution phase, a= 0.3165 nm (ICDD # 04-003-2225). In the diffraction pattern, along with the principal *bcc* reflections, dove-tail shaped diffused intensity between the main spots and very feeble satellite spots can also be observed. The diffuse intensity is because of the presence of ω phases (discussed in detail in the following sections) whereas the satellite spots appear because of a possible phase separation phenomenon. All the major reflections in the diffraction pattern are unequivocally indexed with V-50Ti alloy with cI2 structure (ICDD # 04-003-2225) and the SAD pattern does not contain any signature for the formation of any metal-carbides. An electron energy-loss spectrum of the observed alloy is shown in figure 5.1(c). Distinct energy loss edges seen in the figure at 462 eV and 521 eV correspond to the L edges of Ti and V respectively. Quantitative analysis of the composition from the EELS spectra after suitably modelling the background using power law method shows the composition of the alloy to be V-49Ti, which is very close to the nominal composition of the alloy. Comparison of the energy-loss near edge structure (ELNES) of the Ti-L and V-L edges with data in EELS atlas (Ahn *et al.*, 1983) confirms that the elements are present in solid-solution and not as compound. The colour-composite Energy-filtered TEM (EFTEM) image (figure 5.1d) recorded using Ti-L and V-L edges shows that the striated domains seen in figure 5.1(a) correspond to regions of elemental concentration fluctuation. This indicates that the striations visible in the EFTEM map constitute a phase separation event resulting in Ti- rich and Ti- lean phase regions on the scale of ~ 3-4 nm.

For the as-melted V-40Ti-20Cr alloy, TEM characterisation results are shown in figure 5.2(a-d). Figure 5.2(a) shows the bight field micrograph in the diffraction contrast mode where the striated domains similar to those in figure 5.1(a) can be observed. The microstructural appearance is nearly the same as that of V-50Ti alloy. The intensity modulation length scale is ~ 4-5 nm in this case, which is also nearly the same as that of V-50Ti alloy. Figure 5.2(b) shows the corresponding electron diffraction pattern indexed to be along [0 1 3] zone axis of *bcc* structure. The reflections corresponding to the 200 and $23\bar{1}$ type of planes are marked in the figure. Satellite reflections and diffuse intensity are seen in addition to the principal reflections in the diffraction pattern. The lattice parameter calculated from the diffraction pattern is 0.31 nm which is again very close to the reported lattice parameter for the V-50Ti alloy (ICDD # 04-003-2225). For this alloy also the diffraction pattern does not contain any signature for the formation of carbides. The microchemical nature of the striated domains is shown in figure 5.2(c). The map was generated as a colour-composite using energy filtered images recorded for Ti-L, V-L and Cr-L edges. The chemical contrast across the striated domains can be clearly observed. It can also be inferred from the intensities in the EFTEM image that the phase separation event involves only V and Ti, since Cr-L edge intensity varies little across the field of view: a Ti-rich and a Ti-lean phase separate out or in other words, it can also be said that a V-lean and V-rich phase separates out on solidification of the molten alloy. EELS profile from the region is shown in figure 5.2(d) where the energy loss edges corresponding to Ti-L, V-L and Cr-L are marked. Power law model has been used for

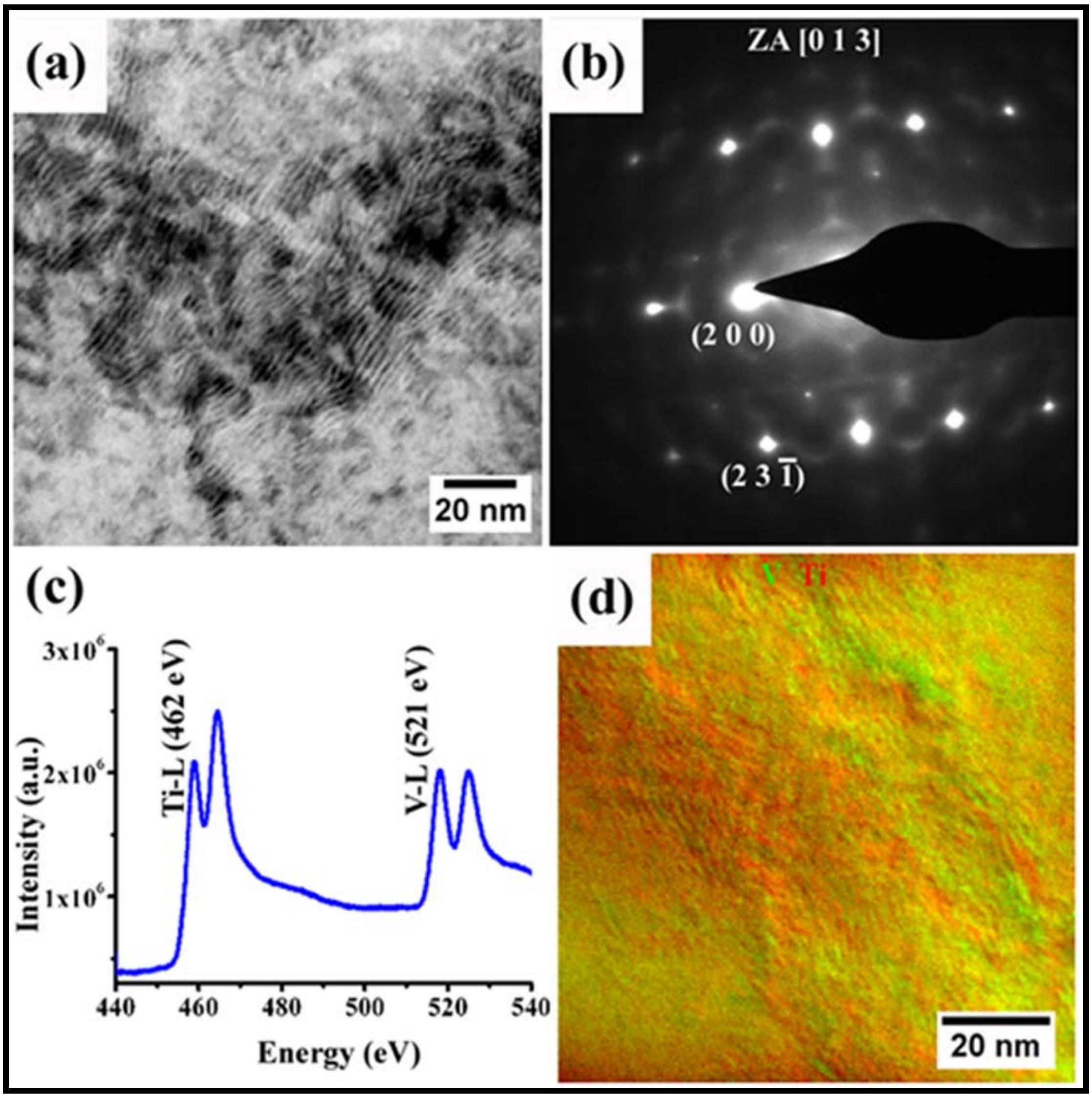

Fig. 5.1: (a) Relatively low magnification bright field micrograph showing the striated regions indicating phase separation in as-melted V-50Ti alloy. (b) Corresponding selected area electron diffraction pattern. Two of the principal reflections are marked in the image. (c) Electron energy loss spectra from the same specimen. Electron energy loss edges corresponding to V-L and Ti-L are shown in the spectra. (d) Energy filtered TEM micrograph showing the chemical distribution of V and Ti in the phase separated domains. V-L signal is shown in green and Ti-L signal in red.

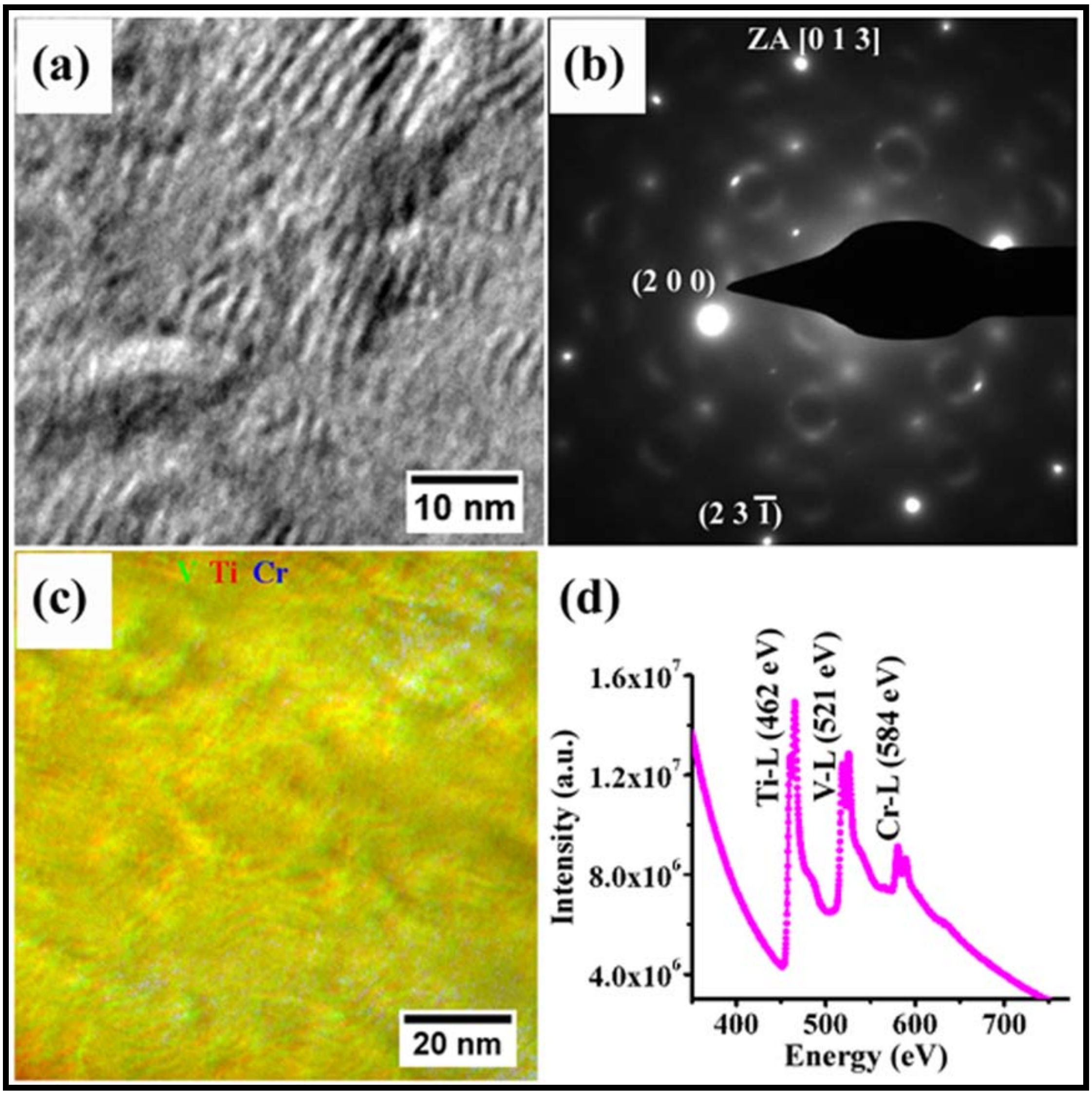

Fig. 5.2: (a) Relatively low magnification bright field micrograph showing the striated regions from the phase separated domain in as melted V-40Ti-20Cr alloy specimen. (b) Selected area electron diffraction pattern along [0 1 3] zone axis from the similar phase separated domain. Two of the principal reflections are marked in the image. (c) Energy filtered TEM micrograph showing the chemical distribution of V, Ti and Cr in the phase separated domains. V, Ti and Cr rich regions are shown in green, red and blue respectively. (d) Electron energy loss spectra from the same specimen. Electron energy loss edges corresponding to Ti-L, V-L and Cr-L are shown in the spectra.

background correction and the composition has been determined to be V-38Ti-22Cr, which is close to the as-melted composition.

To confirm that these striations are generated due to compositional fluctuations and not because of the presence of any secondary carbides or thickness variation of the observed specimen region, EELS studies are carried out for both as melted V-50Ti and V-40Ti-20Cr alloys specimen. Figure 5.3 shows the high-resolution EEL spectra from the phase separated domains of V-50Ti alloy, where the energy loss edges correspond to Ti-L and V-L are marked in the profile itself. Similarly the high-resolution EELS profile from V-40Ti-20Cr alloy specimen is shown in figure 5.4. Moreover, for both the specimen, spectra are acquired with a dispersion value of 0.1eV/channel in the energy range of 250eV to 350eV to check the presence of any energy loss edges corresponding to C-K at 284 eV. However the absence of any energy loss edges at 284 eV confirms that C is not present in the system and these striations are not because of any secondary carbide phases. This is in support of the earlier observations made with the analysis of selected area electron diffraction patterns, which also do not show the reflections correspond to any carbide phases in these alloys.

Thickness determination of the observed specimen regions for both V-50Ti and V-40Ti-20Cr alloys have been carried out using the intensity log ratio method of the acquired zero-loss and plasmon loss EEL profile and is shown in figure 5.5 (a and b) respectively. For both of the specimen t/λ measured as 0.25 and 0.31 respectively which is well below 1 and hence overrules possibility that these striations originated due to thickness variation of the specimen.

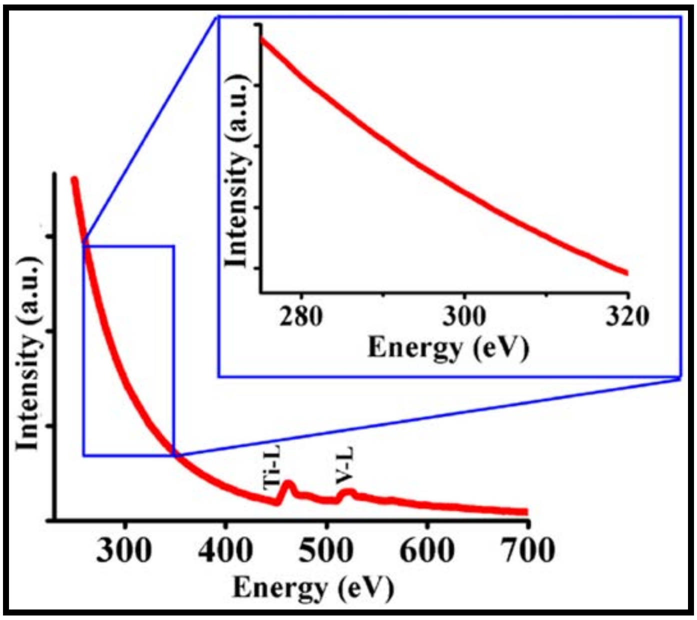

Fig. 5.3: EELS spectrum from the phase separated region of annealed V-50Ti alloy specimen. (inset) high resolution EELS profile does not show any energy loss edge at 284 eV confirming the absence of C in the system.

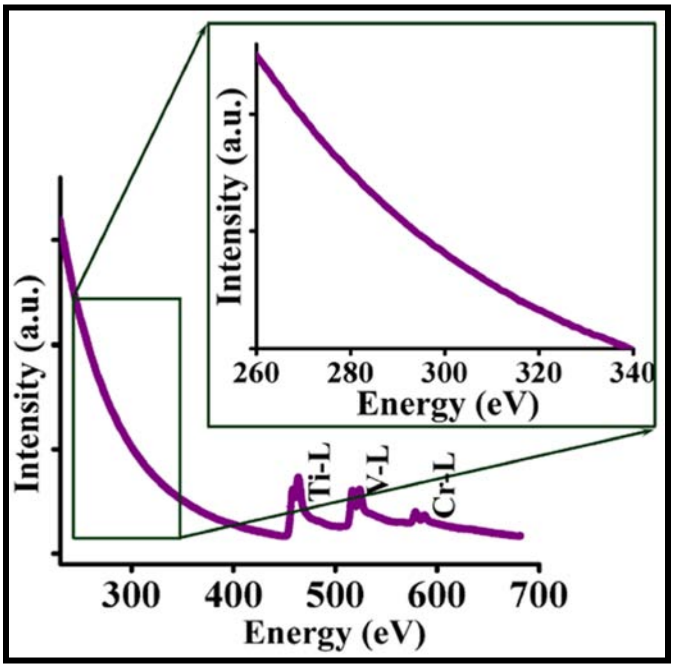

Fig. 5.4: EELS spectrum from the phase separated region of annealed V-40Ti-20Cr alloy specimen. (inset) high resolution EELS profile does not show any energy loss edge at 284 eV confirming the absence of C in the system.

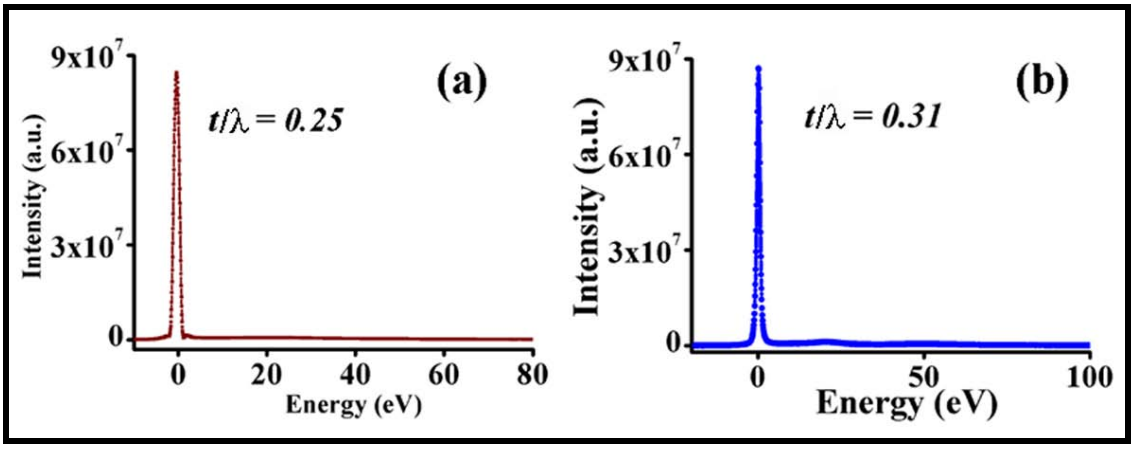

Fig. 5.5: Relative thickness of the observed phase separated domains from both V-50Ti and V-40Ti-20Cr alloy specimen were measured by log ratio method in EELS. The t/λ for both the specimen are measured as 0.25 and 0.31 respectively.

5.3.2: Studies of atomic arrangement and interface modulation along phase separated domains

Phase contrast imaging was carried out to study the structural aspects of the phase separated domains and the interfaces therein. Figure 5.6(a) shows the phase contrast micrograph from a typical phase separated domain of as-melted V-50Ti alloy and the corresponding power spectrum is given in figure 5.6(b). In a similar manner, atomically resolved HRTEM micrograph of the phase separated domains in as-melted V-40Ti-20Cr alloy and its corresponding power spectrum are shown in figure 5.6(c and d) respectively. The power spectra have been indexed to determine that for V-50Ti alloy, specimen region is oriented along [110] zone axis whereas for V-40Ti-20Cr alloy the region is oriented along [111] zone axis; principal reflections marked in figure 5.6(b and d). In the phase contrast micrographs periodic bright and dark intensity variations are still observed over and above the lattice fringes are continuous throughout the phase separated domains. This indicates that the interfaces between the chemically modulated regions are coherent.

This further substantiates the inference of a phase separation event. A common feature observed in both the phase contrast images is that the composition modulation is along the <1 1 0> direction in *bcc* structured matrix.

5.3.3: Role of Cr in binary V-Ti phase transformation: STEM-HAADF and STEM-EELS investigations

The microchemistry of the phase separated domains has been further investigated using STEM-EELS technique. High-angle annular dark field (HAADF) imaging in STEM mode was carried out for both alloys with a detector range of 25 mrad to 150 mrad. The scanning mode allows simultaneous imaging and collection of EELS spectra at / along user defined point, line or region. EELS signal was recorded along a line perpendicular to the composition modulation indicated in the EFTEM data. HAADF image and the corresponding EELS spectra in the fine probe mode from the striations of the V-50Ti as melted alloy specimen are shown in figure 5.7. The corresponding results from the V-40Ti-20Cr alloy specimen are depicted in figure 5.8. In both HAADF micrographs, clear alternate bright and dark fringes can be seen. The HAADF settings used to record the images were optimised for maximal Z-contrast and hence the images in figure 5.7 and 5.8 confirm that the periodic fringes correspond to a composition modulation. EELS spectra from regions within the bright and dark fringes in V-50Ti alloy show that they differ in V content, further confirming that the alloy, on solidification, undergoes phase separation giving rise to compositionally modulated domains. HAADF image, shown in figure 5.8, indicates that the microstructural nature of the phase separated domains is similar to that of V-50Ti alloy. The EELS spectra from the bright and the dark domains are further examined to understand the distribution of Cr

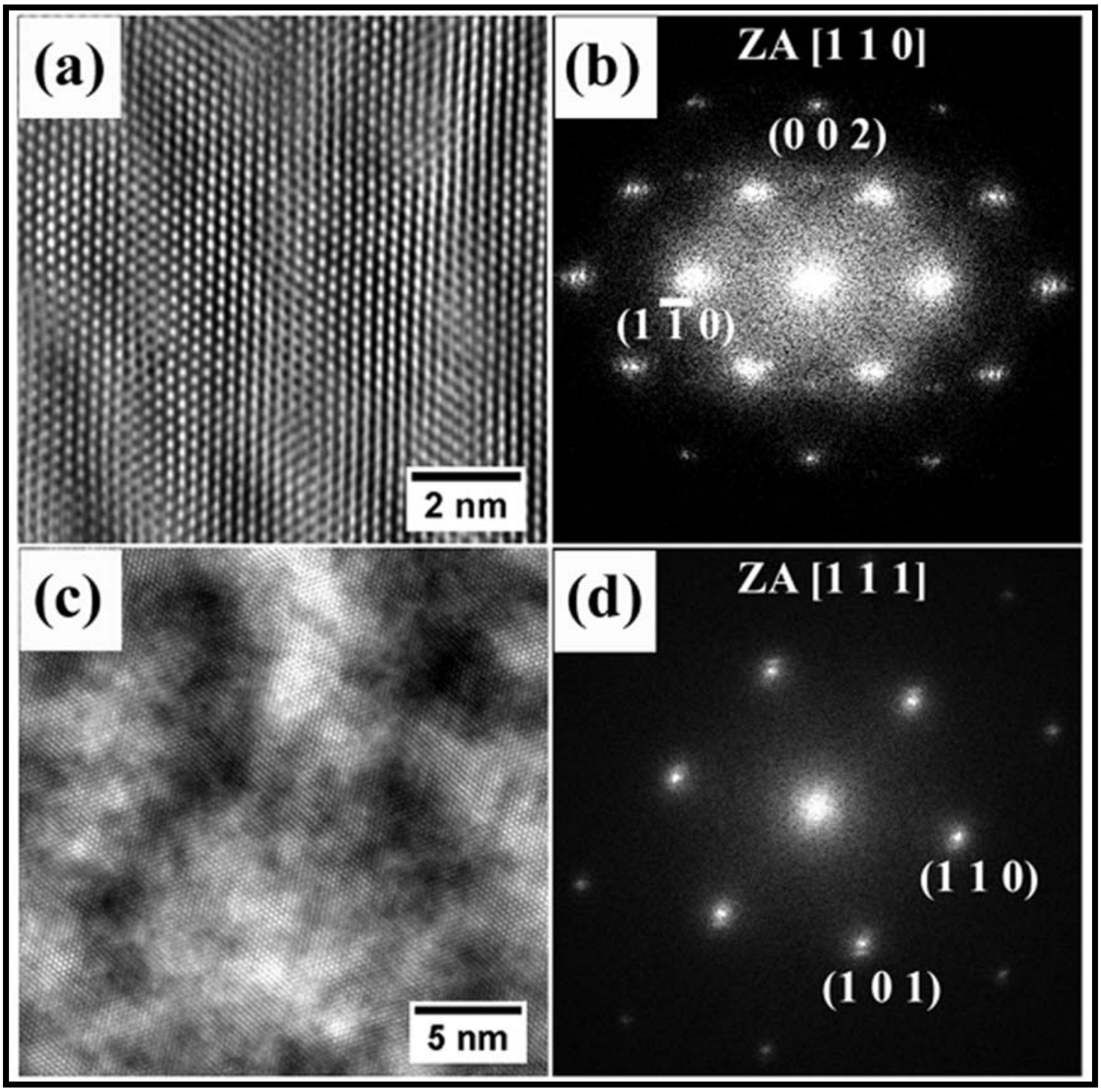

Fig. 5.6: (a) Phase contrast micrograph showing the atomic arrangement along the phase separated domain in as melted V-50Ti alloy. The interfaces between the chemically modulated regions are seen to be coherent and the lattice planes are continuous throughout the phase separated domains. (b) Power spectrum generated from the phase contrast micrograph shown in (a) shows the region to be oriented along [1 1 0]. Two principal reflections are marked in the image. (c) Phase contrast micrograph from the as melted V-40Ti-20Cr alloy specimen. Here also the interfaces between the phase separated domains are seen to be continuous. (d) Corresponding power spectrum shows that the region is oriented along [1 1 1] where two principle reflections are marked.

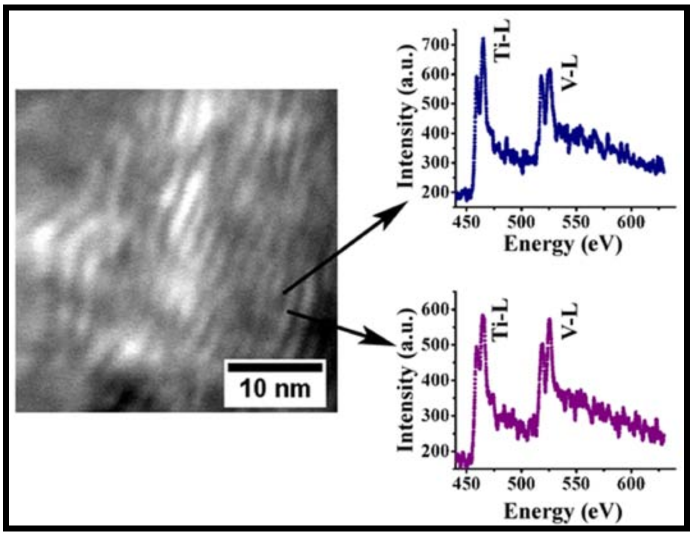

Fig. 5.7: STEM-HAADF micrograph from the as melted V-50Ti alloy specimen showing the average atomic number fluctuation along the striated region. EELS spectrum was recorded in drift corrected profile mode along a direction perpendicular to the striations. Two such fine probe EELS profiles from the dark and bright region show a variation in EEL intensities at the V-L and Ti-L edges.

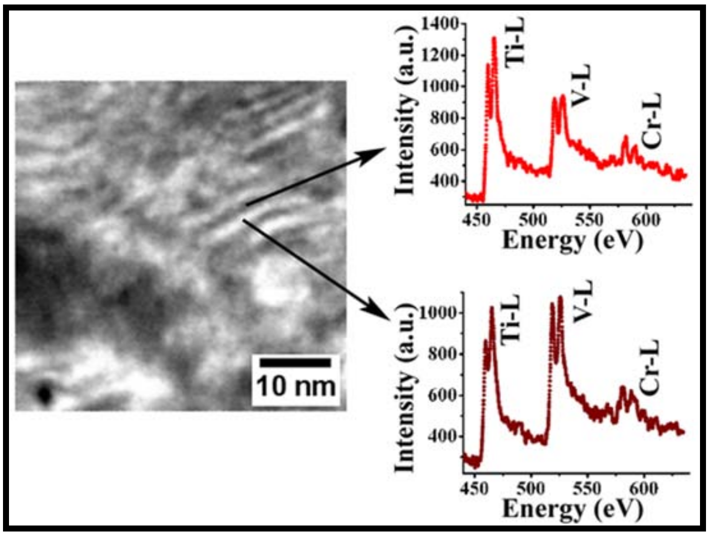

Fig. 5.8: STEM-HAADF micrograph from the as-melted V-40Ti-20Cr alloy specimen showing the average atomic number fluctuation along the phase separated domain. EELS spectrum was recorded in drift corrected profile mode along the perpendicular direction of the striated region. Two such fine probe EELS profiles from the dark and bright region are shown in the image respectively. It is apparent that Cr does not take any significant role in the phase separation event.

in the phase separated domain. Fine probe EELS spectra from the corresponding bright and dark fringe regions indicate that they are V-rich and V-lean. However, electron counts in the Cr-L edge are nearly the same for both. This indicates that V-40Ti-20Cr alloy also undergoes a phase separation upon solidification giving rise to V-rich and V-lean phase with Cr concentration being nearly the same in the two phases. Although the alloy is ternary, the phase separation event is essentially binary.

5.3.4: Effect of thermal aging: Microstructural changes in V-50Ti and V-40Ti-20Cr alloys

As stated earlier, both of these alloys were further heat treated at 750° C followed by ice water quenching. TEM characterisation results from heat treated V-50Ti alloy specimen are shown in figure 5.9(a-d). Figure 5.9(a) shows the microstructure of the phase separated domains in bright field diffraction contrast mode. An interesting feature that can be observed in the micrograph is the appearance of a new intensity modulation over ~ 18-20 nm in the phase separated domains superimposed on the fringes with half wavelength of ~ 3-4 nm, which were seen in the as melted V-50Ti alloy. The nature of the contrast remains same for both of these periodicities. A selected area electron diffraction pattern from the region is shown in figure 5.9(b). The pattern has been indexed as $[\bar{1}13]$ zone axis pattern of pure *bcc* structure. The principal reflections corresponding to 110 and $2\bar{1}1$ type of planes are marked on the diffraction pattern. A closer look into the diffraction pattern reveals that the intensities of the satellites around the major reflections are of higher intensity than in the as-melted alloy, indicating that phase separation reaction has proceeded to a greater extent under thermal ageing.

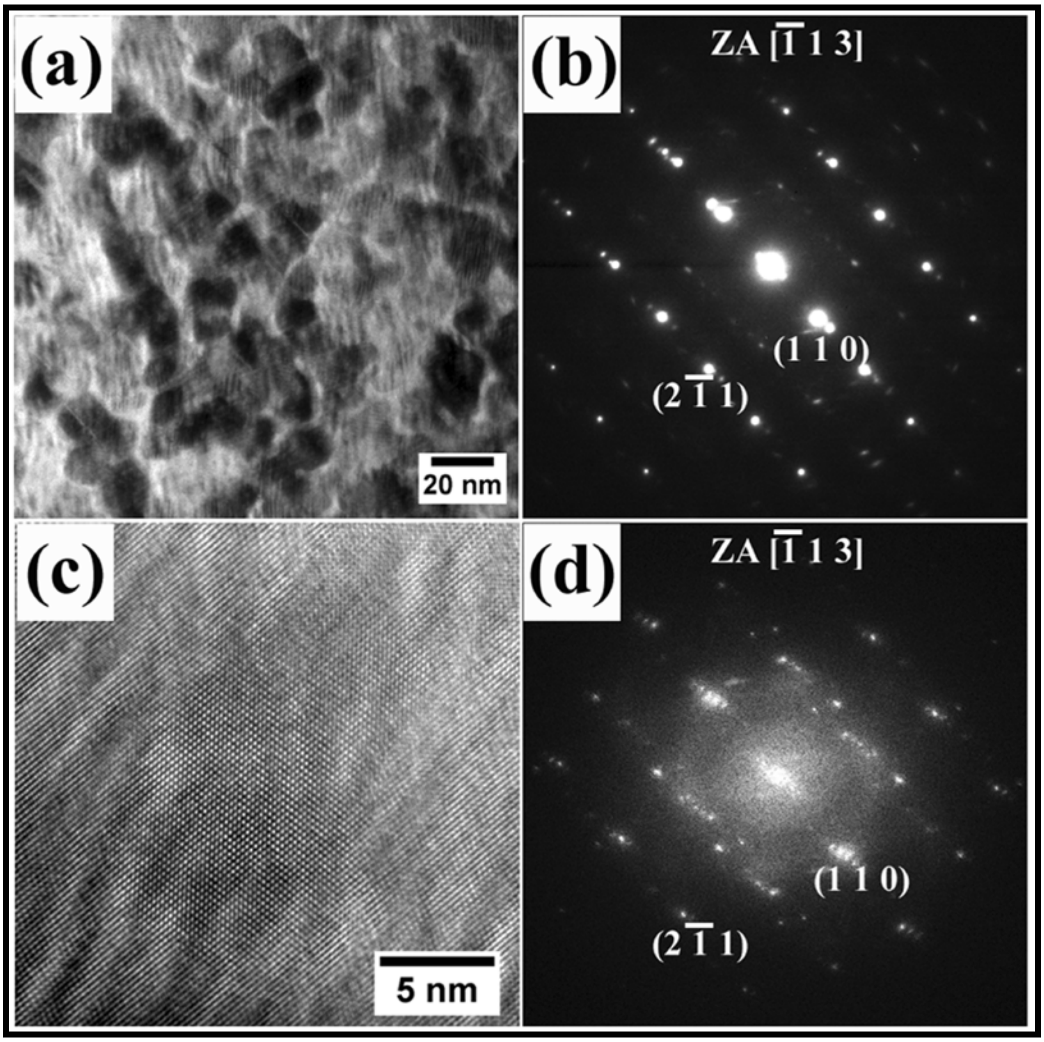

Fig. 5.9: (a) Bright field micrograph from the phase separated domains showing intensity modulation at two wavelengths in aged V-50Ti alloy specimen. The waves are of half wavelength/ modulation length ~ 4-5 nm and ~ 18-20 nm respectively. (b) Electron diffraction pattern recorded from the region. Satellite spots corresponding to the phase separation event are clearly visible in the diffraction pattern. It is evident from the images (a) and (b) that the composition modulation is along the <1 1 0> direction. (c) Phase contrast micrograph showing the interface structure and the atomic arrangement in the phase separated domain. The interfaces seem to be coherent even after ageing. (d) Power spectrum generated from the phase contrast image shows that the region is oriented along [$\bar{1}$ 1 3] zone axis where the principal reflections correspond to 110 and 2 $\bar{1}$ 1 types of planes are shown in the image.

However, the diffuse intensities corresponding to the nanostructured ω domains remain almost same as in the as-melted alloy. The phase contrast image from one such phase separated domain and the corresponding power spectrum are shown in figure 5.9(c-d). The imaging is carried out along $[\bar{1}\ 1\ 3]$ orientation where spots due to 110 and $2\bar{1}1$ planes are marked in the power spectrum. In the phase contrast micrograph, the overall intensity modulation of the phase separated domains is still visible. However, it should also be noted that the lattice fringes are continuous across the domains irrespective of the contrast. This indicates that the interface within the phase separated domains remains coherent in the higher wavelength domains even after thermal ageing.

5.3.5: Estimation of modulation length in chemical fluctuation: EFTEM studies

Energy filtered TEM (EFTEM) studies were also carried out with the aged V-50Ti alloy specimen to study the composition modulation of the phase separated domains. Figures 5.10(a) and (b) show the elemental maps from the fringe regions recorded with V-L (521 eV) and Ti-L (462 eV) edges respectively. The EFTEM maps were taken along $[\bar{1}\ 1\ 3]$ zone axis of *bcc* structured matrix. Three window method of elemental imaging is used to acquire the EFTEM maps where a slit width of 20 eV is used with a collection time of 30 seconds. Three such acquired images were averaged for each elemental map. During the acquisition process, the drift in the microscope was nullified with the in-built auto correlation function. The two pre-edge windows are selected 15 eV and 30 eV ahead of the respective "L" edges while the post-edge window is placed 20 eV beyond the edge. Both V-L and Ti-L elemental maps show the intensity modulation parallel to the <110> *bcc* direction. The curves in figure 5.10(c) represents the modulation profile for V-L and Ti-L edge electron counts as a function of distance, shown in red and green respectively. The elemental profiles are generated along the same line marked in the maps as a red arrow in the V-L map and as a green arrow in the Ti-L map. The average composition modulation is calculated as ~ 18-20 nm, further substantiating the results obtained through diffraction contrast and phase contrast studies. However, the smaller wavelength modulation of ~ 3-4 nm as seen in the diffraction and phase contrast results are suppressed in the EFTEM elemental maps due to the poorer signal to noise ratio in these images relative to the phase contrast image. A colour composite of the maps in figures 5.10(a and b) is shown in figure 5.10(d) where V-rich regions are in red and Ti-rich regions are in green. It is quite evident from the colour composite EFTEM map that a more developed partitioning of elements have occurred to obtain a greater degree of phase separation.

The diffraction contrast and phase contrast results from the heat treated V-40Ti-20Cr alloy specimen are shown in fig 5.11(a-d). Figure 5.11(a) represents relatively low magnification bright field image from a phase separated domain of aged V-40Ti-20Cr alloy specimen. In the micrograph, only one phase separation modulation is observed with modulation length ~ 4-5 nm. Although both V-50Ti and V-40Ti-20Cr alloys were aged in the similar conditions but in contrast to the V-50Ti alloy, the periodicity of modulation has not developed much to give rise to higher degree of phase separation in V-40Ti-20Cr alloy. This is in support of the theoretical predictions made on the basis of Miedema model in earlier reports from the authors' group (Ghosh *et al.*, 2015a) that the addition of Cr reduces the phase separation tendency in binary V-Ti alloy. The electron diffraction pattern from the same region of the specimen is shown in 5.11(b) where the

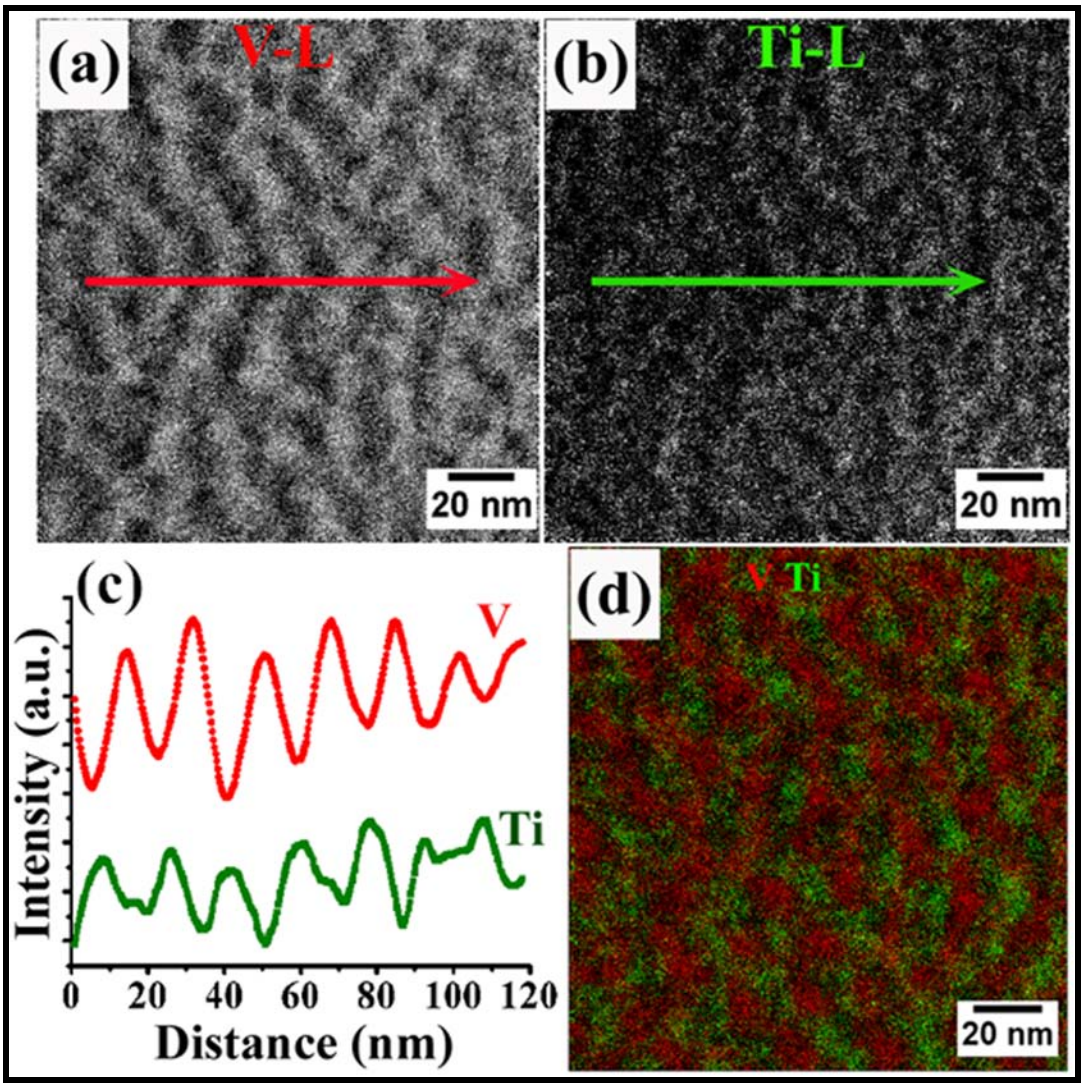

Fig. 5.10: (a) A vanadium EFTEM elemental map and (b) A titanium EFTEM elemental map aquired with V-L and Ti-L energy loss edges respectively from the same region in the aged V-50Ti alloy specimen. Both the maps are taken along $[\bar{1}\ 1\ 3]$ zone axis of the *bcc* phase where the chemical partition is along <1 1 0> direction. (c) The compositonal fluctuation of vanadium (in red) and titanium (in green) along <1 1 0> direction of the *bcc* matrix. The profiles are generated from the same region of both the maps as marked by red and green arrows respectively in V-L and Ti-L maps. The average modulation length for both the fluctuation waves are ~ 18-20 nm. (d) Colour composite of the V-L and Ti-L EFTEM maps shown in (a) and (b). Chemical partitioning of vanadium and titanium are clearly evident from the image.

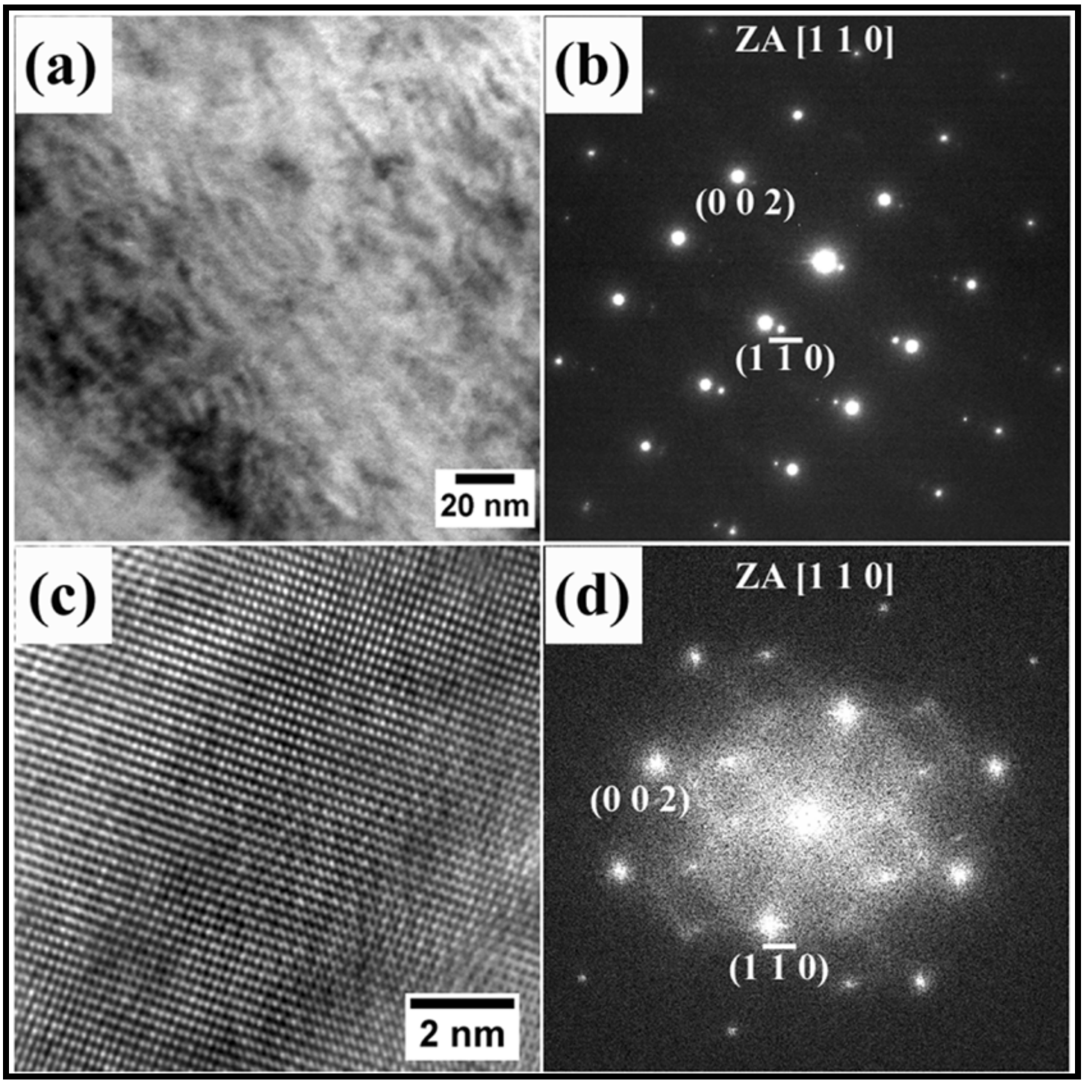

Fig. 5.11: (a) Bright field micrograph from the aged alloy showing the phase separated domains in aged V-40Ti-20Cr alloy specimen. Here only a single fluctuation wave corresponding to ~ 4-5 nm of modulation periodicity is visible. (b) Electron diffraction pattern recorded from the same region shows that the specimen is oriented along [1 1 0] zone axis. It is evident that the phase separated domains are oriented normal to <1 1 0> direction. (c) Phase contrast micrograph showing the interface structure and the atomic arrangements in the phase separated domains. The interfaces are coherent even after aging. (d) Power spectrum generated from the phase contrast image showing the reflections corresponding to 002 and 1 $\bar{1}$ 0 types of planes along [1 1 0] orientation of the specimen.

satellite spots along the principal reflections are clearly visible. The pattern is indexed as [1 1 0] zone axis of *bcc* where 002 and $1\bar{1}0$ types of reflections are marked in the image. Fig 5.11(c-d) represent the high-resolution electron micrograph of the phase separated domain and the corresponding power spectrum. As seen earlier in the case of V-50Ti alloy, here also the lattice fringes are continuous across phase separated domain interfaces indicating the coherency of the interfaces. Power spectrum confirms that the phase contrast image is taken along [1 1 0] orientation of the specimen, where the periodicities due to $1\bar{1}0$ and 002 types of planes are marked in the image. Here too, the compositional modulations of the phase separated domains are parallel to the <1 1 0> direction of the *bcc* matrix.

5.4: Spinodal decomposition *vis-a-vis* nucleation and growth: A comparative study with respect to V-Ti and V-Ti-Cr alloys

5.4.1: Basic understanding of spinodal decomposition and nucleation and growth

The microscopy evidences along with the microchemical analysis unambiguously prove the occurrence of a phase separation event for alloys of compositions V-50Ti and V-40Ti-20Cr. Such a transformation could occur either by classical nucleation and growth mechanism or by spinodal decomposition. In order to analyse the phase transformational aspects in these alloy systems, it is required to understand the detailed mechanism of such processes.

In literature, the spinodal decomposition is described as small in degree but large in extent, whereas, the nucleation event is large in degree but small in extent. In case of spinodal, attraction between like atomic species is large so that the flux of each individual species is against its concentration gradient. This results an increase in concentration in cluster and creation of a depletion zone in the surroundings. The individual like species which are situated in the outer zone of this concentration gradient now also senses the concentration gradient and the cluster formation, but as they are away from the original cluster, it is practically impossible for them to participate in the same cluster formation. However, because of their short-term interaction, they sense the depleted zones in their neighbourhood and want to move away from it, creating a new cluster a short distance away from the original one. Hence a rapid formation of periodic clusters of almost similar concentration takes place (Butler and Thomas, 1970; Livak and Thomas, 1971). On the contrary, in case of classical nucleation and growth the attraction between the similar species is not strong enough to cause the flux up the concentration gradient, but strong enough to create a supercritical nuclei over a localized composition fluctuation. The generated fluctuations grow spontaneously down the concentration gradient and finally develop a supercritical nuclei or embryo in the vicinity of large heterogeneous phases. In the early stages, the compositional fluctuations are of relatively low amplitude and more spatially extended with diffused interface among the compositionally partitioned phases. Gradually they evolve into a distinct two phase mixture. Moreover, in case of nucleation and growth process it is the chance fluctuations or certain heterogeneity to which the individual species are attracted. However, in case of spinodal mechanism these heterogeneities do not have any significant contribution and only the uphill diffusion along the concentration gradient only discriminate between the two mechanisms.

5.4.2: Microstructural evidences in support of spinodal decomposition

It has already been stated that phase separation in the V-50Ti alloy results in the formation of two immiscible phases. These phases are similar in structure but differ in composition (one is Ti rich and the other is Ti lean) and could occur either by nucleation and growth or by spinodal decomposition mechanism. The former is dominated by the conventional long range downhill diffusion process whereas spinodal decomposition occurs through short range uphill diffusion. In the present section a qualitative explanation is presented to understand these mechanisms and also to identify the mechanism that is dominant for the present phase separation process.

In a series of phenomenal works, Cahn had postulated two aspects of spinodal mechanism (Cahn, 1961, 1968). First, the product phases are crystallographically identical to the parent phase, differing only in composition. The second aspect is that the product phases form in a continuous process from the parent solid-solution one. This implies that both the product phases should be coherent and lattice planes should also remain continuous (Cahn, 1962). Another interesting feature associated with the spinodal decomposition mechanism is the association of the elastic energy. Cahn and Hilliard (1958, 1959) proposed that in case of the spinodal free energy calculation, along with the conventional free energy terms, the elastic energy term provides significant contribution. The conventional free energy curves and free energy diagrams are defined for the unstressed homogeneous phases and can be used to calculate the free energies for an unstressed mixture of phases. However in case of a coherent mixture, the free energy is increased by a reversible elastic work which is needed to match the lattices. The quantum of elastic work or in other words the coherency strain does not depend on the interface of the phase separated domains; rather, they are mainly governed by relative fractions of the two phases.

In the present study the microstructural and the microchemical investigations of the phase separated regions indicate the mechanism as a spinodal decomposition dominated process. Figure 5.12(a-c) represents three snapshots of the phase separation event in the binary V-50Ti alloy. In an earlier stage of the phase separation, in the as melted condition, the ~ 4-5 nm modulation length dominates as shown in figure 5.12(a). Subsequently, another modulation wavelength of ~ 18-20 nm is seen to initiates (figure 5.12(b)) and still later this longer modulation length is seen to be the only one which exists in the system (figure 5.12(c)),The composition modulation with the two wavelengths are seen to overlap in some regions and such regions extend spatially over significantly large specimen region. These characteristics of the observed compositional modulation over crystallographically similar phases confirm that the observed features correspond to spinodal decomposition and not a nucleation and growth dominated process. Similar conclusions have been drawn in literature (Westraadt *et al.*, 2015; Müller *et al.*, 2015; Sheibani *et al.*, 2014).

Another clue to the present data representing spinodal decomposition is in the directionality of the composition modulations. In a spinodal decomposition process, the elastic effect influences domain morphology by favouring modulations along specific elastically soft crystallographic directions. At the initiation of the process, though fluctuations are generated isotropically, only selected waves persist with time and eventually predominate. In cubic systems two elastically soft directions are <1 0 0> and <1 1 1> (Cahn, 1968). In case of a compositional modulation along <1 0 0>,

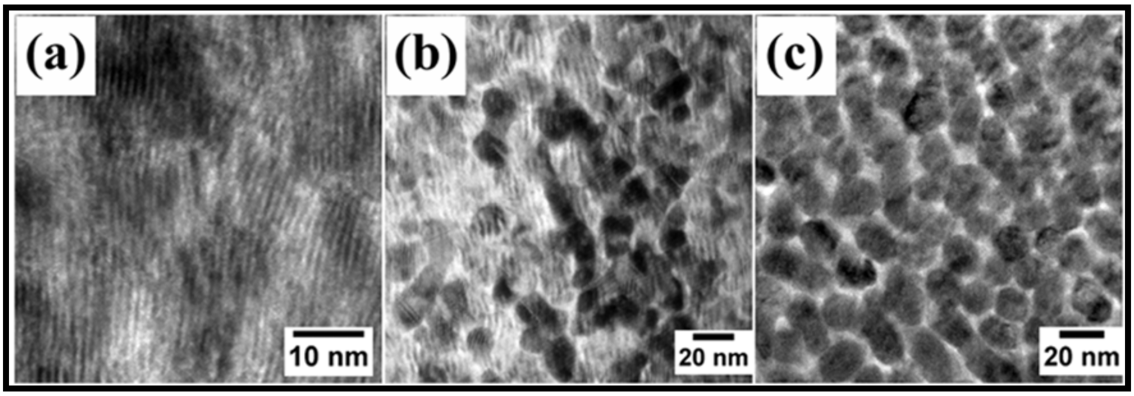

Fig. 5.12: (a-c) Phase separated microstructure showing the fluctuation wave from V-50Ti alloy specimen. (a) shows the compositional fluctuation from as melted alloy where the average modulation length is ~ 4-5 nm. (b) and (c) are from the aged alloy where (b) shows two different modulation lengths of ~ 4-5 nm and ~ 18-20 nm. Whereas in (c) only the fluctuation wave with modulation length ~ 18-20 nm dominates.

superposition of sinusoidal waves of equal amplitude and wavelength leads to a partitioning along the three orthogonal <1 0 0> directions. However, when the composition modulation occurs along the elastically soft <1 1 1> directions, the situation is slightly complicated since mutual interactions between the fluctuation waves along the four equivalent directions have to be considered. Interaction between two <1 1 1> fluctuation waves result in a maxima along the common <1 1 0> directions. And consequently, the other two <1 1 1> fluctuation wave generate the periodic variation among them. Overall, a composition fluctuation wave along any of the four <1 1 1> equivalent directions result in composition modulation along any of the six <1 1 0> directions (Fratzl *et al.*, 1999; Findik, 2012).

5.5: Microscopic investigations of ω structured domains in binary V-50Ti and ternary V-40Ti-20Cr alloys

Both V-50Ti and V-40Ti-20Cr alloys have been investigated to study the morphology of the nanosized ω phase and its crystallographic relations with the *bcc* matrix. Figure 5.13(a-d) present a collage of selected area diffraction patterns from as-melted V-50Ti alloy. The diffraction patterns are recorded along $[\bar{1}\ 1\ 2]$, [0 1 3], [0 1 2] and [0 0 1] directions in the *bcc* matrix. Two principal reflections are marked in each diffraction pattern. The reflections corresponding to ω phase are not sharp and distinct. Rather a diffused arc shaped contrast arises associated with the ω reflections. The selected area electron diffraction patterns from the aged and ice water quenched V-50Ti specimen are shown in figure 5.14(a-c). The diffraction patterns are acquired along $[\bar{1}\ 1\ 3]$, [1 1 0] and [0 1 3] zone axis of the *bcc* phase. The reflections correspond to 110 and $2\bar{1}1$ type of planes are marked in $[\bar{1}\ 1\ 3]$ zone axis pattern. In the similar way, 002 and $\bar{1}10$ types of reflections are marked in [1 1 0] zone axis pattern and $23\bar{1}$ and 200 types of spots are marked in the [0 1 3] zone axis pattern. The arcs-like diffused intensities are still present across the diffraction pattern. However the ω reflection spots become more prominent and distinct in the aged V-50Ti specimen. The experimentally measured lattice parameters for the ω phase from the diffraction pattern turn out to be a= 0.46 nm and c= 0.28 nm which are very close to the reported values of those in V-Ti system, which are a= 0.455 nm and c= 0.278 nm (Banerjee and Mukhopadhyay, 2004).

The dark field images recorded with the ω reflection spots in as melted as well as aged V-50Ti alloy specimen are shown in figure 5.15(a-d). Figure 5.15(a-b) represents

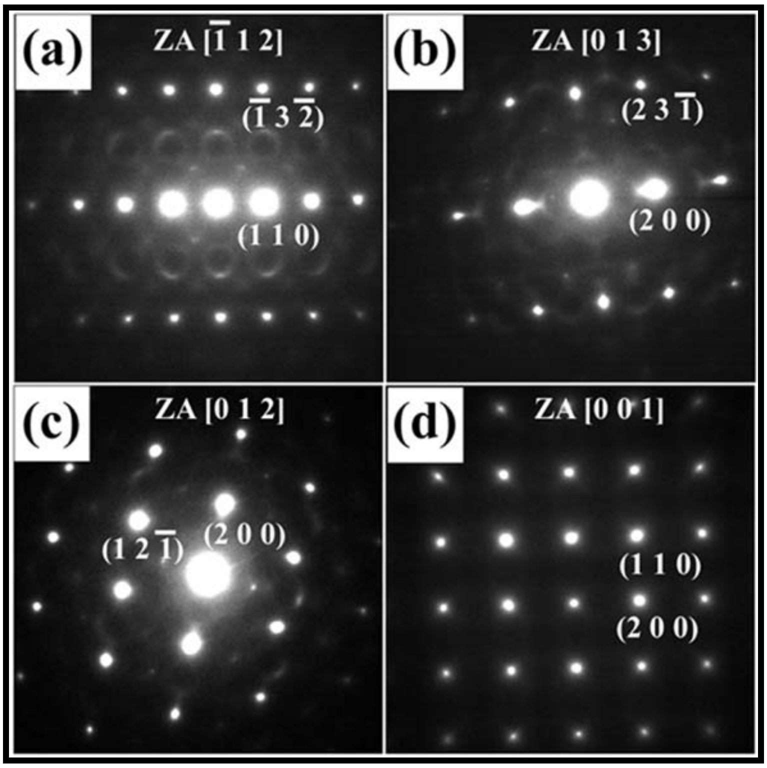

Fig. 5.13: (a-d) Collage of electron diffraction patterns along [$\bar{1}$ 1 2], [0 1 3], [0 1 2] and [0 0 1] zone axis of *bcc* phase in as melt V-50Ti alloy. Two principal reflections are marked in all the images. The diffused intensities corresponding to the reflections from ω structures can be seen in all the diffraction patterns.

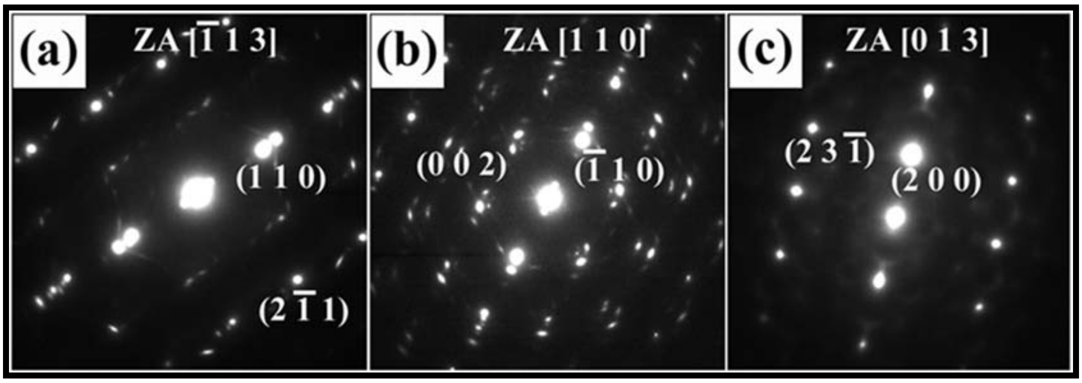

Fig. 5.14: (a-c) Collage of electron diffraction patterns along [$\bar{1}$ 1 3], [1 1 0] and [0 1 3] zone axis of *bcc* phase in aged V-50Ti alloy. Two major principal reflections are marked in all the images. The additional reflections corresponding to the ω structures can be seen in all the diffraction patterns.

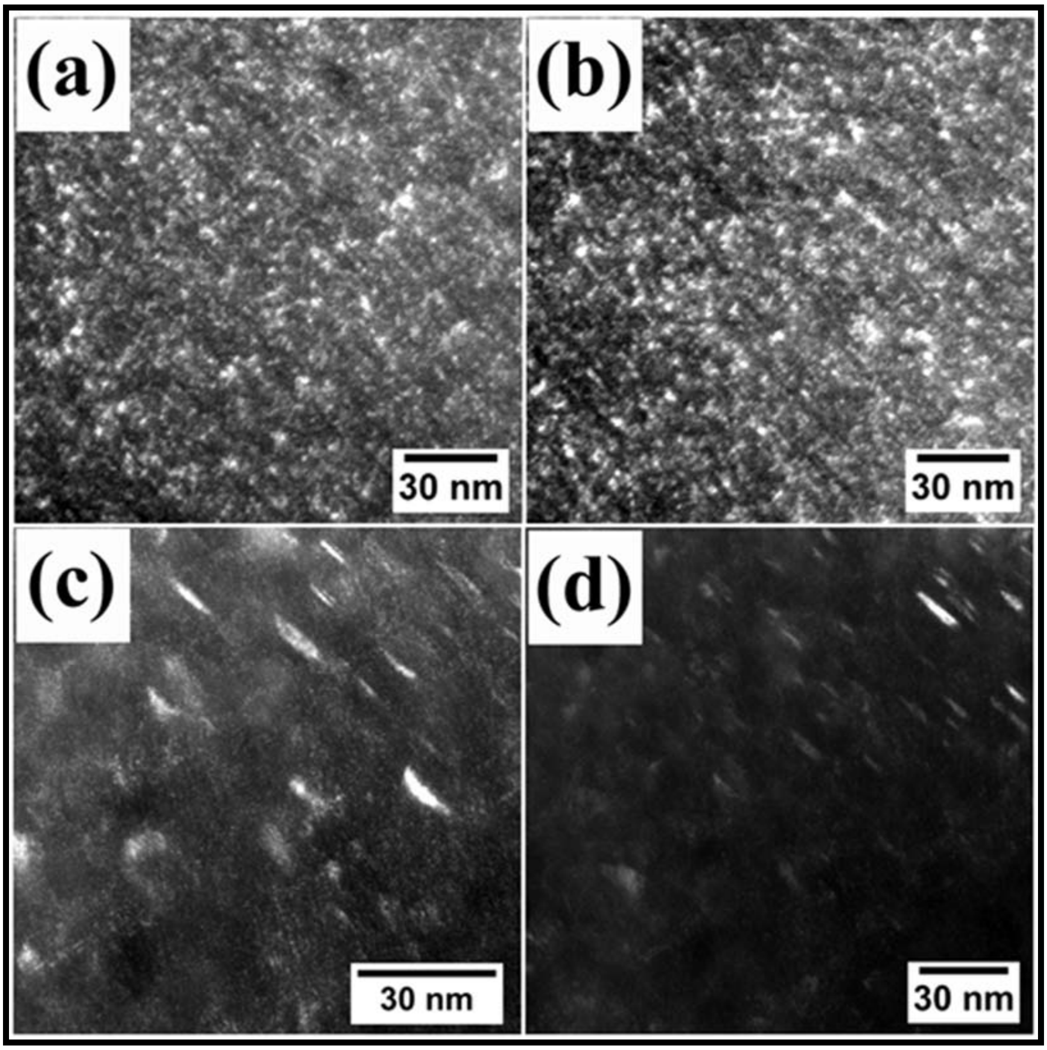

Fig. 5.15: (a-b) Dark field images from the as-melted V-50Ti alloy showing the size and distribution of the ω particles in the matrix. They are athermal in nature. (c-d) Dark field images from the aged V-50Ti alloy showing the morphology of the nanostructured ω particles. The particles are of elliptical shape indicating that they are isothermal ω.

the dark field micrograph from the as melted V-50Ti specimen whereas; figure 5.15(c-d) represents the same from aged V-50Ti alloy. The characteristic mottled contrast from the nanoscale precipitates of the ω phase can be seen in dark field images from as melted V-50Ti specimen. The ω particles are homogeneously distributed throughout the matrix with an average size of ~ 3-4 nm. The dark field images from the aged V-50Ti alloy show well developed and relatively coarser ω particles. The particles have an elliptical morphology in two-dimensional projection where the major axis measures ~ 10-12 nm and the minor axis ~ 3-4 nm. Further observation from the aged V-50Ti alloy dark field micrograph indicates that the ω particles are arranged in a linear array along their major axis and each of the columns are separated by a distance of ~ 12-15 nm.

Systematic study of selected area electron diffraction patterns along different zone axes have been carried out for V-40Ti-20Cr alloy specimen also. Figure 5.16 shows the Möbius triangle generated from the various zone axis diffraction patterns of as melted V-40Ti-20Cr alloy. The acquired diffraction patterns along the zone axes of [1 1 1], [1 1 3], [$\bar{3}$ 1 0], [0 1 2] and [0 1 1] are shown at their relative position on a schematically indexed Kikuchi pattern for *bcc* systems. Apart from the [1 1 1] zone axis pattern the diffuse arc shaped intensities are visible in all the other zone axis patterns. Diffuse intensity in the [1 1 1] type of pattern is absent as the collapse takes place along <111>. Figure 5.17(a-d) represents the structural aspects of the ω phase and the corresponding phase contrast microscopy results. The atomic structure model for a pure *bcc* structure projected along [1 1 0] zone axis is shown in figure 5.17(a). The <1 1 0>, <2 0 0> and <1 1 1> directions of *bcc* structure are marked in the figure along with the schematic of the stacking layers of A, B and C of *bcc* phase. During *bcc* to ω transformation process, a systematic collapse occurs along <1 1 1> direction of *bcc* which results in the atomic level rearrangement of the B and C layers. In case of ideal ω transformation the B and C layers collapse towards each other along <1 1 1> direction, resting at plane halfway between the original B and C stacking layers. This transformation gives rise to the ideal

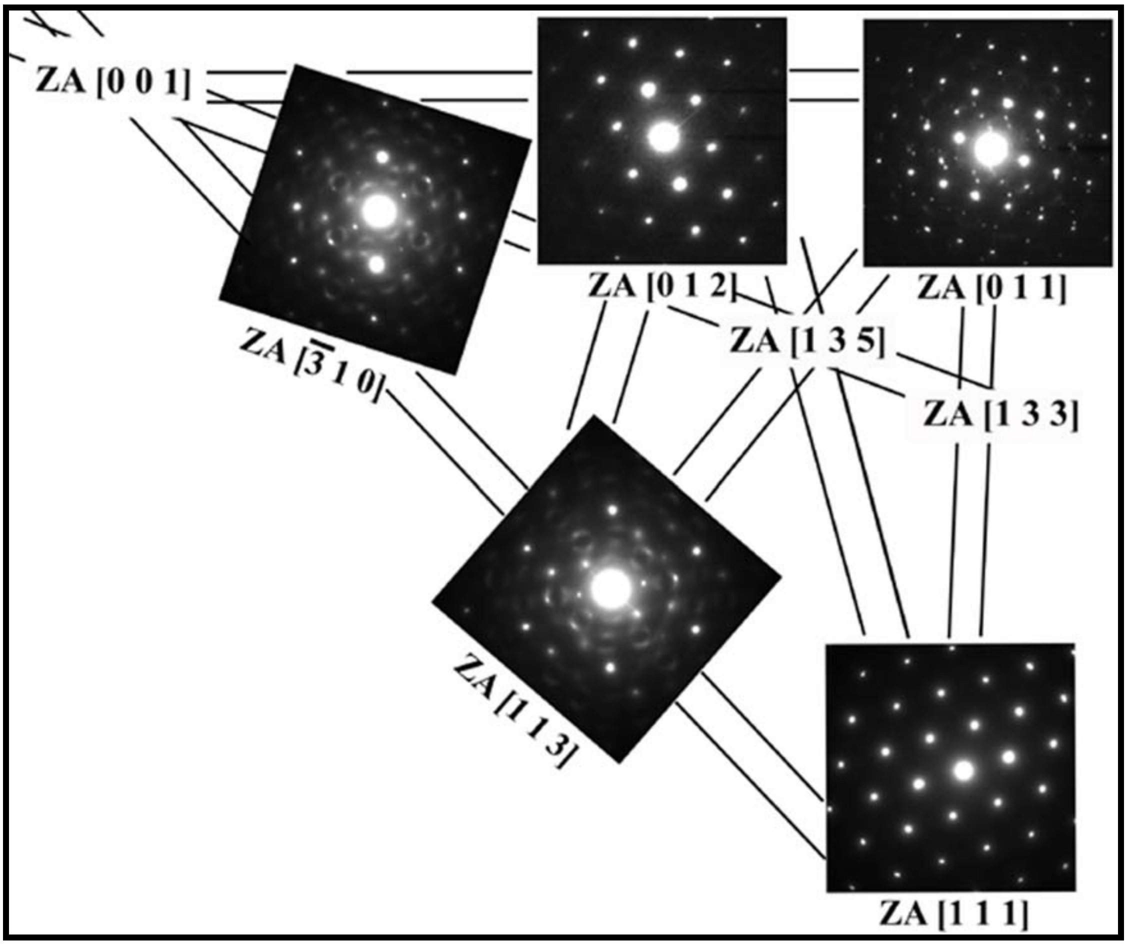

Fig. 5.16: A series of electron diffraction patterns along [1 1 1], [1 1 3], [$\bar{3}$ 1 0], [0 1 2] and [0 1 1] zone axes of *bcc* structure in as melted V-40Ti-20Cr alloy specimen. The diffused intensities corresponding to the ω structures can be seen in all the images except [1 1 1] zone axis pattern. All the diffraction patterns are shown in their respective positions in a schematic stereographic projection.

hexagonal structure as shown. However, in most situations the collapse is incomplete, resulting in a ω phase with trigonal symmetry. Hence, a systematic scan along the traces of 200 types of planes can indicate whether the collapse is partial or complete. Figure 5.17(b) shows the atomically resolved *bcc* structured phase of aged V-50Ti alloy specimen where the specimen is oriented along [1 1 0] zone axis. The distance between two atoms along 200 types of planes is measured to be 0.16 nm as expected for a cubic system having the lattice parameter a = 0.32 nm. This implies a value of 0.48 nm for the distance between four consecutive atomic columns. However the situation does not remain the same for the nanostructured ω shown in figure 5.17(c). As stated earlier, in case of ω transformation, the B and C stacked atomic columns tend to come in a single plane resulting in an atomic level rearrangement along 200 types of planes. One such unit of collapsed ω structure is shown in the figure where the two collapsed atomic columns are surrounded by four corner atomic columns. Further analysis shows that though the distance between four successive atomic columns is 0.48 nm, the individual distances between the second and the third atomic columns is reduced to 0.11 nm due to the partial atomic collapse. Hence the structure is giving rise a trigonal symmetry. The power spectrum generated from the phase contrast image is shown in figure 5.17(d). It clearly indicates that the region is oriented along [1 1 0] zone axis of the *bcc* structured phase. The diffuse arcs correspond to the nanostructured ω phase are also clearly visible in the image.

Structural imaging of ω is attempted along $[\bar{1}\ 1\ 3]$ zone axis of *bcc* and one such combination of the phase contrast micrographs from *bcc* phase along $[\bar{1}\ 1\ 3]$ zone axis, nanostructured ω phase along $[1\,\bar{2}\ 1\ 3]$ zone axis and the corresponding power spectrum from aged V-50Ti alloy specimen are shown in figure 5.18(a-c). The traces of the 110 type of planes are clearly visible in the micrograph corresponding to the *bcc* phase. Moreover, the planes are continuous throughout without any visible change of the atomic contrast. However, for figure 5.18(b) the atomic structural contrast appears quite different

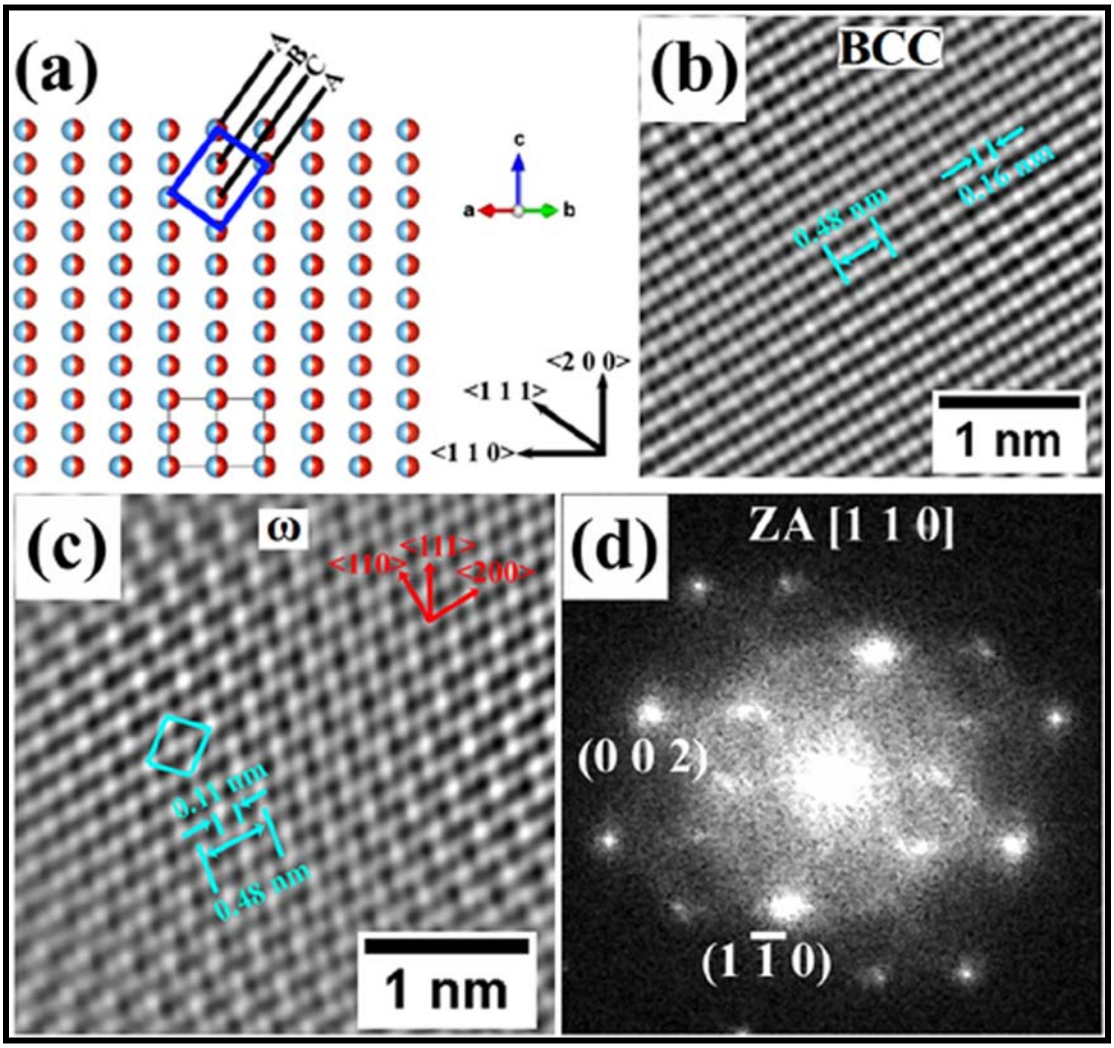

Fig. 5.17: (a) Schematic of the atomic arrangement along [1 1 0] zone axis of *bcc* structure. The stacking sequence of A, B and C and the collapse direction along <1 1 1> are marked in the image. (b) Phase contrast micrograph showing the atomic arrangement along [1 1 0] orientation of a *bcc* phase in an aged V-50Ti alloy specimen. (c) Phase contrast micrograph showing the partially collapsed ω structure with trigonal symmetry. A unit of the ω structure is marked in the image itself. (d) Power spectrum generated from the phase contrast image shows the diffused reflections correspond to ω structured phase along [1 1 0] orientation of the specimen.

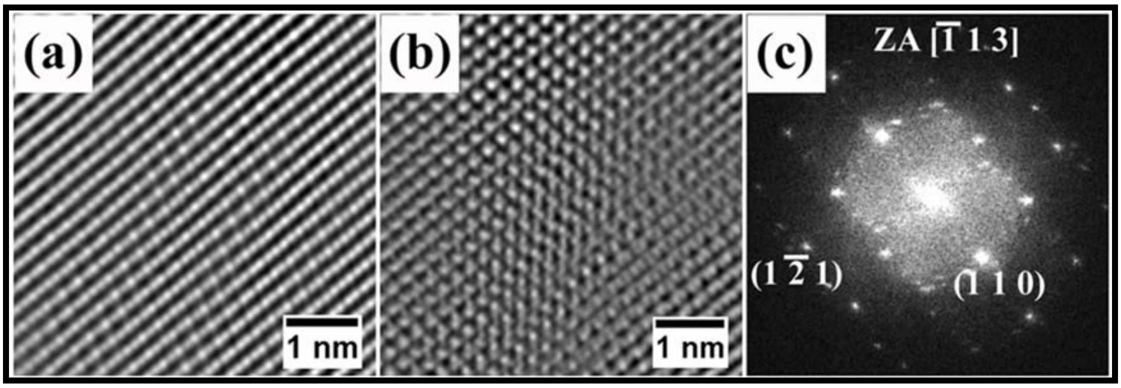

Fig. 5.18: (a) Phase contrast micrograph showing the atomic arrangement along $[\bar{1}\ 1\ 3]$ orientation of a *bcc* structured phase in an aged V-50Ti alloy specimen. (b) Phase contrast micrograph showing the ω structure along $[1\ \bar{2}\ 1\ 3]$ zone axis. The characteristic 'jagged' contrast of the ω structure is clearly visible in the micrograph. (c) Power spectrum confirms the orientation of the specimen as $[\bar{1}\ 1\ 3]$ where the principal reflections correspond to 110 and $2\ \bar{1}\ 1$ types of planes are marked in the image.

from the pure *bcc* phase. Here the triangular zig-zag type atomic contrasts substantiates that the contrast is indeed from a ω like embryo. Power spectrum recorded from the region is shown in figure 5.18(c) where the reflections due to 110 and $1\ \bar{2}\ 1$ type of planes from the *bcc* phase are marked in the image itself.

Formation of ω–phase is not favoured at the nominal alloy compositions of V-50Ti and V-40Ti-20Cr. However, based on the experimental results, a mechanism can be proposed for the formation of the ω embryos in the *bcc* matrix. As has already been stated, on solidification, the instability in the *bcc* phase manifests itself as compositional modulation. This phenomenon leads to phase separation which in turn gives rise to Ti rich and Ti lean regions. This has already been substantiated through EFTEM results and it is further quantified through STEM-EELS techniques. The details of the micrographs (figures 5.7, 5.8 and 5.10) showing the compositional partitioning and the spinodal decomposition process has already been discussed earlier. The compositional fluctuations increases with aging treatment, which in turn increases the modulation length of the phase separated domains. The compositional partitioning leads to the Ti-rich cluster formation and eventually a structural instability is generated within itself. This further relaxes down through the initiation of the collapse of [1 1 1] *bcc* planes forming the embryonic ω structure.

In the light of the present discussion it can be explicitly said that for V-50Ti and V-40Ti-20Cr alloys, phase separation of the *bcc* phase acts as a precursor to the precipitation of ω phase. In the literature almost in all the cases where the ω precipitation in Ti-V alloys has been observed are with vanadium concentration ≤ 20 wt.% (Ng *et al.*, 2011, Ramsteiner *et al.*, 2008, Banerjee and Mukhopadhyay, 2004, Banerjee *et al.*, 2003) and the studies regarding the ω phase transformation in the higher V side are relatively sparse. In the present thesis, alloys with nominal compositions of V-50Ti and V-40Ti-20Cr have been considered to study the feasibility of phase separation and ω transformation. For these present set of alloys, the existence of a miscibility gap has been already confirmed through thermodynamic calculations as shown in chapter 3. This miscibility gap has been shown experimentally to manifest as phase separation reaction in the V-50Ti alloy resulting in the formation of Ti-rich and Ti-lean phases. Composition of these Ti-rich domains falls within the ω phase regimes. Based on the known features of the Gibbs free energy – composition curve that results in a phase separation, the miscibility gap has been represented as a region with positive enthalpy of mixing. An infinitesimal compositional fluctuation in this region can trigger a phase separation reaction towards the energy minimization resulting in the formation of two compositionally different domains - one in Ti-rich and another in Ti-lean side. There would be a composition in this energy landscape where the *bcc* and ω free energy curves intersect satisfying the criteria as $\Delta G_{bcc} = \Delta G_{Omega}$. The phase separation in *bcc* phase progresses till this point and beyond this the ω precipitation in the Ti-rich phase becomes thermodynamically feasible. Beyond this intersection point, the Ti-rich regions become susceptible to structural instability and subsequently undergo a partial collapse of 111_{bcc} planes leading to formation of ω like embryos. Further progress of this phase reaction depends on the applied thermal conditions at that stage. This has been schematically shown by earlier researchers, particularly Devaraj *et al.* (2012) and Nag *et al.* (2011) in case of Ti-Mo alloys. A comprehensive analysis regarding the free energy landscape as a function of atomic shear in case of Ti-Nb alloys has been given by Lai *et al.* (2015). In the present context it is worth mentioning that the ω precipitation phenomena are highly dependent on the alloy chemistry. In case of V-Ti alloy, it can unambiguously be claimed that the phase separation of the *bcc* phase acts as a precursor of the ω precipitation. However, the generalization of similar claim to other ω forming systems requires extensive studies.

Another interesting aspect of the present study is the diffuse intensity distribution in the electron diffraction pattern along with deviation of the ω reflections from their ideal positions. One of the main reasons for the diffuse intensity in the reciprocal space is the presence of atomic planes with different extent of collapse in the real space.

Deviation from ideal ω structure results because the system may have moved away from the region of relative ω stability in the phase diagram either along the composition or the temperature axis (McCabe and Sass, 1971; Banerjee and Mukhopadhyay, 2004). For the ideal ω structure, the ω reflections should positioned around 1/3rd and 2/3rd distance of the line joining the centre and 112 type of *bcc* spots along [1 1 0] zone axis. However, in the present case, all diffraction patterns show arc shaped diffused intensity and the intensity maxima are located in slightly different positions from the ideal ω positions. Stability of the ω phase is decided upon the composition of the *bcc* stabilizer which is V in the present case. Moreover, with the increase in the *bcc* stabilizer, the formation tendency of the ω-phase reduces. The diffused arcs of the ω reflection can be generated because of its departure from the *bcc* to ω athermal transition temperature M_s (*bcc* → ω) also. The kinetics of the *bcc* to ω transformation is another interesting aspect of the present work which needs to be discussed here. *bcc* to ω transformation occurs under two different conditions; one during quenching from the *bcc* phase field and the other during isothermal holding of the alloy just below the *bcc* to ω forming temperature, which is ~ 780° C for binary Ti-V alloys. Both of the domains can be identified based on their salient characteristic feature. The ω which forms directly on quenching from the *bcc* phase field is athermal in nature. The athermal ω initiates at a very high quench rate where the diffusion of the atoms is not feasible. In the reciprocal space they give rise to diffuse intensity which transforms into sharp and definite ω reflections over further thermal treatment. The other type of ω is termed as the isothermal ω, where nanostructured ω particles grow within the *bcc* matrix during ageing at a temperature below the *bcc* → ω transformation temperature. These precipitates are usually elliptical in shape as a consequence of interfacial strain energy minimization. In the reciprocal space also the diffusivity in the arcs reduces and distinct ω reflections appear because of the increase in the volume fraction.

Present studies also demand a comprehensive discussion regarding the composition range over which ω phase is encountered in V-Ti and V-Ti-Cr alloy system. Over the last four decades several researchers have studied on ω phase transformation in Ti-V alloys (Ng *et al.*, 2011, Ramsteiner *et al.*, 2008, Banerjee and Mukhopadhyay, 2004, Banerjee *et al.*, 2003, Sikka *et al.*,1982). Almost in all the cases of this alloy where the ω precipitation has been observed are with vanadium concentration ≤ 20 wt.%. Studies regarding the ω phase transformation in the higher V side are relatively sparse. McCabe and Sass (1971) in their classic paper had discussed about the feasibility of ω phase formation in the Ti-V alloys with variation in the V addition from 10 to 55 at.% through electron diffraction experiments. They further concluded that beyond 25 at.% of V addition the ω reflections in the electron diffraction pattern become significantly diffuse and can be interpreted as the scattering by atomic displacement waves of large amplitude in the *bcc* structure that is close to transform in ω phase. The present work deals with the ω phase transformation studies in an equiatomic V-Ti alloy. However in the present context it can be stated that though the nominal composition of the alloy is V-50Ti, but the local composition of the alloy where the ω precipitation occurs does not remain the same. It has been already shown that this alloy undergoes phase separation resulting in the formation of Ti-rich and Ti-lean phases. The ω precipitation has been observed in these Ti-rich domains, where the local V concentration is ≤ 25 wt.% as measured from the STEM coupled spectroscopy studies. In a true sense, though the nominal composition of the alloy is V-50Ti, but the local composition where the omega phase forms is in accordance with the omega forming Ti-V composition range as reported in the literature.

5.6: Studies of interfaces between ω and *bcc* structured phases

Another interesting aspect of the present study is the interface structure between the ω and *bcc* structure. Figure 5.19 represents a phase contrast micrograph showing the interface between the *bcc* and the ω structure from two distinct regions of the aged V-50Ti alloy. The image was acquired along [1 1 0] zone axis of *bcc* phase. ω and *bcc* phases are marked in the image itself. A careful look at the interface reveals that the structure is coherent. The interface is spanning over ~ 6-7 atomic layers during which a complete transformation between *bcc* to ω occurs. The contrast that is seen along the interface is because of the structural transformation between *bcc* and ω and not because of the presence of a tilted interface. The interface is devoid of any defects. Figure 5.20(a) shows the *bcc* – ω interface along [1 1 0] zone axis from another region of the specimen. In similar fashion, the interface structure between the ω phase and the *bcc* phase along [$\bar{1}$ 1 3] zone axis of *bcc* is shown in figure 5.20(b). Here also the interface appears to be coherent. Complete transformation from *bcc* to ω structure occurred within a span of 3-4 atomic layers. Just after the interface in the ω side the jagged contrast is not much evident, indicating that the collapse is partial. However, after ~ 6-7 atomic layers of the interface the triangular jagged contrast is very much evident, indicating complete transformation into ω.

5.7: Conclusions

Conclusions from the present chapter are as follows,

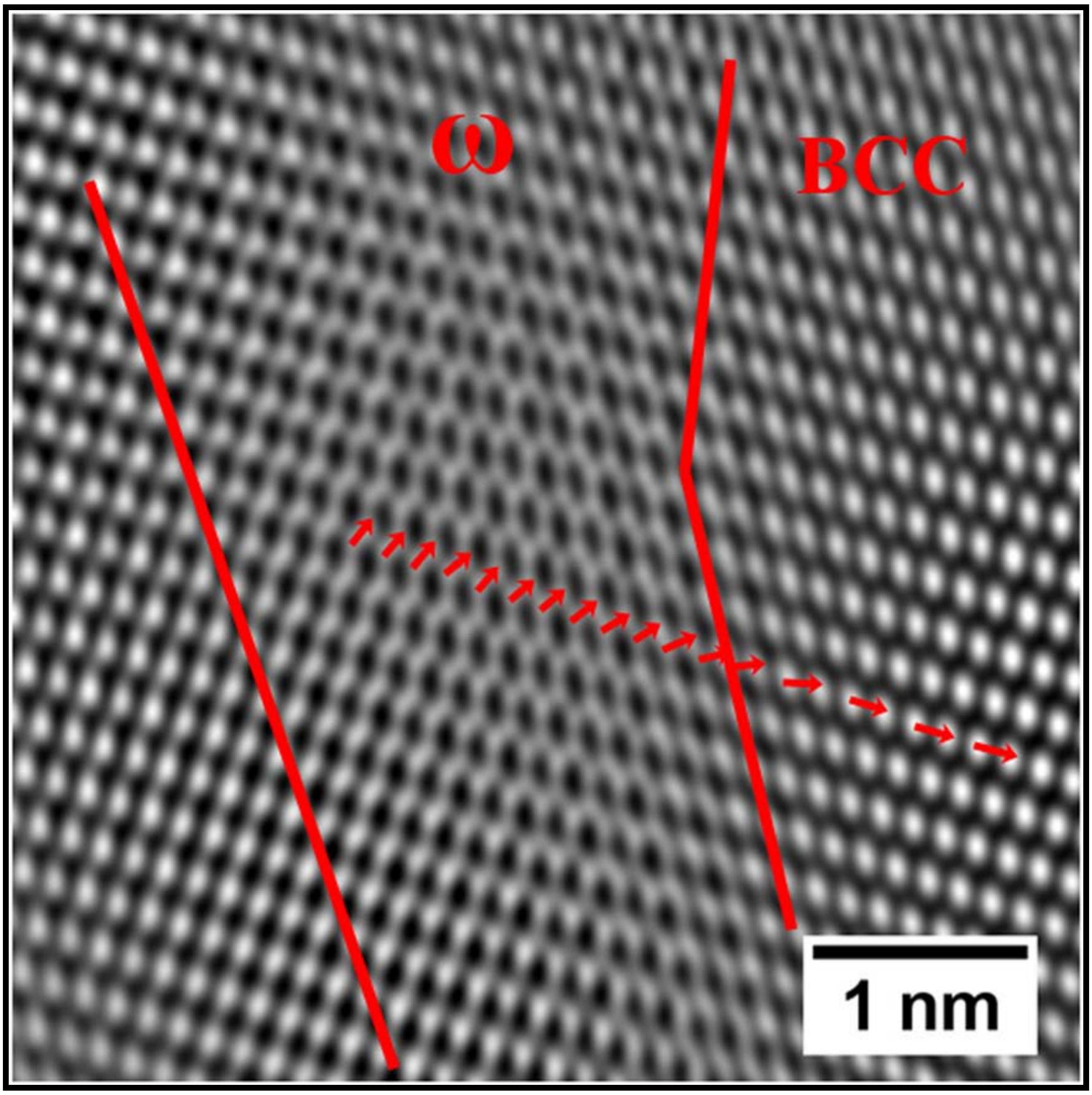

Fig. 5.19: Phase contrast micrograph along the *bcc* – ω interface. The complete transformation occurs over a span of 6-7 atomic layers.

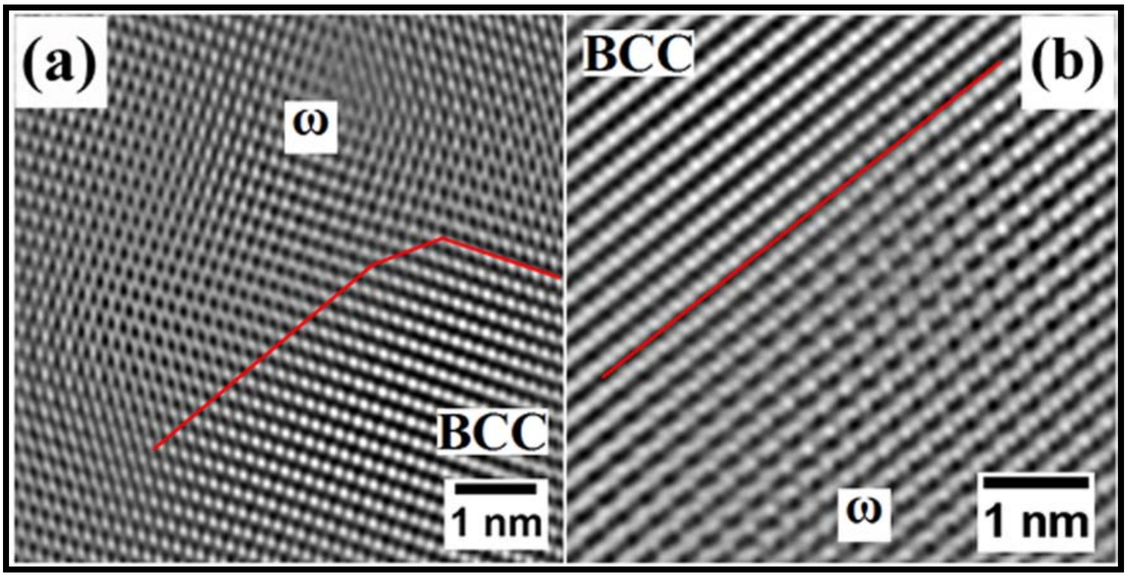

Fig. 5.20: (a) HRTEM images acquired along [1 1 0] zone axis of *bcc* structure showing the atomic arrangements at the interface between the nanostructured ω region and *bcc* matrix in aged V-50Ti alloy. The ledges at the interface are marked with red lines. (b) Phase contrast micrograph recorded along [$\overline{1}$ 1 3] zone axis of *bcc* phase showing the interface between the nanostructured ω region and *bcc* matrix. Here also the ledges at the interface are marked with red lines.

(i) V-50Ti and V-40Ti-20Cr alloys undergo a phase separation on solidification. The process is dominated by the spinodal decomposition mechanism where compositionally modulated regions are seen along <1 1 0> direction.

(ii) The initial composition fluctuation wave in binary V-50Ti alloy is of wavelength ~ 4-5 nm. Gradually another wave with wavelength ~ 18-20 nm initiates and finally this wave only persist.

(iii) The composition partitioning gives rise to a Ti rich and Ti lean domains in both the alloys. It is apparent from the results that the phase separation is essentially a binary event involving only Ti and V. Cr is essentially homogeneously distributed in the matrix.

(iv) *bcc* to ω transition occurs in the Ti rich arm of the phase separated domain for both the as melt as well as aged alloy.

(v) The atomic collapse occurs along the <1 1 1> direction of the *bcc* matrix and the phase contrast micrographs showing the collapse are recorded along <1 1 0> and <$\bar{1}$ 1 3> zone axis of the *bcc* phase. In most of the cases the collapse is partial, giving the trigonal ω phase symmetry.

Chapter VI

Structure Imaging of ω Domains in Phase Separated V-Ti-Cr Alloys

Chapter VI

Structure imaging of ω Domains in Phase Separated V-Ti-Cr Alloys

6.1: Introduction

Feasibility of the formation of ω structured phases in binary V-50Ti and ternary V-40Ti-20Cr alloys as well as the microscopic investigations over their detection in the *bcc* matrix have been elaborately discussed in the previous chapter. A mechanism has also been proposed to explain the origin of the ω embryos in the *bcc* matrix of equiatomic V-Ti and ternary V-40Ti-20Cr alloys. However, questions remained over the atomic level understanding of ω structure domains and also over the contrast seen in the phase contrast micrographs.

In the last four decades the ω phase and the associated phase transformation phenomena have attracted considerable attention resulting in a wide range of discussions in the literature. However, a lion share of them described about the ω formation mechanism mainly on the basis of diffraction contrast microscopy studies and over the change of its mechanical behaviour. Till date only a limited of them has addressed the ω structure and composition of the transformed domains. This is mainly because of the limitation over the spatial and compositional resolution of the previous generation microscopes. Structure imaging of ω phase, nature and extend of collapse and interfaces have received relatively little attention. However, with the development in the instrumentation of the electron microscopes more attempts are being made to reveal to structural details of ω phase. More recently, Ng and his colleagues (2011), Devaraj and co-workers (2012), Bennett *et al.* (2015) have investigated the structure, composition and 3-D morphology of ω precipitates in the binary Ti-Mo alloys with aberration corrected electron microscopes and atom probe techniques. Nag and his co-workers have also discussed the structural aspects of ω in the phase separated domains of Ti based alloys by coupling aberration-corrected HAADF-STEM with atom probe tomography and density functional theory calculations (Nag *et al.*, 2009, 2011). Okunishi *et al.* (2013) have studied the athermal and the isothermal ω–phases in Zr alloys with the aid of STEM-HAADF imaging. Sankaran *et al.* (2014) studied the structural aspects of ω –phase with probe corrected HAADF imaging along three distinct atomic motifs in multicomponent gum metal alloys and further verified the presence of trigonal ω phase with the aid of multislice STEM simulation. Most of the efforts on the structural interpretation were dealing with HAADF characterization of the ω structure. An excellent and comprehensive review has been published by Dehai *et al.* (2014) depicting the recent efforts in the studies of ω-phase in *bcc* metals and alloys.

Phase contrast microscopy aided with multislice image simulation can also be a viable tool to study the structural details of ω phase. Certain efforts were there amongst researchers to study the atomic structures of the ω phase by high-resolution imaging (Sukedai *et al.*, 1993, 1994, 1997). However, the structural imaging of the ω phase structure along different orientation of the *bcc* matrix has still not been explored much. Especially, to the best of the knowledge of the authors, ω transformation has not been reported in literature for V-Ti-Cr alloys. In literature, the reported ω structures are mostly along [1 1 0] orientation of the *bcc* structured matrix. Though, it will be interesting to look at those structures along different orientation of the matrix also. In the present chapter attempts have been made to explore the structural details of the ω phase through high-resolution electron microscopy along different zone axis of the *bcc* structured matrix. Another interesting aspect of the present work is the interpretation of the channelling behaviour in the ω structure through systematic studies of phase and amplitude part of the generated exit waves along different orientation.

The scope of this chapter is as follows,

(i) Structural imaging of partially collapsed ω embryos along different zone axis in the *bcc* matrix with aid of quantitative and experimental phase contrast microscopy in binary V-Ti and ternary V-Ti-Cr alloys.

(ii) Quantum mechanical understanding of the contrast as seen for the corner atoms as well as for the collapsed atoms in the ω structured domains.

(iii) A qualitative study of the electron channelling behaviour in the atomic columns of the ω structured domain.

6.2: Compositional partitioning in V-50Ti and V-40Ti-20Cr alloy: Driving force for ω phase formation

In chapter 3, it is already shown with the aid of thermodynamic calculations that a phase separation tendency exists for binary equiatomic V-Ti system and this tendency got suppressed with the addition of Cr in the alloy. Microstructural and microchemical studies of the selected alloy compositions are also in support of the thermodynamic results. A few of these results are revisited in the present section to maintain the continuity in understanding the origin and the structure of the ω phases. Figure 6.1(a-d) represents the phase separated domains and the corresponding selected area electron diffraction patterns from binary V-50Ti and ternary V-40Ti-20Cr alloy specimens in the as melted condition. Figure 6.1(a) shows relatively low magnification STEM-HAADF micrograph showing the striation contrast from the phase separated domain in V-50Ti alloy specimen. The striations are almost periodic in nature with an observed wavelength of ~ 3-4 nm. Selected area electron diffraction pattern from the corresponding region is shown in figure 6.1(b). The diffraction pattern has been indexed as [0 1 3] zone axis pattern of a *bcc* structured phase. The reflections correspond to 200 and $03\bar{1}$ type of planes and are marked in the figure. Indexing has been done after careful measurement of the diffraction spots and the corresponding interplanar angles. Calculated lattice parameter from the diffraction pattern turns out to be a= 0.32 nm which is very close to the reported lattice parameter for the *bcc* V-Ti solid-solution phase (a= 0.3165 nm). In the diffraction pattern, along with the principal reflections, dove shaped diffuse intensities connecting main diffraction spots and very feeble satellite spots can also be observed. The diffuse intensity arises due to the nanostructured ω phase (which will be discussed in details in the following sections). The satellite spots appear because of the phase separation phenomenon. The STEM-HAADF image of the phase separated domain from V-40Ti-20Cr alloy and the corresponding electron diffraction pattern are shown in figure 6.1(c-d). The microstructural nature of the domain is almost same as that of V-50Ti alloy. The wavelength of the periodicity is ~ 4-5 nm, which is also same as that of V-50Ti alloy. Electron diffraction pattern indicates that the specimen is oriented along [0 1 3] zone axis of *bcc* structure. The reflections corresponds to the 200 and $03\bar{1}$ type of planes are marked in the image itself. Apart from the principal reflections, the satellite

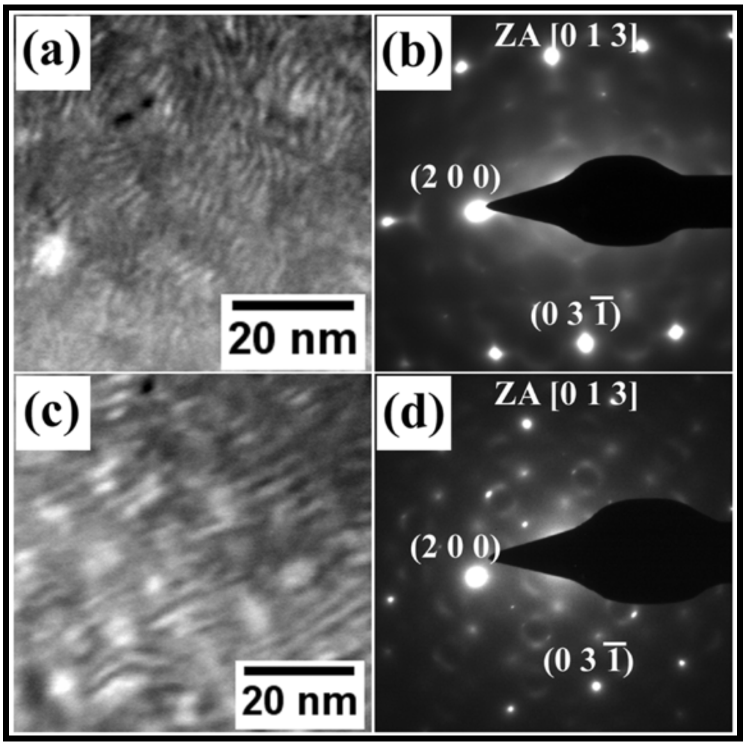

Fig. 6.1: (a & c) STEM-HAADF micrographs showing the chemical partitioning in the phase separated domains of as melted binary V-50Ti alloy and ternary V-40Ti-20Cr alloy specimens respectively. (b & d) Selected area electron diffraction pattern from the similar phase separated domain shown in (a) and (c) respectively. In both the diffraction patterns two major principal reflections are marked.

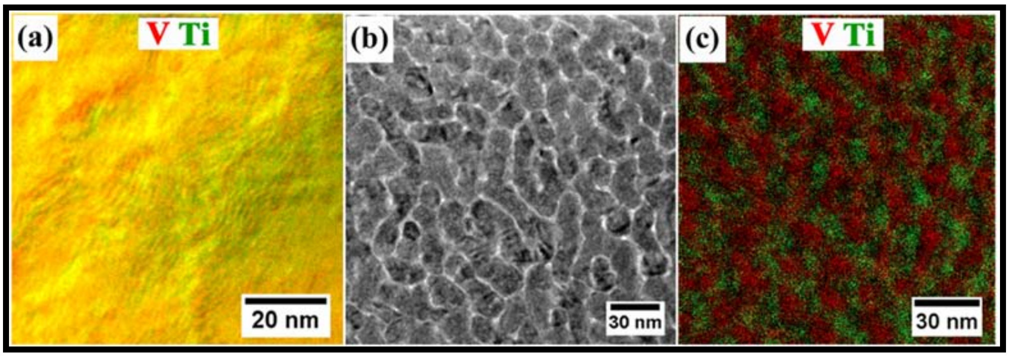

Fig. 6.2: EFTEM micrograph showing the chemical partitioning between V- rich and Ti- rich domains in as-melted [in (a)] and heat treated [in (c)] V-50Ti alloy specimen. In the heat treated specimen the modulation length is ~ 18-20 nm. (b) Bright field micrograph from the phase separated domain in aged and quenched V-50Ti alloy specimen.

reflections corresponding to the phase separation and the diffuse intensity corresponding to the ω phase are also seen in the diffraction pattern. The lattice parameter calculated from the diffraction pattern is of 0.31 nm which is very near to the reported lattice parameter for the reported V-50Ti alloy.

As already informed in the previous chapter that both of the alloys were aged at 750° C for 5 hours and subsequently been quenched in ice water to promote the phase separation kinetics further. Fig 6.2(a-c) shows a collage of energy-filtered TEM (EFTEM) micrographs from as melt V-50Ti alloy, relatively low magnification bright field image from the aged and quenched V-50Ti alloy specimen and the corresponding EFTEM map. EFTEM map of the as-melted alloy confirms the presence of chemical partitioning between V rich (in red) and Ti rich (in green) regions over solidification. The modulation length of the phase separated domain ~ 4-5 nm. In the bright field image from the aged and quenched alloy, periodically spaced and interconnected dark and bright striated contrast can be seen. Here the modulation lengths are in the range of ~ 18-20 nm. EFTEM maps were acquired from the same region of the alloy specimen to study the chemical nature of the phase separated domains. Colour composite of the EFTEM map in fig 6.2(c) clearly shows the phase separated domains where V rich regions are shown in red and the Ti rich regions are shown in green. Three window method of elemental imaging is used to acquire the background-corrected chemical maps for both the EFTEM maps where a slit width of 20 eV is used with a collection time of 30 seconds. V and Ti elemental maps are generated with the energy loss edge of V-L (521 eV) and Ti-L (462 eV) respectively.

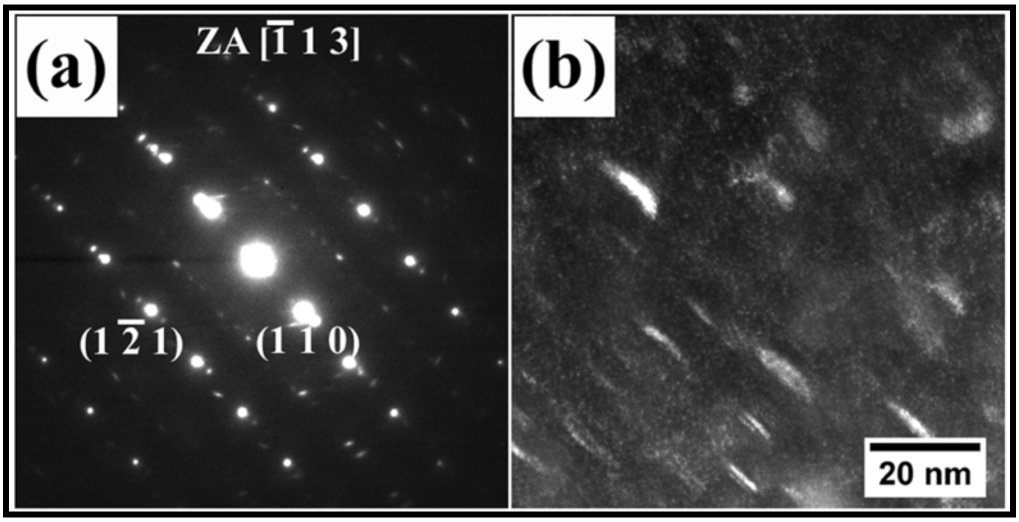

Fig. 6.3: (a) Selected area electron diffraction pattern along [$\bar{1}$ 1 3] zone axis of *bcc* phase in aged V-50Ti alloy. Two major principle reflections of *bcc* phase are marked in the micrograph. The additional reflections corresponding to the ω structures can be seen in the diffraction pattern. (b) Dark field image from the aged V-50Ti alloy showing the morphology of the nanostructured ω domains. The domains are elliptical in shape.

6.3: Structure imaging of nanostructured ω domains

6.3.1: Morphology and distribution of ω phase

Both V-50Ti and V-40Ti-20Cr alloy specimens have further been investigated to study the structure and morphology of the nanostructured ω phase. Figure 6.3(a-b) represents the dark field micrograph and selected area electron diffraction pattern corresponding to a ω reflection from aged V-50Ti alloy. The diffraction pattern is indexed as [$\bar{1}$ 1 3] zone axis pattern of the *bcc* structured matrix. Principal reflections correspond to 110 and 1 $\bar{2}$ 1 planes and are marked in the image itself. Careful observation of the diffraction pattern indicates that the reflections of ω phase are not very sharp and distinct. Rather diffuse arcs arise because of the ω phase. The experimentally measured lattice parameters for the ω phase from the diffraction pattern turn out to be a= 0.46 nm and c= 0.28 nm which are very close to the reported values of those in V-Ti system, which are a= 0.455 nm and c= 0.278 nm (Banerjee and Mukhopadhyay, 2004). The dark-field images recorded with the ω reflection spots show the characteristic patchy contrast from the nanoscale precipitates of the ω phase. The precipitates have an elliptical morphology in two-dimensional projection where the major axis measuring ~ 10-12 nm and the minor axis measures ~ 3-4 nm.

6.3.2: Direct structure imaging along [1 1 0]$_{bcc}$ zone axis

Figure 6.4(a-b) represents the atomic structure model for a pure *bcc* structure along [1 1 0] zone axis and for a hexagonal structure along [1 1 $\bar{2}$ 0] zone axis respectively. The directions <1 1 0>, <2 0 0> and <1 1 1> of *bcc* structure are marked in the figure. A schematic of the stacking sequence A, B and C of *bcc* are indicated in the image for illustration of the atomic collapse mechanism. During *bcc* to ω transformation process, a systematic collapse occurs in the <1 1 1> direction, which results in the atomic level rearrangement of B and C layers. In case of ideal ω transformation, the B and C layers collapse towards a plane halfway between B and C planes. This transformation gives rise to the ideal hexagonal structure as shown in figure 6.4(b). However, in most of the cases the collapse is incomplete, which results in a trigonal ω phase structure. Hence, a systematic scan along the traces of {200} planes can provide clue whether the collapse is partial or complete. These issues are explained with the direct structural analysis of pure *bcc* and ω phases.

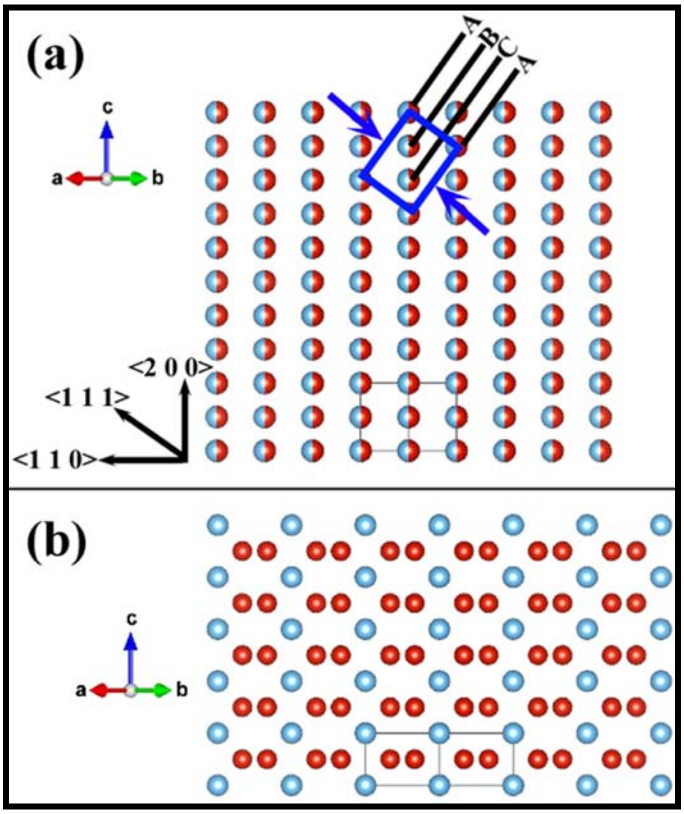

Fig. 6.4: (a) Schematic representation of the atomic arrangement along [1 1 0] zone axis of *bcc* structure. The stacking sequence of A, B and C and the collapse direction along <1 1 1>are marked in the image. (b) Schematic representation of the atomic arrangement along $[1\ 1\ \bar{2}\ 0]$ zone axis of hexagonal ω structure.

Phase contrast image from the *bcc* phase and from the nanostructured ω phase in an aged V-50Ti alloy specimen are shown in figure 6.5 (a-b). Figure 6.5(a) shows the atomic arrangement from a pure *bcc* phase where the specimen is oriented along [1 1 0] zone axis. The spacing between two atoms along 200 planes is measured as 0.16 nm and also been marked in the micrograph. This is consistent with a cubic system for which the lattice parameter is a = 0.32 nm. The distance across four consecutive atomic columns is hence measured to be 0.48 nm. However, the situation does not remain the same for the nanostructured ω shown in figure 6.5 (b). As stated earlier, in case of ω transformation,

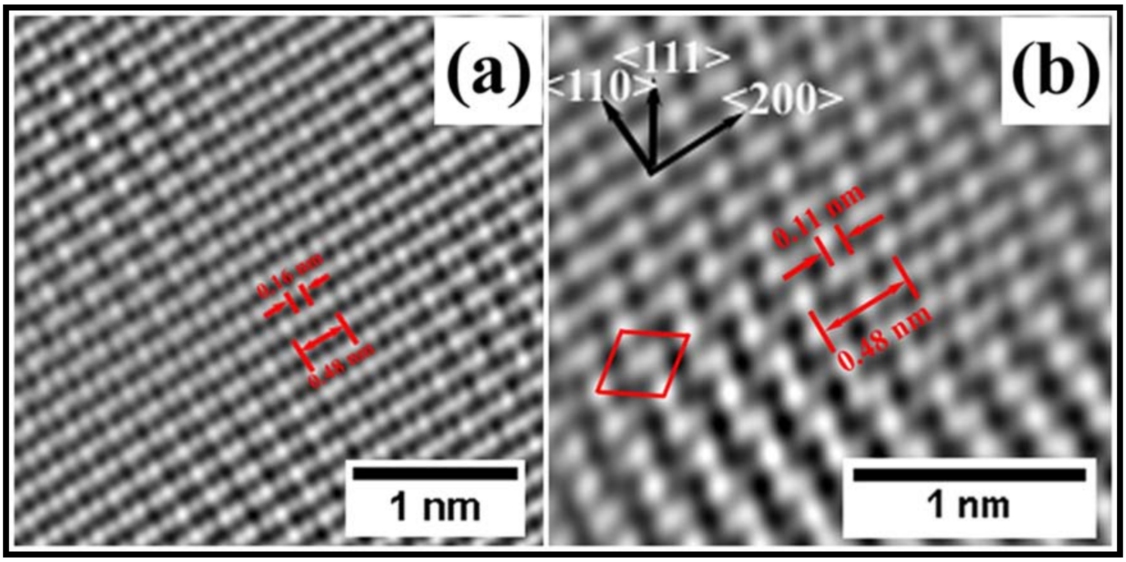

Fig. 6.5: (a) Phase contrast image showing the atomic arrangement along [1 1 0] orientation of a *bcc* structured phase in an aged V-50Ti alloy specimen. (b) Phase contrast image showing the partially collapsed ω structure with trigonal symmetry. A unit of the ω structure is marked in the image itself.

the B and C planes tend to collapse on to a single plane resulting in atomic displacements along 200 types of planes. One such unit of collapsed ω structure is shown in the figure where the two collapsed atomic columns are surrounded by four corner atomic columns. Further quantitative analysis reveals that the spacing between four successive atomic columns is 0.48 nm, the individual spacings do not remain the same: the spacing between the second and the third atomic columns reduces to 0.11 nm due to the partial atomic collapse. Hence the phase exhibits a trigonal symmetry.

6.3.3: Direct structure imaging along [$\bar{1}$ 1 3]$_{bcc}$ zone axis

Structural imaging of ω has been carried along [$\bar{1}$ 1 3] zone axis of *bcc* also and one such combination of atomic structure model of *bcc* along [$\bar{1}$ 1 3] and ω along

$[1\bar{2}13]$ are shown in figure 6.6 (a-b). It is very much evident from the image that the collapsed layers along $[1\bar{2}13]$ zone axis of ω gives rise a zig-zag like contrast bounded by two planes. In continuation of the described model, figure 6.7(a-c) represents the phase contrast micrographs from *bcc* phase along $[\bar{1}13]$ zone axis, nanostructured ω phase along $[1\bar{2}13]$ zone axis and the corresponding power spectrum from aged V-50Ti alloy specimen. The traces of the 110 types of planes are clearly visible in the micrograph, which corresponds to the *bcc* phase. Moreover, the planes are continuous throughout without any visible change of the atomic contrast. However, for figure 6.7(b) the structural contrast appears quite different from the pure *bcc* phase. Here the triangular zig-zag type atomic contrasts are quite clearly visible. Power spectrum recorded from the similar region is shown in figure 6.7(c) where the reflections due to 110 and $2\bar{1}1$ type of planes from the *bcc* phase are marked in the image itself. Phase contrast micrographs of the *bcc* phase along $[\bar{1}13]$ zone axis, ω phase along $[1\bar{2}13]$ zone axis and the corresponding power spectrum from another region of the specimen are shown in figure 6.8(a-c). As expected, the atomic arrangements of the nanostructured ω phase in figure 6.8(b) shows a triangular zig-zag type of contrast which is very much similar to the model described for the ω structured phase along $[1\bar{2}13]$ zone axis. The corresponding power spectra confirms that the specimen is oriented along $[\bar{1}13]$ zone axis of the *bcc* phase.

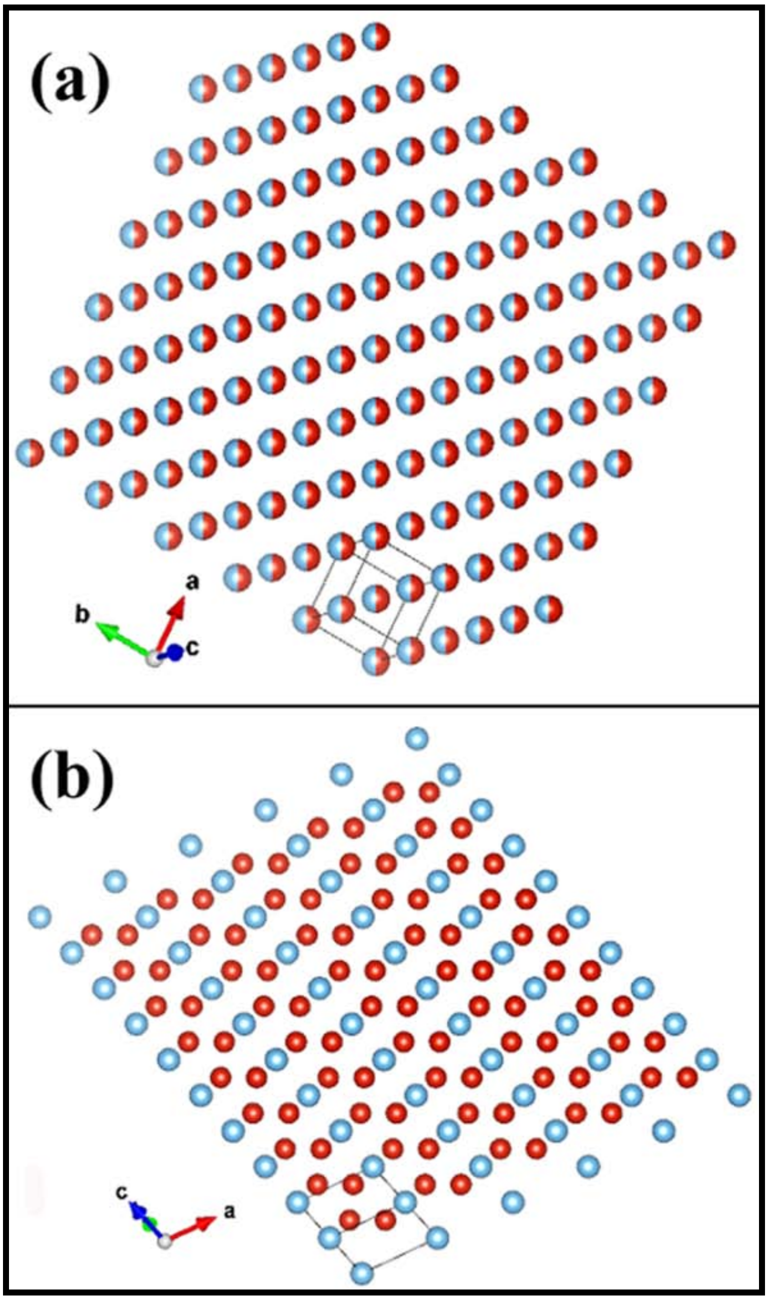

Fig. 6.6: (a) Schematic representation of the atomic arrangement along [$\bar{1}$ 1 3] zone axis of *bcc* structure. (b) Schematic of the atomic arrangement along [1 $\bar{2}$ 1 3] zone axis of hexagonal ω structure.

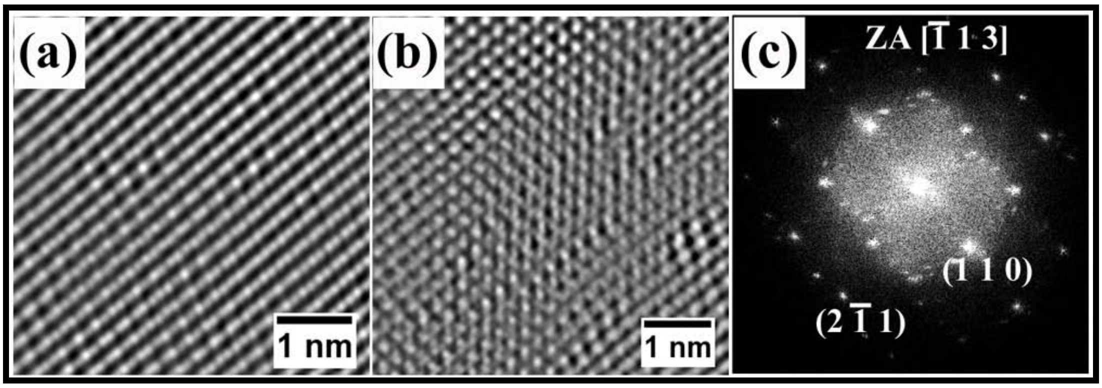

Fig. 6.7: (a) Phase contrast image showing the atomic arrangement along [$\bar{1}$ 1 3] orientation of a *bcc* structured phase in an aged V-50Ti alloy specimen. (b) Phase contrast image showing the ω structure along [1 $\bar{2}$ 1 3] zone axis. The characteristic 'jagged' contrast of the ω structure is clearly visible in the micrograph. (c) Power spectrum confirms the orientation of the specimen as [$\bar{1}$ 1 3] where the principle reflections corresponding to 110 and 2 $\bar{1}$ 1 types of planes are marked in the image.

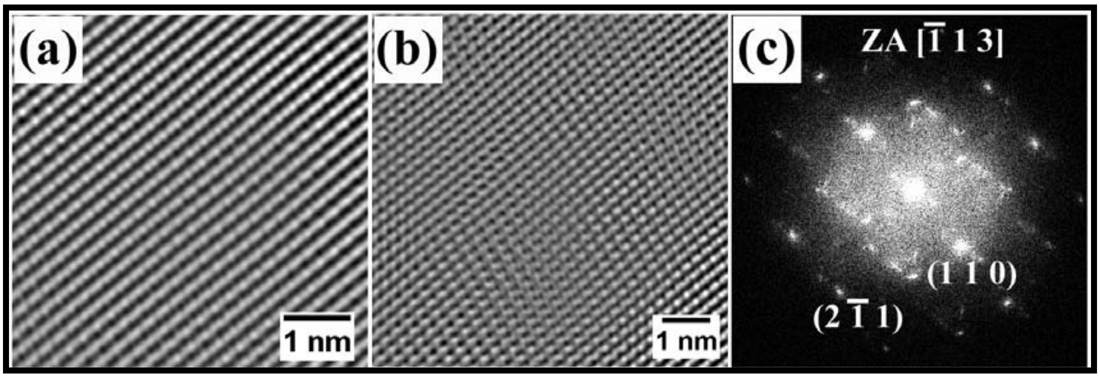

Fig. 6.8: (a-b) Phase contrast image showing the atomic arrangement along [$\bar{1}$ 1 3] orientation of a *bcc* structured phase and along [1 $\bar{2}$ 1 3] zone axis of the ω structured phase from another location in an aged V-50Ti alloy specimen. (c) Corresponding power spectrum confirms the orientation of the specimen as [$\bar{1}$ 1 3]

6.3.4: Site specific contrast generation for atomic columns

One interesting observation from the phase contrast image of the ω phase shown in figure 6.7(b) is the dark atom contrast for the surrounding atoms of the collapsed atomic layers. It is described in figure 6.6(b) that the atomic structure of ω domain along $[1\ \bar{2}\ 1\ 3]$ appears as a jagged contrast produced by the collapsed atoms and the surrounding atoms provide a linear contrast on either side of the collapsed atoms. A careful look into figure 6.7(b) confirms that bright atom contrast appears only for the jagged contrast atoms i.e. only for the collapsed atoms. Moreover, the absence of the linear contrast affirms that the surrounding atoms are dark in the present thickness-defocus condition.

Dark atom contrast along the ω like embryo can also be observed along other orientation of the specimen. Figure 6.9(a-b) represents the phase contrast micrograph and the corresponding power spectrum from the ω like embryo of the specimen. The power spectrum confirms that the micrograph is recorded along [1 1 0] zone axis of the *bcc* matrix where the reflections due to 002 and $1\ \bar{1}\ 0$ type of planes are marked on the image itself. The contrast seen in the phase contrast micrograph confirms that the collapsed atomic column appear bright whereas the corner atoms appear dark for the particular imaging condition. A unit of ω structure and the directions of the atomic planes are marked in the image itself. For further confirmation, dark atom contrast for the corner atoms of ω phase has imaged from another region of the specimen and is shown in figure 6.10(a-b). Here also the specimen is oriented along [1 1 0] zone axis of the *bcc* phase as evident from the power spectrum. Here the corner atoms are seen to be dark while the

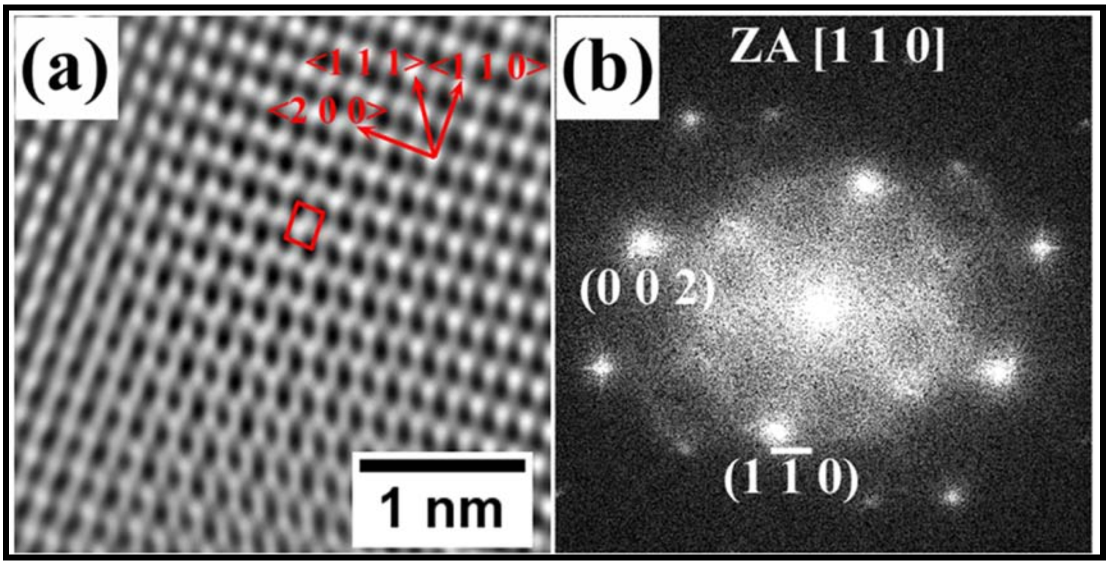

Fig. 6.9: (a) Phase contrast image showing the atomic arrangement from a partially collapsed ω structure. It is clearly evident from the image that the collapsed atoms are bright whereas the corner atoms are dark. A unit of the ω structure is marked in the micrograph. (b) Power spectum from the similar region shows that micrograph is aquired along [1 1 0] zone axis of *bcc* phase.

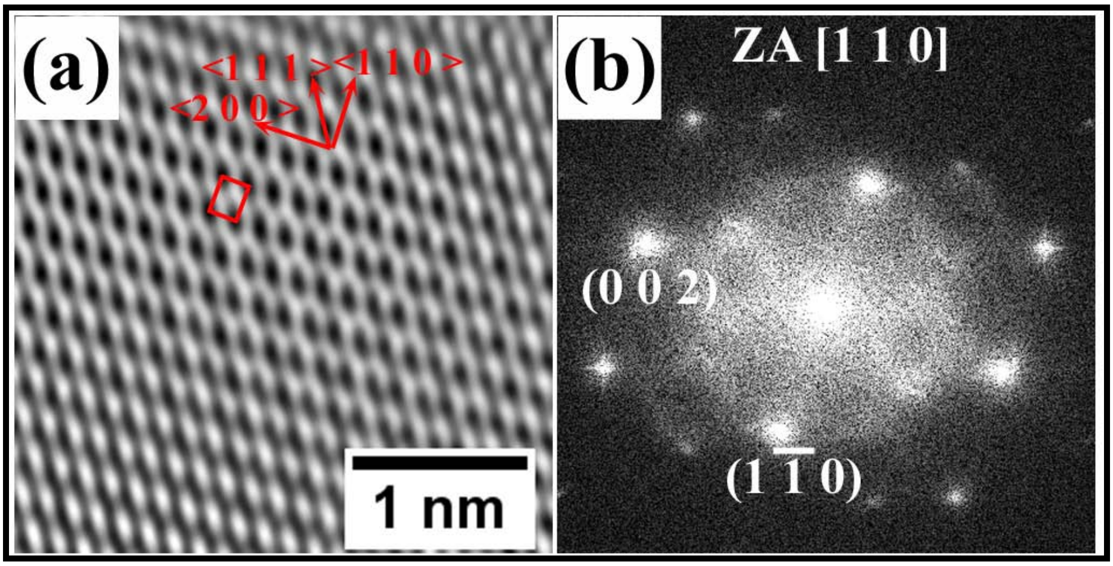

Fig. 6.10: (a) Phase contrast image showing the atomic arrangement from a partially collapsed ω structure from another region of the specimen. Here also the collapsed atoms appear bright whereas the corner atoms are dark. (b) Power spectum from the similar region shows that micrograph is aquired along [1 1 0] zone axis of *bcc* phase.

partially collapsed atoms are bright in the phase contrast micrograph. The details of the plane orientation and one of the ω structural units are marked in the image. A sincere effort has been made in the following sections to understand the origin of this dark atom contrast for the corner atoms of ω structured domains along [1 1 0] and [$\overline{1}$ 1 3] zone axis of the *bcc* matrix.

6.4: Multislice image simulation for the verification of contrast generation

6.4.1: t – Δf map for bcc and ω phase along $[1\ 1\ 0]_{bcc}$

In order to substantiate the contrast observed in the above phase contrast images and also to validate the dark atom contrast for the corner atoms of the ω structure, multislice simulation is carried out for *bcc* structured phase along [1 1 0] zone axis and ω structure along [1 1 $\overline{2}$ 0] orientation. Corresponding thickness – defocus (*t –Δf*) maps for the *bcc* and ω structured phases are shown in figs. 6.11 and 6.12 respectively.

Figure 6.11 shows the thickness – defocus map of the *bcc* V-50Ti alloy along [1 1 0] zone axis. It can be observed from the t-Δf map that for the *bcc* phase the contrast of the 110 types of lattice planes varies predominantly with the defocus. For the defocus values of around the Scherzer defocus i.e. ~ -30 nm to -40 nm ranges all the atomic columns appear bright and the channels appear dark throughout the entire thickness range. Whereas, for the defocus value in the range of -20 nm to -10 nm, all the channels are bright and the atoms are dark apart from the lower thickness of 17 nm and below, where the contrast is reversed again. The contrast is again reversed and the atomic columns become bright and the channels become dark for the higher defocus values i.e. in the range of -10 nm to 0 nm. For the present experimental conditions, where the

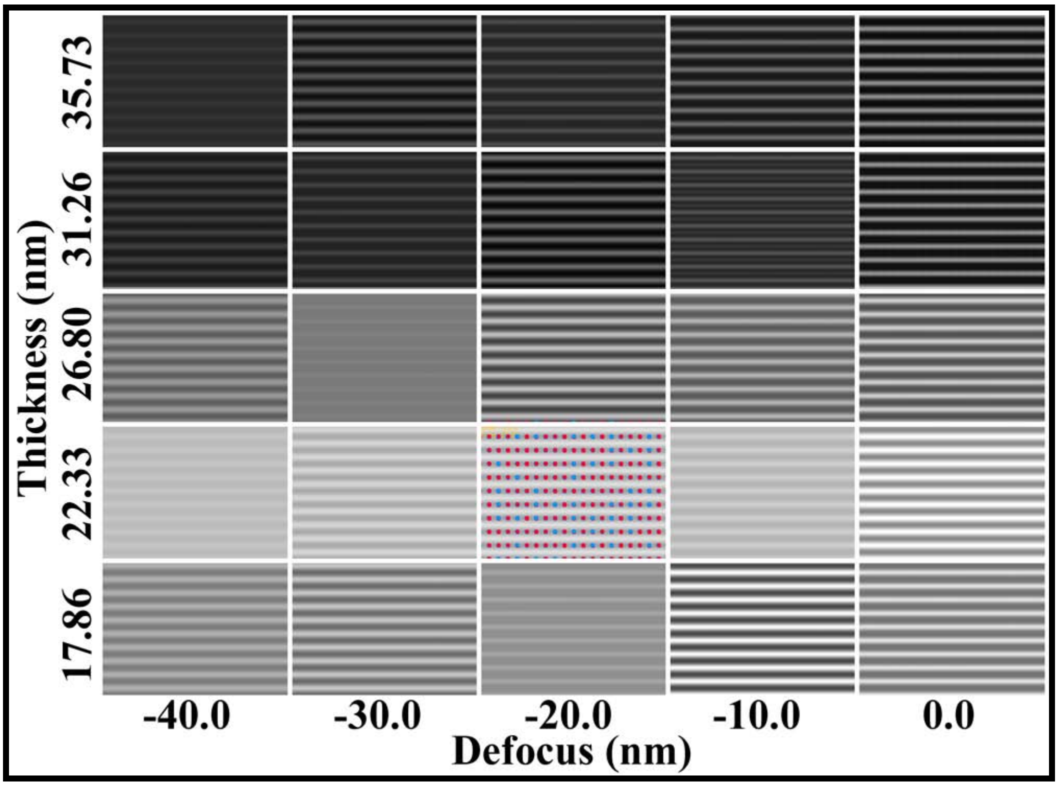

Fig. 6.11: Simulated thickness-defocus (t - Δf)map of the *bcc* V-50Ti structure (Pearson symbol = cI2) along [1 1 0] zone axis by multislice method. V-50Ti structure is also projected on the simulated image. Accelerating voltage = 300 kV and C_s = 0.65 mm.

thickness of the specimen ~ 25 nm and defocus ~ -10 nm, all the atom columns appear bright for the *bcc* phase and is also in support of the experimental observations.

In all the cases, for the ω structure simulation, the collapse along c direction assumed to be 1, i.e., the symmetry is assumed to be pure hexagonal symmetry and not the trigonal symmetry for which the extent of the collapse lies within 0 and 1. The experimental images were captured ~ 20 - 25 nm above the Scherzer defocus, which is -36 nm for the microscope with Cs = 0.65 mm at an operating voltage of 300 kV. The thickness of the specimen is measured by the log ratio method from the corresponding EELS profile and it is ~ 34 nm. As seen from the simulated image in figure 6.12, the

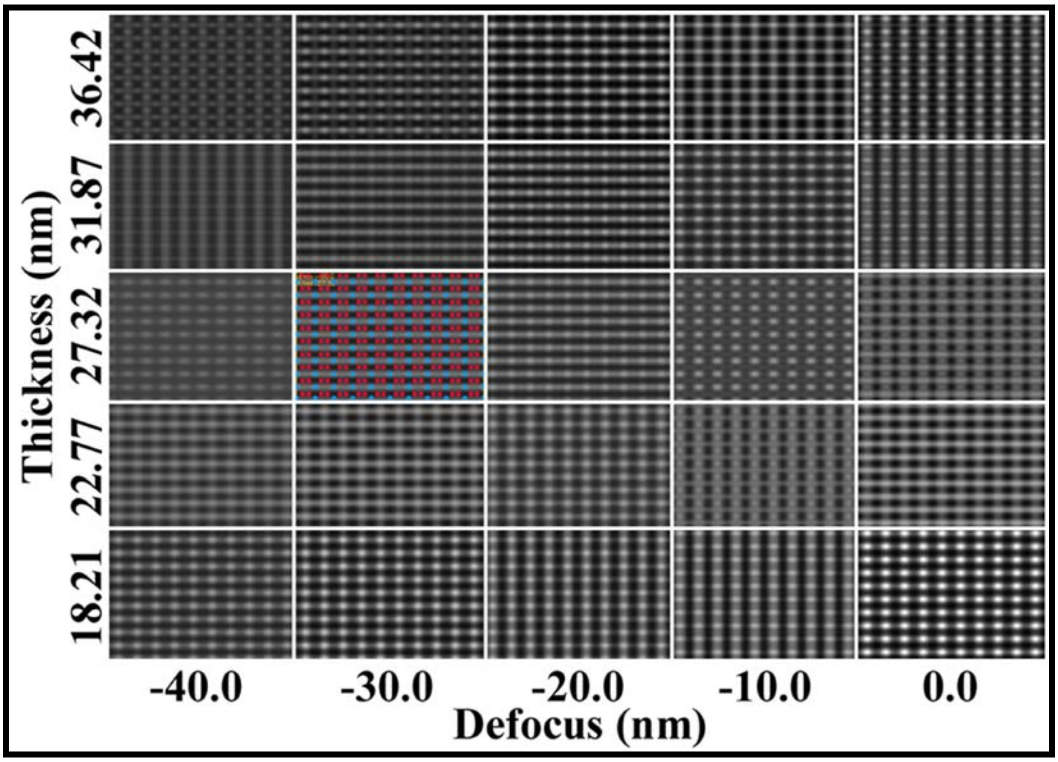

Fig. 6.12: Simulated thickness-defocus (t - Δf) map of ω structure along $[1\,1\,\bar{2}\,0]$ zone axis by multislice method. ω structure is also projected on the simulated image. Accelerating voltage = 300 kV and C_s = 0.65 mm.

contrast for ω structure varies significantly with thickness and defocus. In and around the Scherzer defocus value, the corner atoms are giving the bright contrast. In this defocus range the channels between the corner atoms are also providing faint bright contrast, making a linear contrast for the entire row of the corner atoms. The bright contrast from the channels is enhanced in the higher defocus values i.e. in the defocus range of -30 nm to -20 nm and the contrast from the corner atoms appear bright and the collapsed atoms appear dark. With further increase in the defocus values i.e. ~ -10 nm and beyond, the corner atoms become dark and the collapsed atoms become bright. For the present experimental conditions as already stated earlier, all the corner atoms appear dark and the collapsed atoms appear bright. This is in support of the dark atom contrast seen in the experimental phase contrast micrographs.

6.4.2: t – Δf map for bcc and ω phase along $[\bar{1}\ 1\ 3]_{bcc}$

In order to understand the contrast and match the phase contrast image of *bcc* structure along $[\bar{1}\ 1\ 3]$ zone axis of V-50Ti alloy, multislice simulation is carried out for the same structure under similar experimental conditions. The thickness-defocus (*t - Δf*) map for the *bcc* structure of V-50Ti alloy along $[\bar{1}\ 1\ 3]$ orientation is shown in figure 6.13. The experimental images were captured around Scherzer defocus which is ~ -36 nm under 300 kV acceleration voltage and C_s = 0.65 mm. The map is generated for the thickness range of ~ 17 nm to 38 nm. It can be observed from the *t–Δf* map that the contrast of the lattice planes varies significantly with thickness and defocus. In the defocus range of -40 nm to -30 nm, the atomic columns appear bright and the channels are dark at a thickness of 20 nm and above. However, for the lower thickness, the contrast reverses. Again for the defocus values of -20 nm to 0 nm, the atoms appear dark and the channels appear bright for the thickness above 20 nm and below that the contrast reverses.

In the similar manner to understand the contrast and match the phase contrast image of ω structure along $[1\ \bar{2}\ 1\ 3]$ of V-50Ti alloy, multislice simulation is carried out for the same structure under pre-recorded experimental conditions. The thickness-defocus (t *–Δf)* map corresponding to the $[1\ \bar{2}\ 1\ 3]$ zone axis of ω is shown in figure 6.14. The experimental images were captured around Scherzer defocus which is ~ -36 nm under

300 kV acceleration voltage and C_s = 0.65 mm. The map is generated for the thickness range of ~ 16 nm to 37 nm. Here a periodic arrangement of bright jagged contrast associated with a wide linear contrast can be observed. In other words, a jagged contrast surrounded by two bright linear contrasts can be observed in the simulated image. These jagged contrasts correspond to the collapsed atoms of the ω structured phase whereas the linear contrast is generated from the surrounding atoms in the ω domain. However, for the ω structure also the contrast varies significantly with the variation of thickness and defocus. In the defocus range of -40 nm to -30 nm, the collapsed atoms appear bright and the corner atoms are dark at and above 20 nm of thickness. Further down in the thickness range i.e. below 20 nm of thickness in the same defocus range all the atoms appear bright. In the higher defocus values i.e. in the range of – 20nm to 0 nm defocus, the collapsed atoms are bright throughout the entire thickness range. Moreover, the corner atoms give dark atom contrast in the thickness of 20 nm and above and bright atom contrast for the thickness below 20 nm. For the present experimental condition, the phase contrast image was acquired nearby Scherzer defocus i.e. at ~ -36 nm with a thickness value of ~ 26 nm. The thickness of the specimen is measured by the log ratio method in electron energy loss spectroscopy technique. It is evident from the $t - \Delta f$ map that for this particular window, the collapsed atomic layers appear bright and the rest of the atoms appears dark.

6.5: Origin and interpretation of contrast generation in structural imaging of ω

6.5.1: Structural correspondence between bcc and ω structured phase

Present section discusses the contrast generation during structural imaging of partially collapsed ω structure and its lattice correspondence with the *bcc* phase. High-

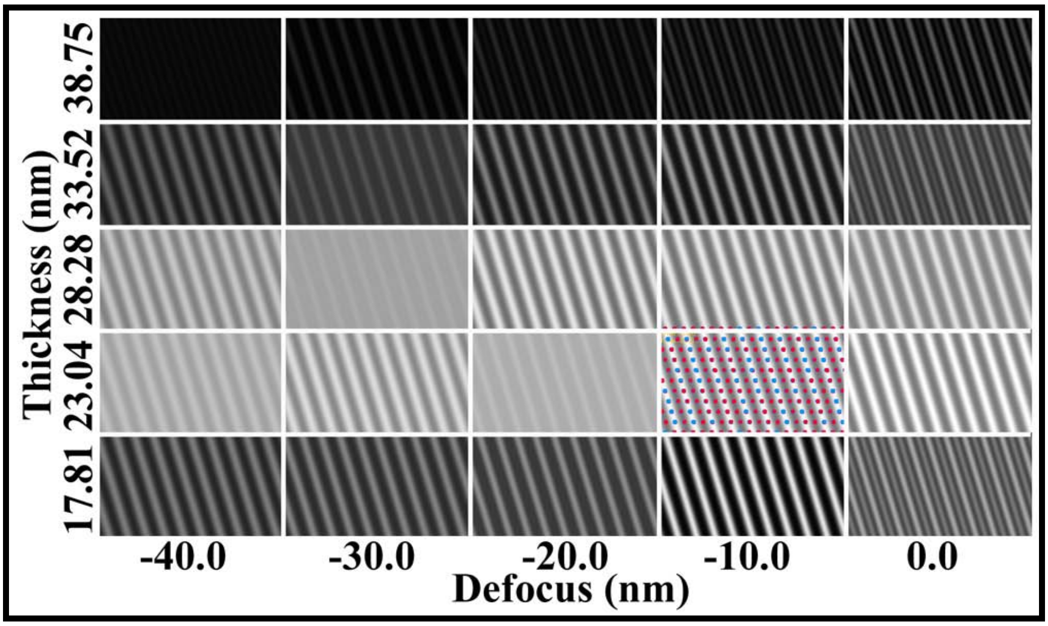

Fig. 6.13: Simulated thickness-defocus (t - Δf) map of *bcc* V-50Ti structure (Pearson symbol = cI2) along [$\bar{1}$ 1 3] zone axis by multislice method. V-50Ti structure is also projected on the simulated image. Accelerating voltage = 300 kV and C_s = 0.65 mm.

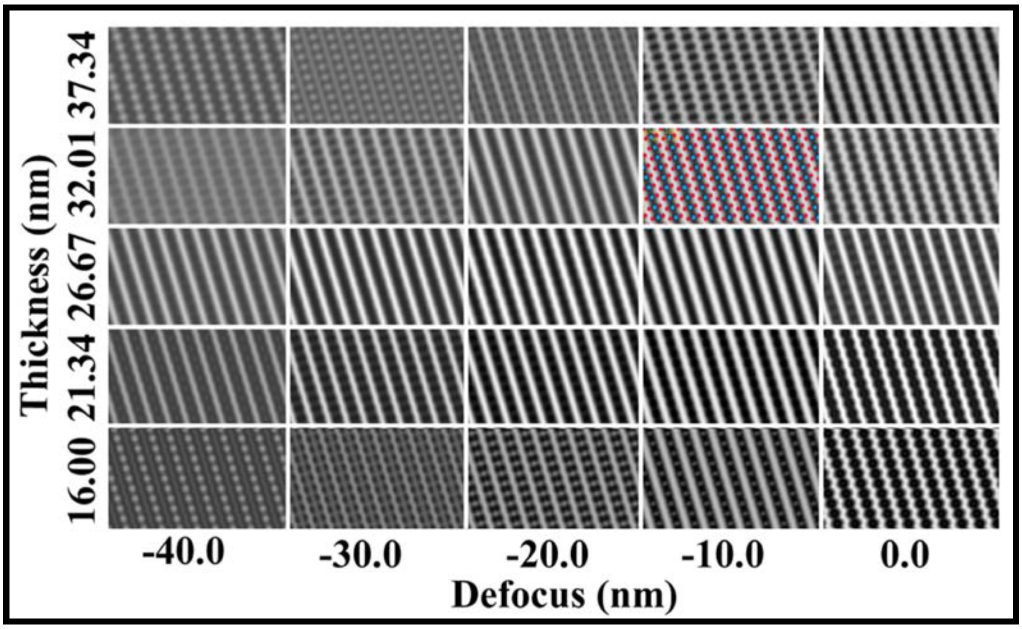

Fig. 6.14: Simulated thickness-defocus (t - Δf) map of ω structure along [1 $\bar{2}$ 1 3] zone axis by multislice method. ω structure is also projected on the simulated image. Accelerating voltage = 300 kV and C_s = 0.65 mm.

resolution TEM characterization with the aid of phase contrast image simulation and atomic structure modelling has been carried out to study the structural aspects of the nanostructured ω. The ω structure has been reported to be stabilized either in hexagonal (P6/mmm) or trigonal ($P\bar{3}m1$) structure. The stability between these two structures depends on the atomic scale shear mechanism of the ω formation and also on the relative composition of the *bcc* stabilizer. The orientation relationship between ω and *bcc* phase are studied by a large number of researchers and unambiguously described as $\langle 1\ 1\ 0\rangle_{bcc} \parallel \langle 1\ 1\ \bar{2}\ 0\rangle\omega$ and $\langle \bar{1}\ 1\ 3\rangle_{bcc} \parallel \langle 1\ \bar{2}\ 1\ 3\rangle\omega$. Present work discusses about the atomic arrangement of the ω structured domains as well as the extent of the collapse through systematic phase contrast microscopy studies.

6.5.2: Estimation of channelling behaviour: Projected potential and exit wave function calculation

Another interesting aspect of the present section is the dark atom contrast as seen for the corner atoms of the ω structure, which is further substantiated with multislice simulation. In the literature, even though the direct structure matching is explored as the most viable tool for the contrast matching in the phase contrast images, absolute intensities of simulated images often do not match with that of the experimental micrographs (Boothroyd, 1998). Apart from the Stobbs factor, CCD modulation factor, inelastic scatterings are the major causes for the intensity mismatch. Mathematically the contrast in the phase contrast image can be described as the convolution of three different contributions. They are the background intensities which in turn depend on the amplitude of the direct beam and the diffracted beams; second, the linear component of the intensity, which in turn depends on the phase and amplitude of the direct and diffracted beams and third, the non-linear component which also depends on the phase and amplitude of the direct and the diffracted beams (Van Dyck *et al.*, 1982; Kirkland, 2009). Thus a critical study of the exit wave of the ω structure and its phase and amplitude part can provide the crucial reason behind the dark atom contrast if not quantitatively, at least qualitatively and has already discussed in chapter 4 of this thesis. Figure 6.15 represents the collage of the simulated results of the projected potential, exit plane wave function, phase and amplitude part of the exit plane wave function for ω structure along $[1\ 1\ \bar{2}\ 0]$ zone axis. All the calculations are carried out as a function of thickness varying from 8 nm to 46 nm, keeping it independent from the change in defocus variation. It can be observed from the potential plot that both the corner atoms and the collapsed atoms appear bright throughout the entire thickness range. However, the Phase and the amplitude part of the exit wave function from the corner atoms and the collapsed atoms of the ω structure show substantial difference among them. The grey scale profile of the phase part and the amplitude part for both the corner atoms and the collapsed atoms along $[1\ 1\ \bar{2}\ 0]$ orientation of ω structure with thickness are plotted and shown in figure 6.16. For the corner atoms three phase reversals can be observed in the given thickness range, at ~ 11 nm, 27 nm and at 32 nm. In contrary, for the collapsed atoms, the intensity of the exit wave phase increases with the thickness at a constant rate. For the amplitude part of the exit wave, again the intensity of the corner atoms behaves in a different manner than that of the collapsed atoms. The corner atoms appear bright throughout the wave-amplitude map. However, in the lower thickness range the contrast is high. The contrast from the atoms and the channels are very feeble in the thickness range ~ 22 nm to 27 nm.

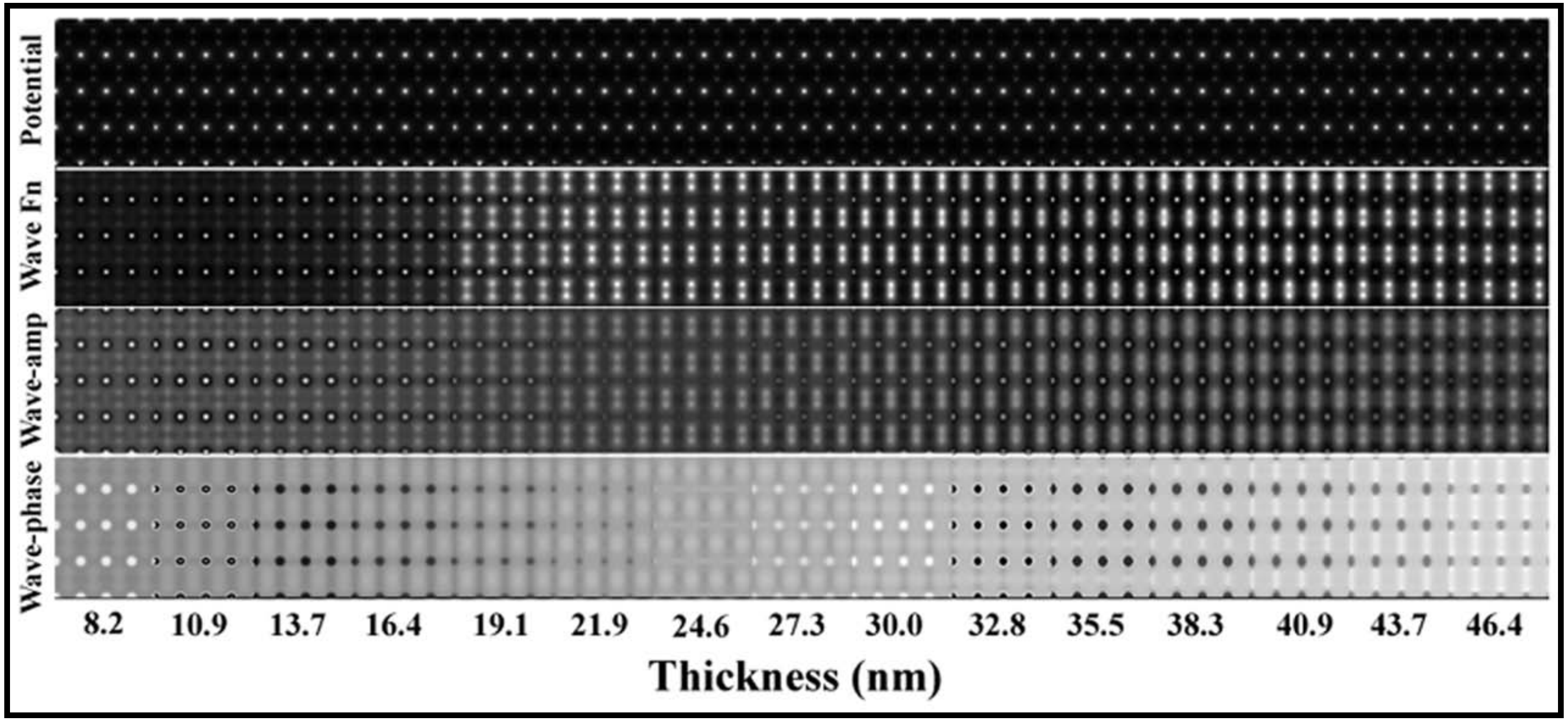

Fig. 6.15: Plot of projected potential and exit-plane wave function, wave amplitude and wave phase with thickness, for hexagonal ω structured phase along $[1\,1\,\overline{2}\,0]$

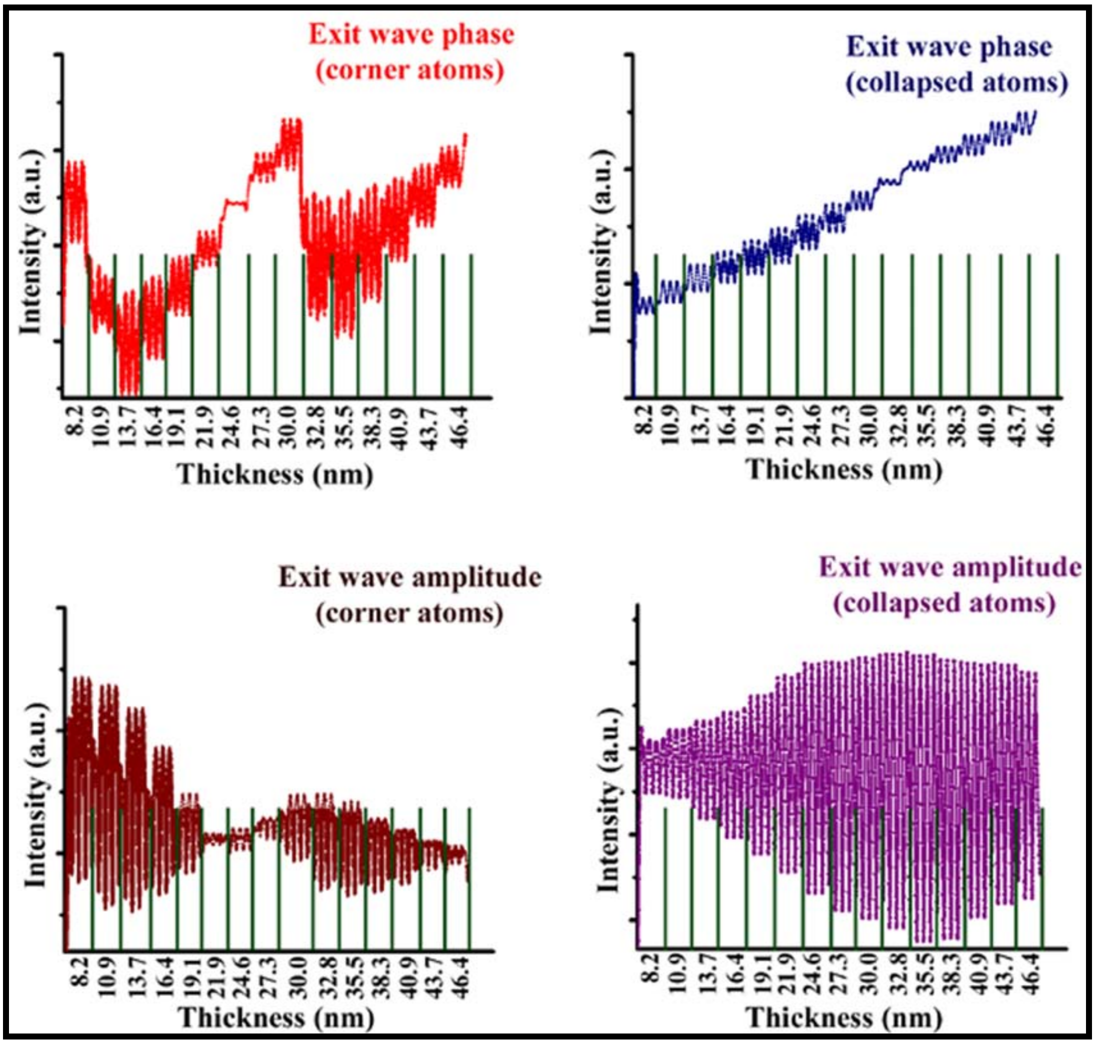

Fig. 6.16: Variation with thickness of the exit-plane wave phase and amplitude along the corner and collapsed atomic columns in hexagonal ω structured phase along $[1\ 1\ \bar{2}\ \ 0]$ orientation

Again beyond 27 nm of thickness, the contrast increases but not upto the extent seen below 22 nm of thickness range. On the contrary, for the collapsed atoms, the brightness increases with the increase in thickness. In a more quantitative manner it can be said that the phase wave of the corner atoms are asymmetrical in nature and it changes more often over the thickness. A combination of these two effects convoluted with the instrument distortion function results in either disappearance or weak presence of intensity from the corner atoms in the thickness range of ~ 34 - 36 nm, which is the case for the micrograph shown in figures 6.9(b) and 6.10(b). Similar analysis has also been done for the atomic columns present along $[1\bar{2}\,1\,3]$ zone axis of ω structure. Figure 6.17 shows the collage of potential map, exit wave map and the amplitude and the phase part of the exit wave map with a function of thickness. The thickness varies in the range of ~ 10 nm to 55 nm. In the potential map both the array contrast of the corner atoms and the jagged contrast of the collapsed atoms are present. Though, the corner atoms appear much brighter than the collapsed atoms. However, the situation is not same for the phase and the amplitude part of the exit wave for the corner atoms and the collapsed atoms. Detailed intensity profile analysis for the phase and the amplitude part of the exit wave for both the corner atoms and the collapsed atoms are shown in figure 6.18. A critical analysis of the profile plots indicates that the contrast from the corner atoms undergo three successive phase reversal in the given thickness range which are at ~ 13 nm, 29 nm and at 38 nm. Whereas, the exit wave phase part for the collapsed atoms does not show any phase reversal, rather the phase intensity increases with the increasing thickness. The amplitude of the exit wave for corner atoms shows brighter contrast throughout the entire thickness range. However, the contrast difference between the collapsed atoms and the corner atoms become minimal in the thickness range of 25 nm to 35 nm. The intensity of the exit wave amplitude for the collapsed atoms remains constant throughout. The combination of phase reversal along with the amplitude modulation results the disappearance or weak contrast for the corner atoms at the given experimental condition as shown in figure 6.7(b).

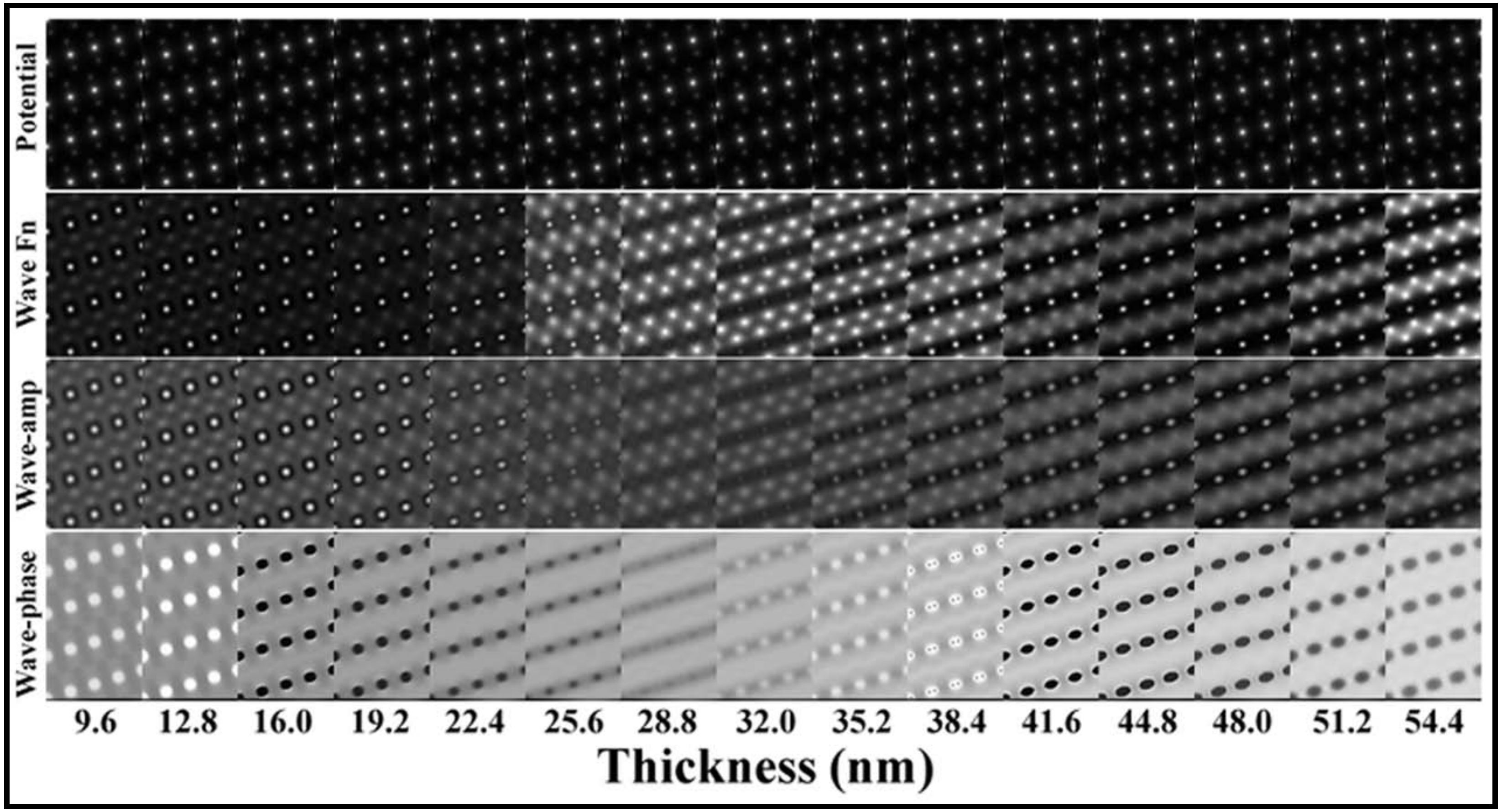

Fig. 6.17: Plot of projected potential and exit-plane wave function, wave amplitude and wave phase with thickness, for hexagonal ω structured phase along $[1\bar{2}\ 1\ 3]$

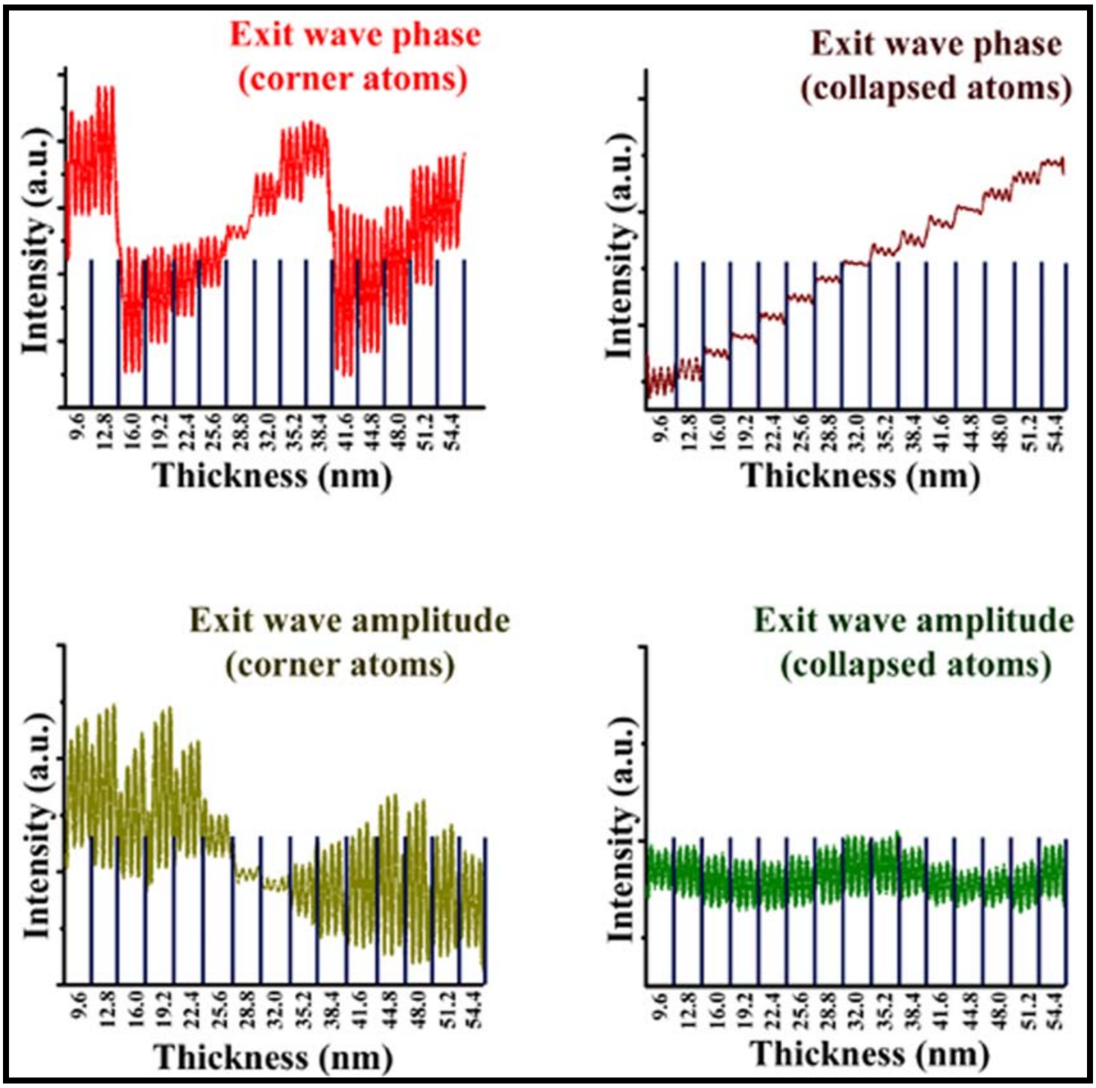

Fig. 6.18: Variation with thickness of the exit-plane wave phase and amplitude along the corner and collapsed atomic columns in hexagonal ω structured phase along $[1\,\overline{2}\,1\,3]$ orientation

6.6: Conclusions

Conclusions from the present chapter are as follows,

(i) *bcc* to ω transition occurs in the phase separated domain for both binary V-50Ti and ternary V-40Ti-20Cr alloy specimen.

(ii) The atomic collapse have been imaged along [1 1 0] and [$\bar{1}$ 1 3] zone axis of the *bcc* phase through phase contrast microscopy and in most of the cases the collapse is partial, making the ω phase of trigonal symmetry.

(iii) Direct structure imaging of ω confirms that for certain defocus and thickness range, the corner atoms of the ω structured phase along both [1 1 0] and [$\bar{1}$ 1 3] zone axis of *bcc*, gives dark atom contrast.

(iv) Multislice image simulations indicate that the difference in the channelling behaviour of the electron waves along the corner atoms and the collapsed atoms are responsible in preferential imaging of one type of atoms to the others.

Chapter VII

Summary and Future Scope

Chapter VII

Summary and Future Scope

7.1: Summary of the thesis

Present thesis has focused on the investigation of phase stability and microstructural evolution in V-Ti-Cr system involving the formation of pseudo-binary Laves phase as well as the β (*bcc*) phase instabilities. During the course of the thesis alloy design principles are used to evaluate the phase stability in binary V-Ti, Ti-Cr, V-Cr and ternary V-Ti-Cr alloys for their entire phase fields. Theoretical predictions are further supported through different electron microscopy based techniques and quantitative simulations. Several fundamental problems were also addressed with systematic investigations during the process – both from the materials and techniques.

Thermodynamic calculations based on the Miedema approach predict the stability of a *bcc* structured phase for the V-rich corner of the ternary V-Ti-Cr diagram. Alloy composition in the Ti-Cr rich side, near the vicinity of $TiCr_2$ Laves phase should stabilize as an intermetallic phase over solidification. For the equiatomic V-Ti alloy, thermodynamic calculations predict a phase separation tendency which would get reduced with the addition of Cr. The validity of these calculations is established through preparation of the alloys and subsequent microstructural and microchemical characterizations. The validation of theoretical predictions through experimental methods confirms that Miedema model can successfully be applied for V-Ti-Cr system.

Zero-loss energy filtered TEM coupled with phase contrast image simulation and atomic structure modeling confirms that Ti-55Cr-7V alloy, selected near the Ti-Cr rich arm of the ternary V-Ti-Cr system, precipitates Laves phase as one of the solidification products. It is further confirmed that vanadium does not occupy any independent ternary positions in $TiCr_2$ lattices; rather V preferentially substitutes the Ti-lattice in the $TiCr_2$ Laves phase. This has also been confirmed by density functional theory calculations which show that the defect formation energy for V in Ti lattice and in the Cr lattice are 0.29 eV and 0.40 eV respectively. Electron intensity profile comparison between the experimental image and the simulated micrographs has been used to study the preferential site occupancy of V atoms in cubic $TiCr_2$ lattice.

A detailed investigation was carried out to study the mechanism of the phase separation in equiatomic V-Ti alloy composition and also in ternary V-40Ti-20Cr alloy. Phase contrast and STEM-HAADF imaging aided with different electron spectroscopy techniques e.g. XEDS and EELS confirms that compositional fluctuation in these alloys manifests through a spinodal decomposition mechanism and not through nucleation and growth. Energy filtered TEM experiments further confirm that the modulation length, which was ~ 4-5 nm in the as-melted V-50Ti alloy gradually diminishes over heat treatments with time and another new wave of modulation length ~ 18-20 nm form and dominate over the system. In contrast, for V-40Ti-20Cr only one modulation length of ~ 4-5 nm generate over solidification and exists throughout entire heat treatment procedure. Both of V-50Ti and V-40Ti-20Cr alloys are given similar types of thermal treatments for a fixed time schedule; however, spinodal decomposition proceeds to an advanced state only in V-50Ti alloy, establishing that Cr reduced the tendency of phase separation in V-

Ti alloy. In both the alloys, composition partitioning gives rise to a Ti rich and Ti lean domains. STEM-EELS and EFTEM studies confirm that the phase separation is essentially a pseudo-binary event involving only Ti and V. Cr is homogeneously distributed throughout the matrix.

Another interesting observation in the present work is the formation of nanostructured ω phase in the phase separated domains of V-Ti and V-Ti-Cr alloys. Phase separation in both of these alloys gives rise to a Ti rich and Ti lean domains in nm scale over solidification. This chemical segregation in the phase separated alloy acts as a driving force for further phase transformation reactions and gives rise to ω structured domains. Structure imaging of these ω domains with the aid of phase contrast microscopy and multislice image simulation have also been carried out and reported in the present thesis. During *bcc* → ω transition, ω phase stabilizes either in hexagonal or trigonal structures depending upon the extent of collapse of the atomic planes. In the present thesis systematic studies are carried out to determine the nature of these collapses. The contrast of the collapsed atoms and the corner atoms are understood through systematic studies of the experimental images and the intensities, as seen along simulated exit waves and their phase and amplitude parts along different zone axis. A method has been described to understand the qualitative nature of the electron channeling behaviour along different atomic positions of the ω structure. Attempts have also been made to study the interface modulation between the *bcc* and ω domains.

From the aspect of electron microscopy techniques and simulations, two more issues are encountered in the present thesis. First one is deriving spectroscopic information through high-resolution imaging which is essentially the determination of single atomic column chemistry through high-resolution electron microscopy. Systematic experiments and simulations are carried out to demonstrate that it is possible to extract compositional information of the sample by detailed analysis of an image obtained under carefully controlled conditions. With precisely determined thickness and orientation of the specimen and acquisition with a well-characterized microscope, the high resolution micrographs can be subjected to comparison with simulated images in order to identify its compositions. Images consisting of elements with large single atom potential variations are most easily recognizable and in some cases can even be used to reveal compositional variations. This procedure in principle should work for any high resolution images and can be exploited as an alternative to STEM-HAADF.

Another issue dealt in the present thesis is the utilization of complementary nature of the electron microscopy techniques for understanding materials phenomena. Advent of nanotechnology over last couple of decades has not only reduced the size of basic building block of materials by several orders of magnitude, complexity of materials architecture and chemistry has also increased enormously. In such a scenario, judicious application of suitable microscopy techniques as well as a combination of them can only provide answer to a particular question. In the present thesis, a combination of diffraction contrast, phase contrast and Z contrast microscopy with the aid of X-ray and electron spectroscopy techniques, multislice image simulation and atomic structure modeling are applied to solve the complex materials related issues encountered in V-Ti-Cr alloys which is otherwise not possible by any of these individual techniques. Though all of these techniques fetch the materials information at the atomistic scale, still each one of them is unique by electro-optical configuration and interaction with the materials. In another word all of these techniques are complementary to each other and only a combination of all of these techniques can provide the complete solution of the materials related issues.

7.2: Scope for future work

There is a huge scope for further investigations in this field of study. Some of the most prominent ones are mentioned below.

(i) Thermodynamic calculations, successfully applied to understand the phase structural information in V-Ti-Cr alloys, can be extended for other transition metal based alloy systems and the predictions can be verified through similar experimental procedures. First principles based calculations can also be carried out to study the phase stability in transition metal alloy systems.

(ii) Conclusions obtained for the V-Ti-Cr system in the present thesis can be re-verified through different other characterization techniques e.g. Atom Location by Channeling Enhanced Microanalysis (ALCHEMI), 3D- Atom Probe techniques (3DAP) and so on.

(iii) Detailed microstructural and microchemical characterization associated with image simulation is required to study the interface between the spinodal decomposed regions and also along the ω - *bcc* interface. It would be interesting to study the interface modulation both in terms of structure and chemistry as a function of heat treatments also. Strains associated with the spinodal decomposed regions can also be estimated through Geometrical Phase Analysis (GPA) or Peak Pair Analysis (PPA).

(iv) Present thesis described phase transformation and microstructural evolution for different model compositions of V-Ti-Cr alloy system essentially prepared in a clean environment. However, the situation may not remain same for most of the engineering alloys used in practical purposes. Higher affinity of vanadium and V-alloys towards the interstitial impurities poses a major challenge in its engineering applications. Microscopic understanding of vanadium-interstitial interaction is required for better assessment of V alloys at in-service condition. Hence the present set alloys can be re-visited after incorporation of interstitial impurities (eg. C, O, N) through controlled experiments. V-Ti-Cr alloys specific model experiments can be designed and carried out to study the structural stability of these alloys in presence of interstitial impurities.

During the course of the thesis sincere efforts have been made to provide significant contribution in understanding the phase stability and microstructure evolution in V-Ti-Cr alloys using phase contrast, HAADF imaging and electron spectroscopy techniques. However, the efforts are to be continued using both experimental and theoretical tools to develop newer materials with suitable thermodynamic and kinetic properties and also to assess their phase stability and structure-property behaviors.

References

Ahn, C.C., Krivanek, O.L., Burgner, R.P., Disko, M.M. and Swann, P.R. (1983) EELS Atlas: A reference guide of electron energy loss spectra covering all stable elements, ASU HREM facility and Gatan.

Akiba, E. and Iba, H. (1998) *Intermetallics* 6(6):461-470.

Arashima, H., Takahashi, F., Ebisawa, T., Itoh, H. and Kabutomori, T. (2003) *J Alloy Compd.* 356-357:405-408.

Asano, K., Hayashi, S., Nakamura, Y. and Akiba, E. (2010) *J Alloy Compd.* 507:399-404.

Ashby, M.F. (2011). Materials selection in mechanical design 4th edn., Oxford, Elsevier BH.

Atwater, H.A. and Polman, A. (2010) *Nature Mat.* 9:205-213.

Banerjee, R., Collins, P.C., Bhattacharyya, D., Banerjee, S. and Fraser, H.L. (2003) *Acta Mater.* 51:3277-3292.

Banerjee, S. (2013). Studies on Advanced Materials for Hydrogen Storage. Bhabha Atomic Research Centre, Mumbai, India.

Banerjee, S. and Cahn, R.W. (1983) *Acta Metall.* 31(10):1721-1735.

Banerjee, S. and Mukhopadhyay, P. (2004). Phase Transformaitons: Examples from titanium and zirconium alloys, first ed., Oxford: Pergamon Press.

Banerjee, S., Kumar, A., Ruz, P. and Sengupta, P. (2016) *Int. J. Hydrog. Energy* dx.doi.org/10.1016/j.ijhydene.2016.07.088.

Basak, S., Sashikala, K., Sengupta, P. and Kulshreshtha, S.K. (2007) *Int. J. Hydrog. Energy* 32:4973-4977.

Basak, S., Shashikala, K. and Kulshreshtha, S.K. (2008) *Int. J. Hydrog. Energy* 33:350-355.

Basu, J. (2004). Glass Forming Ability and Stability: Bulk Zr-based and Marginal Al-based Glasses. Indian Institute of Science, Bangalore, India.

Basu, J. and Ranganathan, S. (2008) *Acta Mater.* 56:1899-1907.

Basu, J. and Ranganathan, S. (2009) *Intermetallics* 17:128-135.

Basu, J., Murty, B.S. and Ranganathan, S. (2008) *J. Alloys Comp.* 465:163-172.

Basu, J., Nagendra, N., Li, Y. and Ramamurty, U. (2003) *Philos. Mag.* 83:1747-1760.

Bendersky, L.A., Boettinger, W.J., Burton, B.P., Biancaniello, F.S. and Shoemaker, C.B. (1990a) *Acta Metall. Mater.* 38(6):931-943.

Bendersky, L.A., Burton, B.P., Boettinger, W.J. and Biancaniello, F.S. (1990b) *Scripta Metall. Mater.* 24(8):1541-1546.

Bennett, J.M., Barnard, J.S., Stone, H.J., Midgley, P.A., Rugg, D. and Jones, N.G. (2015) *Scripta Mater.* 107:79-82.

Bera, S., Mazumdar, S., Ramgopal, M., Bhattacharyya, S. and Manna, I. (2007) *J. Mater. Sci.* 42:3645-3650.

Berry, R.L. and Raynor, G.V. (1953) *Acta Cryst.* 6:178-186.

Bobet, J.L., Chevalier, B. and Darriet, B. (2000) *Intermetallics* 8:359-363.

Boothroyd, C. B. (1998) *J. Microsc.* 190:99-108.

Bououdina, M., Grant, D. and Walker, G. (2006) *Int. J. Hydrog. Energy* 31(2):177-182.

Bououdina, M., Soubeyroux, J.L. and Fruchart, D. (2001) *J. Alloys Comp.* 327:185-194.

Bridgman P.W. (1952) *Proc. Am. Acad. Arts Sci.* 81(4):165-251.

Browning, N. D. and Pennycook, S. J. (1996) *J. Phys. D: Appl. Phys.* 29:1779-1798.

Browning, N. D., Buban, J. P., Nellist, P. D., Norton, D. P., Chisholm, M. F. and Pennycook, S. J. (1998) *Physica C* 294:183-193.

Bundy, F.P. (1965) Formation of new materials and structures by high-pressure treatment, Irreversible effect of high pressure and temperature on materials, ASTM special Technical Publication 374:52-67, A symposium presented at the International Conference of Materials, ASTM, Philadelphia, Pa.

Butler, E.P. and Thomas, G. (1970) *Acta Metall.* 18:347-365.

Cahn, J.W. (1961) *Acta Metall.* 9:795-801.

Cahn, J.W. (1962) *Acta Metall.* 10:907-913.

Cahn, J.W. (1964) *Acta Metall. – Letter to the editor* 1457

Cahn, J.W. (1965) *The Jour. Chem. Phys.* 42(1) 93-99.

Cahn, J.W. (1968) *Trans. Metall. Soc. AIME* 242:166-180.

Cahn, J.W. and Hilliard, J.E. (1958) *The Jour. Chem. Phys.* 28(2) 258-267.

Cahn, J.W. and Hilliard, J.E. (1959) *The Jour. Chem. Phys.* 31(3) 688-699.

Candra, Y., Fukumoto, K., Kimura, A. and Matsui, H. (1999) *J. Nuclear Mater.* 271-272:301-305.

Chen, J., Xiao, W., Dargusch, M.S. and Ma, C. (2015) Sci. Rep. 5:14632(1-6).

Chen, J.M, Nagasaka, T., Muroga, T., Qiu, S.Y., Li, C. and Nita, N. (2008) *J. Nucl. Mater.* 374:298-303.

Chen, J.M., Chernov, V.M., Kurtz, R.J. and Muroga, T. (2011) *J. Nucl. Mater.* 417:289-294.

Chernov, D.B., Molokanov, V.V., Budberg, P.B. and Shinyaev, A.Y. (1982). In J.C. Williams and A.F. Belov (Eds.), Titanium and Titanium alloys. (Vol. 2, 1307). New York, Plenum Press.

Cho, S-W., Han, C-S., Park, C-N. and Akiba, E, (1999) *J Alloy Compd.* 288:294-298.

Chu, F., Thoma, D. J., Kotula, P. G., Gerstl, S., Mitchell, T. E., Anderson, I. M. and Bentley, J. (1998) *Acta Mater.* 46:1759-1769.

Cook, H.E. (1974) *Acta Metall.* 22:239-247.

Cook, H.E. (1975a) *Acta Metall.* 23:1027-1039.

Cook, H.E. (1975b) *Acta Metall.* 23:1041-1054.

Crewe, A.V., Wall, J. and Langmore, J. (1970) *Science* 168:1338-1340.

Curtarolo, S., Hart, G.L.W., Nardelli, M.B., Mingo, N., Sanvito, S. and Levy, O. (2013) *Nature Mater.* 12:191-201.

Daniel, V. and Lipson, H. (1943) *Proc. R. Soc. London (Ser. A)* 181A:368-378.

de Fontaine, D. (1970) *Acta Metall.* 18:275-279.

de Fontaine, D. (1988) *Metal .Trans. A* 19A:169-175.

de Fontaine, D. and Buck, O. (1973) *Philos. Mag.* 27(4):967-983.

de Fontaine, D. and Kikuchi, R. (1974) *Acta Metall.* 22:1139-1146.

de Fontaine, D., Paton, N.E. and Williams, J.C. (1971) *Acta Metall.* 19:1153-1162.

Dehai, P. (2014) *Acta Metall. Sinica (Eng. Letters)* 27(1):1-11.

Devaraj, A. (2011). Phase separation and second phase precipitation in beta Titanium alloys. University of North Texas, USA.

Devaraj, A., Nag, S., Srinivasan, R., Williams, R.E.A., Banerjee, S., Banerjee, R. and Fraser, H.L. (2012) *Acta Mater.* 60:596-609.

Dey, G.K., Tewari, R., Banerjee, S., Jyoti, G., Gupta, S.C., Joshi, K.D. and Sikka, S.K. (2004) *Acta Mater.* 52:5243-5254.

Dickey, E. C., Fan, X. and Pennycook, S. J. (1999) *Acta Mater.* 47:4061-4068.

Dresselhaus, M.S. and Thomas, I.L. (2001) *Nature* 414:332-337.

Duerig, T.W. and Williams, J.C. (1984). Overview: Microstructure and properties of β Titanium alloys. *Proc. of β Titanium alloys in the 80's,* (pp. 19-67) Atlanta, GA, USA.

Duerig, T.W., Terlinde, G.T. and Williams, J.C. (1980). The ω phase reaction in Titanium alloy, in: H. Kimura, O. Izumi (Eds.), Titanium '80 Science and Technology – Proc of the 4th Intl. Conf. on Titanium, Vol 2 (pp. 1299-1308).

Duffey, R.B. (2005) *Prog. Nucl. Energy* 47(1-4):535-543.

Dutta, J., Ananthakrishna, G. and Banerjee, S. (2012) *Acta Mater.* 60:556-564.

Dyakonova, N.B., Lyasotsky, I.V. and Nosova, G.I. (2008) *Rev. Adv. Mater. Sci.* 18:703-710.

Dyck, D. V., Tendeloo, G. V. and Amelinckx, S. (1982) *Ultramicroscopy* 10:263-280.

Ehrlich, K. (1999) *Phil. Trans. R. Soc. Lond. A* 357:595-623.

Enomoto, M. (1992) *J. Phase Equilibria* 13(2):195-200.

Farrar, P. and Margolin, H. (1967) *ASM Trans. Q.* 60:57-66.

Favvas, E.P. and Mitropoulos, A.C. (2008) *J. Engg. Sci. Tech. Rev.* 1:25-27.

Figueroa, I.A., Plummer, J.D., Lara-Rodriguez, G.A., Novelo-Peralta, O. and Todd, I. (2013) *J. Mater. Sci.* 48:1819-1825.

Findik, F. (2012) *Mater. Design* 42:131-146.

Fratzl, P., Penrose, O. and Lebowitz, J.L. (1999) *J. Stat. Phys.* 95 (5-6):1429-1503.

Frost, P.D., Parris, W.M., Hirsch, L.L., Doig, J.R. and Schwartz, C.M. (1954) *Trans. Am. Soc. Metals* 46:231-256.

Fuming, W. and Flower, H.M. (1989) *Mater. Sci. Tech.* 5:1172-1177.

Gale, W.F. and Totemeier, T.C. (2004): Smithells Metals Reference Book, 8th ed., 8.1-8.58 Oxford: Elsevier Butterworth-Heinemann.

Gallego, L.J., Somoza, J.A. and Alonso, J.A. (1990) *J. Phys.: Condens. Matter* 2:6245-6250.

Ghosh, C., Basu, J., Divakar, R. and Mohandas, E. (2015a) *Mater. Characterization* 106:292-301.

Ghosh, C., Basu, J., Khan, S., Divakar, R., Mohandas, E. and Vijayalakshmi, M. (2013) *Trans. Ind. Inst. Metals* 66:381-385.

Ghosh, C., Sharma, V., Basu, J., Divakar, R. and Mohandas, E. (2015b) *Philos. Mag.* 95(22):2403-2426.

Ghosh, G. (2002) *J. Phase Equilibria* 23:310-328.

Ghosh, S., Basu, J., Divakar, R., Mohandas, E. and Vijayalakshmi, M. (2012) *Intermetallics* 23:148-157.

Gibbs, J.W. (1948) “Collected Works” 1:105,252.

Giovanni, M. (2008) *Int. J. Hydrog. Energy* 34:7116-7121.

Glaisher, R. W., Spargo, A. E. C. and Smith, D. J. (1989a) *Ultramicroscopy* 27:19-34.

Glaisher, R. W., Spargo, A. E. C. and Smith, D. J. (1989b) *Ultramicroscopy* 27:.117-130.

Glaisher, R. W., Spargo, A. E. C. and Smith, D. J. (1989c) *Ultramicroscopy* 27:131-150.

Grätzel, M. (2001) Nature 414:338-344.

Gronsky, R. (1988) *Ultramicroscopy* 24:155-168.

Gschneidner, Jr. K.A., and Pecharsky, V.K. (2006) *Z. Kristallogr.* 221:375-381.

Gupta, C.K. and Krishnamurthy, N. (1992). *Extractive metallurgy of Vanadium,* first ed., Amsterdam: Elsevier science publishers B.V.

Haider, M., Uhlemann, S., Schwan, E., Rose, H., Kabius, B. and Urban, K.W. (1998) Nature 392:768-769.

Hatakeyama, M., Muroga, T., Tamura, S. and Yamagata, I. (2011) *J. Nucl. Mater.* 417:303-305.

Hazzledine, P. M., Kumar, K. S., Miracle, D. B. and Jackson, A. G. (1992) *MRS Symps. Proc.* 288:591-594.

Hickman, B.S. (1969) *J. Mater. Sci.* 4:554-563.

Hillert, M. (1961) *Acta Metall.* 9:525-536

Hoelzer, D. T., West, M. K., Zinkle, S. J. and Rowcliffe, A. F. (2000) *J. Nuclear Mater.* 283-287:616-621.

Iba, H. and Akiba, E. (1995) *J. Alloys Compd.* 231:508-512.

Iijima, S. (1973) *Acta Crystallogr. A* 29:18-24

Iijima, S. and Allpress, J.G. (1973) *J. Solid State. Chem.* 7:94-105

Inoue, A. (2000) *Acta Mater.* 48:279-306.

Jamieson, J.C. (1963) *Science* 140:72-73.

Jayaraman, A., Klement, Jr. W. and Kennedy, G.C. (1963) *Phys. Rev.* 131 (2):644-649.

Jeong, J., Im, J., Song, K., Kwon, M., Kim, S.K., Kang, Y.B. and Oh, S.H. (2013) *Acta Mater.* 61:3267-3277.

Jiang, C. (2007) *Acta Mater.* 55:1599-1605.

Kanoh, T. (2006) *Nucl. Eng. Des.* 236:1455-1459.

Kauffmann, Y., Oh, S. H., Koch, C. T., Hashibon, A., Scheu, C., Ruhle, M. and Kaplan, W. D. (2011) *Acta Mater.* 59:4378-4386.

Kazantzis, A.V., Aindow, M., Jones, I.P., Triantafyllidis, G.K. and De HossenJ.T.M. (2007) Acta Mater. 55:1873-1884.

Khaled, T., Narayanan, G.H. and Copley, S.M. (1981) *Metall. Trans.* 12A:293-298.

Kim, S-H, Kang, S.J., Park, M-H, Yang, C-W, Lee, H-C, Han, H.N. and Kim, M. (2015) *Acta Mater.* 83:499-506.

Kirkland, E. J. (2009). *Advanced Computing in Electron Microscopy*; 2nd ed. New York: Springer.

Kirkland, E.J. (2016) *Acta Cryst.* A72:1-27.

Koul, M.K. and Breedis, J.F. (1970a) *Acta Metall.* 18:579-588.

Koul, M.K. and Breedis, J.F. (1970b) *Scri. Metall.* 4:877-880.

Kresse, G. and Furthmuller, J. (1996a) *Computational Materials Science* 6:15-50.

Kresse, G. and Furthmuller, J. (1996b) *Phys. Rev. B* 54:11169-11186.

Kresse, G. and Hafner, J. (1994) *Phys. Rev. B* 49:14251-14269.

Kumar, A., Banerjee, S., and Bharadwaj, S.R. (2015) *J. Alloys Compd.* 649:801-808.

Kumar, S. (2012). Studies on Hydrogen Interaction with Vanadium and Vanadium-Aluminium Alloys. Bhabha Atomic Research Centre, Mumbai, India.

Kuo, K. (1953) *Acta Metall.* 01:720-724.

Kuriiwa, T., Tamura, T., Amemiya, T., Fuda, T., Kamegawa, A., Takamura, H. and Okada, M. (1999) *J. Alloys Compd.* 293-295:433-436.

Kurtz, R.J., Abe, K., Chernov, V.M., Hoelzer, D.T., Matsui, H., Muroga, T. and Odette, G.R. (2004) *J. Nuclear Mater.* 329-333:47-55.

Kurtz, R.J., Abe, K., Chernov, V.M., Kazakov, V.A., Lucas, G.E., Matsui, H., Muroga, T., Odette, G.R., Smith, D.L. and Zinkle, S.J. (2000) *J. Nucl. Mater.* 283-287:70-78.

Lai, M.J., Tasan, C.C., Zhang, J., Grabowski, B., Huang, L.F. and Raabe, D. (2015) *Acta Mater.* 92:55-63.

Le Flem, M., Gentzbittel, J-M. and Wident, P. (2013) *J. Nucl. Mater.* 442:S325-S329.

Lee, J.Y., Kim, J.H. and Lee, H.M. (2000) *J. Alloys Comp.* 297:231-239.

Lee, J.Y., Kim, J.H., Park, S I1. And Lee, H.M. (1999) *J. Alloy Compd.* 291:229-238.

Levin, I., Krayzman, V., Chiu, C., Moon, K. W. and Bendersky, L. A. (2012) *Acta Mater.* 60:645-656.

Li, R., Zhang, P., Li, X., Zhang, C. and Zhao, J. (2013) *J. Nucl. Mater.* 435:71-76.

Lin, H.C., Lin, K.M., Wu, K.C., Hsiung, H.H. and Tsai, H.K. (2007) *Int. J. Hydrog. Energy* 32:4966-4972.

Liu, B.H., Kim, D.M., Lee, K.Y. and Lee, J.Y. (1996) *J. Alloys Compd.* 240:214-218.

Liu, C.T., Zhu, J.H., Brady, M.P., McKamey, C.G. and Pike, L.M. (2000) *Intermetallics* 8:1119-1129.

Liu, X.P., Cuevas, F., Jiang, L.J., Latroche, M., Li, Z.N. and Wang, S.M. (2009) *J. Alloy Compd.* 476:403-407.

Livak, R.J. and Thomas, G. (1971) *Acta Metall.* 19:497-505.

Loomis B.A., Nowicki, L.J. and Smith, D.L. (1994) *J. Nuclear Mater.* 212-215:790-793.

Loomis, B.A. and Smith, D.L. (1992) *J. Nuclear Mater.* 191-194:84-91.

Lototsky, M.V., Yartys, V.A. and Zavaliy, I.Y. (2005) *J. Alloys Compd.* 404-406:421-426.

Malm, J.O. and O'Keefe, M.A. (1997) *Ultramicroscopy* 68:13-23.

Marban, G. and Solis, T.V. (2007) *Int. J. Hydrog. Energy* 32:1625-1637

Matsui, K., Ujita, H. and Tashimo, M. (2008) *Prog. Nucl. Energy* 50:97-102.

Matsunaga, T., Kon, M., Washio, K., Shinozawa, and Ishikiriyama, M. (2009) *Int. J. Hydrog. Energy* 34:1458-1462.

Matumara, T., Yukawa, H. and Morinaga, M. (1999) *J. Alloy Compd.* 284:82-88.

McCabe, K. K. and Sass, S.L. (1971) *Philos. Mag.* 23:957-970.

Menter, J.W. (1956) *Proc. R. Soc. London (Ser. A)* 236:119-135.

Merica, P.D. (1932) *Trans. AIME* 99:13-54.

Miedema, A. R. (1976) *Philips Tech. Rev.* 36:217-231.

Ming, L.-c., Manghnani, M.H. and Katahara, K.W. (1981) *Acta Metall.* 29:479-485.

Miracle, D.B., Sanders, W.S. and Senkov, O.N. (2003) *Philos. Mag*. 83(20):2409-2428.

Momma, K. and Izumi, F. (2011) *J. Appl. Crystallogr.* 44:1272-1276.

Morgan, D., Ceder, G. and Curtarolo, S. (2005) *Meas. Sci. Technol.* 16:296-301.

Müller, C.M., Sologubenko, A.S., Gerstl, S.S.A. and Spolenak, R. (2015) *Acta Mater.* 89:181-192.

Muller, D.A. (2008) Science 319:1073-1076

Muller, D.A. (2009) *Nature Mater.* 8:263-270.

Muroga, T., Chen, J.M., Chernov, V.M., Kurtz, R.J. and Le Flem, M. (2014) *J. Nucl. Mater.* 455:263-268.

Muroga, T., Nagasaka, T., Abe, K., Chernov, V. M., Matsui, H., Smith, D. L., Xu, Z. Y. and Zinkle, S. J. (2002) *J. Nuclear Mater.* 307-311:547-554.

Murray, J.L. (1988). In T.B. Massalski (Eds.). Binary alloy phase diagrams, (Vol. 2, 2134). Metals Park, OH, ASM International.

Nag, S. (2008). Influence of beta instabilities on the early stages of nucleation and growth of alpha in beta Titanium alloys. The Ohio State University, USA.

Nag, S., Banerjee, R., Srinivasan, R., Hwang, J.Y., Harper, M. and Fraser, H.L. (2009) *Acta Mater.* 57(7):2136-2147.

Nag, S., Devaraj, A., Srinivasan, R., Williams, R.E.A., Gupta, N., Viswanathan, G.B., Tiley, J.S., Banerjee, S., Srinivasan, S.G., Fraser, H.L. and Banerjee, R. (2011) *Phys. Rev. Lett.* 106:245701 1-4.

Narayanan, G.H. and Archbold, T.F. (1970) *Scr. Metall.* 4:873-876.

Nature Materials editorial (2009) *Nature Materials* 8:81.

Nature Materials editorial (2010) *Nature Materials* 9:89.

Ng, H.P., Devaraj, A., Nag, S., Bettles, C.J., Gibson, M., Fraser, H.L., Muddle, B.C. and Banerjee, R. (2011) *Acta Mater.* 59:2981-2991.

Niessen, A.K., de Boer, F.R., Boom, R., de Chatel, P.F., Mattens, W.C.M. and Miedema, A.R. (1983) *Calphad* 7:51-70.

Nomura, K. and Akiba, E. (1995) *J. Alloy Compd.* 231:513-517.

Ohmuri, Y., Ogo, T., Nakai, K.and Kobayashi, S. (2001) *Mater. Sci. Engg. A* 312:182-188.

Ohnuki, S., Takahashi, H., Kinoshita, H. and Nagasaki, R. (1988) *J. Nuclear Mater.* 155-157: 935-939.

Ohta, Y and Pettifor, D.G. (1992) *J. Phys.: Condens. Matter* 2:8189-8194.

Okaniwa, H., Shindo, D., Yoshida, M. and Takasugi, T. (1999) *Acta Mater.* 47:1987-1992.

Okunishi, E., Kawai, T., Mitsuhara, M., Farjami, S., Itakura, M., Hara, T. and Nishida, M. (2013) *J. Alloy Compd.* 577S:S713-S716.

Palit, M., Chelvane, J. A., Basumatary, H., Banumathy, S., Singh, A. K., Pandian, S. and Chandrasekaran, V. (2010) *Intermetallics* 18:1027-1032.

Paufler, P. (2011) *Intermetallics* 19:599-612.

Pei, P., Song, X.P., Liu, J., Zhao, M. and Chen, G.L. (2009) *Int. J. Hydrog. Energy* 34:8597-8602.

Pennycook, S. J., Dickey, E. C., Nellist, P. D., Chisholm, M. F., Yan, Y. and Pantelides, S. T. (1999) *J. European Ceram. Soc.* 19:2211-2216.

Perdew, J. P., Kieron, B. and Matthias, E. (1996) *Phys. Rev. Lett.* 77:3865-3868.

Pettifor, D.G. (1986) *J. Phys. C: Solid State Phys.* 19:285-313

Pettifor, D.G. (1988) *Physica B* 149:3-10.

Pynn, R. (1978) *J. Phys .F: Metal Phys.* 8(1):1-13.

Raj, B. and Rajan, M. (2007) *Int. J. Environ. Stud.* 64(6):729-747.

Ramsteiner, I.B., Schöps, A., Phillipp, F., Kelsch, M., Reichert, H., Dosch, H. and Honkimäki, V. (2006) *Phys. Rev. B* 73:(024204)1-7.

Ramsteiner, I.B., Shchyglo, O., Mezger, M., Udyansky, A., Bugaev, V., Schöder, S., Reichert, H. and Dosch, H. (2008) *Acta Mater.* 56(6):1298-1305.

Ranchal, R., Gutiérrez-Diaz, V and González Martín, V. (2012) *Acta Mater.* 60:1840-1845.

Ranganathan, S. and Inoue, A. (2006) *Acta Mater.* 54:3647-3656.

Reilly, J.J. and Wiswall, R.H. (1970) *Inorg. Chem.* 9(7):1678-1683.

Rose, H. (2008). History of direct aberration correction. In P. Hawkes (Eds.) Advances in Imaging and Electron Physics. (Vol. 153, pp. 1-39). San Diego, USA, Elsevier.

Samsonova, N.N. and Budberg, P.B. (1967) *Inorg. Mater.* 3:730-735.

Sanchez, J.M. and de Fontaine, D. (1978) *Acta Metall.* 26:1083-1095.

Sankaran, R.P., Ophus, C., Ozdol, B., Radmilovic, V.R., Minor, A.M. and Morris, Jr. J.W. (2014) *Philos. Mag.* 94(25):2900-2912.

Santos, D. S. d., Bououdina, M. and Fruchart, D. (2002) *J. Alloy Compd.* 340:101-107.

Sathyanarayanan, S., Basu, J., Moitra, A., Sasikala, G. and Singh, V. (2013) Met. Mater. Trans. A 44:2141-2155.

Schryvers, D. and Tanner, L.E. (1990) *Mater Sci. Forum* 56-58:329-334.

Scott, M.C., Chen, C.C., Mecklenburg, M., Zhu, C. Xu, R., Ercius, P, Dahmen, U, Regan, B.C. and Miao, J.W. (2012) Nature 483:444-448.

Senkov, O.N., Senkova, S.V., Woodward, C. and Miracle, D.B. (2013) *Acta Mater.* 61:1545-1557.

Sharma, V., Pilania, G., G. A. Rossetti, J., Slenes, K. and Ramprasad, R. (2013) *Phys. Rev. B* 87:1341091-1341097.

Shashikala, K., Banerjee, S., Kumar, A., Pai, M. R. and Pillai, C. G. S. (2009) *Int. J. Hydrog. Energy* 34:6684-6689.

Shashikala, K., Kumar, A., Betty, C. A., Banerjee, S., Sengupta, P. and Pillai, C. G. S. (2011) *J. Alloys and Comp.* 509:9079-9083.

Sheibani, S., Heshmati-Manesh, S., Ataie, A., Caballero, A. and Criado, J.M. (2014) *J. Alloys Comp.* 587:670-676.

Sikka, S.K., Vohra, Y.K. and Chidambaram, R. (1982) *Prog. Mater. Sci.* 27:245-310.

Singh, B.K., Cho, S.W. and Bartwal, K.S. (2014) *Int. J. Hydrog. Energy* 39:8351-8356.

Sinkler, W. (1996) *Acta Mater.* 44:1623-1636

Sluiter, M. and Turchi, P.E.A. (1991) *Phys. Rev. B* 43(15):12251-12266.

Smith, D. J. (2012) *Micron* 43:504-508.

Smith, D.L., Chung, H.M., Loomis, B.A., Matsui, H., Votinov, S. and van Witzenburg, W. (1995) *Fusion Eng. Des.* 29: 399-410.

Smith, D.L., Chung, H.M., Matsui, H. and Rowcliffe, A.F. (1998) *Fusion Eng. Des.* 41(1-4):7-14.

Smith, D.L., Loomis, B.A. and Diercks, D.R. (1985*) J. Nuclear Mater.* 135:125-139.

Song, X.P., Pei, P., Zhang, P.L. and Chen, G.L. (2008) *J. Alloy Compd.* 455:392-397.

Stadelmann, P.A. (1987) *Ultramicroscopy* 21(2):131-145.

Steele, B.C.H. and Heinzel, A. (2001) Nature 414:345-352.

Stein, F., Palm, M. and Sauthoff, G. (2005) *Intermetallics* 13:1056-1074.

Stein, F., Palm, M., and Sauthoff, G. (2004) *Intermetallics* 12:713-720.

Sukedai, E., Kitano, Y. and Ohnishi, A. (1997) *Micron* 28(4):269-277.

Sukedai, E., Lim, W.Y. and Hida, M. (1993) *J. Mater. Sci.* 28(18):4918-4924.

Sukedai, E., Liu, W., Awaji, M. and Horiuchi, T. (1994) *Ultramicroscopy* 54:192-200.

Suwarno, S., Solberg, J.K., Maehlen, J.P., Krogh, B. and Yartys, V.A. (2014) *J. Alloys Comp.* 582:540-546.

Takasugi, T., Yoshida, M. and Hanada, S. (1996) *Acta Mater.* 44:669-674.

Tamura, T., Kazumi, T., Kamegawa, A., Takamura, H. and Okada, M. (2003) *J Alloy Compd.* 356-357:505-509.

Tarascon, J-M. and Grätzel, M. (2011) Research Initiatives towards sustainable handeling of energy. In V. Dusastre, (Eds.), Materials for sustainable energy (pp. xiii-xxvii). Singapore: Nature publishing group.

Tavoosi, M., Karimzadeh, F., Enayati, M.H., Joo, S-H and Kim, H.S. (2011) *J. Mater. Sci.* 46:7633-7638.

Tewari, R., Mukhopadhyay, P., Banerjee, S. and Bendersky, L.A. (1999) *Acta Mater.* 47(4):1307-1323.

Tsisar, V., Nagasaka, T., Muroga, T., Miyazawa, T. and Yeliseyeva, O. (2013) *J. Nucl. Mater.* 442:528-532.

Tsukahara, M. (2011) *Mater. Trans.* 52(1):68-72.

Urban, K.W. (2008) *Science* 321:506-510.

Van Dyck, D., Van Tendeloo, G. and Amelinckx, S. (1982) *Ultramicroscopy* 10:263-280.

Van Tendeloo, G., Bals, S., Van Aert, S., Verbeeck, J. and Van Dyck, D. (2012) *Adv. Mater.* 1-19, DOI:10.1002/adma.201202107.

Villars, P. (1997). Pearson’s Handbook (Desk edition) for crystallographic data, Vol. 1 & 2, ASM International, Materials Park, OH 44073, USA

Villars, P. (Eds.). (2007). ASM alloy phase diagram centre. ASM International, Materials Park, OH, USA. http://www.asminternational.org/ AsmEnterprise/ APD.

Vujić, J., Antić, D.P. and Vukmirović, Z. (2012) *Energy* 45:31-42.

Wang, H.B., Wang, Q., Dong, C., Yuan, L., Xu, F. and Sun, L.X. (2008) *J. Phys.: Conf. Series* 98:0120181-0120188.

Wang, Y., Chen, L.Q. and Khachaturyan, A.G. (1993) Acta Metall. Mater. 41:279-296.

Wang, Z.R., Qiang, J.B., Wang, Y.M., Wang, Q., Dong, D.D. and Dong, C. (2016) *Acta Mater.* 111:366-376.

Westraadt, J.E., Olivier, E.J., Neethling, J.H., Hedström, P., Odqvist, J., Xu, X. and Steuwer, A. (2015) *Mater. Characterization* 109:216-221.

Williams D.B. and Carter C.B. (2009). Transmission Electron Microscopy. 2nd Edn. New York: Springer Science + Business Media Inc.

Yang, J.C., Small, M.W., Grieshaber, R.V. and Nuzzo, R.G. (2012) *Chem. Soc. Rev.* 41:8179-8194.

Yang, Z. Q., Chisholm, M. F., Yang, B., Ma, X. L., Wang, Y. J., Zhou, M. J. and pennycook, S. J. (2012) *Acta Mater.* 60:2637-2646.

Yao, Q., Sun, J., Zhang, Y. and Jiang, B. (2006) *Acta Mater.* 54:3585-3591.

Young, K-h. and Nei, J. (2013) *Materials* 6:4574-4608.

Yu, X.B., Walker, G.S., Grant, D.M., Wu, Z., Xia, B.J. and Shen, J. (2005) *Appl. Phys. Lett.* 87:133121(1-3).

Zheng, P.F., Nagasaka, T., Muroga, T., Chen, J.M. and Li, Y.F. (2011) *Fusion Eng. Des.* 86:2561-2564.

Zhu, B., Yang, S., Ding, J., Zhang, W., Long, Y. and Wan, F, (2015) *Mater. Lett.* 161:609-612.

Zhu, B., Yang, S., Zhang, M., Ding, J., Long, Y. and Wan, F. (2016) *Mater. Charact.* 111:60-66.

Zinkle, S.J. (2005) *Fusion Eng. Des.* 74(1-4):31-40.

Zinkle, S.J., Matsui, H., Smith, D.L., Rowcliffe, A.F., van Osch, E., Abe, K. and Kazakov, V.A. (1998) *J. Nucl. Mater.* 258-263:205-214.

Züttel, A. (2003) *Mater. Today* 6(9):24-33.